# Modeling and Control of E-jet Printing Process for Multi-layer Structures

by

Zahra Afkhami

A dissertation submitted in partial fulfillment
of the requirements for the degree of
Doctor of Philosophy
(Mechanical Engineering)
in the University of Michigan
2022

Doctoral Committee:

Associate Professor Kira Barton, Chair
Associate Professor David Hoelzle, The Ohio State University
Professor Ilya Kolmanovsky
Associate Professor Chinedum Okwudire
Professor Max Shtein

Zahra Afkhami

zafkhami@umich.edu

ORCID iD: 0000-0003-2251-5171

To my parents Masoumeh and Elyas,
and my loving husband Mohammad.

## ACKNOWLEDGMENTS

I would like to thank my advisor, professor Kira Barton, for giving me the opportunity to learn from her and providing a supportive environment for success. I am forever thankful for her thoughtful guidance and caring patience. I would like to thank my committee members professors David Hoelzle and Max Shtein who have contributed to this research during five years of collaborations. I would also like to thank the remaining committee members Professors Ilya Kolmanovsky and Chinedum Okwudire for their time and guidance. This dissertation would not have been possible without funding from the National Science Foundation and the University of Michigan Rackham Graduate School ( Rackham Conference Travel Grants). Thank you to all my friends for always being there for me and making so many ordinary moments, extraordinary. I would also like to thank the many students and researchers from whom I learned or worked with including: Leo Tse, Christopher Pannier, Isaac Spiegel, Efe Balta, Farhan Javed and Brian Iezzi.

Thank you to my parents Masoumeh and Elyas for their love, support and many sacrifices that they made for my growth and success. Thank you to my sister Azadeh and my brother Reza for being a blessing in my life.

Finally, I am more grateful to my loving husband, Mohammad Kazemi, than the words can express. I thank you for being my soulmate, my love, and my everything.

# TABLE OF CONTENTS

# LIST OF FIGURES

# LIST OF TABLES

# ABSTRACT

Electrohydrodynamic jet (e-jet) printing is a high-resolution additive manufacturing (AM) technique that holds promise for the fabrication of customized micro-devices. Through e-jet printing, a 3D structure is generated by sequential addition of material on the surface [1, 6, 7]. The performance of such structures depends on the uniformity and consistency of the layers [1]. Depending on the application, in order to have high performance and yield, the fabrication process must be able to provide strict adherence to the desired thickness and spatial resolutions. The lack of real-time monitoring methods that can capture, analyze and react to in situ measurements has been a challenge for most AM systems, and in particular $\mu$-AM systems, in which the key dynamics occur at the micro-/nano-scales. Most AM processes run in open-loop and system parameters are tuned by human operators through trial and error. AM processes are innately iteration varying and system parameters change from layer to layer. Control methods that leverage the iterative nature of AM-processes are needed. In this dissertation, e-jet printing is investigated for its capability in depositing multi-layered thin-films of multiple materials with microscale spatial resolution and nanoscale thickness resolution. The traditional method to close the loop in these processes should be feedback control. However, feedback control requires real-time measurement at the microscale, which is not possible with $\mu-$scale AM processes such as e-jet printing, in which, the millisecond time scale and micro to nano-scale length scale make the online measurements difficult. We leverage spatial iterative learning control (SILC) and model predictive control (MPC) to enable robust and intelligent controllers to autonomously direct material addition at the microscale. This dissertation focuses on

*modeling* material deposition at the microscale, and *controlling* the deposition process to fabricate thin-film multi-layered and multi-material structures. First, the material interactions at the microscale are investigated to derive better models of the spatial interactions within the 3D printing, which led to the development of an empirical model of the deposition process that relates process and material parameters to the thickness and uniformity of the layers in multi-layered structures. Then, spatial iterative learning control (SILC) is used to regulate and automate material deposition at the microscale to improve the performance and reliability of the AM processes, without requiring a human operator to physically be in the environment to heuristically tune the process parameters. The proposed SILC framework addresses the combined challenges of incorporating multiple dynamic models into the framework due to the interactions driven by the different build materials and addressing iteration varying initial conditions due to the roughness of previous surfaces by leveraging iteration-to-iteration and layer-to-layer learning with the ability to correct the errors of previous layers. Additionally, this dissertation focuses on extending the SILC framework through the integration of model predictive control (MPC) in order to impose input constraints associated with AM processes and improve robustness and performance of the additive process. The feasibility of the proposed spatial control frameworks to direct the deposition process at the microscale are demonstrated through the experimental validations and simulation case studies using a model of an electrohydrodynamic jet (e-jet) printing process.

# CHAPTER 1

# Introduction

This dissertation investigates modeling and spatial control solutions for sub-micron fabrication using a class of microscale additive manufacturing (AM) techniques known as, Electrohydrodynamic jet (e-jet) printing, with the goals of 1) understanding material interactions at the microscale and 2) enabling high fidelity $\mu$-AM through design and integration of intelligent control frameworks in order to achieve autonomous control of material addition in a layer-by-layer manner. The results of this dissertation are part of a collaboration between the Barton Research Group at the University of Michigan, Shtein Research Lab at the University of Michigan, and Hoelzle Research Lab at The Ohio State University.

## 1.1 Additive Manufacturing

There has been a growing interest in the past decade in the fabrication of high-resolution, thin-film devices such as optical sensors [8–10], flexible electronics [11], memristor devices [12], photonic crystals [13], organic lasing cavities [14], and transistors [15, 16]. To realize high-performance, thin-film devices, the manufacturing process requires deposition of consistent, uniform layers with a repeatable thickness distribution across multiple material classes. Different manufacturing methods such as spin or dip coating [17], lithography [18], doctor blading [19], chemical vapor deposition [20], and others have been used to fabricate thin-film devices. However, most of these methods are limited by substrate planarity, high temperatures, harsh chemistries, or the dissolution of previous layers by non-orthogonal solvents [21]. Furthermore, in certain situations, it is desirable to deposit a customized pattern or to selectively place components on an existing device structure without disturbing it. For example, creating a pixelated array similar to the desired pattern in Figure 1.1a requires many costly lithographic steps as described in Figure 1.1a. Expanding to a larger array with each pixel having multiple materials with different thickness distribution similar to the desired pattern in Figure 1.1b requires a corresponding increase in

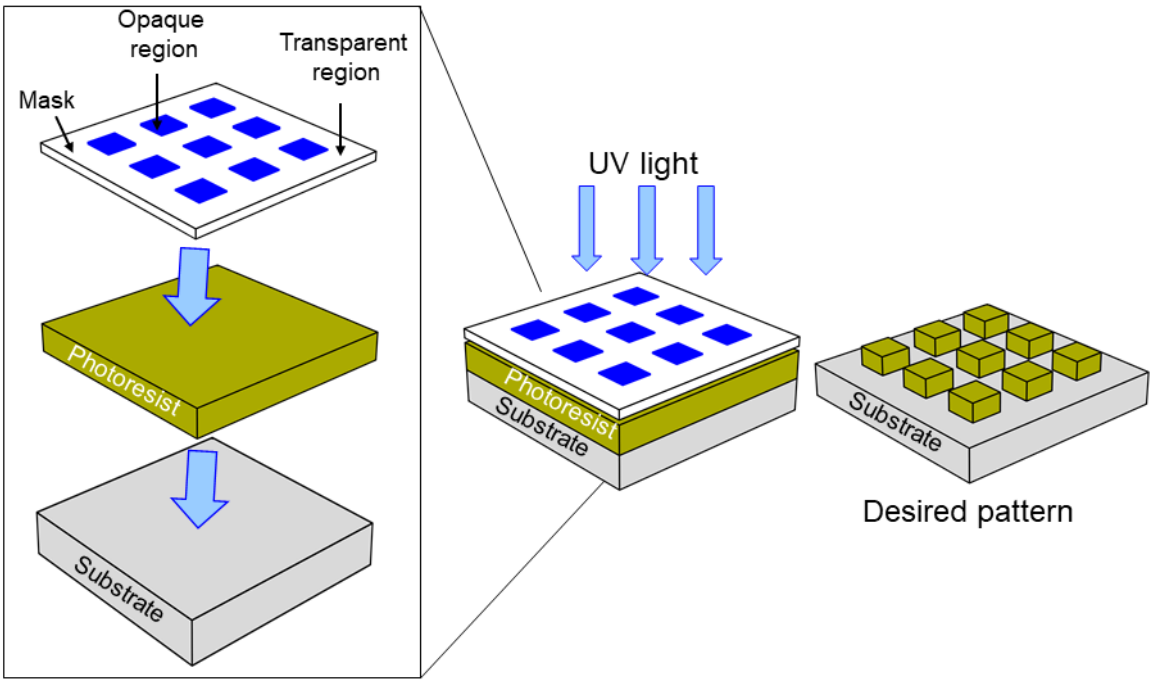


(a)

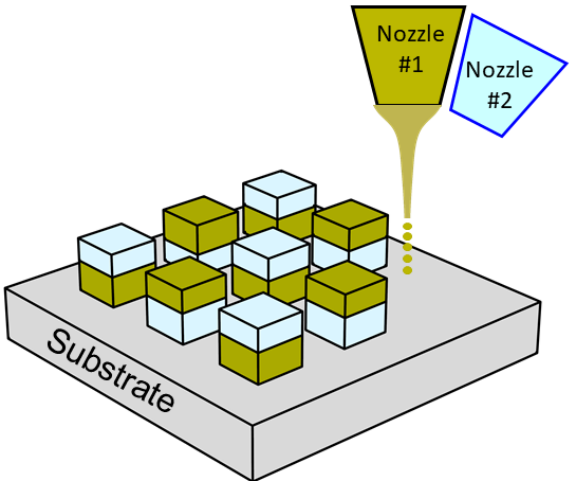


(b)

Figure 1.1: **Manufacturing methods**: a) Lithography: a light sensitive polymer ink is spun into a thin-film. By selective exposure of UV-light through a photomask with defined opaque area, the desired topography is achieved. b) Additive manufacturing achieves flexible designs by direct addition of material on the surface without the masking steps required with Lithography.

masking steps. It is therefore desirable to use Additive manufacturing (AM) technology as a mask-free, direct-deposition method that can print complex structures with less material waste as shown in Figure 1.1b.

To address the challenges noted above, this dissertation examines a micro scale Additive Manufacturing (AM) approach and uses it to realize vertically stacked, thin-film devices using multiple materials. AM processes, also known as 3D printing, are a class of processes that enable fabrication of a printed device, which could be structural or contain other functional characteristics such as a sensor, through selective addition of material in a layer-by-layer manner [1,6,7]. $\mu$m-AM technology in principle enables material deposition on nonplanar surfaces at the microscale, by direct addition of material on existing topographies, without requiring cleanroom facilities and the use of masking steps more commonly used with lithography, and less material waste.

Despite the many advantages of $\mu-$AM techniques over competing microscale manufacturing techniques, models describing in-layer and layer-to-layer material interactions at the microscale are limited or missing for most AM processes. At the microscale, geometric surface effects dominate the wetting behavior of materials on the surface. The formation of thin-films from individually printed droplets requires an understanding of the complex interactions between the printed droplets and previously printed layers. Recent studies have considered the interactions between a single printed droplet and a previously printed layer [2, 22, 23]; however, a systematic method to achieve thin-film patterns from the merging of multiple individual printed droplets is lacking. **This introduces an important gap in understanding how to determine appropriate material combinations to enable multi-material deposition in a layer-by-layer manner**. An important aspect of deriving this understanding in material interactions requires the ability to monitor these interactions in situ. However, for most AM systems, it is difficult to integrate real-time sensing capabilities that can adequately measure the necessary physics in real-time [24]. The lack of real-time monitoring devices that can capture *in situ* measurements is particularly challenging for $\mu$-AM systems where the interactions are at time and length scales that are too fast or too small for many sensing modalities. To address this issue, output and subsequent error measurements are often available after a layer of material has been deposited onto the substrate. Additionally, AM processes are iteration varying, and system parameters and plant dynamics change from layer to layer. Thus, the behavior of a printed layer depends on material and topology interactions from previous layers, which vary in real-world applications. **Control methods that leverage the iterative nature of these processes in the presence of iteration varying plant models are needed**.

# Background

***Thin-film Devices***: A thin-film device is defined as a structure that is fabricated from single or multiple uniform layers ranging from nanometer to several micrometer in thickness. These devices are in demand for many applications, such as optical sensors [8–10], flexible electronics [11], memristor devices [12], photonic crystals [13], organic lasing cavities [14], and transistors [15, 16]. Lithography is the most popular and widely used micro patterning technology to fabricate thin-film devices. Here, we use electrohydrodynamic jet (e-jet) printing to deposit multi-material thin-film structures with resolution comparable to Lithography without the planarity restrictions of Lithography and other subtractive processes. To realize high-performance devices, the manufacturing process requires deposition of consistent, uniform layers with a repeatable thickness distribution across multiple material classes. Figures 1.2c, 1.3 and 2.3 are examples of thin-film micro devices that are fabricated using e-jet printing.

***Inkjet printing***: Inkjet printing, which is probably the most well-known $\mu-$AM technology, has been studied extensively for the creation of multi-material, thin-film devices with demonstrated transistors [23, 25, 26] and optical sensors [27]. The thermal or piezo-driven excitation [28] used to deposit materials in a liquid phase in inkjet printing limits the achievable spatial resolution to larger than 20 $\mu$m. Furthermore, high viscosity inks (>50 cP) necessary for certain applications cannot be printed using inkjet technology [29]. To enable the use of a range of photopolymerizable inks, which can have high viscosity (>500 cP), and acheive high resolution patterns, electrohydrodynamic jet (e-jet) printing is utilized.

***Electrohydrodynamic jet printing***: Electrohydrodynamic jet (e-jet) printing is a solution-based fabrication AM technique enabling thin-film fabrication and patterning without the planarity restrictions of lithography and other subtractive processes. Compared to inkjet technology, e-jet printing has a much higher spatial resolution (0.05-30 $\mu$m), comparable to the resolution of lithographic processes [29, 30], while also providing a high degree of freedom in creating customized patterns. Complex structures can be fabricated with high controllability and precision in desired locations from the micro- to nanoscale. E-jet is also capable of depositing a wide range of fluid viscosities from $10^0$ – $10^5$ cP, several orders of magnitude larger than that of inkjet printing [28]. This further enables flexibility in the classes of materials deposited, from biological materials to polymers and conductive inks [29–31]. Manufacturing speed can also be increased by integrating multiple parallel

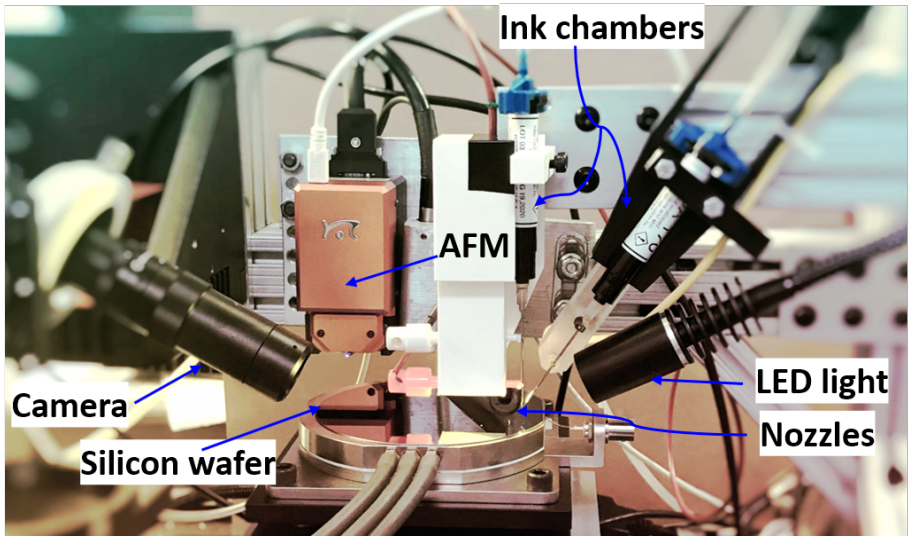


(a)

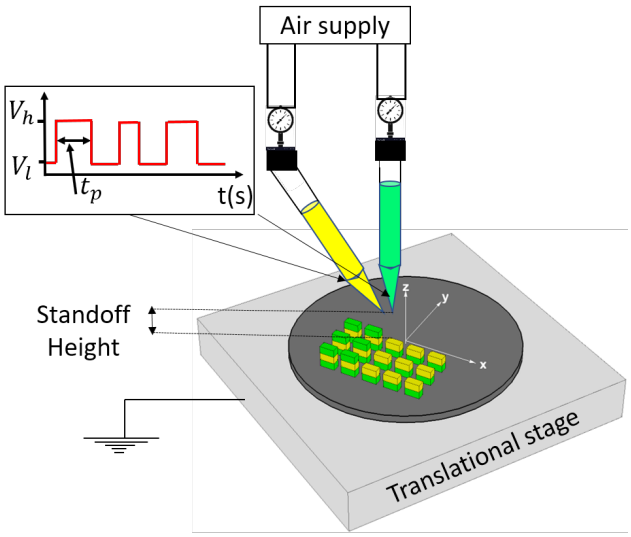


(b)

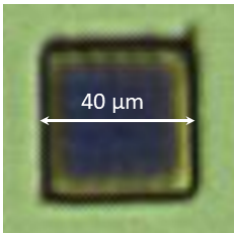


(c)

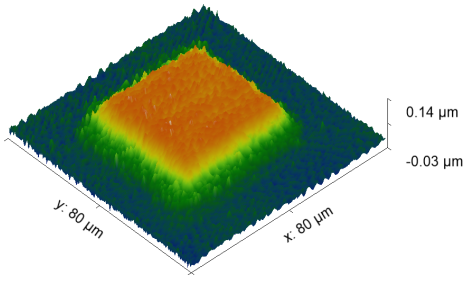


(d)

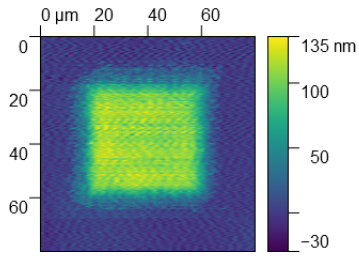


(e)

Figure 1.2: **High-resolution fabrication using e-jet printing technology.** a) E-jet Printer testbed located at the University of Michigan, b) Schematic of e-jet printer with dual nozzles for multi-material deposition. c), d) and e) AFM scans and optical microscopy of a 40 $\times$ 40 $\mu$m$^2$ thin-film pattern deposited by the e-jet system in Figure 1.2b.

printheads depositing multiple materials onto one platform [32].

The main elements of an e-jet printer (see Figure 1.2) include a conductive nozzle holding the build material, conductive substrate, and voltage amplifier. We use a previously developed customized e-jet printer [33] with two printheads. An electric field is created by applying a voltage difference between the nozzle tip and the grounded substrate, changing the meniscus profile from a pendant shape to a cone shape, defined as a Taylor cone jet [29]. As the field strength increases, electrostatic forces overcome ink capillary tension and the liquid build material jets from the tip of the cone to the substrate [30]. The applied voltage can be pulsed with a pulse-width, $t_p$, from low voltage, $V_l$, to high voltages, $V_h$, as described in Figure 1.2b. Custom structures can be fabricated by synchronizing the stage motion with the voltage pulses as instructed by a digital file, which enables a **drop-on-demand** printing mode with the ability to deposit sessile droplets at pre-defined locations. It should be noted that a continuous jet-printing mode (with constant voltage) can also be used to deposit material on the substrate similar to line printing in [34]. However, the fabrication of uniform thin-films (film spatial resolution $< 100 \times 100\ \mu m^2$, film thickness $< 100n$m) similar to the one in Figure 1.2c requires the deposition of high-resolution droplets (droplet diameter $< 2\mu$m, droplet height $< 100nm$). In a continuous jet-printing mode, high-resolution droplets are generated by increasing the applied voltage, which simultaneously results in higher frequency jetting. High stage speed is then required to space out the printed material on the substrate to form sessile droplets rather than large conglomerations of printed droplets. As the stage speed increases, additional dynamics and noise are introduced into the process, thus reducing the overall quality of the printed patterns. Therefore, drop-on-demand printing offers more stability at a particular spatial resolution by controlling the release of a small volume of material at a desired coordinate and at a desired time. Throughout this dissertation, we use drop-on-demand printing for thin-film fabrication, unless it is mentioned otherwise.

## 1.2 Closed-loop Spatial Control of E-jet Printing

For most AM systems, it is difficult to actuate and sense in real-time due to the speed and spatial resolution of the dynamics [24]. The lack of real-time monitoring devices that can capture *in situ* measurements has been a challenge for most AM systems, and in particular $\mu$-AM systems such as e-jet printing process, in which, the output and subsequent error measurements are typically only available using distributed sensing devices (e.g. atomic force microscopy) after the material is deposited onto the substrate. In many AM structures, such as the optical sensor presented in Figure 2.11, spatial factors such as droplet

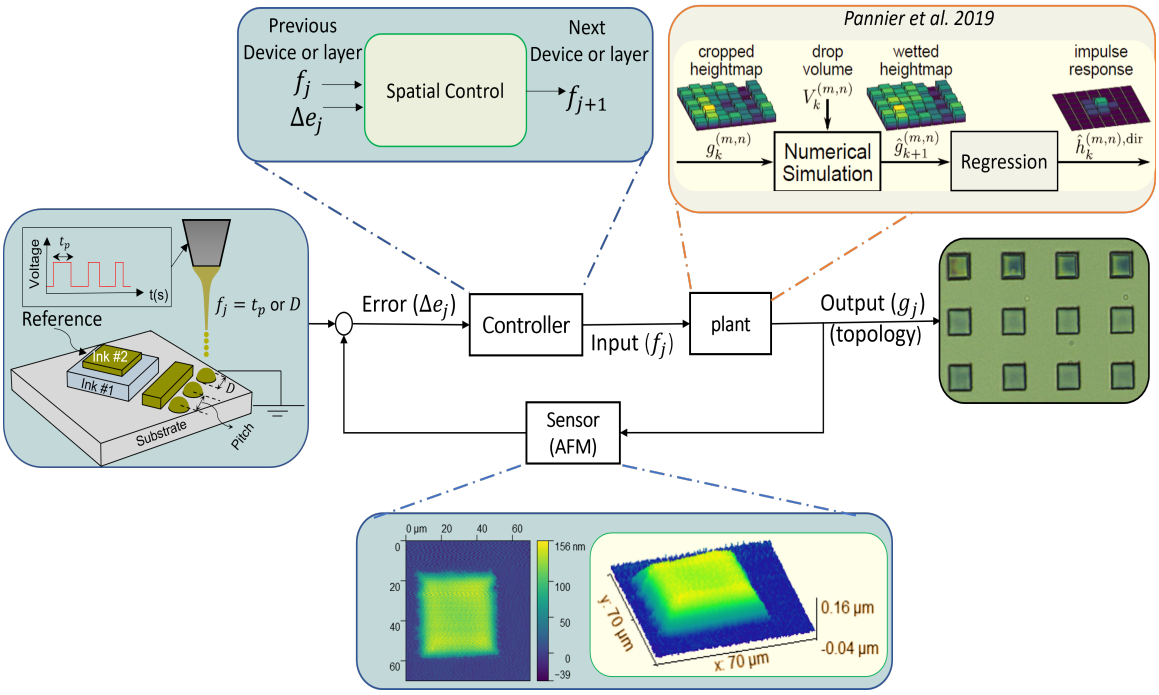


Figure 1.3: **Closed-loop control of e-jet printing process**: Material is released from the nozzle tip to form droplets on the surface. It is assumed that the droplet-to-droplet distance, known as pitch, is fixed. By adjusting droplet sizes at each spatial location, 3D structures are formed. The control input is the droplet size at each spatial coordinate, $(x,y)$, which is controlled through the applied pulse-with, while the low and high voltages are fixed. The measured output is the topography at each spatial coordinate. The spatial controller uses the 2D input and error signals to recursively update the input signal.

coalescence or film flatness and consistency play a larger role in device performance than temporal events. Therefore, for these systems, the spatial tracking errors $e(x,y)$ are more important than temporal errors $e(t)$. A model of the printed droplet interactions with the surface must incorporate changes from layer-to-layer since the process spatial dynamics are iteration varying. Models of iteration varying dynamics provide theoretical and practical challenges for the development of robust and efficient controllers. An important aspect of this research is to investigate the formulation of **robust control frameworks** that can leverage the iterative nature of these processes, while considering in-layer and layer-to-layer interactions in order to close the topography loop iteratively as described in Figure 1.3 (controller block). In the next sections, possible spatial control frameworks are described in detail.

### 1.2.1 Spatial Iterative Learning Control

Iterative learning control (ILC) is a control technique that has been widely used in systems with repetitive characteristics, even those that lack real-time feedback signals, in order to achieve (near) perfect output tracking of a reference trajectory over a short number of iterations [35]. Temporal ILC uses past information in the time domain in order to build an appropriate feedforward control signal with the aim of ensuring convergence of the tracking error from iteration to iteration. Previous studies [36–38] have considered ILC architectures that address bounded iteration varying model parameters, and provide convergence guarantees to a bounded neighborhood of a nominal system over finite iterations [37, 38]. However, these methods have primarily been considered for temporal rather than spatial dynamics.

Due to the challenges in real-time monitoring and control, spatial ILC (SILC) provides an appealing option for recursive control during the additive process ( [39–44]). SILC is an extension of temporal ILC ( [36, 37, 45]) reformatted for the spatial domain that uses spatial data (e.g. layer height) from previous iterations to derive a feedforward control signal for the next printed iteration. In these systems, the SILC algorithm aims to decrease the spatial tracking error $e(x,y)$ from iteration to iteration. SILC has been demonstrated for topography control in additive manufacturing (AM) [40]. Here, I integrate different versions of SILC with the additive process to track a specific trajectory over the spatial domain by learning from previously fabricated samples.

#### 1.2.1.1 First-Order SILC

In the literature, First-order ILC (FO-ILC) has been extensively used for reference tracking of systems with repetitive characteristics that execute the same task repetitively. FO-ILC leverages the data from the most recent iteration, to construct an optimal feedforward signal. First-order SILC (FO-SILC) has been used in AM processes for topography regulation of single-layer structures [39–41, 44]. Despite the progress in the area of spatial dynamics, current SILC algorithms do not consider multiple sets of spatial dynamics due to multi-materials, nor surface variations in multi-layer structures. Multiple layers leads to initial condition variability due to previous layer dynamics. Furthermore, in multi-material structures, the change in spatial dynamics due to the different materials requires a MIMO SILC approach. Here, I develop a FO-SILC framework for the deposition of multi-material 3D constructs such as the one in Figure 1.4 that incorporates model uncertainties and spatially varying dynamics for multiple plant models. In addition, the proposed control method is useful to regulate material addition for multi-layered structures.

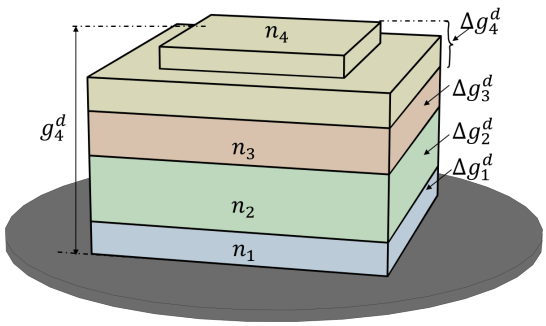


Figure 1.4: Demonstrative multi-material 3D structure fabricated by AM. $n_l$ are arbitrary build materials at layer $l$. $\Delta g_l^d$ is the desired incremental topography at layer $l$, while $g_l^d$ is the desired total heightmap at layer $l$ with respect to the substrate.

#### 1.2.1.2 Higher-Order SILC

Most ILC literature focuses on first-order ILC (FO-ILC) where the feedforward signal comes from the most recent iteration. While FO-ILC has proven to be useful for reference tracking of repetitive systems, it loses performance when uncertainties are high. To improve performance and robustness to iteration varying uncertainties, higher-order ILC (HO-ILC) has been developed where the feedforward signal is synthesized from data from multiple past-history iterations [46–50]. HO-ILC systems have shown faster convergence to nominal behavior and more robustness to uncertainties as compared to FO-ILC systems [48]. Here, I extend the proposed FO-SILC framework in the previous section towards the development of a multi-dimensional higher order SILC framework in the lifted- and frequency-domains. The proposed HO-SILC scheme encompasses interval model uncertainties and spatially varying dynamics arising in the printing of multi-layered constructs. The proposed HO-SILC framework incorporates **vertical learning** through the combined effect of previous layer spatial dynamics and layer-to-layer learning, and **horizontal learning** from part-to-part. The proposed HO-SILC differs from traditional HO-ILC frameworks due to the 2D aspect of the learning. Traditional HO-ILC considers information from previous data across the iteration axis. The proposed HO-SILC presented here incorporates learning over two axes; along the part-axis ($j$ horizontal) and over multiple iterations in the layer axis ($l$ vertical).

### 1.2.2 Model Predictive Control

In addition to the layer to layer dynamics, it is important to consider process constraints within the AM system, such as the requirement of strictly positive control inputs, $f(x,y)$. Model predictive control (MPC) is a control framework that works especially well for con-

strained systems and incorporates a forward projection process that is useful for AM systems in which the current layers directly impact future layers. Similar to ILC, MPC is a predictive control technique that tries to prevent errors, rather than react to them. MPC leverages the system model and data from past iterations to predict optimized control actions for multiple steps ahead in the future ( [51–56]). MPC has been applied to AM processes to control 1D height increments with a varying reference signal for single material structures ( [56]). Similarly, predictive iterative learning control in [57, 58] uses a similar idea to leverage past information to predict future iterations in order to update the control input. In this work, I combine an MPC framework with HO-SILC to improve the performance of the e-jet printing process. Specifically, the combined framework focuses on enhancing topography control by looking forward through a prediction of future layers and backward through the incorporation of the available data from previously printed layers to make appropriate control decisions.

## 1.3 Contributions and Organization of the Dissertation

This research addresses fundamental gaps in modeling and control of the e-jet printing process that currently prohibit robust fabrication of thin-film devices. These gaps can be more formally framed in the context of the following research questions:

1. **What is the relationship between material interactions and film quality at the microscale?**

    (a) How can we use our understanding of material/film quality relationships to select successful material combinations?

    (b) Can we derive an enhanced understanding of the mapping between process parameters/material parameters/film quality that will be used to inform model structure and quantify model uncertainty?

2. **How can we use data to design more robust and intelligent controllers?**

    (a) What control architecture should be used to enable learning to be achieved from layer-to-layer?

    (b) Can the integration of MPC into the learning control framework be used to reduce model uncertainty and improve robustness?

    (c) How can AM constraints be integrated into a learning-based topography controller?

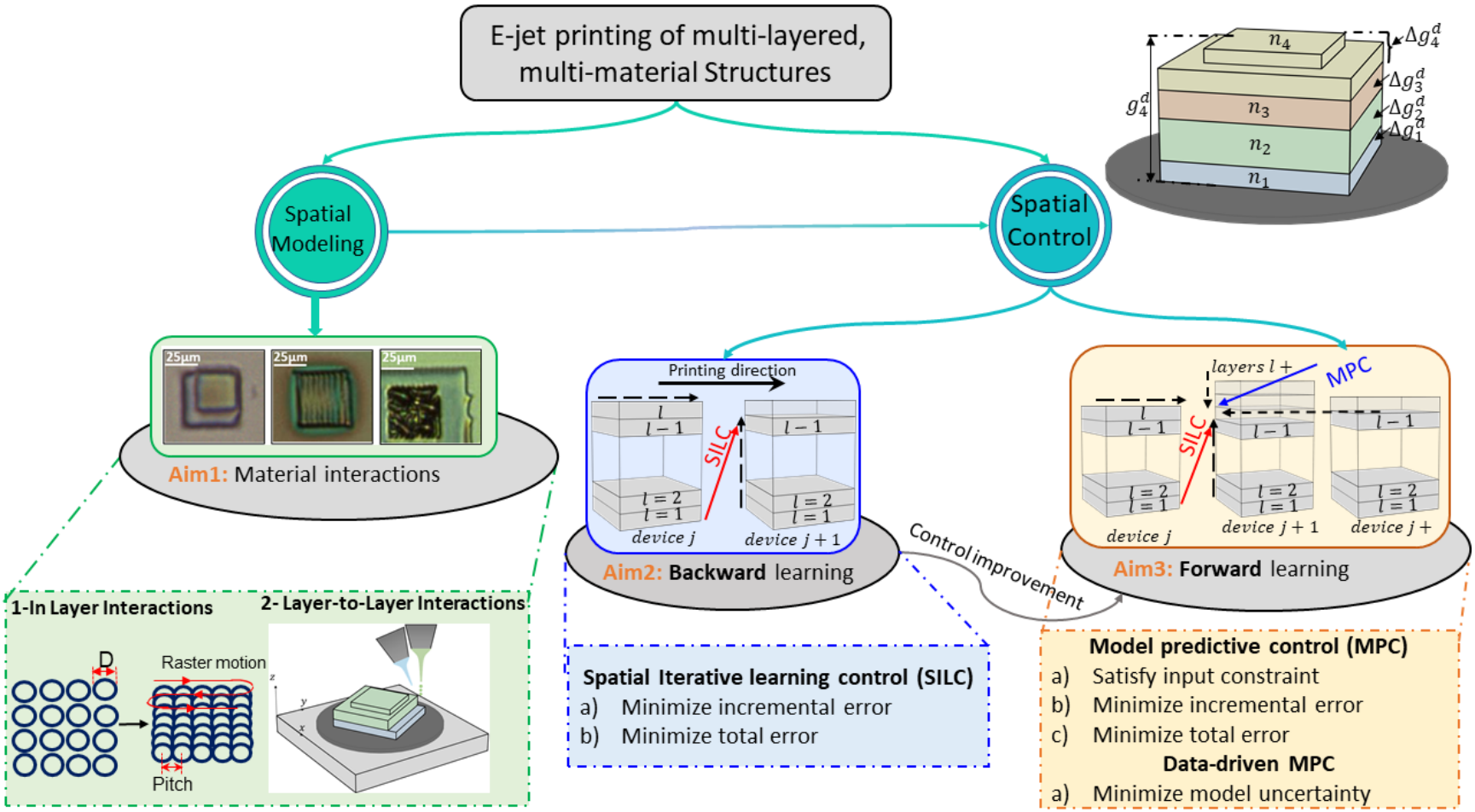


Figure 1.5: Hierarchy of novel contributions

To answer these questions, the research tasks have been organized into three research aims.

**Aim 1: Derive an understanding of material interactions at the microscale that will inform the development of spatial models to achieve better control decision in 3D printing**

The goal of this task is to understand material interactions at the microscale and leverage this knowledge to derive appropriate control decisions to achieve high-quality thin-film devices. E-jet employs a complex ejection mechanism that is affected by the fluidic properties of the build material, surface energy of the substrate, and process parameters. My approach in chapter 2 explores in-layer interactions by adjusting the process parameters of e-jet printing to achieve high-quality films. In addition, my approach investigates layer-to-layer interactions by measuring 1) the contact angle of a single droplet of one material on a uniform surface of another material at the microscale, 2) the liquid surface tension of the build material, and 3) the solid surface energy of the previous layer. The key contributions from this task are presented in the chapter 2 as follows:

1. An empirical model is developed for multi-material, multi-layered deposition that relates material and process parameters to the uniformity of thin-films.

2. An experimentally derived understanding that the fabrication of thin-films at the microscale is contingent on material interactions that demonstrate: (1) low contact angle at the microscale, (2) high surface tension of the build material, and (3) high surface energy of the previous layer.

3. Identification of a set of compatible materials (NOA170 and Loctite3526) that enables multi-material deposition and will be used in the control framework.

To demonstrate the feasibility of e-jet printing for thin-film device fabrication, a high-resolution Bayer filter array is fabricated using two high viscosity inks. The optical properties of the array are varied by adjusting the layer thickness.

**Aim 2: Development of a backward control-learning strategy to close the topography loop iteratively**

The objective of this aim is to achieve an automated topography controller for microscale additive manufacturing of 3D structures using the information from previous devices/layers that are already printed in order to improve the performance of future devices/layers that are going to be deposited. To achieve this objective, I have proposed a spatial iterative learning

control formalism in conjunction with the additive process to address the combined challenges of multiple dynamics due to multiple build materials and varying initial conditions due to roughness of the previous layer surface. The main contributions from this task are:

1. Development of a spatial iterative learning control framework for multi-layered and multi-material structures.

2. Development of a design methodology for deriving learning filters that directly embed stability criteria for nominal HO-SILC system.

3. Design of a boundary prediction of a maximum allowable uncertainty around the nominal plant for monotonic convergent of the iterative HO-SILC algorithm.

**Aim 3: Development of a forward control-learning strategy to close the topography loop iteratively**

The goal of this task is to achieve an automated topography learning control framework by looking forward through a prediction of future devices/layers to make appropriate control decisions. To realize this objectives, I propose to implement a SILC-MPC method that projects forward the data from future devices/layers using model predictive control (MPC), and integrates the control framework with the information from previous devices/layers using SILC. Unlike the proposed SILC framework in Aim 2 that uses a saturation function to force the negative inputs to zero, Aim 3 can be formulated in a way that imposes non-negativity constraint of the input signal to preserve the additive nature of AM processes. In addition, similar to other iteration varying control systems, a performance/robustness trade-off happens with the proposed SILC framework in Aim 2. The proposed SILC algorithm loses the performance benefits that could be achieved by designing an overly robust learning strategy that is designed for the worst possible model uncertainty. Integrating MPC with the SILC framework can improve the performance and result in faster convergence to the desired behavior.

The remainder of this dissertation is organized as follows. In chapter 2, Aim 1 is accomplished. We investigate the effect of process parameters on film quality and explore material requirements for multi-material fabrication. A set of compatible materials for multi-material deposition is introduced that will be used to inform the development of model-based control designs in multi-material fabrication in chapter 4. In chapter 3, the preliminaries and notations are presented that will be used in control designs. Additionally, the plant models are developed in chapter 3 and will be used in chapters 4 to 6 to predict the behavior of droplets on nonflat surfaces for the materials identified in chapter 2. In

chapter 4, as part of Aim2, a first-order SILC (FO-SILC) design is developed as a recursive control strategy that enables closed-loop control of e-jet printing process. The proposed FO-SILC frameworks is used in multi-material/multi-layer deposition process. At each iteration, a thin-film pattern is printed and its topography is measured using an integrated AFM (see Figures 1.2 and 1.3). The FO-SILC design in chapter 4 is extended to a higher-order SILC (HO-SILC) to improve the controller performance and accomplish Aim 2. A MIMO configuration is developed that incorporates **vertical learning** through consideration of previous layer spatial dynamics [33], and **horizontal learning** from part to part to derive a **diagonal** SILC framework. In chapter 6, Aim 3 is addressed. We implement an SILC-MPC method that leverages the information from previous layers using spatial iterative learning control (SILC) and projects forward the data from future layers using model predictive control (MPC) to improve the tracking performance of iteration varying AM processes. The proposed controllers in chapters 4 and 5 are validated through various experimental tests using an e-jet printer testbed located at the University of Michigan. The conclusions are given in chapter 7.

# CHAPTER 2

# An Empirical Model for Multi-material Multi-layer Fabrication Using E-jet Printing

Many applications require multi-material, layered structures with well-defined areas, smooth interfaces between layers, and controllable thicknesses; however, a systematic method to achieve these structures by e-jet is lacking. E-jet employs a complex ejection mechanism that is affected by the fluidic properties of the build material (e.g., surface tension, electrical conductivity, viscosity, density, etc.) and process parameters (e.g., nozzle size, electric field, the surface energy of the substrate, etc.). There are many challenges in material ejection and spreading that need to be investigated to understand the printing process and material interactions at the micro and nanoscale toward realizing the full potential of the e-jet printing process. In this chapter, e-jet printing is investigated for its capability in depositing multi-layer thin-films with microscale spatial resolution and nanoscale thickness resolution to create arrays of one-dimensional photonic crystals (1DPC) such as the one in Figure 2.1 as an example of multi-material deposition. First, the deposition of individual droplets and how they merge to form continuous layers is studied. Second, this result is extended to multiple stacked layers comprising different materials, enabling structures like the vertical Bragg reflectors in Figure 2.1b. An empirical model is developed that correlates process parameters with material properties in multi-material, multi-layer structures with control of thickness at the nanoscale, and control of in-plane patterning at the microscale. The model is validated with several photopolymer inks, a subset of which is used to create pixelated, multilayer arrays of 1DPCs with uniformity and resolution approaching standards in the optics manufacturing industry.

## 2.1 Motivation

Archetypal 1DPCs are comprised of alternating layers of high and low refractive index materials with an optical thickness on the order of the wavelength of the incident light.

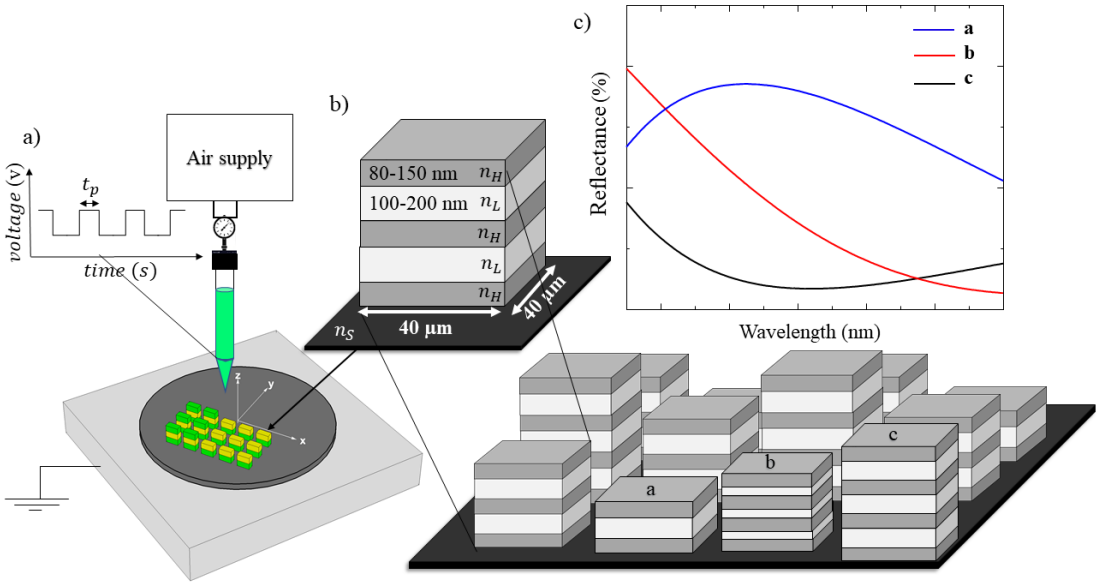


Figure 2.1: **Multi-Material thin-film fabrication by E-jet printing**. A) Schematic of e-jet printing process. A high voltage pulse is applied to the nozzle to eject a droplet of material with droplet volume related to pulse-width, $t_p$. B) One-dimensional photonic crystals (1DPCs) to be fabricated by e-jet printing. $n_L$ and $n_{\mathrm{H}}$ are low and high refractive indices of the corresponding polymeric materials. C) Reflectance response of a 1DPC can be tuned by modulating the number of layers and corresponding thicknesses.

As optical filters or mirrors, the transmittance or reflectance of light by these 1DPCs can be tuned by adjusting the sequence, thickness, and refractive index in the stack. 1DPCs have found wide ranging applications; from conventional lasers and optical filtering to novel mechanical and chemical sensing devices [59–61]. Polymeric 1DPCs in particular have attracted attention recently due to their potential for simplified processing, as well as freedom to design chemically and structurally derived capabilities for new sensory applications [62]. In a collaboration with the Stein group, the 1D photonic crystals (1DPCs) in Figure 2.2 are designed and fabricated using e-jet printing, with commercially available photopolymers [1]. In the next sections, a step-by-step methodology for material selection and deposition to fabricate multi-layer/multi-material structures such as the optical sensor in Figure 2.2 is presented. The Stein group developed design criteria to select material combinations with favorable optical properties for the fabrication of the photonic crystal. The candidate materials are then tested using the e-jet system to find a set of compatible materials that enable multi-layer and multi-material deposition in a layer-by-layer manner. Note that the optical response of the printed photonic crystal can be tuned by the number of layers and corresponding thicknesses (see Figure 2.1c). The photonic responses of the

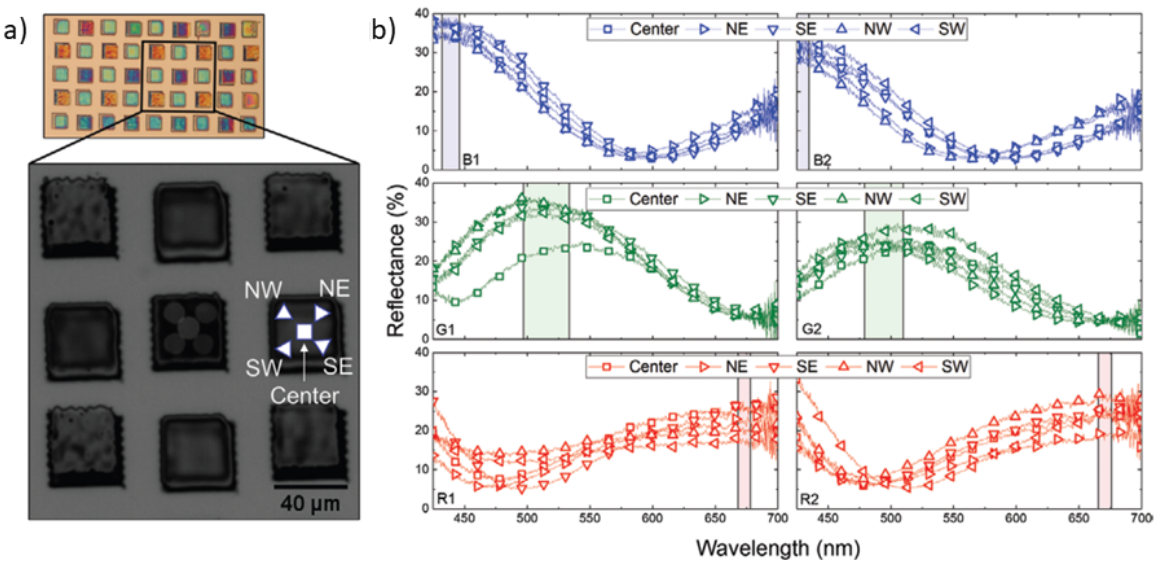


Figure 2.2: Bayer filter array fabricated by e-jet printing [1]. a) Optical image of Bayer filter array with zoomed region indicating the locations across the area of a specific pixel that were measured using the optical microreflectance (OM) system. Circles overlaid on the central sample show exact locations of data collection while the square/triangle symbols indicate the locations (center, NW, SW, NE, SE) of corresponding information in the reflectance plots. b) Optical response of two samples each of blue, green, and red spectra samples.

structures printed in this work are quantified via a custom developed microspectroscope. Due to the flexibility in design provided by the e-jet process, the findings in this chapter can be generalized for fabricating additional multi-material, multi-layer micro- and nanostructures with applications beyond the field of optics.

## 2.2 Experimental Methods

In this section, a series of experiments are conducted to find a set of compatible materials that demonstrate **stable jetting behavior** during deposition as well as **merging characteristics** after the material has reached the substrate. Stable jetting behavior describes materials that form a stable, single Taylor cone jet [63] at the meniscus without clogging or evaporating. Good merging characteristics describe build materials that spread to a uniform thin-film on existing topography. Standard macroscale measurements of solid surface energy and liquid surface tension are used in conjunction with microscale contact angle measurements to understand the length scale dependence of material properties and their impact on droplet merger into uniform microscale thin-films. Moving forward, we will

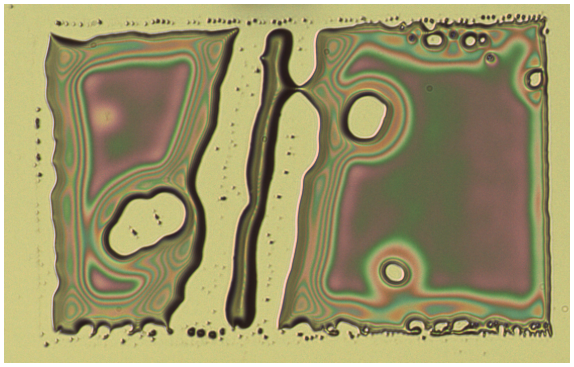

(a)

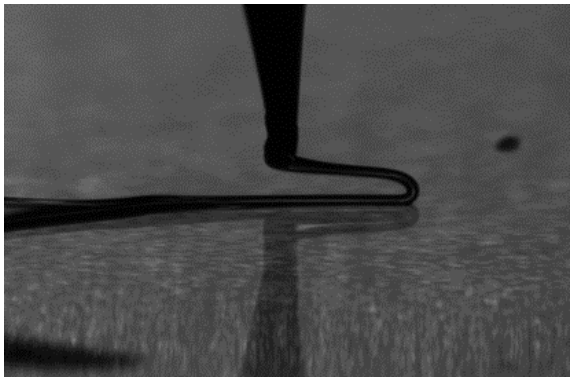

(b)

Figure 2.3: **Thin-film fabrication failures in e-jet printing.** a) NOA138 evaporated on the substrate. b) NOA1327 with a low flash point solidifies before landing on the substrate.

refer to the silicon wafer as the primary substrate, while previously deposited, fully merged and cured photopolymer surfaces will be referred to as secondary substrates.

- **Material preparation**: In this work, several optical adhesives (Norland Optical Products (NOA)) are utilized as well as a commercial Loctite formulation. For high-resolution patterning, nozzles smaller than 1 $\mu$m in inner diameter are used with a 20 $\mu$m standoff height. Some inks contain large particles (e.g. comprising resin, a long chain oligomer, or foreign moieties) that must be filtered in order to reduce the chance of nozzle clogging. Before running the experiments, we filtered Loctite3526 using high pressure and a filter with 0.22 $\mu$m diameter pores. The removal of large particles has the added benefit of reducing the surface roughness of the printed patterns. We note, however, that filtering in some cases changes other ink properties, e.g., filtered NOA170 has a smaller refractive index value than unfiltered NOA170, while also exhibiting an unstable spray jet [64] instead of a single stable jet mode at

the same standoff height and voltage.

- **Material requirements for thin-film fabrication**: Through the experiments, it is observed that inks should have a boiling temperature higher than the printing environment since evaporation precludes the ink from forming a uniform film on the substrate as can be seen in Figure 2.3a . For example, NOA1348, NOA138, NOA142, NOA144 gradually evaporate on the silicon substrate. Another critical aspect of jetting behavior is understanding the flashpoint of the inks. Specifically, several of the photopolymers investigated have a low flash point and become polymerized before landing on the substrate. For example, we are able to eject both NOA1327 and NOA1328 with a flashpoint of 10 °C from the nozzle tip. However, the jetting stream from both of these inks becomes solidified before reaching the substrate, as presented in Figure 2.3b. This problem has not been observed in other NOA inks with flashpoints larger than 175 °C.

- **Contact Angle Measurement**: To measure contact angles at the microscale in Figures 2.4 and 2.7a, an array of droplets of a build material is deposited onto a surface (primary or secondary substrate of another material). The droplets are cured, and their topographies are measured using an integrated Nanite AFM (inset of the horizontal axis in Figure 2.7a). It is assumed that the contact angle of a droplet does not change with UV-curing; this assumption was confirmed using a slightly larger droplet ($> 20\ \mu$m) and an integrated camera. The raw AFM data are then post-processed in the software package 'Gwyddion' to measure the topography and the corresponding contact angles. We deposit fifteen droplets with varying $t_p$ to generate droplets with diameters ranging from 2 to 10 $\mu$m. These droplets were used to measure the average contact angle and corresponding standard deviations. The standard deviation of the printed droplets is low ($< 6°$, except for NOA13825 that exhibited clogging issue) as shown in Figure 2.7a. This indicates that the contact angle at the microscale does not depend on the droplet diameter. At the macroscale, contact angle measurements are conducted on a Ramé-Hart goniometer by placing millimeter-scale droplets of various inks on the respective surfaces as presented in Figure 2.4b. 'DROPImage' software is used to fit a curve to the acquired image of the droplet and measure the contact angle.

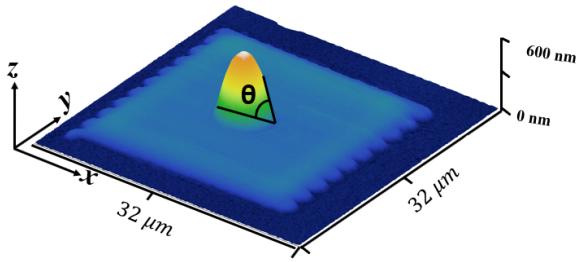


(a)

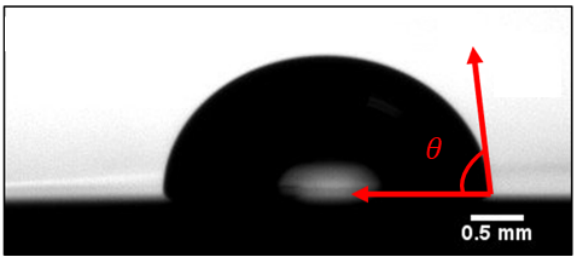


(b)

Figure 2.4: **Contact angle measurement** a) at the microscale: 3D view of an AFM scan of an e-jet printed droplet of NOA13825 on a uniform pattern of NOA170 (thickness=85 nm, RMS roughness=6 nm, b) at the macroscale using a goniometer with droplet diameter ranging from 1-3 mm.

## 2.3 Process Parameter Investigation for Single Material Thin-film Fabrication

Thin-film fabrication, using drop-on-demand e-jet printing, is a result of droplet ejection, droplet spreading, and droplet coalescence. Materials with stable jetting behavior will form a single stable Taylor cone jet [29] at the meniscus. After the material is ejected from the nozzle tip, a sessile droplet is formed on the substrate with a spherical cap shape that is defined based on the droplet diameter and contact angle [22]. The droplet geometry depends on the electric field, the kinetic energy imparted on the droplet at ejection, the surface tension of the droplet, surface energy of the substrate, rheological properties of the ink, and the viscous energy lost during spreading. Several previous studies on e-jet behavior have utilized UV-curable photopolymer inks deposited onto conductive, smooth silicon wafers as a model system. They are chosen here again for their combination of fluid properties as well as having the ability to be cured in situ, without requiring high temperature operations. As an example, NOA170 was chosen to investigate the formation of thin-films on a polished silicon substrate based on varying process parameters. In this

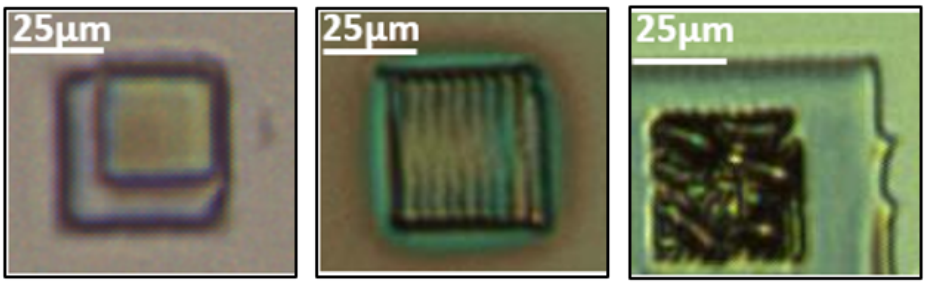


Figure 2.5: Material interactions at the microscale. a) Fully merged: Loctite3526 fully merges on NOA170 with thickness and RMS roughness of 90 nm and 6 nm, respectively. b) Partially merged: NOA170 partially merges on NOA144 with thickness and RMS roughness 175 nm and 40 nm, respectively. c) Unmerged: NOA170 does not merge on NOA1348 with thickness and RMS roughness 250 nm and 200 nm, respectively.

section, the process parameters that determine the quality of film formation, which in turn influences device functionality, are outlined.

The controllable process parameters that can affect the applied electric field, and subsequent droplet volume, include: high voltage value, low voltage value, pulse-width ($t_p$), nozzle size, and standoff height (distance between the nozzle tip and the substrate in Figure 1.2). Here, the droplet volume of a specific material is intentionally adjusted using $t_p$, while keeping all other process parameters constant. $t_p$ is chosen because it has a direct mapping to droplet volume [65] and reduces the introduction of additional jetting dynamics and disturbances, such as nozzle arcing, which are more likely to occur with changes in other process parameters like high voltage value or standoff height. By design, each droplet is a result of a single droplet released within the designated $t_p$. Successive droplets can be placed at a certain distance (center to center) from each other, defined as pitch, to form a film as shown in Figures 1.3 and 2.6b. The average thickness of a film, $\bar{g}$ and the root mean square (RMS) surface roughness, $s_q$, are defined as:

$$\bar{g} = \frac{1}{N_1 \times N_2} \sum_{i=1}^{N_1} \sum_{j=1}^{N_2} g_{i,j} \tag{2.1a}$$

$$s_q = \frac{1}{N_1 \times N_2} \sqrt{\sum_{i=1}^{N_1} \sum_{j=1}^{N_2} (\bar{g} - g_{i,j})^2} \tag{2.1b}$$

where $g_{i,j}$ is the topography of the pattern at the discretized coordinate $(i, j)$, and $N_1$ and $N_2$ are the total number of discretized coordinates in the $X$ and $Y$ direction. Note that both $\bar{g}$

and $s_q$ are measured using an integrated AFM. Surface roughness is a representation of the merging quality of a film such that a low $s_q$ value indicates a smoother film. The thickness and roughness of the printed films can be regulated by adjusting the droplet volume and pitch. As such, pitch and $t_p$ are independent variables while film thickness and roughness are dependent variables. At small $t_p$ or large pitch values (pitch>>D), the droplets become smaller than the pitch, which yields voids in the pattern and increases the film's roughness. To quantify film quality, we define a thin-film pattern with a thickness smaller than 200 *nm* as fully merged if it has an $s_q$ value less than 20 *nm*, partially merged for $s_q$ values between 20 *nm* and 50 *nm*, and unmerged for $s_q$ values greater than 50 *nm*. Figure 2.5 shows these interactions at the microscale.

Figure 2.6a shows the effect of $t_p$ on the average thickness and corresponding RMS surface roughness (represented as error bars) of NOA170 films (60 $\mu$m $\times$ 60 $\mu$m). The controlled process parameters include: $V_h$ =500 V, $V_l$ =250 V, nozzle size=1 $\mu$m, standoff height= 20 $\mu$m, and pitch = 2.4 $\mu$m. The pulse width, $t_p$, is varied between 0.5-12 ms to investigate its effect on film quality. Note that the diameter of a droplet is varied by changing $t_p$. It is observed that decreasing $t_p$ from 12 ms to 2 ms decreases the pattern thickness and roughness. A pulse-width of 1 ms ($t_p$ =1 ms) resulted in the lowest roughness ($s_q$ =7.23 *nm*) with a film thickness of 95 *nm*.

The influence of pitch on average thickness and roughness of NOA170 films is presented in Figure 2.6b. We use a raster type motion to print a continuous line that merges to form films, as presented in the inset of Figure 2.6b. The controlled process parameters are the same as those used to evaluate the effect of pulse width; however, we set $t_p$ to be 1 ms, which yields an average droplet diameter of D=2.83 $\pm$ 0.12 $\mu$m, and vary the pitch between 1-2.9 $\mu$m. As the pitch increases, both the roughness and thickness decrease. A pitch of 2.5 $\mu$m resulted in the lowest roughness ($s_q$ =8.41 *nm*) with an average thickness of 89.63 *nm*.

These results suggest that the thin-film fabrication process has two parameter selection steps: (1) eject controlled droplets by pulsing from low to high voltage over a designed time period (shorter $t_p$ leads to smaller droplets), and (2) adjust the pitch between deposited droplets to achieve thin, uniform patterns (pitch values $\sim$ droplet diameter D).

## 2.4 Material Requirements for Multi-material Fabrication

In the previous section, process parameters governing the deposition of smooth, nanoscale films onto a uniform surface (e.g. polished silicon) were investigated. However, in some

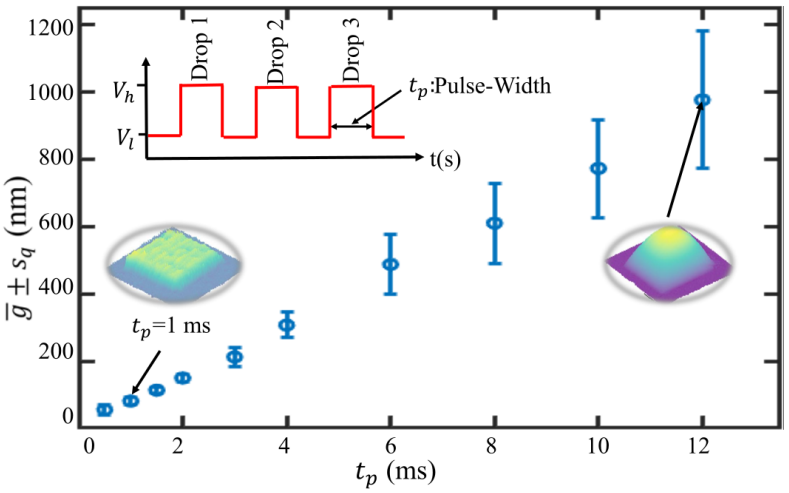


(a)

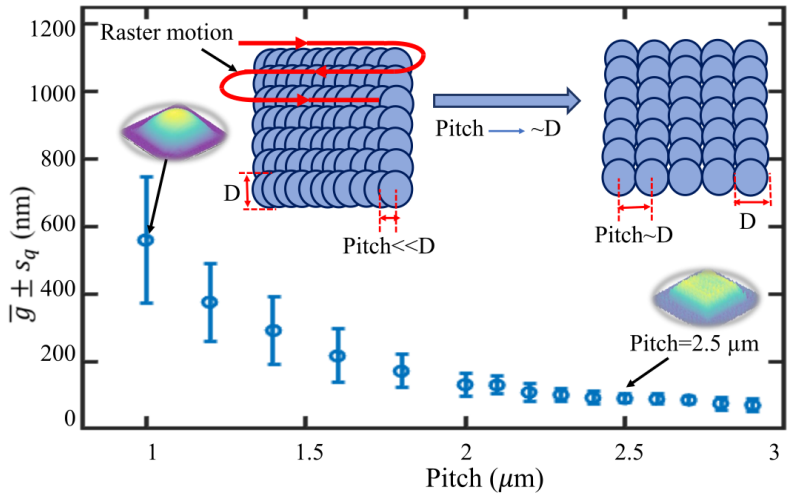


(b)

Figure 2.6: Effect of process parameters on average thickness ($\bar{g}$) and surface roughness ($s_q$) of NOA170 films. Error bars indicate RMS roughness measured by an integrated AFM. Patterns are printed on bare Silicon using drop-on-demand e-jet printing in a raster motion. a) Effect of pulse-width ($t_p$) on pattern thickness and roughness for a fixed pitch=2.4 $\mu$m. b) Effect of pitch on pattern thickness and roughness for a fixed $t_p$ =1 ms (droplet diameter of D=2.83 ± 0.12 $\mu$m). Convex patterns result for pitch << $D$, uniform patterns result for pitch~D, and rough patterns result for pitch >D.

cases, tuning the process parameters does not guarantee a fully merged film. It is possible for a build material to merge into a uniform film on one material, but not on a different material (see Figure 2.5c). This raises the question of how to determine appropriate material interactions in multi-material structures that are fabricated in a layer-by-layer fashion. For example, to create a multi-material structure such as a photonic crystal in Figure 2.1a, a refractive index contrast ($\Delta n = n_{\mathrm{H}} - n_{\mathrm{L}}$) must be achieved between neighboring layers, which introduces variations in surface energy for each additional layer being deposited. To quantify the impact of these variations, we study the shape of sessile droplets of a build material on a previous surface. A range of photopolymers are investigated: NOA170, Loctite3526, NOA144, NOA142, NOA13825, NOA138, NOA13775, NOA1369, and NOA1348, with refractive indices ranging from $n$=1.35 to 1.71, which provides an index contrast maximum of $\Delta n$=0.35. We chose NOA170 as the $n_{\mathrm{H}}$ material due to its high refractive index, $n_{\mathrm{H}}$ =1.70, and search for a low refractive index material ($n_{\mathrm{L}}$) to fabricate a multi-layer structure such as Figure 2.1a. The low refractive index materials in this work include: Loctite3526, NOA144, NOA142, NOA13825, NOA138, NOA13775, NOA1369, and NOA1348. In this section, the material properties and their scale-dependence that contribute to high-quality film formation are highlighted.

The substrate-ink interaction can be defined by the contact angle, which is a function of fluidic properties of the build material (Liquid surface tension (LST), viscosity, evaporation rate, density, etc.), and surface energy of the previous layer [22]. Several previous studies have investigated how tuning the solid surface energy (SSE) of a substrate can affect droplet shape and subsequent feature resolution in inkjet printing [34, 65]. This has been extended to high-resolution e-jet printing, where the microscale contact angles of droplets were used to predict the merging quality of lines [66] on varying SSE surfaces. Micro- and macroscale contact angles are also used here to predict the roughness of a deposited layer of a build material on the surface of a previously printed material.

The microscale material interactions in Figure 2.7a include: NOA170 printed on the primary substrate (Figure 2.1b, layer 1), the $n_L$ materials printed on top of a secondary substrate of NOA170 (unfilled markers in Figure 2.7a, layer 2 in Figure 2.1b), and NOA170 printed on secondary substrates of $n_L$ photopolymers (filled markers in Figure 2.7a, layer 3 in Figure 2.1b). Three regimes defined by the roughness of the formed film (60 $\mu$m $\times$60 $\mu$m) of a build material on a substrate are delineated for ease of characterization. A monotonically increasing linear relationship on a log-log plot is found between the contact angle of a single droplet (2-10 $\mu$m) of a build material on a substrate (primary/secondary of a different material) and the roughness of a printed film of the same build material on the substrate. It is observed that build materials with a low contact angle have a higher likeli-

hood of adhering to previous surfaces and forming a uniform thin-film on them. Focusing on the microscale measurements in Figure 2.7a, a printed layer of NOA170 serves as the secondary substrate for the deposition of low index materials. All low index inks exhibit fully merged thin-films (< 200 nm) with low contact angles (< 15°) and low RMS surface roughness (< 10 nm). Interestingly, the deposition of NOA170 on top of low refractive index materials (layer 3) does not perform as smoothly. Depending on the material in the previous layer, the contact angles range from 10° to 50° with resultant pattern roughness values ranging from less than 20 nm to greater than 200 nm. The only low index material that NOA170 fully merges onto is filtered Loctite3526, while NOA170 printed onto several other low index ink secondary substrates shows partial merging.

It should be mentioned that the results in Figure 2.7a describe material spreading on a uniform surface with low roughness (<10 nm). Previous work has demonstrated the impact of previous layer roughness on material spreading [2]. Our investigations in this work suggest that at the microscale, in addition to the topography, chemical heterogeneity of the previous layer may play a role in surface roughness (Figure 2.7a). Future studies will explore the relationship between thickness of the current layer and roughness of the previous layer.

Next, we explored if macroscale surface energetic measurements could be used to gain insights into material behavior at the microscale. Figure 2.7b shows the experimental contact angle of NOA170 as a build material on various substrates at the macroscale (with test droplets $\sim$ 1-3 mm) versus roughness of an NOA170 films (60 $\mu$m×60 $\mu$m) at the microscale on various substrates. Comparing the experimental results in Figure 2.7a and Figure 2.7b, it is observed that microscale contact angle measurements are not in agreement with the macroscale contact angle measurements. This highlights the fact that material interactions at the microscale are different from the macroscale, and subsequently previous theories derived for the macroscale are not sufficient to describe the layer-to-layer dynamics at the microscale. For instance, microscale contact angle measurements return a low value of the contact angle related to the NOA170 – filtered Loctite3526 combination ($\theta$=13°±0.8°), indicating that this combination is favorable for forming uniform films. However, at the macroscale, droplets of NOA170 on a spin-coated film of filtered Loctite3526 demonstrate one of the highest contact angles at $\theta$=108.3°±0.8°. With the viscosity and liquid surface tension of the NOA170 ink held constant, the variables that differ between the two deposition systems are the heterogeneity of the solid surface energy and the velocity with which the droplet is impacting the surface.

To further explore material spreading, a macroscale surface energetics study is undertaken using the standard method of Owens & Wendt [67] and Wu [68] (more details are

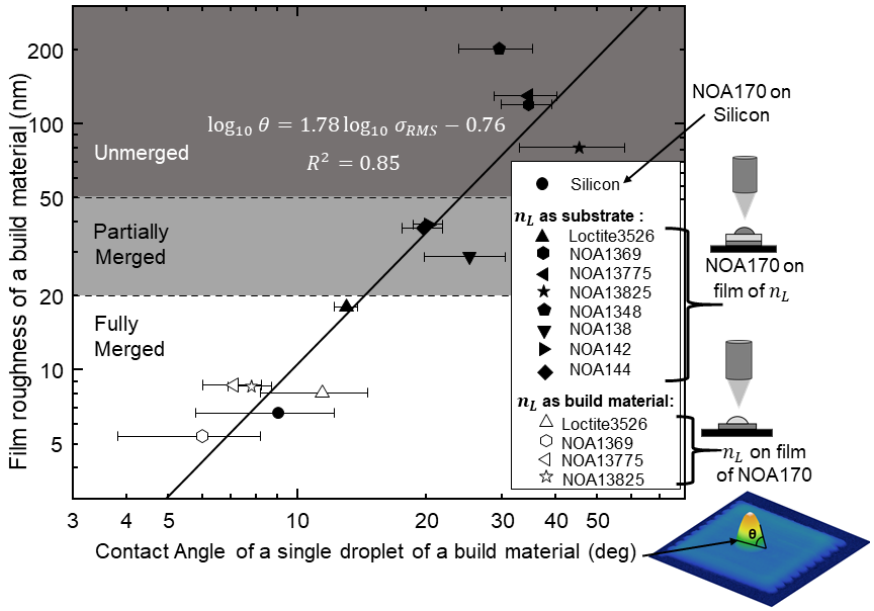


(a)

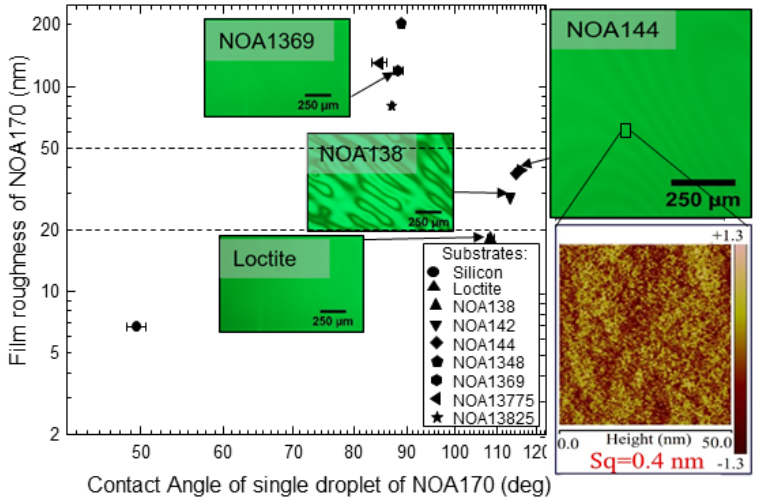


(b)

Figure 2.7: **Film quality at the microscale vs micor- and macroscale contact angles** a) Contact angle measurements of a single droplet (2-10 $\mu$m) versus RMS roughness of a film (60 $\mu$m $\times$ 60 $\mu$m) of the same build material onto a primary or secondary substrate. 3D view of an AFM scan of a single droplet of a build material on a secondary substrate is shown near the horizontal axis. Filled markers describe interactions of NOA170 on $n_L$materials, while unfilled markers represent $n_L$materials on NOA170 films. Results indicate: full merging for $\theta < 15°$, partial merging for $15° < \theta < 25°$, and failure to merge for $\theta > 25°$. Further details are provided on Tables 2.3 and 2.4. b) Contact angle of a single droplet ($\sim 2-4mm$) of NOA170 at the macroscale versus RMS roughness of NOA170 on various $n_L$ materials at the microscale. Note that at the macroscale, we only measured the interaction of NOA170 on $n_L$ materials).

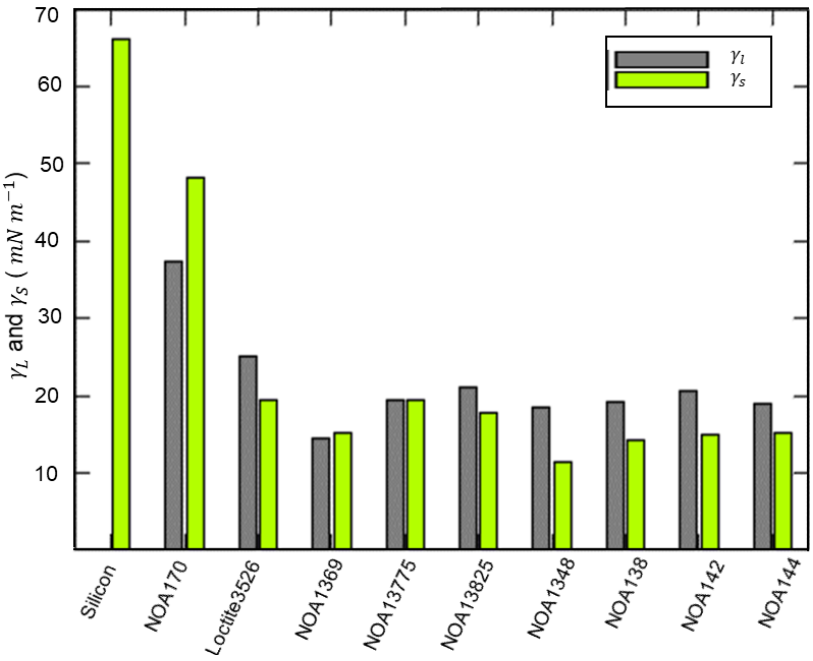


Figure 2.8: Solid surface energy and liquid surface tension of all inks in this work.

given in the supplemental). While this work focuses on controlling material behaviors at the microscale, measuring SSE at these length scales is quite difficult; thus, requiring a surface energetics study at the macroscale. The results of this study are summarized in Figure 2.8. The silicon wafer showed the highest average SSE ($\gamma_s$ =66.3 $mNm^{-1}$), followed by NOA170 ($\gamma_s$ =48.3 $mNm^{-1}$), while the lower index materials ( $n_L$=1.35-1.51) exhibited significantly lower SSE values ($\gamma_s$ =11.5-19.5 $mNm^{-1}$). From previous reports [34], it is expected that a material with a high SSE value will be a more favorable substrate for realizing uniform film formation of the next layer. This supports our observations that NOA170 is a favorable substrate for the low index materials evaluated here.

The LST values of all inks are evaluated using the pendant droplet method [69]. In this work, a highly cohesive ink is defined as an ink that has a high LST value and exhibits poor wetting behavior due to a preference for attaching to itself rather than adhering to a substrate. On the other hand, poorly cohesive inks (low LST values) are not able to remain bonded to themselves to form a uniform pattern on existing topographies. Based on the values provided in Figure 2.8, NOA170 has a relatively high LST value (37.3 $mNm^{-1}$). Note that NOA170 will spread readily on a silicon substrate ($\gamma_s$ (silicon)> $\gamma_l$ (NOA170)), but exhibits mixed merging behavior on lower SSE valued surfaces. It is observed that a highly cohesive ink (e.g. NOA170) is unlikely to adhere to a low surface energy substrate, ($\gamma_l$ (NOA170)> $\gamma_s$ ( $n_L$materials)). Through our studies we identified two approaches for

managing these interactions. First, the SSE value of a merged layer of an $n_L$ material could be increased using in-situ modifications such as atmospheric plasma treatments [70]. Second, efforts may be spent in determining methods for decreasing the LST of a high index material (NOA170 in this case) to promote improved merging quality.

From these studies, we have concluded that material interactions at the microscale are a result of a trade-off between **contact angle**, **SSE**, and **LST** values. For example, printed droplets of NOA170 on NOA1348 and NOA138 secondary substrates exhibit similar contact angles at the microscale (Figure 2.9a). However, a lower SSE value for NOA1348 may help explain why NOA170 fails to result in a merged film on this surface. We also note that the filtered Loctite3526 and NOA13775 have similar SSE values; however, the higher contact angle of printed droplets of NOA170 on the printed NOA13775 surface results in a rougher surface deposition for films of NOA170. In addition, partial merging was observed with the deposition of NOA170 on NOA138, NOA142, and NOA144; which also showed moderate contact angles of printed NOA170 droplets ($15° < \theta < 25°$) as compared to NOA1369 with similar SSE values.

### 2.4.1 Possible reasons for contact angle mismatch between the micro- and macroscale

Previous reports have shown that surface heterogeneity can lead to significant changes in SSE values and an artificial increase or decrease in the contact angle of droplets on a surface depending on the length scale of the heterogeneity and the size of probe droplets used [71]. Furthermore, high deposition velocities with the e-jet process coupled with high viscosity inks (> 5,000 cP for NOA170) could, at the microscale, overcome surface energetic limitations apparent at the macroscale [72]. Specifically, a high viscosity ink may flatten out under high deposition velocities. In Figure 2.7b optical micrographs utilizing a 532 nm bandpass filter were taken of the spun coat layers of NOA138, NOA144, Loctite3526, and NOA1369. The filter allows the topography of these layers to be investigated at longer length scales. It was found that NOA138 and NOA144 both demonstrated irregular surface topography while NOA1369 and Loctite3526 were both relatively smooth. Referencing the behavior of the same materials at the microscale, it can be seen that the heterogeneous topography exhibited in NOA138 and NOA144 could artificially increase the contact angle. Specifically, AFM measurements of NOA144 with a scan area $<2500\mu m^2$ indicate extremely smooth surfaces (sq < 1 nm), but this does not hold for larger areas (indicated by interference patterns in the optical micrograph taken by an optical microscope). Interestingly, this does not explain the merging quality between NOA170 – filtered Loctite3526.

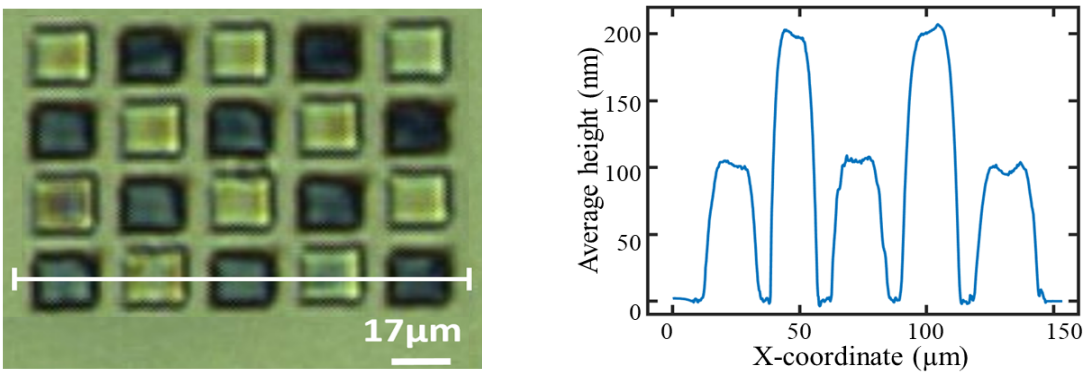


(a) (b)

Figure 2.9: **High resolution printing using e-jet technology**. a) Multi-material, single layer fabrication of high-resolution thin-film patterns. The white line shows the height average across five pixels in the Y direction. The lighter color patterns are NOA13825 with thickness and roughness of 205 nm and 12 nm, respectively, and the darker color patterns are NOA170 with thickness and roughness of 101 nm and 5 nm. b) Average pattern height across five pixels through the center of the last row.

This could potentially be explained by chemical heterogeneity in the sample, which can lead to pinning of the droplet.

## 2.5 Results

This section provides a demonstration of e-jet printing of multi-layer thin-film structures. The results presented in the previous sections were used to select appropriate ink combinations. The experimental results in this section were heuristically obtained by determining appropriate process parameters that would yield the desired film thicknesses. The desired thickness values were derived from simulation results provided in our paper in [1] and chosen as values that would provide a specific optical outcome.

Figure 2.9a shows multi-material microstructures that were fabricated by e-jet printing of two high viscosity adhesives at room temperature. The design goal is to deposit uniform high-resolution NOA170 and NOA13825 patterns with layers of 100 nm and 200 nm average thickness, respectively. The darker color patterns were 20×20 $\mu$m films of NOA170 (4400-5000 cP) with an average thickness and RMS roughness of 101 nm and 5 nm, respectively. The lighter colors were deposited 17×17 $\mu$m films of NOA13825 (5600 cP) with an average thickness and RMS roughness of 205 nm and 12 nm, respectively. The distance between the patterns was set at 5 $\mu$m. The pattern profile across the last row of the printed structure (shown in Figure 2.9b) highlights the flexibility and repeatability of the

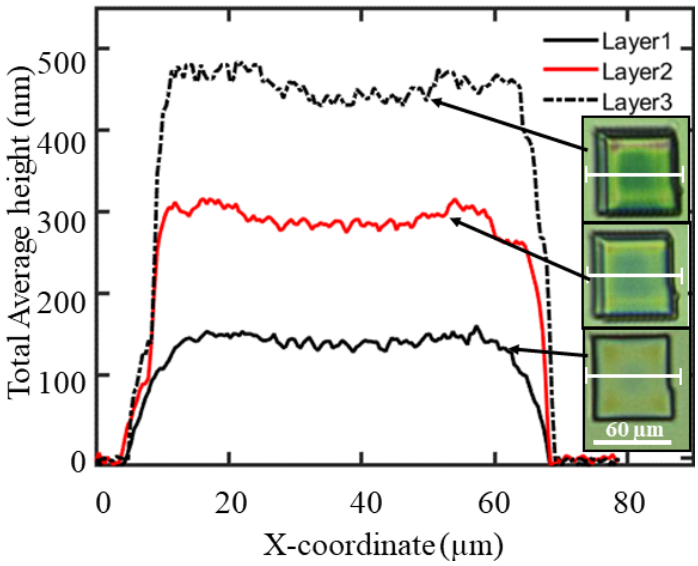


Figure 2.10: Multi-material and multi-layer fabrication using e-jet printing.

e-jet printing process.

The multi-material, multi-layer fabrication of two high viscosity materials using e-jet printing is presented in Figure 2.10: NOA170 was printed in layers 1 and 3, while filtered Loctite3526 was printed in layer 2. To achieve the desired effect, each layer is designed to be approximately 160nm thick. The e-jet process parameters for NOA170 were $V_h$ =600 V, $V_l$ =200 V, $t_p$ =1 ms, f=20 Hz, and pitch=1.8 $\mu$m. The e-jet process parameters for Loctite3526 were $V_h$ =500 V, $V_l$ =250 V, $t_p$ =5 ms, f=20 Hz, and pitch=2 $\mu$m. At each layer, the liquid patterns were UV-cured and their topography was measured using the integrated AFM. Figure 2.10 shows the corresponding average total height map over five pixels from the middle of the pattern at each layer. The overall variation (roughness/ total height) in the total stack height was less than 6%across a single layer and 4% across the entire stack. The average total height is 159±9 nm for layer 1, 325 ±13 nm for layer 2, and 489±17 nm for layer 3, respectively. The maximum RMS roughness in all layers is less than 17 nm, which is a demonstration of the flatness in the overall height. The integration of control to the e-jet process could be used to mitigate height variations.

Figure 2.11 presents a high-resolution e-jet printed Bayer filter array using a high refractive index polymer (NOA170, n =1.7) and a medium refractive index material (Loctite3526, n =1.51). Patterns 1, 2, and 3 are associated with the red, blue, and green color spectrum, respectively, and are equally spaced with a 15 $\mu$m offset with roughness smaller than 13 nm. One goal in creating these bi-layer samples was to show the e-jet process could independently control layer thickness, regardless of the previous printed layer thick-

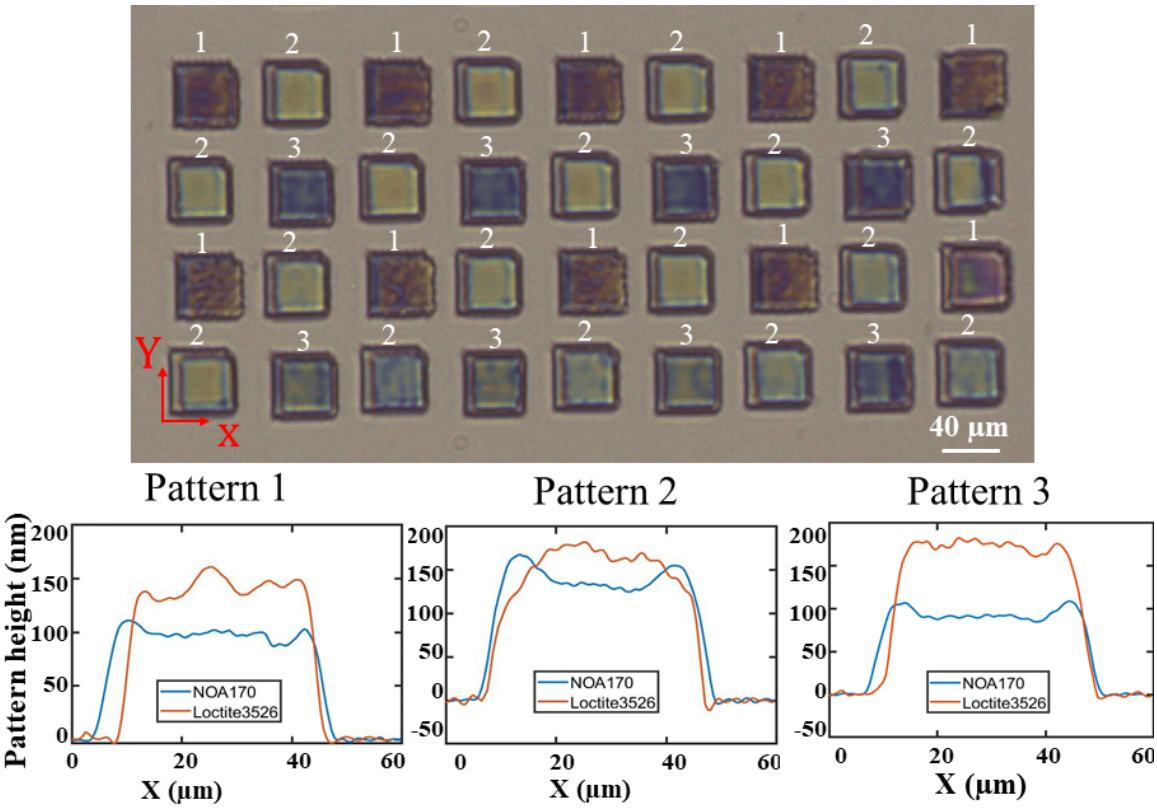


Figure 2.11: Multi-material and multi-layer e-jet printed Bayer array filter.

ness, with the end result being control over the reflected light intensity at specific areas of the spectrum. Thus, the following layer goals were set with the first and second layers at 90 nm and 130 nm for pattern 1, 130 nm and 180 nm for pattern 2, and 90 nm and 180 nm for pattern 3, respectively. These combinations achieved red, green, and blue reflected peak intensity with differing combinations of thickness of both the NOA170 as base layer and Loctite3526 as the second layer. The optical response of these structures is explored further in [1]. Through drop-on-demand e-jet printing, we controlled the thickness of each layer precisely and by design. As demonstrated, it is possible to create a variable color spectrum using e-jet printing, as the color spectrum is correlated with the layer thickness and the corresponding refractive indices of each layer [62]. Therefore, for a fixed material combination, the optical properties can be varied by adjusting the layer thickness.

The experimental results in this section show that the thickness variation is within 6% across a single layer. Different factors affect these variations: 1) The integrated Nanite AFM has ± 10 nm thermal noise that directly affects the roughness measured 2) Commercial inks may contain large particles that increase thickness variations. 3) E-jet is an iteration varying process and different factors such as nozzle clogging, environment tem-

perature and humidity, and more can affect the deposition process and eventually affect the roughness. Future work will explore the integration of control strategies to minimize variations and achieve higher fidelity printed patterns.

## 2.6 Conclusion

In this Chapter, we presented an empirical model for e-jet printing that influences the merging quality of UV-curable polymers in thin-film, multi-material, layered microstructures. A set of material criteria were introduced that are required for material ejection as well as material merging in e-jet printing. The experimental results highlighted the potential of e-jet printing as a substitute for other manufacturing techniques, such as lithography, to fabricate high-resolution devices that are made of multiple thin layers of different materials. Furthermore, it was experimentally demonstrated that at the microscale, high-quality films were most probable with the following material combinations (1) low contact angle, (2) high surface tension of the build material, and (3) high surface energy of the previous layer. The effects of process parameters demonstrated in Figure 2.6, combined with the empirical model determined from Figure 2.7a, provide the first steps toward the development of a generalized model for describing material spreading of printed layers of polymers as a function of process parameters and the contact angle of printed single droplets. Additional material interactions should be explored along with a parameterization of different material properties such as density, viscosity, and conductivity to derive a normalized model that can be used to predict material spreading for a broad range of materials at the microscale. Ultimately, the controllability and repeatability of e-jet printing were demonstrated by fabricating a Bayer filter that consisted of different colors across the spectrum using drop-on-demand printing.

## 2.7 Supplemental

Table 2.1: Density and liquid surface tension of all inks studied in this work.

| Ink | Density (g cm $^{-3}$) | $\gamma_l$ (mN m$^{-1}$) |
|---|---|---|
| NOA170 | 1.94±0.11 | 37.3±2.1 |
| Loctite3526 | 0.94±0.04 | 25.1±2.1 |
| NOA1369 | 1.16±0.07 | 14.5±0.9 |
| NOA13775 | 1.40±0.04 | 19.4±0.4 |
| NOA13825 | 1.57 ± 0.21 | 21.1 ± 2.5 |
| NOA1348 | 1.50 ± 0.15 | 18.6 ± 1.8 |
| NOA138 | 1.02 ± 0.03 | 19.3 ± 0.7 |
| NOA142 | 1.04 ± 0.16 | 20.7 ± 2.9 |
| NOA144 | 0.90 ± 0.18 | 19.1 ± 3.3 |

**Rheological properties of the inks**: Generally, we utilized the manufacturer provided viscosity data. However, we conducted a rheological study to determine the viscosity dependence on the shear rate for Loctite3526. The manufacturer-supplied value of 17,500 cP was confirmed at shear rates up to 200 s$^{-1}$. However, higher shear rates led to a decrease in the apparent viscosity. Future work will focus on the rheological behavior of all the inks under relevant shear rates encountered while printing.

**Liquid Surface Tension Characterization**: Based on the density of the ink and the resulting droplet shape underneath a nozzle, it is possible to compute the LST of an ink. This study was also carried out on a Ramé-Hart goniometer. Density measurements were conducted by weighing a known volume of each ink. A summary Table of density measurements and resulting LST measurements is given in Table 2.1.

**Solid Surface Energy (SSE) Characterization**: All of the photopolymers studied in this work were spin-coated onto silicon wafers (approximately 2 cm × 2 cm) at 6000 RPM within an inert glove box and cured under 365 nm light for 15 minutes to ensure a full cure. The contact angle-based methods of Owens-Wendt and Wu were selected for this study to estimate the SSE value [65, 66]. Three droplets of two different probe liquids, deionized water ($\gamma_l$ = 72.8 mN m$^{-1}$) and diiodomethane (50.8 mN m$^{-1}$), were placed at three different positions on the spin-coated samples (as well as the silicon substrate), and the contact angles were measured using a Ramé-Hart goniometer. The SSE values of

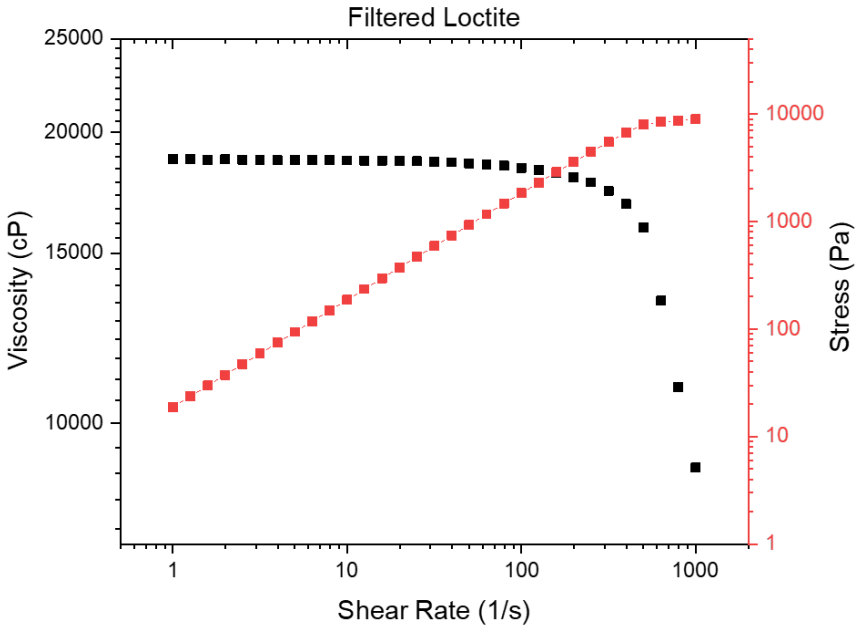


Figure 2.12: Experimental results for viscosity versus shear rate of Loctite3526.

all inks studied in this work are given in Table 2.2. It should be mentioned that material deposition has been done in an ambient atmosphere. However, the patterns were cured in a nitrogen atmosphere due to oxygen inhibition of the photopolymerization of the inks (excluding Loctite 3526). This was achieved by creating an enclosure around the LED curing bulb and flowing nitrogen at a high rate over the surface. The surface energies were not measured in an inert atmosphere. The macroscale surface energetics were determined at room temperature and pressure.

**SSE and LST Measurements**: The static contact angle of probe liquids is used to calculate SSE values via the methods of Owens-Wendt and Wu. These methods are chosen based on the wide use of the Owens-Wendt method and the accuracy of the Wu method in measuring low surface energy polymers. They differ primarily in the calculation of the mean of the polar and dispersive components of the energy, with the Owens-Wendt method using a geometric mean and Wu using a reciprocal mean;

$$\begin{aligned} \text{Owens-Wendt:} \quad & \gamma_{ls} = \gamma_s + \gamma_l - 2\left(\sqrt{\gamma_s^D \gamma_l^D} + \sqrt{\gamma_s^P \gamma_l^P}\right) \\ \text{Wu:} \quad & \gamma_{ls} = \gamma_s + \gamma_l - 4\left(\frac{\gamma_s^D \gamma_l^D}{\gamma_s^D + \gamma_l^D} + \frac{\gamma_s^P \gamma_l^P}{\gamma_s^P + \gamma_l^P}\right) \end{aligned} \tag{2.2}$$

Table 2.2: Static contact angles and solid surface energy of all primary and secondary substrates. All contact angles are in degrees and all solid surface energies are in mN $m^{-1}$.

| | | | Owens-Wendt | | | Wu | | | |
|---|---|---|---|---|---|---|---|---|---|
| Substrate | $\theta_s^{water}$ | $\theta_s^{DIM}$ | $\gamma_s^P$ | $\gamma_s^D$ | $\gamma_s^T$ | $\gamma_s^P$ | $\gamma_s^D$ | $\gamma_s^T$ | Average |
| Silicon | 27.1±1.0 | 52.0±3.8 | 46.6 | 18.5 | 65.1 | 38.6 | 28.8 | 67.4 | 66.3±0.8 |
| NOA170 | 66.8±0.3 | 35.5±3.9 | 10.5 | 34.5 | 45.0 | 36.5 | 15.1 | 51.6 | 48.3±1.4 |
| Loctite3526 | 109.8±11.6 | 79.9±4.9 | 0.4 | 17.3 | 17.7 | 1.7 | 19.5 | 21.2 | 19.4±2.6 |
| NOA1369 | 109.8±0.8 | 90.3±1.3 | 1.3 | 11.4 | 12.7 | 3.5 | 14.5 | 18.0 | 15.3±0.5 |
| NOA13775 | 104.4±4.6 | 81.2±3.3 | 1.6 | 15.4 | 17.0 | 4.1 | 17.8 | 22.0 | 19.5±2.1 |
| NOA13825 | 109.0±1.5 | 84.0±3.8 | 0.9 | 14.6 | 15.5 | 2.8 | 17.2 | 20.0 | 17.7±1.7 |
| NOA1348 | 118.7±0.5 | 98.9±0.6 | 0.5 | 8.5 | 9.0 | 1.7 | 12.2 | 13.9 | 11.5±0.2 |
| NOA138 | 111.9±0.3 | 92.3±3.8 | 1.1 | 10.7 | 11.8 | 3.1 | 13.8 | 16.9 | 14.3±1.3 |
| NOA142 | 113.5±5.8 | 90.2±4.8 | 0.6 | 12.0 | 12.6 | 2.1 | 15.1 | 17.2 | 14.9±2.3 |
| NOA144 | 108.8±1.1 | 91.8±5.8 | 1.8 | 10.4 | 12.2 | 4.2 | 13.7 | 17.9 | 15.1±1.9 |

where $\gamma_{ls}$ the liquid-solid interfacial tension, $\gamma_s$ is the SSE, $\gamma_l$ is the LST, $\gamma_l^D$ the dispersive portion of the liquid surface tension, $\gamma_l^P$ is the polar portion of the liquid surface tension, $\gamma_s^D$ is the dispersive portion of the solid surface energy, and $\gamma_s^P$ is the polar portion of the solid surface energy. Using the Young-Dupre equation, which relates these quantities to the contact angle on the surface, it is possible to calculate $\gamma_s^D$ and $\gamma_l^P$. Table 2.2 summarizes the contact angles measured and the resulting solid surface energies. The values listed in the main text are taken as the average of the Owens-Wendt and Wu methods (listed in the far-right column).

The work of cohesion, $W_C$, of a particular liquid is defined as the work per unit area needed to divide that homogeneous liquid from itself. In contrast, the work of adhesion, $W_A$, is defined as the amount of work needed to separate a liquid from a solid surface of another material;

$$W_c = 2\gamma_l \tag{2.3a}$$

$$W_A = \gamma_l(1 + cos\theta) \tag{2.3b}$$

$$R = \frac{W_A}{W_C} = \frac{(1 + cos\theta)}{2} \tag{2.3c}$$

where $\theta$ is the angle the liquid makes with the surface. In general, more energy is required to separate a liquid from itself ($W_C$) than from a solid surface ($W_A$). Thus, the R ratio in Eq. (2.3c) is typically less than 1 and has been used previously to show that liquid/surface combinations with higher R ratios have a higher chance of merging to form a uniform line [65]. Another benefit to using this ratio is that it is solely dependent on the contact angle a specific liquid makes with a specific substrate.

Tables 2.3 and 2.4 show material interactions at the micro and macroscale. White cells

Table 2.3: Contact angle and surface energetic measurements of various low index ($n_L$) photopolymers on NOA170 ($n_H$) films at the macro and microscale. $\bar{g}$ and $s_q$ are the average thickness and RMS roughness of the e-jet printed films.

| | | | | Micro measurement ($n_L$ droplet on $n_H$ surface) | | | Macro measurement ($n_L$ droplet on $n_H$ surface) | | | $n_L$ film on $n_H$ surface | |
|---|---|---|---|---|---|---|---|---|---|---|---|
| Build material | $\gamma_l$ | $\gamma_s$ | $W_C$ | $\theta^\circ$ | $W_A$ | R | $\theta^\circ$ | $W_A$ | R | $\bar{g}$ (nm) | $s_q$ (nm) |
| Loctite3526 | 25.1 | | 50.14 | 11.4±3.2 | 49.6 | 0.990 | 27.7±1.5 | 47.2 | 0.943 | 130.7 | 8.1 |
| NOA1369 | 14.5 | | 29.06 | 6±2.2 | 28.9 | 0.997 | 33.2±1 | 26.7 | 0.918 | 85.5 | 5.4 |
| NOA13775 | 19.4 | 48.3 | 38.8 | 7.12±1.1 | 38.6 | 0.996 | 92.6±5 | 18.5 | 0.477 | 123.3 | 8.7 |
| NOA13825 | 21.1 | | 42.1 | 7.8±0.9 | 41.9 | 0.995 | 88.3±7.6 | 21.7 | 0.515 | 100.6 | 8.6 |
| NOA138 | 19.3 | | 38.6 | - | - | - | 0 | 38.6 | 1 | 280.5 | 100.2 |
| NOA142 | 20.7 | | 41.48 | - | - | - | 0 | 41.4 | 1 | 250.6 | 130.6 |
| NOA144 | 19.1 | | 38.18 | - | - | - | 0 | 38.1 | 1 | 280.3 | 140.1 |

Table 2.4: Contact angle and surface energetic measurements of NOA170 ($n_H$) on various low index surfaces ($n_L$) at the macro and microscale. $\bar{g}$ and $s_q$ are the average thickness and RMS roughness of the e-jet printed films.

| | | | | Micro measurement ($n_H$ droplet on $n_L$ surface) | | | Macro measurement ($n_H$ droplet on $n_L$ surface) | | | $n_H$ film on Silicon/ $n_L$ surface | |
|---|---|---|---|---|---|---|---|---|---|---|---|
| Build material | $\gamma_l$ | $\gamma_s$ | $W_C$ | $\theta^\circ$ | $W_A$ | R | $\theta^\circ$ | $W_A$ | R | $\bar{g}$ (nm) | $s_q$ (nm) |
| Silicon | | 66.3 | | 9±3.2 | 74.1 | 0.993 | 49.5±1.1 | 61.5 | 0.825 | 85.2 | 6.7 |
| Loctite3526 | | 19.4 | | 13±0.8 | 73.6 | 0.987 | 108.3±0.8 | 25.6 | 0.343 | 199.1 | 18.1 |
| NOA1369 | | 15.3 | | 34.5±4.7 | 68.0 | 0.912 | 88.3±0.9 | 38.4 | 0.515 | 290.2 | 120.2 |
| NOA13775 | 37.3 | 19.5 | 74.6 | 34.5±5.8 | 68.1 | 0.912 | 84.7±1.4 | 40.8 | 0.547 | 200.6 | 130.2 |
| NOA13825 | | 17.7 | | 45.3±12.4 | 63.5 | 0.852 | 87.1±0.3 | 39.2 | 0.525 | 210.3 | 80.2 |
| NOA1348 | | 11.5 | | 29.5±5.7 | 69.8 | 0.935 | 89.0±0.5 | 37.9 | 0.509 | 295.8 | 202.7 |
| NOA138 | | 14.3 | | 25.1±5.4 | 71.1 | 0.952 | 113.1±0.1 | 22.7 | 0.304 | 193.1 | 28.9 |
| NOA142 | | 14.9 | | 20.2±1.6 | 72.3 | 0.960 | 115.7±0.1 | 21.2 | 0.284 | 195 | 39.1 |
| NOA144 | | 15.1 | | 19.63±2.1 | 72.4 | 0.970 | 114.6±0.3 | 21.9 | 0.294 | 152.5 | 37.8 |

indicate full merging, light gray cells indicate partial merging, and dark gray cells indicate no merging at the microscale. Elucidating the actual discrepancy between microscale and macroscale measurements could potentially be addressed via a future study using picoliter-sized droplets to determine the microscale surface energy ($\gamma_l$ and $\gamma_s$ at the microscale) [73]. As mentioned before, material merging at the microscale is a trade-off between the contact angle at the microscale, the surface energy of the previous layer, and the surface tension of the build material. The zero contact angles in Table 2.3mean complete wetting that was observed at the macroscale. It should be noted that NOA138, NOA142, and NOA144, quickly evaporate on the substrate and we could not measure their contact angles. To measure the contact angle of NOA 170 on these materials, we spin-coated the samples in a glove box and cured them immediately to reduce the evaporation rate, before e-jet depositing droplets of NOA170 on top of them. In summary, a material combination with a low micro-contact angle ($< 15^\circ$) and high SSE and LST values such that $\gamma_l < \gamma_s$ has a higher proclivity to merge. We can quantify all of these parameters by comparing the value

of R for all material combinations. Based on results in Tables 2.3 and 2.4, and Figures 3 and 6A, full merging at the microscale happens with $0.987<R<1$, partial merging with $0.952<R<0.97$, and failure to merge with $R<0.952$.

# CHAPTER 3

# Preliminaries of Spatial Iterative Control

In the previous chapter, e-jet printing was introduced and its ability to fabricate high-resolution features was demonstrated. The following chapters will investigate how to exact greater control over the addition of material for device fabrication. In particular, the next few chapters will investigate control strategies that are available to integrate with the e-jet process to close the topography loop in order to regulate material addition without requiring a human operator to manually tune the process parameters. In this chapter, preliminary notations, definitions, and models that describe the layer-to-layer material addition are presented.

## 3.1 Notation

- The finite set of $\mathbb{Z}_n$ for an odd and positive integer $n$, with $\mathbb{Z}_1 \triangleq \{0\}$ is defined as,

$$\mathbb{Z}_n \triangleq \{\frac{1-n}{2}, \frac{3-n}{2}, ..., \frac{n-3}{2}, \frac{n-1}{2}\}.$$

- A generic scalar function $p(x,y)$ sampled at discrete values can be combined in the following matrix form,

$$p(x,y) = \begin{bmatrix} p(\frac{1-n_x}{2}\frac{1-n_y}{2}) & p(\frac{1-n_x}{2}\frac{3-n_y}{2}) & \cdots & p(\frac{1-n_x}{2}\frac{n_y-1}{2}) \\ p(\frac{3-n_x}{2}\frac{3-n_y}{2}) & p(\frac{3-n_x}{2}\frac{3-n_y}{2}) & \cdots & p(\frac{3-n_x}{2}\frac{n_y-1}{2}) \\ \vdots & \vdots & \ddots & \vdots \\ p(\frac{n_x-1}{2}\frac{1-n_y}{2}) & p(\frac{n_x-1}{2}\frac{3-n_y}{2}) & \cdots & p(\frac{n_x-1}{2}\frac{n_y-1}{2}) \end{bmatrix},$$

where finite support of $p$ is $supp(p) = \{(x,y) \in \mathbb{Z}_{n_x} \times \mathbb{Z}_{n_y} : p(x,y) \neq 0\}$. Setting $n_x$ and $n_y$ as positive odd integers, makes the central location of $p$ at $(0,0)$. An example of this generic function is the heightmap in $\mu$-AM systems defined as a 2D array of printed droplets in the spatial domain.

- The 2D discrete Fourier transform (DFT) representation of $p(x, y)$ is defined as,

$$\boldsymbol{P}(u, v) = \sum_{x=0}^{n_x-1} \sum_{y=0}^{n_y-1} (p(x + x^{\Delta}, y + y^{\Delta}) e^{-i2\pi(\frac{ux}{n_x} + \frac{vy}{n_y})},$$

where $x^{\Delta} = \lfloor \frac{n_x}{2} \rfloor + 1$, $y^{\Delta} = \lfloor \frac{n_y}{2} \rfloor + 1$, and $\lfloor . \rfloor$ is the floor operator. Hereafter, we will use bold capital italic font to show the frequency domain variables.

- A vectorization operator $v(.)$ can be applied to a matrix, $p \in \mathbb{R}^{n_x \times n_y}$, to convert the matrix into a column vector form, $\vec{p} \in \mathbb{R}^{n_x n_y \times 1}$, given as

$$\vec{p} \triangleq v(P) = vec(P^{\mathrm{T}}).$$

where $vec(.)$ is the conventional column-wise vectorization operator.

- The notation $\preceq$ *and* $\succeq$ are element-wise inequalities such that

$$A \preceq B \implies [A]_{ij} \leq [B]_{ij} \, \forall \, i, j.$$

- The Frobenius norm of a matrix $A \in \mathbb{R}^{n_x \times n_y}$is defined as

$$\|A\|_F = \sqrt{\sum_{i=1}^{n_x} \sum_{j=1}^{n_y} |A_{i,j}|^2}.$$

- The Frobenius norm of a matrix $P \in \mathbb{R}^{n_x \times n_y}$ is related to the $l_2$ norm of the vectorized matrix by:

$$\|\vec{p}\|_2 = \frac{1}{\sqrt{n_x \times n_y}} \|P\|_F.$$

## 3.2 Definitions

- A scalar $h$ is denoted as an interval parameter if it lies between upper and lower bounds, $\overline{h}$ and $\underline{h}$ as follows

$$h \in [\overline{h}, \underline{h}].$$

- $\mathbf{H}$ is denoted as an interval matrix if all elements within the matrix, $\mathbf{H}_{i,j}$ are interval

parameters, and it is a member of the following matrix set:

$$\mathbf{H}^I = \{\mathbf{H} \in \mathbb{R}^{MN \times MN} \,|\, \underline{\mathbf{H}} \preceq \mathbf{H} \preceq \overline{\mathbf{H}}\}.$$

- $circ(p_1, p_2, ..., p_n)$ is defined as a block circulant matrix with square submatrices of the same size, $p_1, p_2, ..., p_n$, where $n$ is an odd number. The $i$th block of the middle column in $circ(p_1, p_2, ..., p_n)$ is always $p_i$ [39]. For example, if $n = 3$,

$$circ(p_1, p_2, p_3) = \begin{bmatrix} p_2 & p_1 & p_3 \\ p_3 & p_2 & p_1 \\ p_1 & p_3 & p_2 \end{bmatrix}$$

- A matrix is said to be block circulant with circulant blocks (BCCB) if it is defined as

$$\mathbf{H} \triangleq circ(\mathbf{H}_{\frac{1-n_x}{2}}, \mathbf{H}_{\frac{3-n_x}{2}}, ..., \mathbf{H}_{\frac{n_x-1}{2}}) \in \mathbb{R}^{n \times n}$$
$$\mathbf{H}_i \triangleq circ(h(i, \frac{1-n_y}{2}), h(i, \frac{3-n_y}{2}), ..., h(i, \frac{n_y-1}{2})), \in \mathbb{R}^{n_y \times n_y}$$

  where $h(x, y)$ is a discrete function, with the same support as $p(x, y)$. Note that the $l_2$ norm of $\mathbf{H}$ equals the maximum modulus of its DFT representation; i.e., $\|\mathbf{H}\|_2 = \|\boldsymbol{H}(u, v)\|_\infty = max_{(u,v)}|\boldsymbol{H}(u, v)|$. The BCCB property of a matrix makes Fast Fourier Transforms (FFT) possible, which has been demonstrated to be computationally less expensive in calculating matrix products and norms [40], especially in applications with large $n$ values.

## 3.3 General iteration varying systems

In order to enable automated topography control for droplet based AM processes, models that describe heightmap evolution in a layer-by-layer fashion are needed. Examples of these models are presented in [2, 3, 74–76] and Eq. (3.1). In these models, the printed topography of the current layer, $g_l \in \mathbb{R}^{n_x \times n_y}$, is a linear or nonlinear function ($\mathbb{f}$) of the previous layer topography, $g_{l-1} \in \mathbb{R}^{n_x \times n_y}$, and the input signal of the current layer, $f_l \in \mathbb{R}^{n_x \times n_y}$.

$$g_l = \mathbb{f}(g_{l-1}, f_l) \tag{3.1}$$

The following assumptions are considered for the AM process described in Figure 3.1 and Eq. (3.1),

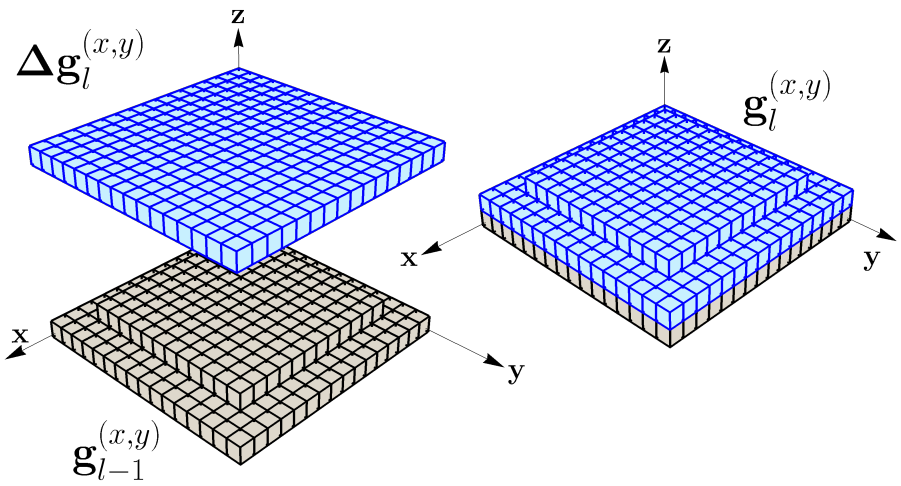


Figure 3.1: Schematic of AM spatial dynamics described in Eq. (3.1).

$\mathbf{A}_1$ : The spreading behavior of a printed material on a flat surface is different from that on a nonflat surface [2].

$\mathbf{A}_2$ : The spatial dynamics are causal in the temporal and noncausal in the spatial domain, meaning that the applied input at a given position will affect the output in the advanced layers and surrounding coordinates [2, 40, 76].

Assumptions $\mathbf{A}_1$ and $\mathbf{A}_2$ denote that the spatial dynamics of a given AM system are a function of previous layer topography ($\vec{g}_{l-1}$) and the surrounding environment.

## 3.4 Linear Iteration Varying Models

In order to maintain access to linear control, in this work, linear models are used, or nonlinear models are linearized around their equilibrium points. A simple linear time invariant (LTI) representation of such a model is described as follows,

$$\vec{g}_l = \vec{g}_{l-1} + \mathbf{H}(\vec{g}_{l-1})\vec{f}_l, \tag{3.2}$$

with $\vec{f}_l \triangleq \nu(f_l(x,y)) \in \mathbb{R}^{n\times 1}$ is the input signal, $\vec{g}_l \triangleq \nu(g_l(x,y)) \in \mathbb{R}^{n\times 1}$ is the output signal, $\mathbf{H}(\vec{g}_{l-1}) \in \mathbb{R}^{n\times n}$ is the interval plant matrix that describes the relation between system input and output, and $n = n_x \times n_y$. We will use $\mathbf{H}_{l-1}$ instead of $\mathbf{H}(\vec{g}_{l-1})$ for brevity. $\mathbf{H}$ is an interval matrix if all of its elements are interval parameters. In other word, the interval $\mathbf{H}$ is a member of the following matrix set:

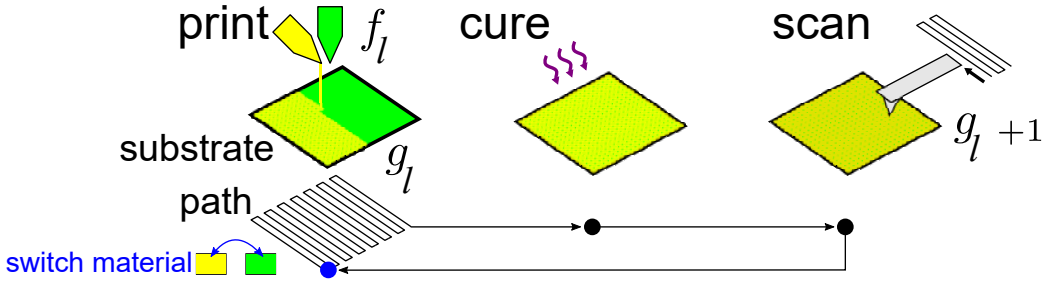


Figure 3.2: Heightmap evolution process. Controlled device fabrication follows the print-cure-scan cycle, with a change in build material at each new layer. Subscript $l$ represents a layer and material combination.

$$\mathbf{H}^I = \{\mathbf{H} \in \mathbb{R}^{n\times n} \,|\, \underline{\mathbf{H}} \preceq \mathbf{H} \preceq \overline{\mathbf{H}}\}.$$

where $\preceq$ is element wise inequality. Note that the plant bounds are known and fixed properties of the iteration varying system, and for the AM-system described in Figure 3.1 they can be measured by running the additive process described in Eq. (3.2) multiple times and measuring maximum and minimum droplet spreading on spatially varying surfaces [2]. In addition to the $\mathbf{A}_1$ and $\mathbf{A}_2$ assumptions in Section 3.3, the following assumption is considered for the LTI system in Eq. (3.2),

$\mathbf{A}_3$ : The plant matrix ($\mathbf{H}$) is considered bounded input, bounded output (BIBO) stable, meaning that there exist positive finite scalars $\xi$ and $\zeta$ such that given a bounded input, $\|\vec{f}_l(x,y)\| < \xi$, the resulted output will always be bounded, $\|\vec{g}_l(x,y)\| < \zeta$, $\forall (x,y) \in \mathbb{R}^{n_x \times n_y}$.

Assumption $\mathbf{A}_3$ holds for the additive system described in Figure 3.1 given that material addition to the substrate is bounded by a pre-defined volume of available material. Furthermore, because of actuator constraints, the input is limited by an upper bound [39]. For a general additive manufacturing process, we are interested in controlling the heightmap increment ($\Delta\vec{g}_l \triangleq \vec{g}_l - \vec{g}_{l-1}$) with respect to the previous layer described as,

$$\Delta\vec{g}_l = \mathbf{H}_{l-1}\vec{f}_l, \quad \mathbf{H}_{l-1} \in \mathbf{H}^I, \tag{3.3}$$

where $\mathbf{H}^I$ is the interval set associated with $\mathbf{H}_{l-1}$. In Section 3.5, we will describe in detail the different available models for the additive process in Eq. (3.2).

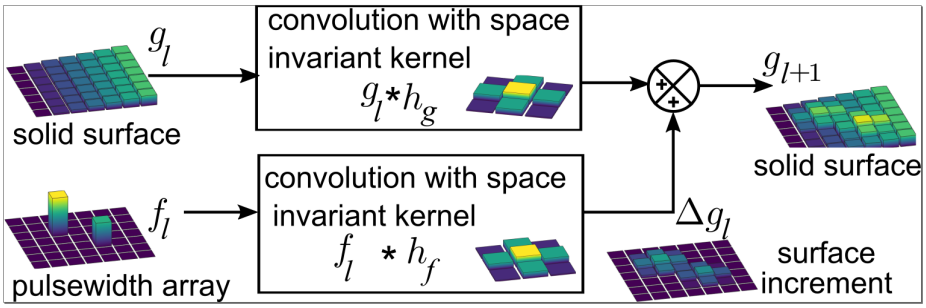


(a)

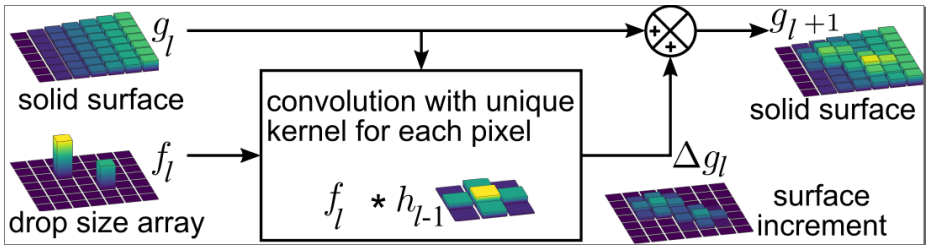


(b)

Figure 3.3: **Linear models for layer-to-layer material addition in AM processes**. a) CLR model: evolution of the solid surface topography as a heightmap signal is modeled by integration of a convolution of input $f_l$ with kernel $h_f$, and a convolution of the previous layer output $g_{l-1}$ with kernel $h_g$. $h_f$ and $h_g$ are integration and space invariant. b) LPV model: evolution of the solid surface topography as a heightmap signal is modeled by integration of the convolution of input $f$ with kernel $h$. $h$ is a function of local variation in $g$ for each pixel in $g$.

## 3.5 AM-Model Approximation

Controlled topography evolution requires topography updates, so printing is performed in a cycle of: 1) printing an array of droplets of varying sizes at discretized coordinates, 2) curing (solidifying) the droplets, and then 3) scanning the solid surface to obtain a heightmap measurement of topography. This print-cure-scan cycle is depicted in Figure 3.2. In this section, we explore three methods to estimate the spreading model of liquid inks, $\theta$, such that $\|g_{l+1} - \phi(g_l, f_{l+1})\hat{\theta}\|$ is minimized, where $\hat{\theta}$ is an estimation of the true $\theta$, and $\phi(g_l, f_{l+1})$ is a nonlinear transformation between $g_{l+1}$ and $\theta$. Note that a linearized form of $\phi$ can be used for control design. In the upcoming chapters, the models developed in this section will be used in the design of different controllers.

### 3.5.1 Constrained Linear Regression (CLR)

The sequence of material addition in multi-layer structures using a constrained regression model is shown in Figure 3.3a, and can be written mathematically as,

$$\begin{aligned} g_{l+1}(x,y) &= (g_l * h_g)(x,y) + (f_{l+1}^p * h_f)(x,y) \\ &= \sum_{m=0}^{n_x-1}\sum_{n=0}^{n_y-1} g_l(m,n)h_g(x-m,y-n) + \sum_{m=0}^{n_x-1}\sum_{n=0}^{n_y-1} f_{l+1}^p(m,n)h_f(x-m,y-n), \end{aligned} \tag{3.4}$$

where $h_f \in \mathbb{R}^{5\times5}$ is the discrete impulse response to the current layer input, and $h_g \in \mathbb{R}^{5\times5}$ is the discrete impulse response to the previous layer output. $f_{l+1}^p \in \mathbb{R}^{n_x\times n_y}$ is the pulsewidth signal at layer $l$. In Eq. (3.4), it is assumed that the added material will spread on the previous layer to a finite extent [76]. The simplified system model can be described using the following 2-D convolution format. Assuming rotational symmetry of liquid droplets in [76], $h_f$ and $h_g$ are defined by only 6 parameters. To find the unknown $\theta^{LR} = [h_f^{\mathrm{T}}\ h_g^{\mathrm{T}}]^{\mathrm{T}} \in \mathbb{R}^{12\times1}$, the design matrix $\phi(g_l, f_{l+1}^p) \in \mathbb{R}^{n\times12}$ is constructed using the $conv2(.)$ function in MATLAB and the optimization, $\|g_{l+1} - \phi(g_l, f_{l+1}^p)\hat{\theta}^{LR}\|$, is solved using the built-in solver $lsqlin()$ in Matlab. Assuming volume conservation from layer-to-layer, $h_g$ has only one non-zero element at the center, $h_g(3,3) = 1$. For Loctite3526, $h_f$ is calculated as:

$$h_f = \begin{bmatrix} 0.09 & 0.09 & 0.21 & 0.09 & 0.09 \\ 0.09 & 0.21 & 0.38 & 0.21 & 0.09 \\ 0.21 & 0.38 & 0.71 & 0.38 & 0.21 \\ 0.09 & 0.21 & 0.38 & 0.21 & 0.09 \\ 0.09 & 0.09 & 0.21 & 0.09 & 0.09 \end{bmatrix} (\frac{nm}{ms})$$

### 3.5.2 Linear Parameter-Varying Model (LPV)

The layer-to-layer material addition using the LPV model is presented in Figure 3.3b. The LPV model in [2] is described using the following 2-D convolution equation,

$$g_l(x,y) = g_{l-1}(x,y) + \sum_{m=0}^{n_x-1}\sum_{n=0}^{n_y-1} h_{l-1}^{(m,n)}(x-m,y-n) * f_l^{LPV}(m,n). \tag{3.5}$$

This model assumes a known relationship between pulsewidth and droplet size so that the control input can be taken as drop size rather than pulsewidth in Section 3.5.1; therefore, the input signal of the LPV model, $f_l^{LPV} \in \mathbb{R}^{n_x\times n_y}$, is a 2D array of cube roots of drop volumes. $h_{l-1}^{(m,n)} \in \mathbb{R}^{3\times3}$ is the impulse response that describes the spreading behavior of

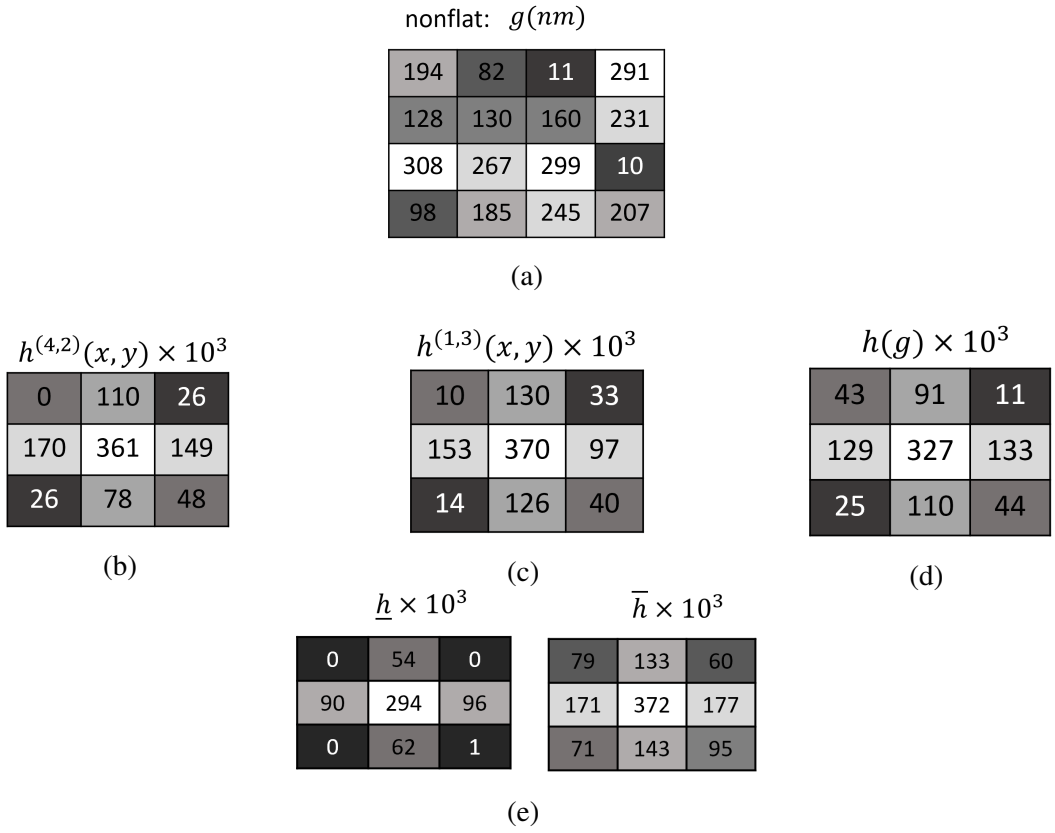


Figure 3.4: **Topography dependent LPV impulse response of Loctite3526 on itself**. a) A $4\times4$ pixel of a random $g$ signal of UV-Cured Loctite3526 to show the effect of significant surface variation. b) M2 method in [2]: the $3\times3$ model's corresponding impulse response at the spatial location $(4,2)$, $h^{(4,2)}(x,y)$. c) using M2 method in [2]: The $3\times3$ model's corresponding impulse response at the spatial location $(1,3)$, $h^{(1,3)}(x,y)$. d) M3 method in [2]: the estimated impulse response of the topography in Figure 3.4a is spatial invariant meaning that it is the same for every spatial coordinate of the $g(x,y)$. e) Upper and lower bounds of $h$, $\bar{h}$, $\underline{h}$, such that $\underline{h} \preceq h \preceq \bar{h}$.

a printed droplet on the neighboring coordinates at steady-state for an input signal with magnitude one applied at coordinate $(m,n)$ and layer $l-1$. Both the input $f^{LPV}$ and output $g$ are heightmaps, but only $g$ represents a scanned topography. Choosing the same height units for both $f$ and $g$ makes $h$, and thus the system, dimensionless.

The dependence of $h_l^{(m,n)}$ on existing topography $g_l$ is modeled using the multivariate regression method proposed in [2]. Importantly, the magnitude of $\mathbf{g}_l$ does not affect the impulse response; only the local variation in $\mathbf{g}_l$ affects $h_l$. In this method, numerical simulations of droplets spreading on nonflat surfaces are pre-computed for equilibrium contact angles associated with a specific material/substrate combination. Subsequently, an ordi-

nary least squares multivariate linear regression is performed, where the elements from each $3 \times 3$ pixel crop of the heightmap $g$ are the predictor variables, and the elements from each measured $3 \times 3$ pixel impulse response $h$ are the response variables. The fitted regression model is used to evaluate the spatially varying impulse response (method M2 in [2]), $h_{l-1}(x, y)$, for the $3 \times 3$ pixel crop of the heightmap $g_l$ centered at pixel coordinates $(x, y)$.

Figures 3.4b and 3.4c show the impulse response of Loctite3526 on a nonflat surface of UV-cured Loctite3526 at different spatial locations, using method M2. Figure 3.4b shows the spreading of the liquid ink on the nearby pixels, if a single droplet with magnitude one micron is applied at the spatial coordinate coordinate (m,n)=(4,2) in Figure 3.4a with total height of 185 nm. Note that in Figure 3.4, x and y indicate row and column numbers, respectively. As it is expected, the model predicts the largest material height at the center pixel (4,2), where the droplet is deposited. In addition, the model predicts no material spreading on the nearby pixel with spatial location (3,1). The reason is that it is expected the liquid droplet does not flow from the lower heights to the higher heights in the nearby pixels. The nearby pixel (3,1) has higher height value (308 nm > 185 nm) compared to the height value at the impulse location (m,n)=(4,2). Note that the last row of the $h^{(4,2)}(x, y)$ in Figure 3.4b is related to the material spill-over from the droplet deposition on the spatial location (m,n)=(4,2). Figure 3.4c shows a similar behavior for the impulse response applied at the spatial location (m,n)=(1,3), with height value 11 nm. Similarly, the first row of $h^{(1,3)}(x, y)$ is related to the material spill-over from the droplet deposition on the spatial location (m,n)=(1,3).

Taking the average of $h_{l-1}(x, y)$ over all spatial coordinates ($x \in \mathbb{Z}_{n_x}$, $y \in \mathbb{Z}_{n_y}$) results in a spatially invariant impulse response (method M3 in [2]), $h_{l-1}$. Note that the spatially invariant approximation results in a less accurate model than the spatially varying model; however, the spatially invariant plant matrix is BCCB. Examples of impulse response calculated using method M2 deposition of Loctite3526 on itself is presented in Figure 3.4d. Unlike Figures 3.4b and 3.4c, the M3 method calculates one single $3 \times 3$ impulse response shown in Figure 3.4d for all spatial locations in Figure 3.4a. Note that the estimated impulse response is still iteration varying.

If method M3 is used to approximate the material addition, the BCCB plant matrices $\mathrm{H}_l$ in Eq. (3.3) can be calculated from the BCCB construction method described in Section 3.2. However, if M2 method is used to estimate the material spreading in the e-jet process, the plant matrices $\mathrm{H}_l$ in Eq. (3.3) will not be BCCB and should be calculated using the lifted domain conversion in the next sections. Impulse response bounds are calculated from the supremum and infimum of each element of $h_l$ determined by simulating the deposition of printed material on multiple topographies of the same substrate material.

### 3.5.3 Convolutional Recurrent Neural Network (ConvRNN)

In this section, the ConvRNN model developed in [3] is used to estimate in-layer and layer-to-layer material addition in e-jet printing process. Although the model is developed in [3], the model's parameters are calculated by the experimental data from e-jet printed samples in Barton Research Lab at the University of Michigan. This model considers the surface tension of liquid droplets, parameterized by $\kappa$ known as the flowability parameter, that causes the droplets to move from higher to lower height locations of nearby pixels.

$$\vec{y}_l^t = \vec{y}_l^{t-1} - D\sigma(\mathrm{K}\mathrm{D}^{\mathrm{T}}\vec{y}_l^{t-1}) + W_u\vec{u}_l^t \tag{3.6a}$$

$$\vec{g}_l(i) = ln(\gamma + e^{\vec{y}_l^n(i)+v_0}), \qquad i,t \in [1,n] \tag{3.6b}$$

$$\vec{y}_l^0 = \vec{g}_{l-1}. \tag{3.6c}$$

where, $\vec{y}_l^t \in \mathbb{R}^{n\times 1}$ defines the network internal states at layer $l$ and time step $t$, which refer to the unmeasured material addition states during in-layer deposition of a single droplet in liquid form. Note that $\vec{y}_l^t$ is considered internal state since our integrated sensor, AFM, cannot measure the in-layer dynamics when a new liquid droplet reaches the surface and interacts with the other liquid droplets on the same layer and the existing solid topography of the previous layer at the microscale and millisecond timescale. $\vec{g}_l \in \mathbb{R}^{n\times 1}$ is the measured topography of layer $l$ once the material has been UV cured. In addition, $\vec{u}_l^t \in \mathbb{R}^{n\times 1}$ is the ratio of the size of the deposited droplet at time step $t$ to the maximum droplet size. The input signal of the entire layer is given by $\vec{f}_l^{ConvRNN} = \sum_{t=1}^{n} \vec{u}_l^t$. Note that we assume the relationship between the applied pulsewidth and droplet size is known. $n_l$ is defined as the number of links between the nodes. The incidence matrix, $\mathrm{D} \in \mathbb{R}^{n\times n_l}$, in Figure 3.5 transforms the height profile of all discretized grids into height differences or links. The circles and arrows in Figure 3.5 represent nodes (each discrete spatial location that a single droplet deposits) and the link between nodes, respectively. D($i$, $j$) is 1 if the link $j$ starts at node $j$, -1 if link $j$ ends at node $i$, and zero if there is no connection between node $i$ and link $j$.

$K = \kappa\mathrm{I} \in \mathbb{R}^{n_l\times n_l}$ is constructed as a diagonal matrix with nonzero elements along the diagonal that captures the material flow along each link. In Eq. (3.6a), $\sigma(l_t)$ represents the Leaky soft threshold function that is set to zero if the effective flow at each time step is smaller than a threshold value $\epsilon$, $l_t = \mathrm{K}\mathrm{D}^{\mathrm{T}}\vec{y}_l^{t-1} < \epsilon$. The matrix $W_u \in \mathbb{R}^{n\times n}$ is a BCCB matrix associated with the convolution kernel $b \in \mathbb{R}^{5\times 5}$, such that $W_u\vec{u}_l^t = \nu(b * u_l^t)$. Note that, $b$ is the kernel related to the spreading behavior of the largest droplet. From the definition of $\vec{u}_l^t$, the elements of the input signal $f_l^{ConvRNN}$ are bounded between $0 \le f_l^{ConvRNN}(i) \le 1$.

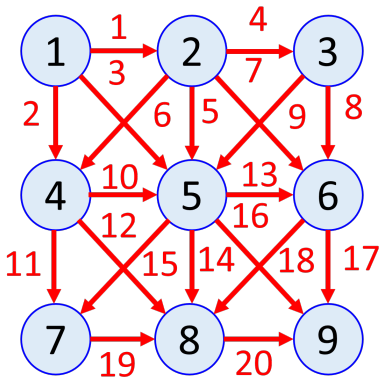


Figure 3.5: **Incidence matrix (D) developed in [3]**: the circles and arrows represent nodes (each discrete spatial location that a single droplet deposits) and the link between nodes, respectively. D($i$, $j$) is 1 if the link $j$ starts at node $j$, -1 if link $j$ ends at node $i$, and zero if there is no connection between node $i$ and link $j$.

Lastly, $v_0$ is the material shrinkage parameter due to UV curing, and $\gamma$ is a non-negative scalar that ensures that the output heightmap remains nonnegative.

To derive the ConvRNN model, the unknown parameters of $\theta^{ConvRNN} = [\epsilon, b, \kappa, \gamma, v_0]$ for the printing material of interest (e.g. Loctite3526), are calculated from experimental data using the steps described in [3]:

$$\epsilon = 6.66,\ \kappa = 1.12 \times 10^{-5},\ \gamma = 1.014,\ v_0 = 56.88(nm),$$

$$b = \begin{bmatrix} -6.77 & -9.99 & 45.58 & -9.99 & -9.98 \\ 23.97 & 28.03 & 58.74 & 2.72 & -1.17 \\ 32.68 & 36.76 & 100.0 & 45.12 & 39.80 \\ 7.60 & 1.08 & 39.91 & -6.38 & 3.30 \\ 24.35 & 6.66 & 26.95 & 0.91 & 20.98 \end{bmatrix} (nm).$$

### 3.5.4 Model Validation

To evaluate the performance of the different modeling approaches, experimental data from printed samples of Loctite3526 on itself are used to derive the difference between the measured and predicted output topography. Figure 3.6 shows the experimental data from [76] that are used for model development and validation. We use 8 devices (63 nodes ×8) in Figure 3.6 for training, and two devices to test the accuracy of the models of linear regression and Convolutional Recurrent Neural Network models in the next sections. The variable $g_1$, $g_2$, and $\Delta g_2$ define material height at layer 1, layer 2, and the incremental height at layer 2. To capture the merging behavior of Loctite3526 with itself, we assume a base layer of

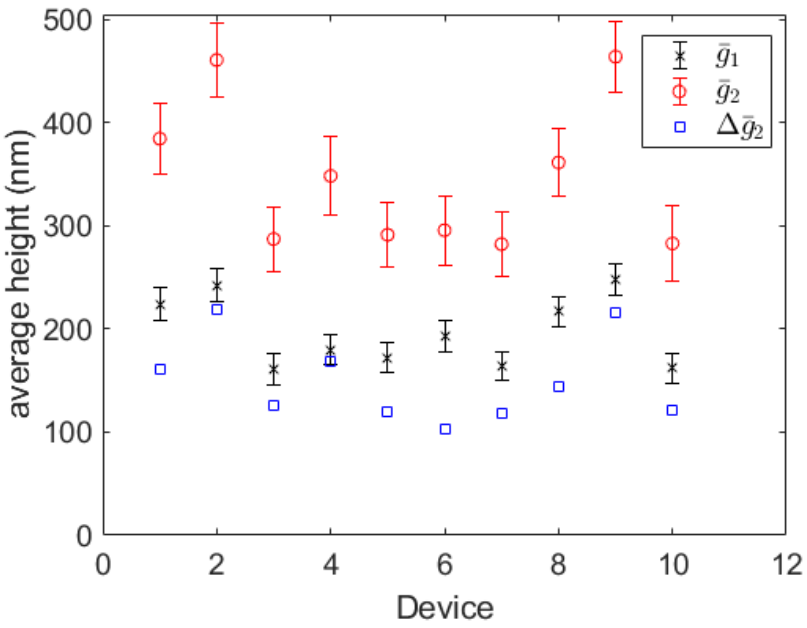


Figure 3.6: Experimental data for deposition of Loctite 3526: $\bar{g}_1$, $\bar{g}_2$, $\Delta\bar{g}_2$ are average height of layers one and two, and incremental height at layer two over a $7\times9$ discritized domain.

material and start the system identification using the input signal at layer two ($f_2$). The layers are printed using a 2D pseudo-random binary sequence (PRBS) pulsewidth signal (described in [76]), with a $35\times45$ $\mu$m spatial plane discretized into 7 by 9 grids for a $5\mu m$ droplet-to-droplet distance known as pitch.

The error metric is defined as $\|g_2^{exp} - \phi(g_1^{exp}, f_{l+1}^{exp})\hat{\theta}\|_2^2$, where $g^{exp}$ refers to the measured experimental values, $f^{exp}$ is the derived input signal, and $\hat{\theta}$ is the model from each method, respectively. Note that the input signal for each model is different.

The results in Figure 3.7 illustrate that the ConvRNN model that considers surface material flowability is more accurate than the other models. However, the ConvRNN model is nonlinear and computationally expensive; thus, it is well suited to represent the *true* system in the simulation case studies, but cannot be used for linear control design. As a comparison, the linear LPV and CLR models are approximately 50% computationally faster than the ConvRNN model. The LPV model captures the wetting nonlinearity due to non-flatness of the previous layer and yet still maintains access to linear control. However, the LPV model does not capture droplet-to-droplet effects due to surface tension since the model assumes that the droplets are placed far away from each other. In this approach, multiples passes are required to form a thin-film by depositing droplets spatially distanced from each other, and curing the material between passes to avoid coalescence effects. Since the experimental layers in Figure 3.6 are fabricated in one printing pass, the LPV model

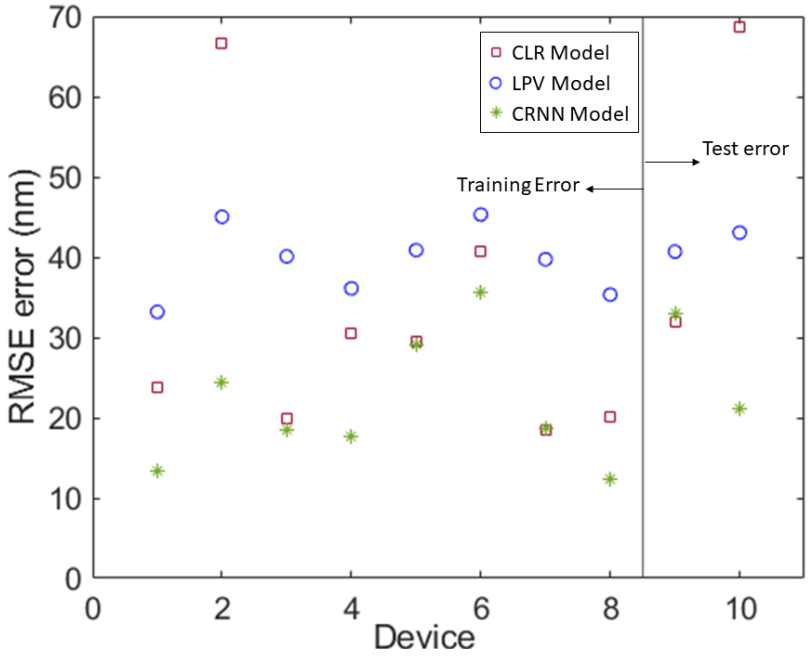


Figure 3.7: **Performance comparison**: Experimental data from printing Loctite3526 is used to compare the different modeling approaches. The error is computed as $e = g_2^{exp} - \hat{g}_2$, where $\hat{g}_2$ is the prediction of $g_2^{exp}$ using different modeling approaches. Note that $\hat{g}_2$ is a function of $g_1^{exp}$ and the input signal at the second layer.

does not capture unmodeled nonlinearities due to surface tension of the droplets for thin-film formation.

### 3.5.5 Lifted Conversion

To leverage standard temporal-domain control algorithms, the system defined in Eqs. (3.4) and (3.5) can be transferred into the lifted-form through the use of a vectorization operator defined in Section 3.1. A full description of the lifted domain conversion can be found in [40]. For brevity, we present the lifted form of Eqs. (3.4) and (3.5) in the following lifted formats,

$$\vec{g}_l = \mathbf{H}_g \vec{g}_{l-1} + \mathbf{H}_f \vec{f}_l^{p} \tag{3.7a}$$

$$\vec{g}_l = \vec{g}_{l-1} + \mathbf{H}(\mathbf{g}_{l-1}) \vec{f}_l^{LPV} \tag{3.7b}$$

with $\vec{f}_l^{LPV} \triangleq \nu(f_l^{LPV}(x,y)) \in \mathbb{R}^{n\times 1}$, $\vec{f}_l^{p} \triangleq \nu(f_l^{p}(x,y)) \in \mathbb{R}^{n\times 1}$, and $\vec{g}_l \triangleq \nu(g_l(x,y)) \in \mathbb{R}^{n\times 1}$. $\mathbf{H}_f$ and $\mathbf{H}(\mathbf{g}_{l-1}) \in \mathbb{R}^{n\times 1}$ are the lifted domain plant matrices associated with $h_f \in \mathbb{R}^{5\times 5}$ and $h(x,y) \in \mathbb{R}^{3\times 3}$ in Eqs. (3.4) and (3.5). Note that the $\mathbf{H}_g \in \mathbb{R}^{n\times 1}$ is the identity matrix, since the identified $h_g \in \mathbb{R}^{5\times 5}$ in Eq. (3.4) has one nonzero element in the center equal to one.

To convert the ConvRNN model in Eq. (3.6) to the lifted domain and enable access to linear control, the nonlinear equation in Eq. (3.6) should be linearized around its equilibrium. Suppose $(\vec{f_e}, \Delta\vec{g}_e)$ are the equilibrium pair of Eq. (3.6). For the multi-layer structure in Figure 3.1a, the desired incremental height at all layers and iterations is fixed to $\Delta\vec{g}^d$. Assume that at the equilibrium, the iteration varying spatial dynamics converge to a nominal behavior and $\lim_{l\to\infty} \Delta\vec{g}_l = \Delta\vec{g}^d$. Since the desired topography is a flat layer with a desired thickness of $d > 0$ nm$(\Delta\vec{g}^d = d\vec{1}_{n\times 1})$, there is no height difference across the layer at the equilibrium and therefore, no droplet-to-droplet movement along the links is expected, $\sigma(l_t) = 0$. In addition, since the reference for all layers is equal, the equilibrium point of layer one is equal to the equilibrium point of other layers. Simplifying Eq. (3.6b), at the equilibrium for layer one, $\vec{y}_e^n$ at the equilibrium is calculated as

$$\vec{y}_e^n = ln(e^{d+v_0} - \gamma e^{v_0})\vec{1}_{n\times 1}, \tag{3.8}$$

where, $\vec{y}_e^n$ is the uncured topography at the equilibrium when the last droplet at layer one is deposited, and $\vec{1}_{n\times 1}$ is a vector of ones. Substituting Eq. (3.8) into Eq. (3.6a), and assuming $\sigma(\mathrm{K}\mathrm{D}^{\mathrm{T}}\vec{y}_l^{n-1}) = 0$ at the equilibrium, the input signal at the equilibrium $\vec{f_e}$ is calculated as,

$$\vec{f_e} = W_u^{-1} ln(e^{d+v_0} - \gamma e^{v_0})\vec{1}_{n\times 1}. \tag{3.9}$$

The linearized approximation model of Eq. (3.6) at $(\vec{f_e}, \Delta\vec{g}_e)$, which approximates the dynamics of the nonlinear Eq. (3.6) around the equilibrium point, is calculated as follows,

$$\Delta\vec{g}_l \simeq (\frac{\partial\vec{g}_l}{\partial\vec{f_l}} - \frac{\partial\vec{g}_{l-1}}{\partial\vec{f_l}})_e(\vec{f_l} - \vec{f_e}) + \Delta\vec{g}_e. \tag{3.10}$$

Note that future layer inputs do not have an impact on previous layer outputs, $\frac{\partial\vec{g}_{l-1}}{\partial\vec{f_l}} = 0$. In addition, the Jacobian matrix at the equilibrium is defined as $\mathrm{H}_J \triangleq \frac{\partial g_l}{\partial f_l}$ and is calculated as

$$\mathrm{H}_J \triangleq \frac{\partial\vec{g}_l}{\partial\vec{f_l}} = \frac{\partial\vec{g}_l}{\partial\vec{y}_l^n}\frac{\partial\vec{y}_l^n}{\partial\vec{f_l}} \tag{3.11a}$$

$$\frac{\partial\vec{g}_l}{\partial\vec{y}_l^n} = diag(\frac{1}{1+\gamma e^(v_0 - \vec{y}_l^n(i))}), \quad i = 1,2,...,n \tag{3.11b}$$

$$\frac{\partial\vec{y}_l^n}{\partial\vec{f_l}} = W_u - D\sum_{t=1}^{n-1}\sigma'(\vec{y}_t)\mathrm{K}\mathrm{D}^T W_u \mathbf{1}_{(1-t)} \tag{3.11c}$$

Eq. (3.11b) is consistent with the results in [3]. Eq. (3.11c) is calculated from step by step partial derivation of Eqs. (3.6a) and (3.6b). $\mathbf{1}_{(1-t)} \in \mathbb{R}^{n\times n}$ in Eq. (3.11) is a block diagonal

matrix with all elements equal to zero, expect the first $t$ diagonal terms which are equal to one. For example, $\mathbf{1}_{(1-1)}$ has only one nonzero element equal to one on $(i,i) = (1,1)$. Similar to [3], $\sigma'(y_t)$ is as follows,

$$\sigma'(y_t) = \begin{cases} 1 & \text{if } \mathrm{KD}^T \vec{y}_t(i) > \epsilon \\ \delta = 0.01 & \text{if } -\epsilon < \mathrm{KD}^T \vec{y}_t(i) < \epsilon \\ 1 & \text{if } \mathrm{KD}^T \vec{y}_t(i) < -\epsilon. \end{cases} \tag{3.12}$$

$$\Delta \vec{g}_l = \mathbf{H}_J \vec{f}_l^{ConvRNN} + \Delta \vec{g}_e - \mathrm{H}_J \vec{f}_e, \tag{3.13}$$

Note that the Jabobian matrix in Eq. (3.11a) is not BCCB, because the second element in Eq. (3.11c) is not BCCB.

## 3.6 Model Assumptions

In addition to the assumptions in $\mathbf{A}_1 - \mathbf{A}_3$, the following assumptions are considered for the ConvRNN or LPV models in Eqs. (3.7) and (3.13),

$\mathbf{A}_4$ : The heightmap increments using the LPV model obey scalar multiplication and linear superposition. Therefore, the model described in Eq. (3.7b) does not capture drop coalescence effects.

$\mathbf{A}_5$ : The ConvRNN model based on [3] in Eq. (3.6) is geometrically independent and the Jacobian matrix in Eq. (3.13) is iteration invariant.

$\mathbf{A}_6$ : The model developed in Eq. (3.7a), is a constant, local model that is valid on the range of pulsewidths used in the system identification.

Assumption $\mathbf{A}_4$ is a major assumption of the additive model in Eq. (3.7b) that simplifies the system dynamics for control design. Many AM processes exhibit coalescence/surface effects that preclude linear super-position [2]. For instance, in a physical AM deposition process, depositing twice the volume of material does not cause the incremental heightmap to double. We capture these nonlinearities through model uncertainty applied to the plant model in Eq. (3.2). The ConvRNN model, on the other hand, considers these surface effects by implementing a graph structure with $n_l$ links between nodes that incorporates the effect of the liquid material flow between nearby droplets. Assumption $\mathbf{A}_5$ implies that the model parameters of the ink are generalizable to any geometry for the ConvRNN model in Eq. (3.6) based on the incorporation of a physical understanding of mass conservation

during height evolution. When we linearize the ConvRNN model around an equilibrium point, the resulting Jacobian matrix is a constant matrix. Assumption $\mathbf{A}_6$ implies that the CLR model highly depends on process variability, such as nozzle size or standoff height variations, that would shift the pulsewidth range, and subsequently the $h_f$ matrix and eventually results in model mismatch. Depending on the ink, after printing for a while, the high resolution nozzles ($< 10\ \mu$m) might clog during printing and a higher range of pulsewidths would be required to pull material out of the nozzle. In addition, although the CLR model captures droplet-to-droplet effects within the $h_f$ matrix, it does not take previous layer topography into consideration, thus ignoring an important consideration for error propagation from layer to layer. On the other hand, both M2 and M3 methods with the LPV model capture previous layer topography within the model. One advantage of the CLR model over method M2 with the LPV approach is that the plant matrix, $\mathbf{H}_f$, in Eq. (3.7a) is BCCB and enables efficient matrix computations using DFT methods. The BCCB formulation comes from the constant $h_f$ for all pixels and layers. Similarly, since the impulse response of the M3 method with the LPV model is constant for every pixel within the same layer, the plant matrix associated with it is BCCB. In contrast, the M2 method with the LPV model calculates the impulse response $h_l(x,y)$ for each spatial location, which considers the effects of previous layer unevenness. Note that if Method M2 is used, the lifted plant matrix, $\mathbf{H}_l$, is not BCCB.

# CHAPTER 4

# First-Order SILC for Multi-material and Multi-layer Additive Manufacturing

In literature, spatial ILC (SILC) has been used in conjunction with additive processes to regulate single-layer structures with only one class of material. However, SILC has the unexplored potential to regulate AM structures with multiple build materials in a three-dimensional fashion. In Figure 2.11 of chapter 2 an example of these multi-material devices was presented that has been fabricated using e-jet printing technology. The optical performance of such devices depends on the uniformity and consistency of the layers; as such, the fabrication process must be able to provide strict adherence to the desired design requirements through robust control of the process. Due to the challenges in real-time monitoring and control in e-jet printing process, SILC provides an appealing option to regulate these process. In this chapter, SILC is used as a recursive control strategy to iteratively construct the feedforward signal to improve part quality of 3D structures that consist of at least two materials in a layer-by-layer manner. Estimating the appropriate feedforward input signal in these structures can be challenging due to iteration varying initial conditions, system parameters, surface interaction dynamics in different layers of multi-material structures. A MIMO configuration is proposed that incorporates **vertical knowledge** through consideration of previous layer spatial dynamics (plant models) [33], and **horizontal learning** from part to part to derive a **diagonal** SILC SILC framework.

## 4.1 Multi-plant System Dynamics

In chapter 3 and Eq. (3.3), the layer-to-layer material addition and heightmap evolution for single material deposition was presented. Eq. (3.3) can be extended to combine multi-plant dynamics into a single MIMO architecture (illustrated in Figure 4.2). As an example, we will consider the fabrication of a two material construct, $n_1$ and $n_2$, with repeated topology

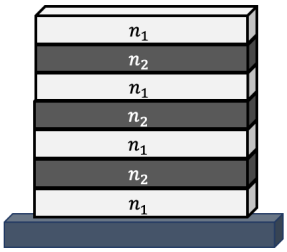


Figure 4.1: Demonstrative multi-material 3D structure fabricated by AM. $n_1$ and $n_2$ are two arbitrary build materials

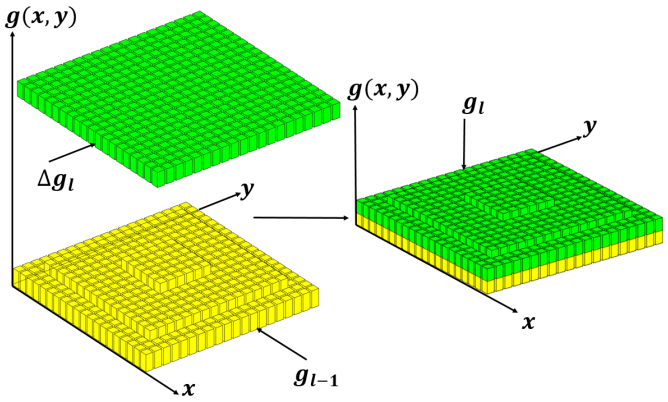


Figure 4.2: Schematic of bi-material AM spatial dynamics described in Eq. (4.1).

(see Figure 4.1). It is assumed that the device in Figure 4.1 is printed on a thin pad of $n_2$ material to maintain consistency in the two spatial systems, $n_1$ on $n_2$ and $n_2$ on $n_1$. Although we assume that the spatial dynamics for a given material are invariant to the layer index, we must still apply the noncausality assumption of $\mathbf{A}_2$ to guarantee that the spatial dynamics of a given layer are a function of previous layer topography and build material. As a result, we consider two plant matrices, $\mathbf{H}_{l-1}^{n_1,n_2} \in \mathbb{R}^{n\times n}$ and $\mathbf{H}_{l-1}^{n_2,n_1} \in \mathbb{R}^{n\times n}$, that describe spreading of the $n_1$ and $n_2$ materials on the corresponding previous layer topographies for the bi-material structure in Figure 4.3. $n = n_x \times n_y$ denotes the total number of discretized spatial locations (nodes). Note that as described in the previous chapter, depending on the model, the plant matrices are not necessarily BCCB matrices, but they are bounded by invariant upper and lower bounds such that $\underline{\mathbf{H}} \preceq \mathbf{H}_{l-1} \preceq \overline{\mathbf{H}}$. The matrix bounds are (BCCB) as described in Section 3.2.

Similar to Eq. (3.3), the spatial dynamics for the bi-material structure described in Figure 4.1 can be expressed as,

$$\begin{bmatrix} \Delta\vec{g}_l^{n_1} \\ \Delta\vec{g}_l^{n_2} \end{bmatrix} = \begin{bmatrix} \mathbf{H}_{l-1}^{n_1,n_2} & 0 \\ 0 & \mathbf{H}_{l-1}^{n_2,n_1} \end{bmatrix} \begin{bmatrix} \vec{f}_l^{n_1} \\ \vec{f}_l^{n_2} \end{bmatrix}, \quad \mathbf{H}_l^{n_1,n_2} \in \mathbf{H}^{I_{n_1,n_2}}, \quad \mathbf{H}_l^{n_2,n_1} \in \mathbf{H}^{I_{n_2,n_1}}, \tag{4.1}$$

with $\Delta\vec{g}_l^{\,i} = \vec{g}_l - \vec{g}_{l-1}$ and $\vec{f}_l^{\,i} \in \mathbb{R}^{n\times 1}$ denoting heightmap increment and the control input of the build material $i \in [n_1, n_2]$ in an layer $l$. Note that $\mathbf{H}^{I_{n_1,n_2}}$ and $\mathbf{H}^{I_{n_2,n_1}}$ are the interval sets corresponding to $\mathbf{H}_l^{n_1,n_2}$ and $\mathbf{H}_l^{n_2,n_1}$.

To aid in analysis and learning filter derivation, we define a nominal system plant matrix for each build material. These matrices are constructed from the impulse response of the desired topography at a given layer $l$,

$$\mathbf{H}_0^{n_1,n_2} = \mathbf{H}^{n_1,n_2}(\vec{g}_{d_l}^{\,n_2}), \quad \mathbf{H}_0^{n_2,n_1} = \mathbf{H}^{n_2,n_1}(\vec{g}_{d_l}^{\,n_1}) \tag{4.2}$$

where $\vec{g}_{d_l}^{\,i}$ is the desired topography of the build material $i \in [n_1, n_2]$ at layer $l$. In multi-material and multi-layer structures, the following assumption holds for the plant matrix along with the assumptions described in $\mathbf{A}_1 - \mathbf{A}_6$.

$\mathbf{A}_7$: Plant spatial dynamics (e.g. $\mathbf{H}_{l-1}^{n_1,n_2}$) are a function of the printing material (e.g. $n_1$), the build material of the previous layer (e.g. $n_2$), and previous layer topography ($\vec{g}_{l-1}^{\,n_2}$).

Assumption $\mathbf{A}_7$ ensures that the surface energy of different materials is captured through the spatial dynamics that describe spreading of a sessile droplet as a function of the interactions induced by a particular material combination and orientation as describes in chapter 2.

To consider an arbitrary number of build materials, Eq. (4.1) can be extended to a general multi-material model,

$$\Delta\vec{g}_l \triangleq \mathbf{H}_{l-1}^{n_l,n_{l-1}}\vec{f}_l, \quad \Delta\vec{g}_l \triangleq \begin{bmatrix} \Delta\vec{g}_1^{\,n_1} \\ \Delta\vec{g}_2^{\,n_2} \\ \vdots \\ \Delta\vec{g}_l^{\,n_l} \end{bmatrix}, \quad \vec{f}_l \triangleq \begin{bmatrix} \vec{f}_1^{\,n_1} \\ \vec{f}_2^{\,n_2} \\ \vdots \\ \vec{f}_l^{\,n_l} \end{bmatrix} \tag{4.3}$$

where $n_l$ is the build material of layer $l$, and $\mathbf{H}_l^{n_l,n_{l-1}}$ is a block diagonal plant matrix describing the spreading of the $n_l$ material on the previous layer topography ($\vec{g}_l^{\,n_{l-1}}$) through the diagonal elements $\mathbf{H}_l^{n_l,n_{l-1}}$.

## 4.2 Diagonal SILC Design for Multi-material Structures

Consider the multi-layer structure shown in Eq. (4.1) with two different spatial plant dynamics. The components of the SILC framework are defined below. For this example, we assume that all devices (denoted by $j$) in the same layer (and hence same material) have

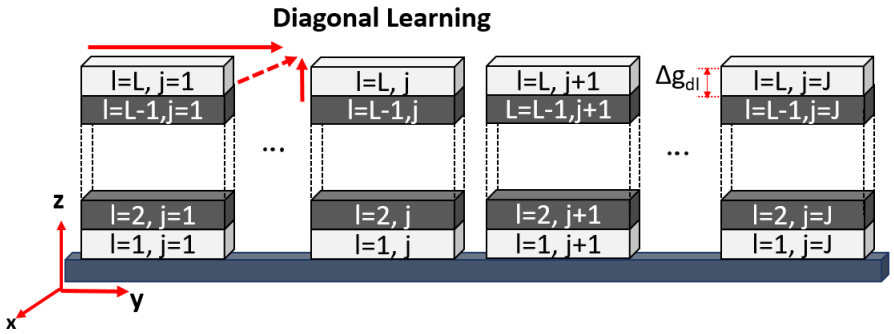


Figure 4.3: **Diagonal SILC**: learning occurs in the horizontal direction from a previous device and vertical direction to incorporate topography. $l$ denotes layer index and $j$ denotes iteration (device) index.

the same desired heightmap increment, $\Delta\vec{g}_{d_l}$. It is assumed that the total number of layers and iterations are limited such that $l = 1, 2, ..., L$ and $j = 1, 2, ..., J$.

$$\Delta\mathbf{e}_{l,j} \triangleq \begin{bmatrix} \Delta\mathbf{e}_{l,j}^{n_1} \\ \Delta\mathbf{e}_{l,j}^{n_2} \end{bmatrix}, \quad \vec{f}_{l,j} \triangleq \begin{bmatrix} \vec{f}_{l,j}^{n_1} \\ \vec{f}_{l,j}^{n_2} \end{bmatrix}$$
$$\Delta\vec{g}_{d_l} \triangleq \begin{bmatrix} \Delta\vec{g}_{d_l}^{n_1} \\ \Delta\vec{g}_{d_l}^{n_2} \end{bmatrix}, \Delta\vec{g}_{l,j} \triangleq \begin{bmatrix} \Delta\vec{g}_{l,j}^{n_1} \\ \Delta\vec{g}_{l,j}^{n_2} \end{bmatrix}$$
$$\mathbf{H}_0 = \begin{bmatrix} \mathbf{H}_0^{n_1,n_2} & 0 \\ 0 & \mathbf{H}_0^{n_2,n_1} \end{bmatrix}, \quad \mathbf{H}_{l,j} = \begin{bmatrix} \mathbf{H}_{l,j}^{n_1,n_2} & 0 \\ 0 & \mathbf{H}_{l,j}^{n_2,n_1} \end{bmatrix}$$

with $\Delta\mathbf{e}_{l,j} \in \mathbb{R}^{2n\times 1}$, $\Delta\vec{g}_{d_l} \in \mathbb{R}^{2n\times 1}$, $\Delta\vec{g}_{l,j} \in \mathbb{R}^{2n\times 1}$, $\vec{f}_{l,j} \in \mathbb{R}^{2n\times 1}$, and $\mathbf{H}_{l,j} \in \mathbb{R}^{2n\times 2n}$. Leveraging the compact form presented above, the predicted error in heightmap increment can be defined as,

$$\Delta\mathbf{e}_{l,j} \triangleq \Delta\vec{g}_{d_l} - \Delta\vec{g}_{l,j} = \Delta\vec{g}_{d_l} - \mathbf{H}_{l-1,j}\vec{f}_{l,j}, \tag{4.4}$$

where $\Delta\vec{g}_{l,j}$ is replaced using the structure in Eq. (4.3). Combining the feedforward signal and corresponding error illustrated in Figure 4.4 yields a SILC update law of the form,

$$\vec{f}_{l,j+1} = \mathbf{L}_{f_{l,j}}\vec{f}_{l,j} + \mathbf{L}_{e_{l,j}}\Delta\mathbf{e}_{l,j} \tag{4.5}$$

with $\mathbf{L}_{f_{l,j}}$ and $\mathbf{L}_{e_{l,j}}$ block diagonal matrices of the input and error filters defined as,

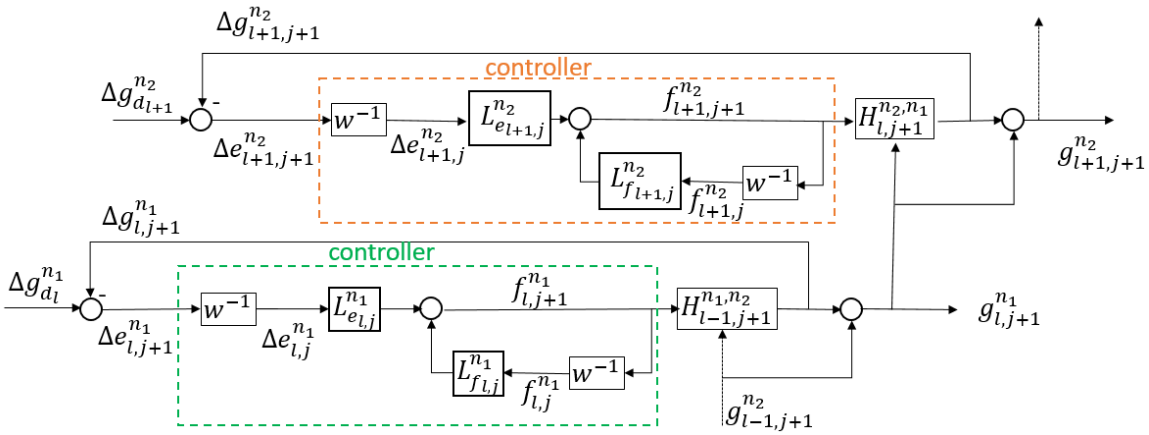


Figure 4.4: **Diagonal SILC**, each layer has its own SILC loop and each device is one iteration. $l$ is layer index and $j$ is iteration (device) index. $w$ is the iteration shift operator, $f_{j+1} = wf_j$, $n_1$ and $n_2$ are the build materials corresponding to layer $l$ and $l+1$. The update filters are iteration varying.

$$\mathbf{L}_{f_{l,j}} = \begin{bmatrix} \mathbf{L}^{n_1}_{f_{l,j}} & 0 \\ 0 & \mathbf{L}^{n_2}_{f_{l,j}} \end{bmatrix}, \quad \mathbf{L}_{e_{l,j}} = \begin{bmatrix} \mathbf{L}^{n_1}_{e_{l,j}} & 0 \\ 0 & \mathbf{L}^{n_2}_{e_{l,j}} \end{bmatrix}.$$

$\mathbf{L}^{i}_{f_{l,j}}$ and $\mathbf{L}^{i}_{e_{l,j}}$ are the input and error filters corresponding build materials, $i \in [n_1, n_2]$. Note that the update law in Eq. (4.5) is based on the error in each layer, $\Delta\mathbf{e}_{l,j}$, not the total error. Layer error was selected as the desired goal to ensure layer repeatability and consistency, which is often a design objective in additively manufacturing constructs. An example of these structures was presented in Figure 2.11.

To construct the feedforward input signal at iteration $j+1$ in Eq. (4.5), the input and error signal of one iteration before ($j$) at the same layer are used; as such, the SILC in Eq. (4.5) is called **first-order SILC** (FO-SILC). In the next chapter, another type of SILC will be introduced, called **higher-order SILC** (HO-SILC), that the information from multiple iterations before is used to construct the feedforward signal.

Substituting Eq. (4.4) into Eq. (4.5) yields the closed-loop SILC algorithm that will be used throughout the paper.

$$\vec{f}_{l,j+1} \simeq (\mathbf{L}_{f_{l,j}} - \mathbf{L}_{e_{l,j}}\mathbf{H}_{l-1,j})\vec{f}_{l,j} + \mathbf{L}_{e_{l,j}}\Delta\vec{g}_{d_l}. \tag{4.6}$$

The term diagonal learning stems from the inclusion of information from both previous iterations and previous layers within the update law. This has been illustrated in Figures 4.3

and 4.4. Note that Eq. (4.6) is used to design the controller in simulation. During the experiment, we still use Eq. (4.5) to construct the feedforward signal. The reason is that, Eq. (4.1) (or Eq. (4.4)), is just an approximation of the spreading behavior of the droplets. In Figure 3.7 of chapter 3, it was demonstrated that depending on the model, there will be always model mismatch between the true and approximated model.

## 4.3 Design of Learning Filters

There are many different methods that can be employed from temporal ILC to design the input and error filters in Eq. (4.6) such as proportional type ILC, model inversion, and Q-filter design [45]. Here, we implement a norm optimal-SILC (NO-SILC) algorithm [40], which seeks to minimize a quadratic cost function in the spatial domain. NO-SILC offers controllability in terms of the convergence behavior and final error. The quadratic cost function that is minimized to solve for the NO-SILC filters is defined as,

$$\mathcal{J} = \Delta\mathbf{e}_{l,j+1}^{T}\begin{bmatrix}\mathbf{Q}_{n_1} & 0\\ 0 & \mathbf{Q}_{n_2}\end{bmatrix}\Delta\mathbf{e}_{l,j+1} + \vec{f}_{l,j+1}^{T}\begin{bmatrix}\mathbf{S}_{n_1} & 0\\ 0 & \mathbf{S}_{n_2}\end{bmatrix}\vec{f}_{l,j+1} + (\vec{f}_{l,j+1}-\vec{f}_{l,j})^{T}\begin{bmatrix}\mathbf{R}_{n_1} & 0\\ 0 & \mathbf{R}_{n_2}\end{bmatrix}(\vec{f}_{l,j+1}-\vec{f}_{l,j}) \quad (4.7)$$

where $\mathbf{Q}_{n_1}$ and $\mathbf{Q}_{n_2} \in \mathbb{R}^{n\times n}$, $\mathbf{S}_{n_1}$ and $\mathbf{S}_{n_2} \in \mathbb{R}^{n\times n}$, $\mathbf{R}_{n_1}$ and $\mathbf{R}_{n_2} \in \mathbb{R}^{n\times n}$ are symmetric positive definite matrices that penalize the layer error, input signal and change in the input signal from iteration to iteration, respectively. We will consider the same weighting matrices for both systems such that $\mathbf{Q}_{n_1} = \mathbf{Q}_{n_2} = \mathbf{Q}$, $\mathbf{R}_{n_1} = \mathbf{R}_{n_2} = \mathbf{R}$, and $\mathbf{S}_{n_1} = \mathbf{S}_{n_2} = \mathbf{S}$. The weighting matrices are defined here as identity matrices multiplied by positive scalars $q$, $s$, and $r$ such that $\mathbf{Q} = q\mathbf{I}$, $\mathbf{S} = s\mathbf{I}$, and $\mathbf{R} = r\mathbf{I}$. Given the assumption of iteration invariant desired reference trajectories, we can relate two successive errors (iteration to iteration) within the same layer using the following equation

$$\Delta\mathbf{e}_{l,j+1} = \Delta\mathbf{e}_{l,j} + \mathbf{H}_{l-1,j}\vec{f}_{l,j} - \mathbf{H}_{l-1,j+1}\vec{f}_{l,j+1} \quad (4.8)$$

Substituting Eq. (4.8) into Eq. (4.7) and setting the partial derivatives of $\mathcal{J}$ with respect to $\vec{f}_{l,j+1}^{n_1}$ and $\vec{f}_{l,j+1}^{n_2}$ equal to zero, the following relationships are obtained for the filters,

$$\mathbf{L}_{f_{l,j}}^{n_1} = ((\mathbf{S}+\mathbf{R}) + \mathbf{H}_{l-1,j+1}^{T_{n_1,n_2}}\mathbf{Q}\mathbf{H}_{l-1,j+1}^{n_1,n_2})^{-1}(\mathbf{R} + \mathbf{H}_{l-1,j+1}^{T_{n_1,n_2}}\mathbf{Q}\mathbf{H}_{l-1,j}^{n_1,n_2}) \quad (4.9a)$$

$$\mathbf{L}_{e_{l,j}}^{n_1} = ((\mathbf{S}+\mathbf{R}) + \mathbf{H}_{l-1,j+1}^{T_{n_1,n_2}}\mathbf{Q}\mathbf{H}_{l-1,j+1}^{n_1,n_2})^{-1}(\mathbf{H}_{l-1,j+1}^{T_{n_1,n_2}}\mathbf{Q}) \quad (4.9b)$$

$$\mathbf{L}_{f_{l,j}}^{n_2} = ((\mathbf{S}+\mathbf{R}) + \mathbf{H}_{l-1,j+1}^{T_{n_2,n_1}}\mathbf{Q}\mathbf{H}_{l-1,j+1}^{n_2,n_1})^{-1}(\mathbf{R} + \mathbf{H}_{l-1,j+1}^{T_{n_2,n_1}}\mathbf{Q}\mathbf{H}_{l-1,j}^{n_2,n_1}) \quad (4.9c)$$

$$\mathbf{L}_{e_{l,j}}^{n_2} = ((\mathbf{S}+\mathbf{R}) + \mathbf{H}_{l-1,j+1}^{T_{n_2,n_1}} \mathbf{Q} \mathbf{H}_{l-1,j+1}^{n_2,n_1})^{-1} (\mathbf{H}_{l-1,j+1}^{T_{n_2,n_1}} \mathbf{Q}) \tag{4.9d}$$

The learning filters in Eqs. (4.9a) to (4.9d) are iteration varying matrices that depend on previous layer topography as well as existing material combinations. If the update law in Eq. (4.6) converges to some finite input value and the iteration varying spatial dynamics converge to the nominal model such that

$$\lim_{\substack{l\to\infty \\ j\to\infty}} \vec{f}_{l,j} = \vec{f}_{\infty}, \quad \lim_{\substack{l\to\infty \\ j\to\infty}} \mathbf{H}_{l,j} = \mathbf{H}_0, \quad \lim_{\substack{l\to\infty \\ j\to\infty}} \mathbf{L}_{f_{l,j}} = \mathbf{L}_{f_0}, \quad \lim_{\substack{l\to\infty \\ j\to\infty}} \mathbf{L}_{e_{l,j}} = \mathbf{L}_{e_0},$$

where $\mathbf{L}_{f_0}$ and $\mathbf{L}_{e_0}$ are based on the nominal plant model, the converged input would tend towards,

$$\vec{f}_{\infty} = (\mathbf{I} - \mathbf{L}_{f_0} + \mathbf{L}_{e_0}\mathbf{H}_0)^{-1} \mathbf{L}_{e_0} \Delta \vec{g}_{d_l}. \tag{4.10}$$

Under these conditions, the performance of the system can be obtained by substituting Eq. (4.10) into Eq. (4.4) as follows

$$\Delta \mathbf{e}_{\infty} = (\mathbf{I} - \mathbf{H}_0^l [(\mathbf{H}_0^{l^T} \mathbf{Q})^{-1} \mathbf{S} + \mathbf{H}_0^l]^{-1}) \Delta \vec{g}_{d_l}. \tag{4.11}$$

The convergence behavior and performance of NO-SILC can be tuned by the weighting coefficients in the filters ( [39,40]). Extending the learning filters in Eqs. (4.9a) to (4.9d) to the general linear iterative model described in Eq. (4.3) results in,

$$\mathbf{L}_{f_{l,j}}^{n_l} = ((\mathbf{S}+\mathbf{R}) + \mathbf{H}_{l-1,j+1}^{T_{n_l,n_{l-1}}} \mathbf{Q} \mathbf{H}_{l-1,j+1}^{n_l,n_{l-1}})^{-1} (\mathbf{R} + \mathbf{H}_{l-1,j+1}^{T_{n_l,n_{l-1}}} \mathbf{Q} \mathbf{H}_{l-1,j}^{n_l,n_{l-1}}) \tag{4.12a}$$

$$\mathbf{L}_{e_{l,j}}^{n_l} = ((\mathbf{S}+\mathbf{R}) + \mathbf{H}_{l-1,j+1}^{T_{n_l,n_{l-1}}} \mathbf{Q} \mathbf{H}_{l-1,j+1}^{n_l,n_{l-1}})^{-1} (\mathbf{H}_{l-1,j+1}^{T_{n_l,n_{l-1}}} \mathbf{Q}). \tag{4.12b}$$

## 4.4 Simulation setup

In this section, we investigate the proposed diagonal SILC framework through a simulation study using a model of an electrohydrodynamic jet (e-jet) printing process. Drop-on-demand of e-jet printing is achieved using synchronized substrate motion and high voltage pulses applied to either nozzle of a bi-material e-jet printer, with the schematic shown in Figure 1.2. Varying the rectangular wave pulsewidth allows for variation in printed droplet size.

For this simulation, the device structure has the topology of Figure 4.3 with layer

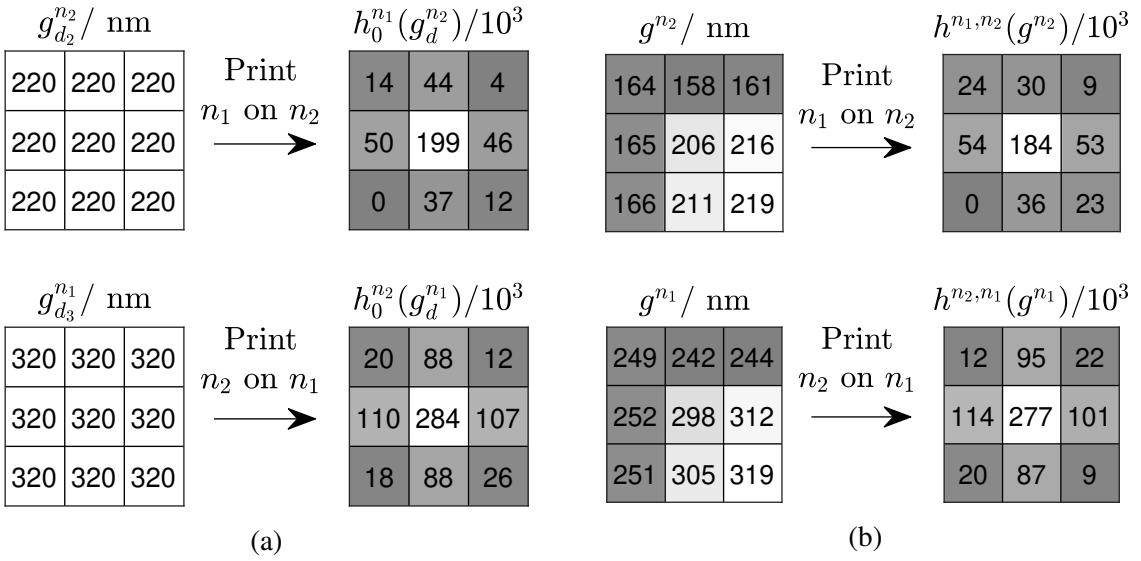


Figure 4.5: **Topography dependent impulse response.** a) Nominal model: at left is a $3\times3$ pixel crop of a layer's reference topography signal away from the edges so that it is uniform in height. At right is the model's corresponding impulse response for printing the alternate material on the flat surface, b) Effect of nonflat surface: at left is a $3\times3$ pixel crop of a $g$ signal, indexed by material. The crop is taken near an edge to show the effect of significant surface variation. At right is the spatially varying impulse response local to a certain pixel (x,y) for printing the alternate material at the location corresponding to the crop at left.

heights of 100 nm for $n_1$ and 120 nm for $n_2$. Each layer is printed in a single printing pass, so the build material alternates between $n_1$ and $n_2$ at each new layer. For the first (bottom) layer in the simulation, composed of material $n_1$, the underlaying surface, ($l = 0$), is assumed to be a pre-layer of cured $n_2$ so that first-layer surface interactions with other substrate materials need not be considered. It is assumed that the spatial dynamics for a given material is independent of the layer index, as long as the same material is used on those layers (Section 4.1). However, due to noncausality of the plants and surface energy of the previous layer, it is still a function of previous layer topography and its build material. Therefore, we only consider two plant matrices of $\mathbf{H}^{n_1,n_2}$ and $\mathbf{H}^{n_2,n_1}$. Output heightmaps are measured relative to the top of the flat pre-layer, and the domain is $256\times256$ pixels. The pitch size is considered 1 $\mu m$ for both materials. The desired output, $g_{d_l}$, at layer $l$ is uniform except for the four outer rings of pixels, which are reduced by half to better represent material dropoff at edges. It is assumed that after a layer of one material is printed, it is UV-cured, and the resulted topography is scanned as described in [33] to measure the output which is $\vec{g}_{l,j}$ at any layer $l$ and device $j$.

To capture material spreading in a layer-by-layer manner, the LPV model in Sec-

tion 3.5.2 is used. This simulation assumes a known relationship between pulsewidth and droplet size (cube root of droplet volume [2]) so that the control input can be taken as droplet size rather than pulsewidth (see Figure 1.3). Heightmap evolution from layer to layer is simulated according to Eq. (4.1), as depicted in Figures 3.2 and 3.3b. The $g_l$ dependence on the convolution kernel $h_{l-1}^{(x,y)}$ is modeled using the multivariate regression model (method M2) of [2]. Since there are two material combinations ($n_1$ printed on $n_2$ and $n_2$ printed on $n_1$), two regression models must be specified. For $n_1$ printed on $n_2$, an equilibrium contact angle of 10° is used in the numerical simulations of droplet spreading, whereas 5° is used for $n_2$ printed on $n_1$. The nominal models $h_0^{n_1}$ and $h_0^{n_2}$, corresponding to the printing of $n_1$ (NOA170) and $n_2$ (Loctite3524(unfiltered)), are calculated using the regression models' prediction of spreading on reference topographies $g_d$, denoted $h_0^{n_1} = h(g_d^{n_2})$ and $h_0^{n_2} = h(g_d^{n_1})$, and shown in Figure 4.5a. In contrast, examples of impulse responses predicted on nonflat surfaces are shown in Figure 4.5b. The nominal plants in Eq. (4.2) can be calculated based on the BCCB matrix construction defined in Section 3.2. Following the model of [2], we take a 2D array of cube roots of droplet volumes to be the input, denoted $f_{l,j}$. Both the input $f$ and output $g$ are heightmaps, but only $g$ represents a scanned topography. Choosing the same height units for both $f$ and $g$ makes $h$, and thus the system, dimensionless.

In addition to the deterministic spatial variation in the system described above, stochastic noise is added to the simulation. For $n_2$ printed on $n_1$, the deterministic term is $h^{n_2,n_1}(g_{l-1,j}^{n_1})$, and the additive uncertainty $\hat{h}^{n_2}$ is used, giving $h_{l,j}^{n_1,n_2} = h^{n_1,n_2}(g_{l-1,j}^{n_2}) + \hat{h}^{n_1}$, and for printing $n_1$ on $n_1$: $h_{l,j}^{n_2,n_1} = h^{n_2,n_1}(g_{l-1,j}^{n_1}) + \hat{h}^{n_2}$. The additive uncertainty is normally distributed as $\hat{h}^i = \mathcal{N}(0,\sigma_i^2)\mathbf{1}(3,3)$, where $\sigma_i$ is the standard deviation of the elements of the nominal model $h_0^i$, $\mathbf{1}(3,3)$ is a $3\times 3$ matrix of 1's for $i \in [n_1, n_2]$. From the impulse responses $h$, the plant matrices $\mathbf{H}_{l,j}$ in Eq. (4.1) are calculated from the lifted domain conversion defined in the Section 3.5.5. The impulse response bounds are chosen such that $\underline{h}^i = h_0^i - \sigma^i\mathbf{1}(3,3)$ and $\overline{h}^i = h_0^i + \sigma^i\mathbf{1}(3,3)$ for $i \in [n_1, n_2]$. Similarly, the plant matrix bounds $\underline{\mathbf{H}}$ and $\overline{\mathbf{H}}$ are calculated from $\underline{h}^i$ and $\overline{h}^i$ by the BCCB construction method described in Section 3.2.

## 4.5 Simulation Results

In this section, the simulation results of the system described in Section 3.3 with repeated topology such as Figure 4.1 using diagonal NO-SILC are investigated. A multi-layer structure with four layers of the $n_1$ material, and three layers of the $n_2$ material is considered as shown in Figure 4.3. For analysis and ease in implementation, we consider the learning

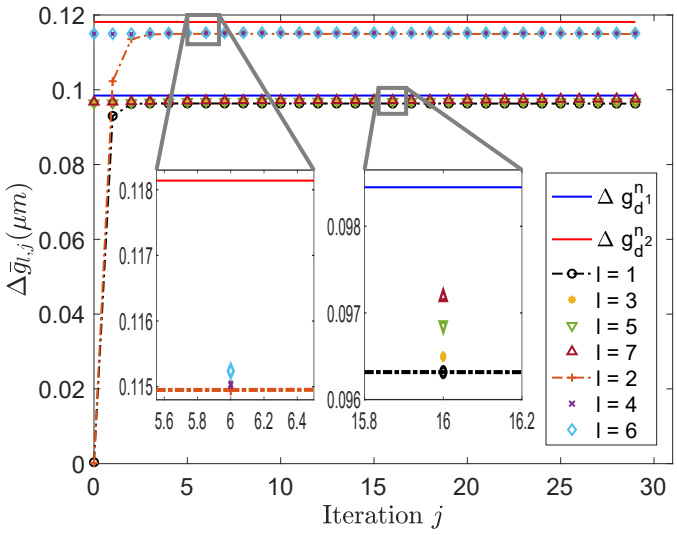


Figure 4.6: Average height increments for both materials approach a nominal value over the iterations (devices). $n_1$ and $n_2$ are the build materials in the odd and even layers, respectively ($q = 1, r = 0.2, s = 0.001$). Iteration $j = 0$ refers to the first device.

filters in Eqs. (4.9a) to (4.9d) based on the nominal dynamic model ($\mathbf{L}_{f_0}$ and $\mathbf{L}_{e_0}$), while the update law Eq. (4.6) will still use the iteration varying plant dynamics $\mathbf{H}_{l-1,j}$.

It is important to note that the inputs of the first iteration at layers 1 and 2 are zero, $\vec{f}^{n_1}_{1,1} = 0$ and $\vec{f}^{n_2}_{2,1} = 0$, implying that there is no prior knowledge on the appropriate inputs for these materials. This results in no material deposition during the first iteration of layers 1 and 2. However, the input of the first device ($j = 1$ at other layers, $l > 2$, comes from the last device in the previous layer with the same material, such that $\vec{f}_{l,1} = \vec{f}_{l-2,J}$ where $J$ is the total number of iterations per layer as shown in Eq. (4.1). A normally distributed white noise signal has been added to the input signal, with the mean and variance of 0.00 and 0.01 $\mu m$, to better represent the experimental environment. The signal to noise ratio is approximately 12 for the $n_1$ and 26 for the $n_2$ material for the mean value of the converged input. Furthermore, the input will be constrained to positive definite values to ensure an additive process. The set of simulations was run for 30 iterations (devices) using MATLAB for different values of $s$ and $r$. In all simulations, the parameter $q$ was set equal to one ($q = 1$). the total heightmap and corresponding standard deviations.

The average height increment and the corresponding desired height increment for each material class are presented in Figure 4.6. The outputs from the layers of a given material all converged to roughly the same offset from the desired height increment where better convergence is observed in higher layers. In additive manufacturing, the design goal often focuses on achieving consistent layers with a repeatable thickness distribution, which is a

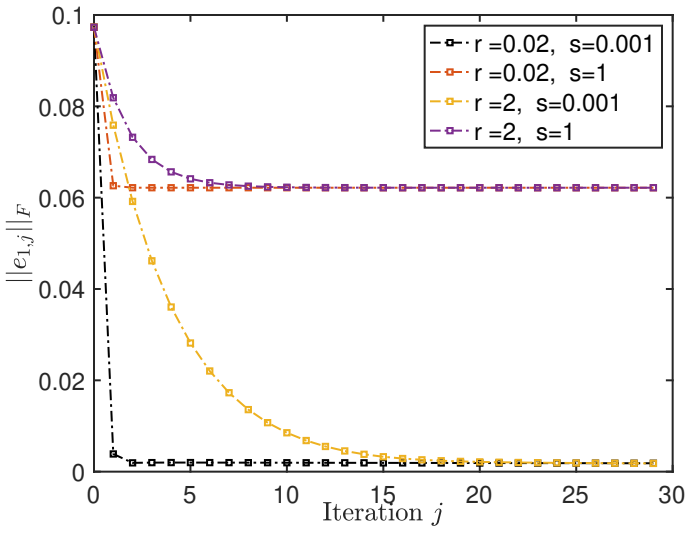


Figure 4.7: SILC convergence for different values of the NO tuning parameters for the first layer with $n_1$ material. Iteration $j = 0$ refers to the first device.

highly desirable characteristic in most sensory applications where uniformity and periodicity of layers are of great importance.

To compare the effects of the tuning parameters, the performance of the SILC system in Frobenius norm is demonstrated in Figure 4.7 for different values of the penalty terms $r$ and $s$ in layer one with $n_1$ material as a representation of all other layers. The weighting coefficients enable NO-SILC to control the rate of convergence, the final converged error, and the converged output (Figures 4.6 and 4.7). Increasing the value of the input penalty, $s$, would increase the final error. On the other hand, increasing the value of $r$ would reduce the convergence speed. Due to the nature of the additive process, it is also very important to use appropriate weighting coefficients to avoid accumulation and propagation of errors in the successive layers.

## 4.6 CONCLUSION

In this chapter, we present a novel spatial FO-ILC framework for repetitive systems that have multiple spatial dynamics with application to microscale additive manufacturing of multi-material 3D structures. To address the combined challenges of multiple plant dynamics due to multiple build materials and varying initial conditions due to roughness of the previous layer surface, a new diagonal SILC algorithm is proposed. To demonstrate the performance of the proposed framework, a bi-material structure is considered in simulation

where the corresponding MIMO configuration involves two subsystems with distinct SILC control loops that are internally connected due to the layer-wise nature of the AM process. Simulation results show that FO-SILC can be successfully employed to regulate the input of the iterative system to improve the heightmap reference tracking and the corresponding surface roughness.

# CHAPTER 5

# Higher-Order Spatial Iterative Learning Control for Improved Micro-Additive Manufacturing

In the previous chapter, a first-order SILC (FO-SILC) framework was introduced that considered in-layer and layer-to-layer dynamics to achieve uniformly printed layers in multi-material 3D-structures [42]. The control input of the proposed FO-SILC was updated from the previously printed device information along the device-axis ($j$ horizontal) within the same layer $l$. A drawback of the proposed FO-SILC framework stems from the additive process. The FO-SILC framework only considers current layer errors, $\Delta e_l(x,y)$ (the difference between $\Delta g_l^d(x,y)$ and actual incremental height $\Delta g_l(x,y)$) rather than total error, $e_l(x,y)$ (the difference between $g_l^d(x,y)$ and actual printed total heightmap $g_l(x,y)$, see Figures 1.4 and 5.1). In this case, the existing layer errors are accumulated over the layers, potentially causing large deviations from the desired total height. The learning process will be more complicated at higher layers in which, large surface variations resulting from the accumulated error lead to large model uncertainties. Hence, the controller should be able to compensate for total error $e_{l,j}(x,y)$ in the third dimension (layer direction $l$ or z-axis), which is especially important in cases when a large number of layers are deposited. Thus, new theories are needed to control in-layer errors as well as the total accumulated error in multi-layered structures.

While FO-ILC has proven to be useful for reference tracking of repetitive systems, it might lose performance when uncertainties are high. To achieve better performance with respect to convergence speed, higher-order ILC (HO-ILC) has been developed, where the feedforward signal is synthesized using historical data from multiple iterations [38,46–50]. There have been several attributes stated in literature that motivate the implementation of HO-ILC over FO-ILC. In [50], the authors presented anecdotal evidence of merit to justify either HO- or FO-ILC depending on the situation. However, in [48,49], the authors argued that a HO-ILC framework demonstrated better convergence speed and robustness than a FO-ILC framework, while [77] asserted that the real motivation behind the use of HO-

ILC was to reduce the effects of disturbances and noise. Similarly, the authors of [46, 47, 78] claimed that a HO-ILC design achieved faster convergence as compared to a FO-ILC framework due to the effects of learning over several previous iterations. In this chapter, a higher-order spatial iterative learning control (HO-SILC) scheme is proposed targeting heightmap tracking of multi-layer structures fabricated by AM technology to achieve better convergence performance as compared to FO-SILC [46] due to the additional information that is leveraged from previous layers. The contributions of this chapter are:

1. A HO-SILC framework for AM structures that combines device-to-device and layer-to-layer learning in the lifted- and frequency-domain, while considering iteration varying spatial dynamics.

2. A detailed methodology for transforming HO-SILC of AM processes to a FO-SILC scheme for stability and robustness analysis.

3. The development of a design methodology for deriving learning filters that directly embed stability criteria for nominal HO-SILC system.

4. The design boundary prediction of a maximum allowable uncertainty around the nominal plant for monotonic convergent of the iterative norm-optimal HO-SILC algorithm.

## 5.1 Higher-Order SILC Design for Multi-layer Structures

In this section, we extend the FO-SILC framework developed in chapter 4 by adding layer-to-layer learning (vertical direction) as presented in Figure 5.1. HO-ILC processes usually have faster convergence compared to FO-ILC, because HO-ILC uses the information from multiple past trials to construct the input control signal. We term the proposed SILC algorithm higher-order SILC because learning occurs over one iteration in the part-axis ($j$, horizontal) and N iterations in the layer axis ($l$, vertical).

For a multi-layer structure as shown in Figure 5.1a, a HO-SILC update law is proposed.

$$\vec{f}_{l,j+1} = (\mathbf{L}_f^h \vec{f}_{l,j} + \mathbf{L}_e^h \Delta\vec{e}_{l,j}) + \sum_{i=1}^{i=\mathrm{N}} (\mathbf{L}_f^{v_i} \vec{f}_{l-i,j+1} + \mathbf{L}_e^{v_i} \Delta\vec{e}_{l-i,j+1}) \tag{5.1}$$

with $\mathbf{L}_f^h$, $\mathbf{L}_e^h$, $\mathbf{L}_f^{v_i}$ and $\mathbf{L}_e^{v_i} \in \mathbb{R}^{n\times n}$ defined as the horizontal input and error filters and vertical input and error filters for $i < l$, respectively. $n$ is total number of discrete point $n = n_x \times n_y$.

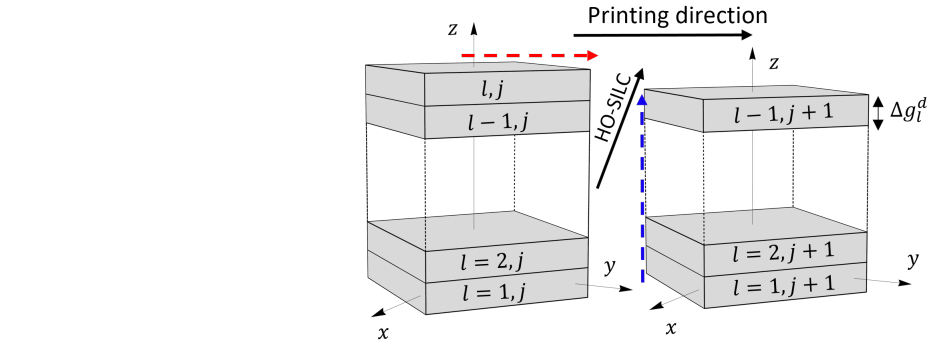


(a)

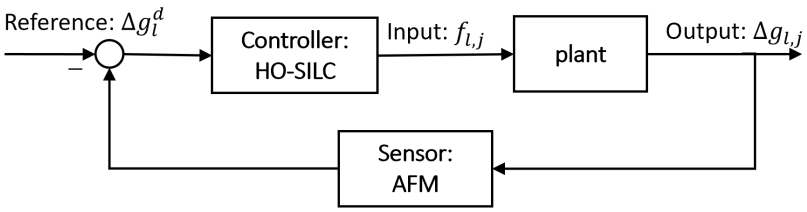


(b)

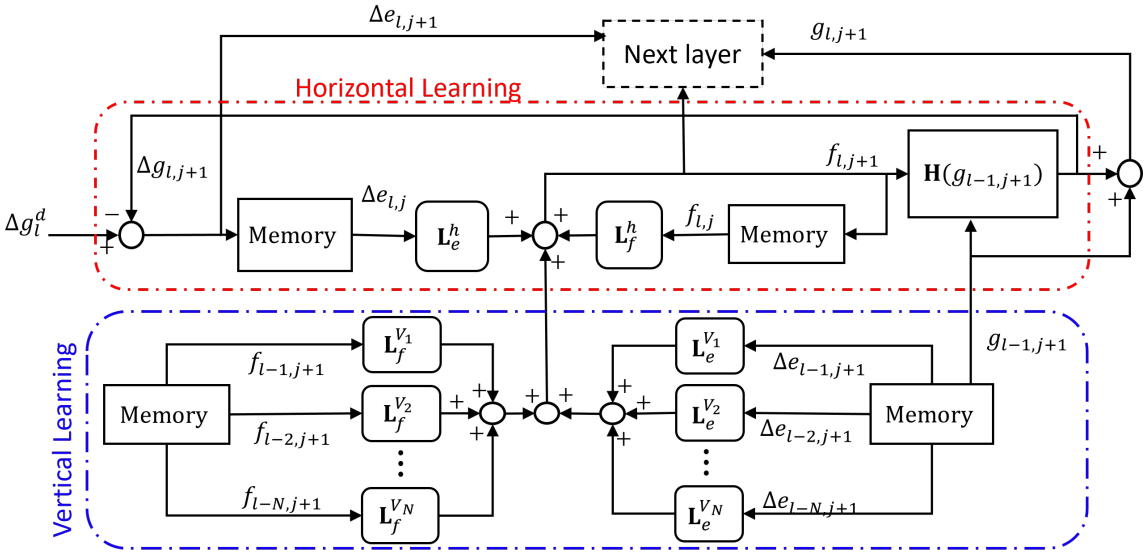


(c)

Figure 5.1: **Closed-loop control of AM process**: a) Learning happens from layer-to-layer (vertical) and device-to-device (horizontal) to control material deposition in 3D structures, b) Higher-order SILC (HO-SILC) is used as a recursive control strategy to close the loop, c) Standard HO-SILC block diagram. $l$ denotes layer index and $j$ denotes iteration index.

Note that in Eq. (5.1), printing is in the horizontal direction from part to part. This is suitable for devices such as [42,79] in which multiple materials are printed at specific layers or the reference incremental height is changing from layer to layer. For single material deposition, the printing can be in the vertical direction, from layer to layer and the SILC update law would be $\vec{f}_{l+1} = \sum_{i=1}^{i=\mathrm{N}} (\mathbf{L}_f^i \vec{f}_{l-i+1} + \mathbf{L}_e^i \Delta\vec{e}_{l-i+1})$.

## 5.2 Design of Learning Filters

To implement a norm optimal-SILC (NO-SILC) algorithm similar to Section 4.3, we define a weighted error vector, $\vec{e}^{w}_{l,j+1}$, as follows

$$\begin{aligned} \vec{e}^{w}_{l,j+1} &\triangleq \Delta\vec{e}_{l,j+1} + \alpha_1 \Delta\vec{e}_{l-1,j+1} + ... + \alpha_{l-1}\Delta\vec{e}_{1,j+1} \\ \vec{\alpha} &\triangleq [\alpha_0, \alpha_1, \alpha_2, ..., \alpha_{l-1}]^{\mathbf{T}}, \end{aligned} \tag{5.2}$$

where $\alpha_i \in [0,1]$ are layer varying user defined control parameters. The quadratic cost function that is minimized to solve for the NO-SILC learning filters is defined as,

$$\begin{aligned} \mathcal{J} = \vec{e}^{w^T}_{l,j+1} \mathbf{Q} \vec{e}^{w}_{l,j+1} + (\vec{f}_{l,j+1} - \vec{f}_{l,j})^T \mathbf{R} (\vec{f}_{l,j+1} - \vec{f}_{l,j}) + \vec{f}^{T}_{l,j+1} \mathbf{S} \vec{f}_{l,j+1} \\ + \sum_{i=1}^{\mathrm{N}} \beta_i (\vec{f}_{l,j+1} - \vec{f}_{l-i,j+1})^T \mathbf{R} (\vec{f}_{l,j+1} - \vec{f}_{l-i,j+1}), \end{aligned} \tag{5.3}$$

where $\mathbf{Q}$, $\mathbf{S}$, and $\mathbf{R} \in \mathbb{R}^{n \times n}$ are symmetric positive definite matrices that penalize the layer error, input signal, change in the input signal from iteration to iteration, and change in the input signal from layer to layer. We design weighting matrices as identity matrices multiplied by positive scalars $q$, $s$, and $r$ such that $\mathbf{Q} = q\mathbf{I}$, $\mathbf{S} = s\mathbf{I}$, and $\mathbf{R} = r\mathbf{I}$; $\beta_i \in [0,1]$ are layer varying user defined parameters to weight the influence of previous layer input signals, such that $\vec{\beta} \triangleq [\beta_1, \beta_2, ..., \beta_{l-1}]^{\mathbf{T}}$. In order to emphasize more recent layers, we set $\alpha'_i = \frac{\alpha^i}{\|\vec{\alpha}\|}$ and $\beta'_i = \frac{\beta^i}{\|\vec{\beta}\|}$, with $\alpha, \beta \in [0,1]$. If $\alpha = 1$ in Eq. (5.2), the cost function Eq. (5.3) is optimized over the total error. Note that the weighted error in Eq. (5.2) is not known, but it can be approximated using any of the models that were developed in Section 3.5 and Eq. (4.4).

### 5.2.1 Lifted-domain Learning Filters

Given the assumption of iteration invariant desired reference trajectories in Eq. (4.8) and substituting Eqs. (4.4), (4.8) and (5.2) into Eq. (5.3) and setting the partial derivatives of $\mathcal{J}$ with respect to $\vec{f}_{l,j+1}$ equal to zero, the following relationships can be obtained for the filters based on the nominal plant, $\mathbf{H}_0$,

$$\mathbf{L}_f^h = ((s+r+r\sum_{i=1}^{l-1}\beta_i')\mathbf{I} + \alpha_0' q \mathrm{H}_0^T \mathrm{H}_0)^{-1}(r\mathbf{I} + \alpha_0' q \mathrm{H}_0^T \mathrm{H}_0) \tag{5.4a}$$

$$\mathbf{L}_e^h = ((s+r+r\sum_{i=1}^{l-1}\beta_i')\mathbf{I} + \alpha_0' q \mathrm{H}_0^T \mathrm{H}_0)^{-1}\alpha_0' q \mathrm{H}_0^T \tag{5.4b}$$

$$\mathbf{L}_f^{v_i} = ((s+r+r\sum_{i=1}^{l-1}\beta_i')\mathbf{I} + \alpha_0' q \mathrm{H}_0^T \mathrm{H}_0)^{-1}\beta_i' r\mathbf{I} \tag{5.4c}$$

$$\mathbf{L}_e^{v_i} = \frac{\alpha_i'}{\alpha_0'}\mathbf{L}_f^h \tag{5.4d}$$

If the iteration varying spatial dynamics converge to the nominal model, $\lim_{l,j\to\infty} \mathbf{H}_{l,j} = \mathbf{H}_0$, the converged input would tend towards,

$$\vec{f}_\infty = [\mathbf{H}_0(1+\sum_{i=1}^{N}\alpha_i) + \frac{s}{q}(\mathbf{H}_0^T)^{-1}]^{-1}(\Delta\vec{g}_l^d + \sum_{i=1}^{N}\alpha_i\Delta\vec{g}_{l-i}^d) \tag{5.5}$$

Under these conditions, the converged performance of the system is obtained by substituting Eq. (5.5) into Eq. (4.4),

$$\Delta\vec{e}_\infty = (\mathbf{I} - [(1-\sum_{i=1}^{N}\alpha_i)\mathbf{I} + \frac{s}{q}(\mathbf{H}_0^T)^{-1}\mathbf{H}_0^{-1}]^{-1})\Delta\vec{g}_l^d - [(1-\sum_{i=1}^{N}\alpha_i)\mathbf{I} + \frac{s}{q}(\mathbf{H}_0^T)^{-1}]^{-1}\sum_{i=1}^{N}\alpha_i\Delta\vec{g}_{l-i}^d \tag{5.6}$$

### 5.2.2 Frequency-domain Learning Filters

If the plant matrix that is used to predict/approximate the error in Eq. (5.3) is BCCB (see Eqs. (4.4) and (5.1), the M3 method with LPV and CLR models in Sections 3.5.1 and 3.5.2), the learning filters and update law in Eqs. (5.1) and (5.4) have frequency representations, which enables us to use computationally efficient fast Fourier transform (FFT) methods. The frequency domain representation of the learning filters in Eq. (5.4) for a BCCB plant matrix are presented as,

$$\boldsymbol{L}_f^h(u,v) = \frac{\alpha_0' q \boldsymbol{H}_0^* \circ \boldsymbol{H}_0 + r 1_{n\times n}}{\alpha_0' q \boldsymbol{H}_0^* \circ H_0 + (s + r + r\sum_{i=1}^{l-1}\beta_i')1_{n\times n}}(u,v) \tag{5.7a}$$

$$\boldsymbol{L}_e^h(u,v) = \frac{\alpha_0' q \boldsymbol{H}_0^*}{\alpha_0' q \boldsymbol{H}_0^* \circ H_0 + (s + r + r\sum_{i=1}^{l-1}\beta_i')1_{n\times n}}(u,v) \tag{5.7b}$$

$$\boldsymbol{L}_f^{v_i}(u,v) = \frac{r\beta_i' 1_{n\times n}}{\alpha_0' q \boldsymbol{H}_0^* \circ H_0 + (s + r + r\sum_{i=1}^{l-1}\beta_i')1_{n\times n}}(u,v) \tag{5.7c}$$

$$\boldsymbol{L}_e^{v_i}(u,v) = \frac{\alpha_i'}{\alpha_0'}\boldsymbol{L}_e^h(u,v) \quad , i = 1,...,N \tag{5.7d}$$

where $\circ$ is the Hadamard or entrywise product of two matrices, and $\boldsymbol{H}_0$ is the frequency domain representation of the nominal plant. $\boldsymbol{L}_f^h$, $\boldsymbol{L}_e^h$, $\boldsymbol{L}_f^{v_i}$, and $\boldsymbol{L}_e^{v_i} \in \mathbb{R}^{n_x\times n_y}$ re 2-D DFTs (discrete fourier transforms) of the learning filters in Eqs. (5.1) and (5.4). Because of the BCCB structure of $\boldsymbol{H}_0$ and the learning filters, the update law in Eq. (5.1) for the BCCB plant model can be equivalently represented in the frequency domain as follows,

$$\boldsymbol{f}_{l,j+1}(u,v) = (\boldsymbol{L}_f^h \circ \boldsymbol{f}_{l,j} + \boldsymbol{L}_e^h \circ \Delta\boldsymbol{e}_{l,j})(u,v) + \sum_{i=1}^{N}(\boldsymbol{L}_f^{v_i} \circ \boldsymbol{f}_{l-i,j+1} + \boldsymbol{L}_e^{v_i} \circ \Delta\boldsymbol{e}_{l-i,j+1})(u,v), \tag{5.8}$$

where $\boldsymbol{f}(u,v) \in \mathbb{R}^{n_x\times n_y}$ and $\Delta\boldsymbol{e}(u,v) \in \mathbb{R}^{n_x\times n_y}$ are frequency domain representation of $f(x,y) \in \mathbb{R}^{n_x\times n_y}$ and $\Delta e(x,y) \in \mathbb{R}^{n_x\times n_y}$. The update law in Eq. (5.8) is expected to be computationally faster compared to the lifted domain update law in Eq. (5.1) due to entrywise product computations using the hadamard product instead of matrix multiplication in Eq. (5.1).

## 5.3 HO-SILC Transformation To FO-SILC

In the literature, there are very few examples of monotonic convergence (MC) condition of HO-ILC frameworks [38, 78], while the stability condition of FO-ILC is well described. It is possible to leverage the proofs for FO-ILC to analyze stability of a HO-ILC system by converting the HO-ILC algorithm to a FO-ILC framework. In this section, we follow methods developed in [36, 80, 81] to convert the HO-SILC framework in Eq. (5.1) to FO-SILC. This modified closed-loop FO-ILC framework will then be used to investigate stability margins for the iteration varying model described in Eq. (3.3). The approach taken here is a bit different than [36, 80, 81]. The transfer functions from HO-SILC to FO-SILC

are constructed based on the layer-by-layer nature of AM-process such that the FO-SILC system incorporates learning along the iteration axis, $j$, as well as the layer axis, $l$.

The HO-SILC algorithm defined in Eq. (5.1) can be expressed based on the closed-loop plant matrices, by inserting Eq. (4.4) into Eq. (5.1) as,

$$\vec{f}_{l,j+1} = \mathbf{T}^{h}_{l-1,j}\vec{f}_{l,j} + \sum_{i=1}^{l-1} \mathbf{T}^{v_i}_{l-i-1,j+1}\vec{f}_{l-i,j+1} + (\mathbf{L}^{h}_{e} + \sum_{i=1}^{l-1} \mathbf{L}^{v_i}_{e})\Delta\vec{g}^{d}, \tag{5.9}$$

with $\mathbf{T}^{h}_{l,j} = \mathbf{L}^{h}_{f} - \mathbf{L}^{h}_{e}\mathbf{H}_{l,j}$ and $\mathbf{T}^{v_i}_{l-i-1,j} = \mathbf{L}^{v_i}_{f} - \mathbf{L}^{v_i}_{e}\mathbf{H}_{l-i-1,j}$ being the closed-loop horizontal and vertical plant matrices, respectively. Eq. (5.9) can be further simplified by concatenating the input signals over the vertical axis, $l$, such that,

$$\vec{z}_{l,j+1} = \mathbf{D}_{l,j}\vec{z}_{l,j} + \mathbf{K}_{l,j}\vec{z}_{l,j+1} + \vec{C}_{l} \tag{5.10a}$$

$$\vec{z}_{l,j} = [\vec{f}^{\mathbf{T}}_{l,j}, ..., \vec{f}^{\mathbf{T}}_{2,j}, \vec{f}^{\mathbf{T}}_{1,j}]^{\mathbf{T}} \in \mathbb{R}^{ln\times 1} \tag{5.10b}$$

$$\vec{z}_{l,\infty} = (\mathbf{I} - \mathbf{D}_{l,\infty} - \mathbf{K}_{l,\infty})^{-1}\vec{C}_{l}, \tag{5.10c}$$

where $\mathbf{D}_{l,j} \in \mathbb{R}^{ln\times ln}$, $\mathbf{K}_{l,j} \in \mathbb{R}^{ln\times ln}$, and $\vec{C}_{l} \in \mathbb{R}^{ln\times 1}$ are a diagonal block matrix, upper triangular block matrix, and constant vector, respectively,

$$\mathbf{D}_{l,j} = \begin{bmatrix} \mathbf{T}^{h}_{l-1,j} & \mathbf{0} & \cdots & \mathbf{0} \\ \mathbf{0} & \ddots & & \vdots \\ \vdots & & \mathbf{T}^{h}_{1,j} & \mathbf{0} \\ \mathbf{0} & \cdots & & \mathbf{T}^{h}_{0,j} \end{bmatrix}, \tag{5.11a}$$

$$\mathbf{K}_{l,j} = \begin{bmatrix} \mathbf{0} & \mathbf{T}^{v_1}_{l-2,j+1} & \mathbf{T}^{v_2}_{l-3,j+1} & \cdots & \mathbf{T}^{v_{l-2}}_{1,j+1} & \mathbf{T}^{v_{l-1}}_{0,j+1} \\ & \mathbf{0} & \mathbf{T}^{v_1}_{l-3,j+1} & \cdots & \mathbf{T}^{v_{l-2}}_{1,j+1} & \mathbf{T}^{v_{l-2}}_{0,j+1} \\ & & \ddots & \ddots & \vdots & \vdots \\ \vdots & & & \mathbf{0} & \mathbf{T}^{v_1}_{1,j+1} & \mathbf{T}^{v_2}_{0,j+1} \\ & & & & \mathbf{0} & \mathbf{T}^{v_1}_{0,j+1} \\ \mathbf{0} & & & \cdots & & \mathbf{0} \end{bmatrix} \tag{5.11b}$$

$$\vec{C}_l = \begin{bmatrix} (\mathbf{L}_e^h + \mathbf{L}_e^{v_1} + \cdots + \mathbf{L}_e^{v_{l-1}})\Delta\vec{g}^d \\ \vdots \\ (\mathbf{L}_e^h + \mathbf{L}_e^{v_1} + \mathbf{L}_e^{v_2})\Delta\vec{g}^d \\ (\mathbf{L}_e^h + \mathbf{L}_e^{v_1})\Delta\vec{g}^d \\ \mathbf{L}_e^h\Delta\vec{g}^d \end{bmatrix} \tag{5.11c}$$

Eq. (5.10) can be further simplified to the following FO-SILC format,

$$\begin{aligned} \vec{z}_{l,j+1} &= \mathbf{F}_{l,j}\,\vec{z}_{l,j} + \vec{F}_r \\ \mathbf{F}_{l,j} &= (\mathbf{I} - \mathbf{K}_{l,j})^{-1}\mathbf{D}_{l,j} \\ \vec{F}_r &= (\mathbf{I} - \mathbf{K}_{l,j})^{-1}\vec{C}_l \end{aligned} \tag{5.12}$$

We used the same notation as [36, 78] for transfer matrix and vector $\mathbf{F}_{l,j}$ and $\vec{F}_r$. The closed-loop FO-SILC algorithm in Eq. (5.12) will be used in the following section to investigate the asymptotic and monotonic properties of the closed-loop HO-SILC update law in Eq. (5.9) following methods described in [36, 38, 39, 78].

## 5.4 Stability and Convergence

In most control systems, a fundamental goal is to guarantee the convergence of the tracking error to zero or within a neighborhood of a nominal value over a small number of iterations. Asymptotic stability of iteration varying systems requires the joint spectral radius of the iterative plant to be less than one, which is a difficult problem [39, 82]. In many manufacturing applications, such as the optical sensor presented in [1] and Figure 2.11, large transient errors may introduce failures in the functional capabilities of the printed device. Therefore, the controller should be designed to regulate material deposition such that the layer errors decrease from iteration to iteration and layer to layer. In this work, we focus on monotonic stability of iterative systems subjected to bounded model uncertainties, which is an often desirable property for additive manufacturing processes. We combine the methods developed in [38, 39, 78] to derive stability conditions for closed-loop HO-SILC algorithms subjected to iteration varying model uncertainties. First, we design the learning filters such that the nominal system is stable. Then a stability radius, $r_{AIU}$, is designed based on the Lyapunov equation such that the iterative system remains stable as long as the magnitude of model uncertainties is less than the stability radius at all iterations. We follow [39] and [38] to design the stability margins of the converted FO-SILC subjected to interval uncertainty.

**Theorem 1** *The system in Eq.* (3.2) *controlled by the FO-SILC in Eq.* (5.12) *(or HO-SILC in Eq.* (5.9)*) is monotonically convergent in the $l_p$ norm, $\|\vec{z}_{l,j+1} - \vec{z}_{l,\infty}\|_p < \|\vec{z}_{l,j} - \vec{z}_{l,\infty}\|_p$, if:*

$$\begin{aligned} &\|\boldsymbol{F}_{l,j}\|_p < 1 \quad \forall l, j \\ &\|\vec{F}_r\|_p < \xi \end{aligned} \tag{5.13}$$

*where $\xi$ is positive scalar that ensures $\|\vec{F}_r\|_p$ remains bounded.*

**Corollary 1.1** *The monotonic stability condition in Eq.* (5.13) *can be expressed as following:*

$$RMC \triangleq \frac{1 - \|\boldsymbol{K}_{l,j}\|_p^{l-1}}{1 - \|\boldsymbol{K}_{l,j}\|_p} \times \|\boldsymbol{D}_{l,j}\|_p < 1 \quad \forall l, j \tag{5.14}$$

**Proof 1** *$\boldsymbol{K}_{l,j}$ is a strictly upper triangular block matrix containing block matrices of higher-order terms, $\boldsymbol{T}_{l,j}^{v_i} \in \mathbb{R}^{n \times n}$, with $l$ block zero matrices and $0 \in \mathbb{R}^{n \times n}$, along the diagonal. From linear algebra, $\boldsymbol{A}^l$ is zero for a strictly triangular matrix $\boldsymbol{A} \in \mathbb{R}^{l \times l}$ with dimension $l$ [83–85]. We use this property for strictly upper triangular block matrix $\boldsymbol{K}_{l,j}$ to avoid matrix inversion in Eq.* (5.12)*, using the fact that $\boldsymbol{K}_{l,j}^l = 0$ ($l$ denotes the number of layers). Here*

$$\boldsymbol{I} - \boldsymbol{K}_{l,j}^l = (\boldsymbol{I} - \boldsymbol{K}_{l,j})(\boldsymbol{I} + \boldsymbol{K}_{l,j} + \boldsymbol{K}_{l,j}^2 + ... + \boldsymbol{K}_{l,j}^{l-1}) \tag{5.15}$$

*implies that*

$$(\boldsymbol{I} - \boldsymbol{K}_{l,j})^{-1} = (\boldsymbol{I} + \boldsymbol{K}_{l,j} + \boldsymbol{K}_{l,j}^2 + ... + \boldsymbol{K}_{l,j}^{l-1}). \tag{5.16}$$

*Inserting Eq.* (5.16) *into Eq.* (5.13) *results in*

$$\begin{aligned} \|\boldsymbol{F}_{l,j}\| &= \|(\boldsymbol{I} - \boldsymbol{K}_{l,j})^{-1} \boldsymbol{D}_{l,j}\| \\ &\leq \|(\boldsymbol{I} + \boldsymbol{K}_{l,j} + \boldsymbol{K}_{l,j}^2 + ... + \boldsymbol{K}_{l,j}^{l-1}) \boldsymbol{D}_{l,j}\| \\ &\leq (1 + \|\boldsymbol{K}_{l,j}\| + \|\boldsymbol{K}_{l,j}\|^2 + ... + \|\boldsymbol{K}_{l,j}\|^{l-1}) \|\boldsymbol{D}_{l,j}\| \end{aligned} \tag{5.17}$$

*where the right side of Eq.* (5.17) *is a geometric sum that can be rewritten as $\frac{1-\|\boldsymbol{K}_{l,j}\|^{l-1}}{1-\|\boldsymbol{K}_{l,j}\|} \times \|\boldsymbol{D}_{l,j}\|$. Therefore, if the RMC parameter $\frac{1-\|\boldsymbol{K}_{l,j}\|^{l-1}}{1-\|\boldsymbol{K}_{l,j}\|} \times \|\boldsymbol{D}_{l,j}\| < 1$, $\|\boldsymbol{F}_{l,j}\|$ will be less than one.*

Note that because of norm properties in Eq. (5.17), the RMC criteria in corollary 1.1 is more conservative than the criteria presented in Eq. (5.13).

### 5.4.1 Nominal Stability and Convergence

For the additive model in Eq. (3.2), the nominal plant matrix results from the desired topography, $\mathbf{H}_0 = \mathbf{H}(\vec{g}_d)$. The nominal matrices are:

$$\mathbf{D}_{0_l} = \begin{bmatrix} \mathbf{T}_0^h & \cdots & \mathbf{0} \\ \vdots & \ddots & \vdots \\ \mathbf{0} & \cdots & \mathbf{T}_0^h \end{bmatrix} \tag{5.18a}$$

$$\mathbf{K}_{0_l} = \begin{bmatrix} \mathbf{0} & \mathbf{T}_0^{\nu_1} & \cdots & \mathbf{T}_0^{\nu_{l-2}} & \mathbf{T}_0^{\nu_{l-1}} \\ & & \ddots & \vdots & \vdots \\ & & & \mathbf{0} & \mathbf{T}_0^{\nu_1} \\ \mathbf{0} & \cdots & & & \mathbf{0} \end{bmatrix} \tag{5.18b}$$

In this case, the following properties are true:

$$\|\mathbf{D}_{0_l}\|_p = \|\mathbf{T}_0^h\|_p \tag{5.19a}$$

$$\|\mathbf{K}_{0_l}\|_p \leq \sum_{i=1}^{l-1} \|\mathbf{T}_0^{\nu_i}\|_p, \tag{5.19b}$$

$$\|\mathbf{T}_0^h\| = \|\mathbf{L}_f^h - \mathbf{L}_e^h \mathbf{H}_0\| \tag{5.19c}$$

$$\|\mathbf{T}_0^{\nu_i}\| = \|\mathbf{L}_f^{\nu_i} - \mathbf{L}_e^{\nu_i} \mathbf{H}_0\|. \tag{5.19d}$$

Eq. (5.19b) has an equal sign for $l_\infty$ norm of BCCB $\mathbf{H}_0$ matrix.

**Theorem 2** *The system in Eq.* (3.2) *controlled by a nominal system representation of FO-SILC in Eq.* (5.12) *(or HO-SILC in Eq.* (5.9)*) is asymptotically stable (AS) for the nominal system if and only if:*

$$\rho(\boldsymbol{T}_0^h) < 1, \tag{5.20}$$

*where $\rho$ is the spectral radius.*

**Proof 2** *To prove the nominal stability of Eq.* (5.9)*, we need to prove the nominal representation of Eq.* (5.12) *is stable. The nominal form of the system given by Eq.* (5.12) *is asymptotically stable if $\rho(\boldsymbol{F}_{0_l}) < 1$, with $\boldsymbol{F}_{0_l} = (\boldsymbol{I} - \boldsymbol{K}_{0_l})^{-1}\boldsymbol{D}_{0_l}$. $(\boldsymbol{I} - \boldsymbol{K}_{0_l})^{-1}$ is a strictly upper triangular block matrix with block-diagonal matrices equal to $\boldsymbol{I}$; therefore, the eigenvalues of $\boldsymbol{F}_{0_l}$ are equal to the eigenvalues of $\boldsymbol{D}_{0_l}$. $\boldsymbol{D}_{0_l}$ is a block diagonal matrix and its spectral radius is equal to the spectral radius of the matrix $\boldsymbol{T}_0^h$. Therefore, the nominal system is stable if $\rho(\boldsymbol{T}_0^h) < 1$.*

The monotonic stability of the FO-SILC algorithm in Eq. (5.12) derives from Eq. (5.13); a nominal system representation of Eq. (5.12) is RMC stable using contraction mapping if

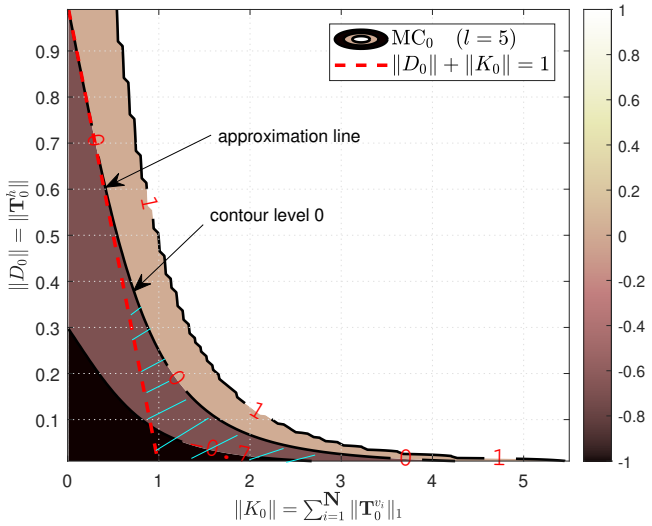


(a) stable region for $l = 5$

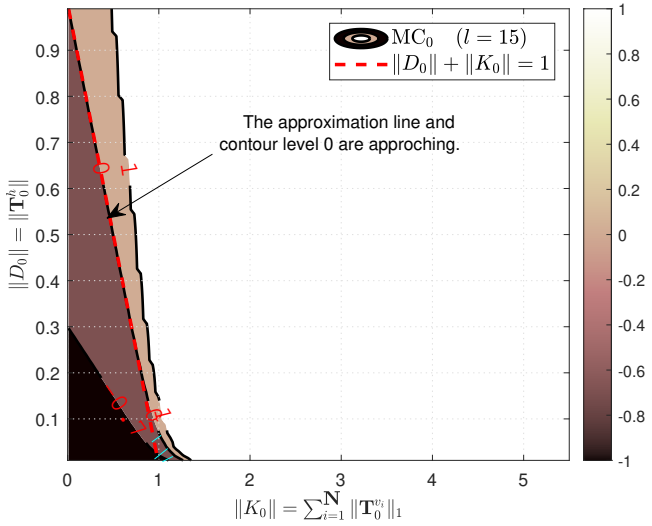


(b) stable region for $l = 15$

Figure 5.2: **Monotonic nominal stability of HO-SILC**: the negative area below contour level **0** is related to the $\mathrm{MC}_0$ stable regions for the nominal system. The area below the dashed red line is the approximated stable regions.

$\|\mathbf{F}_{0_l}\|_p < 1$. Using corollary 1.1, the conservative RMC criteria for the nominal system is defined as: $\text{RMC}_0 \triangleq \frac{1-\|\mathbf{K}_{0_l}\|_P^{l-1}}{1-\|\mathbf{K}_{0_l}\|_p} \times \|\mathbf{T}_0^h\|_p < 1$. Figure 5.2 shows the design regions of learning filters that correspond to $\text{MC}_0 \triangleq \frac{1-\|\mathbf{K}_0\|^{l-1}}{1-\|\mathbf{K}_0\|} \times \|\mathbf{D}_0\| - 1$ for two different layer numbers, where negative values below a contour level of 0 relate to $\text{MC}_0$ stable regions for the nominal system. Note that if $\|\mathbf{K}_0\| << 1$, we can ignore $\|\mathbf{K}_0\|^{l-1}$ for higher layers and the monotonic stability region can be approximated by a line ($\|\mathbf{K}_0\| + \|\mathbf{D}_0\| < 1$). The area below the dashed red line represents an approximation of the stable region defined by the $\text{MC}_0$ parameter. To ensure monotonicity, we design the learning filters such that $\|\mathbf{K}_0\| + \|\mathbf{D}_0\| < 1$ (or $\|\mathbf{T}_0^h\|_1 + \sum_{i=1}^{\text{L-1}} \|\mathbf{T}_0^{v_i}\|_1 < 1$). It can be seen that as the number of layers increases the area related to $\|\mathbf{K}_0\| + \|\mathbf{D}_0\| < 1$ approaches the stable boundary condition deonoted by $\text{MC}_0 = 0$. Alternatively, as the number of layers decreases, $\|\mathbf{K}_0\| + \|\mathbf{D}_0\| < 1$ becomes more conservative, as evident by the missing stable region shown with the dashed blue lines in Figure 5.2a.

**Remark 1** *In order to avoid norm calculations of the high dimensional $\boldsymbol{F}_{0_l}$ or $\boldsymbol{K}_{0_l} \in \mathbb{R}^{ln \times ln}$, the $l_\infty$ norm can be used. Eq.* (5.19b) *has an equality sign for $l_\infty$, which reduces dimensionality in calculating matrix norms of $\boldsymbol{T}_0^{v_i} \in \mathbb{R}^{n \times n}$ instead of $\boldsymbol{K}_{0_l} \in \mathbb{R}^{ln \times ln}$.*

### 5.4.2 Maximum Allowable Interval Uncertainty

In this section, we design the learning gain matrices in Eq. (5.9) such that closed-loop HO-SILC remains stable for the maximum allowable interval uncertainty (AIU) added to the nominal plant. Altin et al. formulated the iteration varying system behavior as that of robustness under interval uncertainties with spatially invariant bounds for a FO-SILC system [39]. In this section, we extend their results to HO-SILC systems.

Assume that the iteration varying plant $\mathbf{H}_{l,j} = \mathbf{H}_0 + \Delta\mathbf{H}_{l,j}$ is an interval matrix, and $\Delta\mathbf{H}_{l,j}$ is additive uncertainty of the nominal plant. In order to quantify the maximum amount of allowable uncertainty, we define the uncertainty radius as $\Delta\mathbf{H}_r \triangleq \frac{\overline{\mathbf{H}}-\underline{\mathbf{H}}}{2}$. Given known upper and lower bounds, we assume that the nominal plant follows the center matrix definition in [39] such that $\mathbf{H}_0 = \frac{\overline{\mathbf{H}}+\underline{\mathbf{H}}}{2}$. In general, ensuring the asymptotic and monotonic stability in Eq. (5.20) and Eq. (5.13) for all $\mathbf{H}_{l,j} \in \mathbf{H}^I$ is a difficult problem [39, 86]. The goal here is to find the maximum allowable interval uncertainty, $r_{AIU}$, such that the RMC criteria in Eq. (5.14) is guaranteed for all $\|\Delta\mathbf{H}_{l,j}\| < r_{AIU}$. We can solve this problem by ensuring the maximum amount of uncertainty in the system remains smaller than $r_{AIU}$ at all iterations. In other words, if the learning filters in Eq. (5.7) are designed such that $\|\Delta\mathbf{H}_r\| < r_{AIU}$, we can ensure $\|\Delta\mathbf{H}_{l,j}\| < r_{AIU}$ for all iterations and layers. Iteration varying matrices in Eq. (5.9) can be written as $\mathbf{T}_{l,j}^h = \mathbf{T}_0^h - \mathbf{L}_e^h \Delta\mathbf{H}_{l,j}$ and $\mathbf{T}_{l,j}^{v_i} = \mathbf{T}_0^{v_i} - \mathbf{L}_e^{v_i} \Delta\mathbf{H}_{l,j}$. We can decompose the rest of the matrices as:

$$\mathbf{D}_{l,j} = \mathbf{D}_{0_l} + \Delta\mathbf{D}_{l,j} \tag{5.21a}$$

$$\mathbf{K}_{l,j} = \mathbf{K}_{0_l} + \Delta\mathbf{K}_{l,j} \tag{5.21b}$$

$$\mathbf{F}_{l,j} = \mathbf{F}_{0_l} + \Delta\mathbf{F}_{l,j} \tag{5.21c}$$

$$\Delta\mathbf{D}_{l,j} = -\mathbf{L}_e^h \begin{bmatrix} \Delta\mathbf{H}_{l-1,j} & \cdots & \mathbf{0} \\ \vdots & \ddots & \vdots \\ \mathbf{0} & \cdots & \Delta\mathbf{H}_{0,j} \end{bmatrix} \tag{5.22a}$$

$$\Delta\mathbf{K}_{l,j} = -\begin{bmatrix} \mathbf{0} & \mathbf{L}_e^{v_1}\Delta\mathbf{H}_{l-2,j+1} & \mathbf{L}_e^{v_2}\Delta\mathbf{H}_{l-3,j+1} & \cdots & \mathbf{L}_e^{v_{l-1}}\Delta\mathbf{H}_{0,j+1} \\ & \mathbf{0} & \mathbf{L}_e^{v_1}\Delta\mathbf{H}_{l-3,j+1} & \cdots & \mathbf{L}_e^{v_{l-2}}\mathbf{H}_{0,j+1} \\ \vdots & & \ddots & & \vdots \\ & & & \mathbf{0} & \mathbf{L}_e^{v_1}\Delta\mathbf{H}_{0,j+1} \\ \mathbf{0} & & \cdots & & 0 \end{bmatrix} \tag{5.22b}$$

inserting Eqs. (5.16) and (5.21) into Eq. (5.12), $\mathbf{F}$ can be decomposed as the following:

$$\begin{aligned} \mathbf{F}_{l,j} &= (\mathbf{I} + (\mathbf{K}_{0_l} + \Delta\mathbf{K}_{l,j}) + ... + (\mathbf{K}_{0_l} + \Delta\mathbf{K}_{l,j})^{l-1})(\mathbf{D}_{0_l} + \Delta\mathbf{D}_{l,j}) \\ &= (\mathbf{a}_{0_l} + \mathbf{a}_{1_l}\Delta\mathbf{K}_{l,j} + \mathbf{a}_{2_l}\Delta\mathbf{K}_{l,j}^2 + ...)(\mathbf{D}_{0_l} + \Delta\mathbf{D}_{l,j}) \end{aligned} \tag{5.23a}$$

$$\mathbf{a}_{0_l} = \mathbf{I} + \mathbf{K}_{0_l} + \mathbf{K}_{0_l}^2 + ... + \mathbf{K}_{0_l}^{l-1} \tag{5.23b}$$

$$\mathbf{a}_{1_l} = \mathbf{I} + 2\mathbf{K}_{0_l} + 3\mathbf{K}_{0_l}^2 + ... + (l-1)\mathbf{K}_{0_l}^{l-2},\ l \geq 2 \tag{5.23c}$$

$$\mathbf{a}_{2_l} = \mathbf{I} + 3\mathbf{K}_{0_l} + 6\mathbf{K}_{0_l}^2 + 10\mathbf{K}_{0_l}^3 + ... + \frac{(l-1)(l-2)}{2}\mathbf{K}_{0_l}^{l-3},\ l \geq 3 \tag{5.23d}$$

Ignoring the higher order terms for small model uncertainties around the nominal plant ($\Delta\mathbf{H}^n \simeq 0$ for $n > 2$),

$$\begin{aligned} &\mathbf{F}_{0_l} = \mathbf{a}_{0_l}\mathbf{D}_{0_l}, \\ &\Delta\mathbf{F}_{l,j} \simeq (\mathbf{a}_{1_l}\Delta\mathbf{K}_{l,j} + \mathbf{a}_{2_l}\Delta\mathbf{K}_{l,j}^2)\mathbf{D}_{0_l} + (\mathbf{a}_{0_l} + \mathbf{a}_{1_l}\Delta\mathbf{K}_{l,j})\Delta\mathbf{D}_{l,j}. \end{aligned} \tag{5.24}$$

**Theorem 3** *Given the learning matrices designed for the nominal plant $\boldsymbol{H}_0$ such that the nominal system is AS ($\rho(\boldsymbol{T}_0^h) < 1$), the iterative system in Eq.* (3.2)*, controlled by the FO-SILC in Eq.* (5.12) *remains AS if*

$$
\begin{aligned}
&\|\Delta \boldsymbol{H}_r\|_p < r_{AIU}^{Asym} \\
&r_{AIU}^{asym} = \frac{-\mu_1 + \sqrt{\mu_1^2 + 4\frac{\mu_2}{\|\boldsymbol{P}\|_\infty}}}{2\mu_2},
\end{aligned}
\tag{5.25}
$$

*where $\mu_1$ and $\mu_2$ are positive scalars that are functions of the learning filters and nominal plant.*

$$
\mu_1 = 2\theta_1 \langle \boldsymbol{F}_{0_l} \rangle_p, \quad \mu_2 = 2\theta_2 \langle \boldsymbol{F}_{0_l} \rangle_p + \theta_1^2 \tag{5.26a}
$$

$$
\begin{aligned}
\theta_1 &= \langle \boldsymbol{a}_{0_l} \rangle_p \langle \boldsymbol{L}_e^h \rangle_p + \langle \boldsymbol{a}_{1_l} \rangle_p \langle \boldsymbol{T}_0^h \rangle_p \sum_{i=1}^{l-1} \langle \boldsymbol{L}_e^{v_i} \rangle_p \\
\theta_2 &= \langle \boldsymbol{a}_{1_l} \rangle_p \langle \boldsymbol{L}_e^h \rangle_p \sum_{i=1}^{l-1} \langle \boldsymbol{L}_e^{v_i} \rangle_p + \langle \boldsymbol{a}_{2_l} \rangle_p \langle \boldsymbol{T}_0^h \rangle_p (\sum_{i=1}^{l-1} \langle \boldsymbol{L}_e^{v_i} \rangle_p)^2,
\end{aligned}
\tag{5.26b}
$$

*where $\langle \boldsymbol{B} \rangle_p \triangleq max(\|\boldsymbol{B}\|_p, \|\boldsymbol{B}^{\boldsymbol{T}}\|_p)$ for an arbitrary square matrix $\boldsymbol{B}$ in $l_p$ norm. In Eq.* (5.25)*, $\boldsymbol{P}$ is a symmetric and positive definite matrix that satisfies the Lyapunov stability of the nominal plant [38],*

$$
\boldsymbol{F}_{0_l}^{\boldsymbol{T}} \boldsymbol{P} \boldsymbol{F}_{0_l} - \boldsymbol{P} = -\boldsymbol{I}. \tag{5.27}
$$

**Proof 3** *Assume the FO-SILC in Eq.* (5.12) *is Asymptotically stable for the nominal plant; from Lyapunov stability, there exist a positive definite $\boldsymbol{P} > 0$ such that Eq.* (5.27) *is satisfied. The iteration varying FO-SILC is asymptotically stable in the Lyapunov sense, if the following inequality is satisfied with the same $\boldsymbol{P}$ from Eq.* (5.27)*:*

$$
\begin{aligned}
&\boldsymbol{F}_{l,j}^{\boldsymbol{T}} \boldsymbol{P} \boldsymbol{F}_{l,j} - \boldsymbol{P} < 0, \\
&l = 1, 2, ..., L, \\
&j = 1, 2, ..., J.
\end{aligned}
\tag{5.28}
$$

*Defining $\|\Delta \boldsymbol{H}\|_p \triangleq \max_{l,j}(\|\Delta \boldsymbol{H}_{l,j}\|_p)$, the following induced norms hold for $\Delta \boldsymbol{K}_{l,j}$ and $\Delta \boldsymbol{D}_{l,j}$:*

$$
\|\Delta \boldsymbol{D}_{l,j}\|_p \leq \|\boldsymbol{L}_e^h\|_p \|\Delta \boldsymbol{H}\|_p \tag{5.29a}
$$

$$
\|\Delta \boldsymbol{K}_{l,j}\|_p \leq (\sum_{i=1}^{l-1} \|\boldsymbol{L}_e^{v_i}\|_p) \|\Delta \boldsymbol{H}\|_p \tag{5.29b}
$$

*Inserting Eqs.* (5.24) *and* (5.27) *into Eq.* (5.28)*, and taking the norm of both sides we have:*

$$
\begin{aligned}
&(\boldsymbol{F}_{0_l} + \Delta\boldsymbol{F}_{l,j})^{\boldsymbol{T}}\boldsymbol{P}(\boldsymbol{F}_{0_l} + \Delta\boldsymbol{F}_{l,j}) - \boldsymbol{P} < 0 \\
&\xrightarrow{\|.\|_p} 2\langle\boldsymbol{F}_{0_l}\rangle_p\langle\Delta\boldsymbol{F}_{l,j}\rangle_p + \langle\Delta\boldsymbol{F}_{l,j}\rangle_p^2 < \frac{1}{\|\boldsymbol{P}\|_p}.
\end{aligned} \tag{5.30}
$$

*Using Eqs.* (5.29a) *and* (5.29b) *and taking $l_p$ norm of both sides of Eq.* (5.24)*, we have:*

$$
\langle\Delta\boldsymbol{F}_{l,j}\rangle_p \leq \theta_2\langle\Delta\boldsymbol{H}\rangle_p^2 + \theta_1\langle\Delta\boldsymbol{H}\rangle_p \tag{5.31}
$$

*where $\theta_1$ and $\theta_2$ are defined in Eq.* (5.26b)*. Neglecting higher order terms for small model uncertainties ($\|\Delta\boldsymbol{H}\|_p^n \approx 0, \ \forall n \geq 3$), Eq.* (5.30) *can be simplified to a quadratic equation for $\langle\Delta\boldsymbol{H}\rangle_p$:*

$$
\mu_1\langle\Delta\boldsymbol{H}\rangle_p + \mu_2\langle\Delta\boldsymbol{H}\rangle_p^2 - \frac{1}{\|\boldsymbol{P}\|_p} < 0, \tag{5.32}
$$

*which is negative when $\langle\Delta\boldsymbol{H}\rangle_p < \frac{-\mu_1+\sqrt{\mu_1^2+4\frac{\mu_2}{\|\boldsymbol{P}\|_\infty}}}{2\mu_2}$. $\mu_1$ and $\mu_2$ are defined in Eqs.* (5.26a) *and* (5.26b)*. Therefore, $r_{AIU}^{asym} = \frac{-\mu_1+\sqrt{\mu_1^2+4\frac{\mu_2}{\|\boldsymbol{P}\|_\infty}}}{2\mu_2}$. Note if Eq.* (5.32) *holds, then Eq.* (5.30) *is true, not vice versa.*

Note that assuming bounded model uncertainty, Theorem 3 provides sufficient condition for BIBO stability of the closed-loop HO-SILC in Eq. (5.9).

**Theorem 4** *Given the learning matrices are designed such that the nominal system is RMC stable ($\|\boldsymbol{F}_{0_l}\| < 1, \ \forall l$ ), the iterative additive process in Eq.* (5.1)*, controlled by the FO-SILC in Eq.* (5.12)*, remains robustly monotonically stable if:*

$$
\begin{aligned}
&\|\Delta\boldsymbol{H}_r\|_p < r_{AIU}^{mono}, \\
&r_{AIU}^{mono} = \frac{-\mu_1 + \sqrt{\mu_1^2 + 4\frac{\mu_2}{\|\boldsymbol{P}_s\|_p}}}{2\mu_2}.
\end{aligned} \tag{5.33}
$$

*$\boldsymbol{P}_s$ is a positive definite matrix that satisfy the following equation:*

$$
\boldsymbol{S}_{0_l}^{\boldsymbol{T}}\boldsymbol{P}_s\boldsymbol{S}_{0_l} - \boldsymbol{P}_s = -\boldsymbol{I}, \quad \boldsymbol{S}_{0_l} = \begin{bmatrix} 0 & \boldsymbol{F}_{0_l}^{\boldsymbol{T}} \\ \boldsymbol{F}_{0_l} & 0 \end{bmatrix} \tag{5.34}
$$

**Proof 4** *As it was explained earlier in Eq.* (5.13)*, monotonic stability of Eq.* (5.12) *is achieved if $\|\boldsymbol{F}_{l,j}\|_p < 1$. If the $l_2$ norm is used, then $\|\boldsymbol{F}_{l,j}\|_2 = \bar{\sigma}(\boldsymbol{F}_{l,j})$. Maximum singular value of a matrix (here $\boldsymbol{F}_{l,j}$ ) is defined as:*

$$\bar{\sigma}(\boldsymbol{F}_{l,j}) = \sqrt{\rho(\boldsymbol{F}_{l,j}^{\boldsymbol{T}}\boldsymbol{F}_{l,j})}. \tag{5.35}$$

*Eq.* (5.35) *implies if* $\rho(\boldsymbol{F}_{l,j}^{\boldsymbol{T}}\boldsymbol{F}_{l,j}) < 1$, *then* $\bar{\sigma}(\boldsymbol{F}_{l,j}) < 1$. *In other words, the maximum singular value problem for monotonic convergence can be solved equivalently as a eigenvalue problem. Following the same steps as Eqs.* (5.28) *to* (5.32), *maximum allowable uncertainty of the nominal plant for monotonic convergence of Eq.* (5.12) *can be achieved [38]. Note that the eigenvalues of* $\boldsymbol{F}^{\boldsymbol{T}}\boldsymbol{F}$ *are equal to the eigenvalues of* $\boldsymbol{S}$,

$$\boldsymbol{S}_{l,j} = \boldsymbol{S}_{0_l} + \Delta\boldsymbol{S}_{l,j},\ \boldsymbol{S}_{l,j} = \begin{bmatrix} 0 & \boldsymbol{F}_{l,j}^{\boldsymbol{T}} \\ \boldsymbol{F}_{l,j} & 0 \end{bmatrix},\ \Delta\boldsymbol{S}_{l,j} = \begin{bmatrix} 0 & \Delta\boldsymbol{F}_{l,j}^{\boldsymbol{T}} \\ \Delta\boldsymbol{F}_{l,j} & 0 \end{bmatrix}. \tag{5.36}$$

*Assume the FO-SILC in Eq.* (5.12) *is monotonically stable for the nominal plant; from Lyapunov stability, there exists a positive definite* $\boldsymbol{P}_s > 0$ *such that Eq.* (5.34) *holds. Similarly, the iteration varying FO-SILC is monotonically stable based on the Lyapunov stability (*$\rho(\boldsymbol{S}_{l,j}) = \bar{\sigma}(\boldsymbol{F}_{l,j}) < 1$*), if the following inequality holds with the same* $\boldsymbol{P}_s$ *from Eq.* (5.34)*:*

$$\boldsymbol{S}_{l,j}^{\boldsymbol{T}}\boldsymbol{P}_s\boldsymbol{S}_{l,j} - \boldsymbol{P}_s < 0 \quad \forall l \ \&\ j. \tag{5.37}$$

*Inserting Eq.* (5.36) *into Eq.* (5.37), *and using Eq.* (5.34) *we have:*

$$\boldsymbol{S}_{0_l}^{\boldsymbol{T}}\boldsymbol{P}_s\Delta\boldsymbol{S}_{l,j} + \Delta\boldsymbol{S}_{l,j}^{\boldsymbol{T}}\boldsymbol{P}_s\boldsymbol{S}_{0_l} + \Delta\boldsymbol{S}_{l,j}^{\boldsymbol{T}}\boldsymbol{P}_s\Delta\boldsymbol{S}_{l,j} < \boldsymbol{I}. \tag{5.38}$$

*Given* $\|\boldsymbol{S}_{0_l}\|_p = \langle\boldsymbol{F}_{0_l}\rangle_p$ *and* $\|\Delta\boldsymbol{S}_{l,j}\|_p = \langle\Delta\boldsymbol{F}_{l,j}\rangle_p$, *and taking* $l_p$ *norm of both sides of Eq.* (5.38) *we have:*

$$2\langle\boldsymbol{F}_{0_l}\rangle_p\langle\Delta\boldsymbol{F}_{l,j}\rangle_p + \langle\Delta\boldsymbol{F}_{l,j}\rangle_p^2 < \frac{1}{\|\boldsymbol{P}_s\|_p}. \tag{5.39}$$

*Using Eqs.* (5.24) *and* (5.31), *Eq.* (5.39) *simplifies to a quadratic equation for* $\|\Delta\boldsymbol{H}\|_p$,

$$\mu_1\|\Delta\boldsymbol{H}\|_p + \mu_2\|\Delta\boldsymbol{H}\|_p^2 - \frac{1}{\|\boldsymbol{P}_s\|_p} < 0, \tag{5.40}$$

*which is negative when* $\|\Delta\boldsymbol{H}\|_p < \frac{-\mu_1+\sqrt{\mu_1^2+4\frac{\mu_2}{\|\boldsymbol{P}_s\|_p}}}{2\mu_2}$. $\mu_1$ *and* $\mu_2$ *are defined in Eqs.* (5.26a) *and* (5.26b). *Therefore,* $r_{AIU}^{mono} = \frac{-\mu_1+\sqrt{\mu_1^2+4\frac{\mu_2}{\|\boldsymbol{P}_s\|_p}}}{2\mu_2}$. *Note that if Eq.* (5.40) *is true, then Eq.* (5.39) *is true, not vice versa.*

**Remark 2** *By direct substitution of* $\boldsymbol{S}_{0_l}$ *into Eq.* (5.34), *it is evident that* $\boldsymbol{P}_s = diag(\boldsymbol{P},\boldsymbol{P})$ *and* $\|\boldsymbol{P}_s\|_p = \|\boldsymbol{P}\|_p$, *which results in* $r_{AIU}^{mono} = r_{AIU}^{asym}$. *We denote* $r_{AIU} \triangleq r_{AIU}^{mono} = r_{AIU}^{asym}$, *as an*

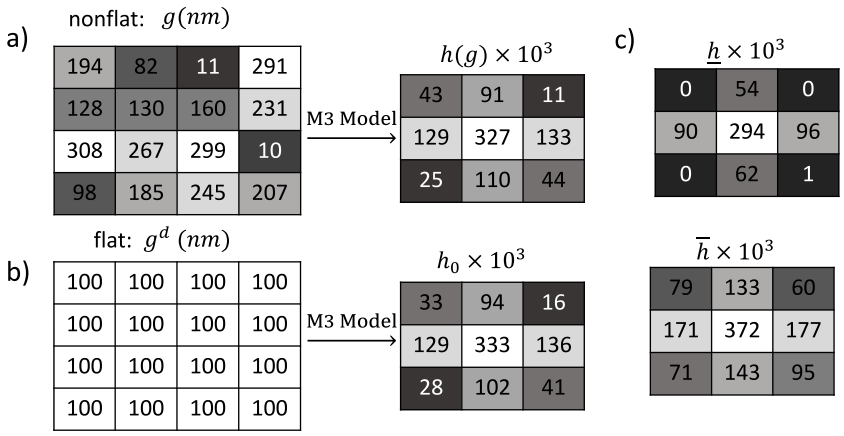


Figure 5.3: **Topology dependent impulse response**. The estimated impulse response is spatial invariant (Method M3 of [2]) meaning that it is the same for every spatial coordinate of the $g(x,y)$. Note that the estimated impulse response is iteration varying. a) Effect of flat surface. At left is a $4\times4$ pixel of a flat reference topography signal. At right is the $3\times3$ model's corresponding nominal impulse response ($h_0$). b) Effect of a nonflat surface. At left is a $4\times4$ pixel of a random $g$ signal to show the effect of significant surface variation. At right is the $3\times3$ model's corresponding impulse response ($h$). c) upper and lower bounds of $h$, $\bar{h}$, $\underline{h}$, such that $\underline{h} \preceq h \preceq \bar{h}$.

*estimate on the maximum allowable interval uncertainty.*

**Remark 3** *The special structure of $\boldsymbol{K}_{0_l}$ in Eq.* (5.18)*, results in $\|\boldsymbol{K}_{0_l}\|_1 = \|\boldsymbol{K}_{0_l}\|_\infty$.*

## 5.5 Simulation setup

For this simulation, a multi-layered structure with L = 6 layers is considered (Figure 5.1a). The LPV and ConvRNN models developed in Section 3.5 are used to describe the spreading of liquid droplets on nonflat surfaces. The reference device structure has the reference height map, $\Delta g^d$, given in Figure 5.1a with 100 nm layer heights for all layers, which is uniform except for the two outer rings of pixels that are reduced by half to better represent material drop-off at the edges. Each layer is printed in a single printing pass on top of a cured surface. For the first (bottom) layer in the simulation, the underlying surface, ($l = 0$), is assumed to be a pre-layer of cured printing material so that first-layer surface interactions with other substrate materials need not be considered. In e-jet printing, droplet volume has a standard variation of 25% over a wide range of droplet sizes [41]. Therefore; a normally distributed white noise is added to the input signal. For example, for the LPV model in Eq. (3.5), a normally distributed white noise with variance of 0.25 $\mu m$ is added to the input

signal such that $\Delta\vec{g}_{l,j} = \mathbf{H}_{l-1,j}\vec{f}^{LPV}_{l,j} \circ (\mathbf{1}_{n\times 1} + \mathcal{N}(0, 0.25^2)_{n\times 1})$, where $\mathbf{1}$ is a vector of ones. The input will be constrained to non-negative values to ensure an additive process.

It is important to note that the input of the first iteration at the first layer is zero, $\vec{f}_{1,1} = \vec{0}$, implying that there is no prior knowledge of the appropriate input. This results in no material being deposited during the first iteration of the first layer. However, the input of the first device at higher layers, $l \geq 2$, comes from the last device in the previous layer, such that $\vec{f}_{l,1} = \vec{f}_{l-1,J}$ where $J = 30$ is the total number of iterations.

The LPV model in Eq. (3.5) is used to design the HO-SILC learning filters in Eq. (5.7) and the results are shown in Figures 5.4, 5.5a and 5.5b and Tables 5.1 to 5.3. The linearized CRNN model in Eq. (3.13) is used to design the learning filters in Eq. (5.4), and the results are shown in Figure 5.6. In the absence of the experimental data, the error is calculated from the difference between the desired and simulated height increment predicted by the nonlinear CRNN model in Section 3.5.3 and Eq. (3.6).

For Loctite3526, the nominal impulse response and the invariant bounds for the M3 method of the LPV model in Section 3.5.2 are shown in Figure 5.4, and the corresponding norms are: $\|\Delta\mathbf{H}_0\|_2 = 0.411$, $\|\Delta\mathbf{H}_r\|_2 = 0.118$, and $\|\Delta\mathbf{H}_r\|_\infty = 0.123$. We set $q = 1$, $r = 0.01$, $s = 0.09$, and look for appropriate $\alpha$ and $\beta$, such that $\|\mathbf{F}_{0_L}\|_p < 1$ and $\|\Delta\mathbf{H}_r\|_p < r_{AIU_p}$. Note that $(\alpha,\beta) = (0,0)$ results in a FO-SILC update law that only leverages device to device (iteration) learning in the horizontal direction [42]. Unlike [39], we use "$dlyap(\mathbf{F}^{\mathrm{T}}_{0_L}, \mathbf{I})$" in MATLAB to solve the discrete-time Lyapunov equation in Eq. (5.27), and calculate $\mathbf{P}$. In this example, $\mathbf{F}_{0_L}$ is not BCCB and we cannot use DFT simplifications from [39].

## 5.6 Simulation Results

In this section, simulation results of the system described in Section 3.3 Section 5.5 using HO-SILC are investigated. Tables 5.1 to 5.3 show that by proper selection of $\alpha$ and $\beta$, the stability radius, $r_{AIU}$, can be tuned. It should be noted that $\alpha$ has direct effect on the total error (performance) as presented in Eq. (5.2). It is expected that higher values of $r_{AIU_p}$ improve robustness to model uncertainties, while smaller values of $\mathbf{F}_0$, ensuring $\|\mathbf{F}_0\|_p < 1$, increase speed of convergence. In addition, for a constant $\beta$, $\alpha$ does not change the maximum singular value of $\mathbf{F}_{0_L}$, $\bar{\sigma} = \|\mathbf{F}_{0_L}\|_2$, which is approximately equal to $\|\mathbf{T}^h_0\|_2$. To be specific, for fixed $\beta$, monotonic stability of the nominal system is achieved if $\|\mathbf{T}^h_0\|_2 < 1$. The reason is that the diagonal elements of $\mathbf{F}^T_{0_L}\mathbf{F}_{0_L}$ are equal to $\mathbf{T}^{h^2}_0(\mathbf{I} + \mathbf{T}^{v_i^j}_0)$, while off diagonal elements are functions of $\mathbf{T}^{h^2}_0(\mathbf{T}^{v_i}_0)^j$ for $j = 1, ..., 2L-2$. Given $\|\mathbf{T}^h_0\|_2 < 1$ and $\|\mathbf{T}^{v_i}_0\|_2 < 1$, the off diagonal elements are smaller compared to the main diagonal elements,

Table 5.1: Design methodology for the LPV model, $\beta = 0.0$

| | $l_2$ norm | | | | | | | $l_\infty$ norm | | | | | | |
|---|---|---|---|---|---|---|---|---|---|---|---|---|---|---|
| $\alpha$ | $\|K_{0_L}\|$ | $\|T_0^h\|$ | $RMC_0$ | $RMC^{app}$ | $\|F_{0_L}\|$ | $\|P\|$ | $r_{AIU}$ | $\|K_{0_L}\|$ | $\|T_0^h\|$ | $RMC_0$ | $RMC_0^{app}$ | $\|F_{0_L}\|$ | $\|P\|$ | $r_{AIU}$ |
| 0.00 | 0.00 | 0.099 | 0.099 | 0.099 | 0.099 | 1.01 | 0.561 | 0.00 | 0.190 | 0.190 | 0.190 | 0.189 | 1.022 | 0.232 |
| 0.25 | 0.308 | 0.099 | 0.144 | 0.408 | 0.099 | 1.01 | 0.442 | 0.598 | 0.189 | 0.459 | 0.788 | 0.210 | 1.024 | 0.136 |
| 0.50 | 0.849 | 0.099 | 0.450 | 0.948 | 0.099 | 1.01 | 0.345 | 1.742 | 0.188 | 12.13 | 1.931 | 0.241 | 1.028 | 0.077 |
| 0.75 | 1.917 | 0.099 | 10.24 | 2.016 | 0.099 | 1.01 | 0.243 | 4.311 | 0.185 | 1552.7 | 4.497 | 0.295 | 1.032 | 0.034 |
| 1.0 | 4.216 | 0.099 | 735.24 | 4.316 | 0.099 | 1.01 | 0.103 | 9.822 | 0.176 | 176100 | 9.998 | 0.394 | 1.038 | 0.012 |

Table 5.2: Design methodology for the LPV model, $\beta = 0.25$

| | $l_2$ norm | | | | | | | $l_\infty$ norm | | | | | | |
|---|---|---|---|---|---|---|---|---|---|---|---|---|---|---|
| $\alpha$ | $\|K_{0_L}\|$ | $\|T_0^h\|$ | $RMC_0$ | $RMC^{app}$ | $\|F_{0_L}\|$ | $\|P\|$ | $r_{AIU}$ | $\|K_{0_L}\|$ | $\|T_0^h\|$ | $RMC_0$ | $RMC_0^{app}$ | $\|F_{0_L}\|$ | $\|P\|$ | $r_{AIU}$ |
| 0.0 | 0.111 | 0.088 | 0.099 | 0.199 | 0.098 | 1.009 | 0.545 | 0.216 | 0.167 | 0.213 | 0.383 | 0.192 | 1.021 | 0.198 |
| 0.25 | 0.301 | 0.088 | 0.126 | 0.389 | 0.098 | 1.009 | 0.475 | 0.670 | 0.167 | 0.476 | 0.837 | 0.201 | 1.022 | 0.135 |
| 0.50 | 0.837 | 0.088 | 0.386 | 0.926 | 0.098 | 1.009 | 0.376 | 1.781 | 0.166 | 11.86 | 1.947 | 0.227 | 1.024 | 0.079 |
| 0.75 | 1.893 | 0.088 | 8.519 | 1.981 | 0.098 | 1.009 | 0.274 | 4.257 | 0.163 | 1268.9 | 4.42 | 0.280 | 1.027 | 0.037 |
| 1.0 | 4.141 | 0.088 | 587.9 | 4.229 | 0.098 | 1.009 | 0.127 | 9.491 | 0.154 | 125870 | 9.645 | 0.379 | 1.032 | 0.014 |

Table 5.3: Design methodology for the LPV model, $\beta = 0.75$

| | $l_2$ norm | | | | | | | $l_\infty$ norm | | | | | | |
|---|---|---|---|---|---|---|---|---|---|---|---|---|---|---|
| $\alpha$ | $\|K_{0_L}\|$ | $\|T_0^h\|$ | $RMC_0$ | $RMC^{app}$ | $\|F_{0_L}\|$ | $\|P\|$ | $r_{AIU}$ | $\|K_{0_L}\|$ | $\|T_0^h\|$ | $RMC_0$ | $RMC_0^{app}$ | $\|F_{0_L}\|$ | $\|P\|$ | $r_{AIU}$ |
| 0.0 | 0.148 | 0.081 | 0.095 | 0.229 | 0.092 | 1.008 | 0.562 | 0.353 | 0.152 | 0.236 | 0.506 | 0.190 | 1.019 | 0.183 |
| 0.25 | 0.297 | 0.081 | 0.115 | 0.378 | 0.092 | 1.008 | 0.501 | 0.799 | 0.152 | 0.601 | 0.952 | 0.199 | 1.019 | 0.128 |
| 0.50 | 0.829 | 0.081 | 0.347 | 0.911 | 0.092 | 1.008 | 0.400 | 1.803 | 0.151 | 11.49 | 1.954 | 0.218 | 1.021 | 0.084 |
| 0.75 | 1.876 | 0.081 | 7.47 | 1.957 | 0.092 | 1.008 | 0.298 | 4.210 | 0.148 | 1085.7 | 4.359 | 0.255 | 1.022 | 0.044 |
| 1.0 | 4.083 | 0.081 | 497.8 | 4.164 | 0.092 | 1.008 | 0.145 | 9.233 | 0.139 | 97126 | 9.373 | 0.342 | 1.026 | 0.017 |

which results in $\|\mathbf{F}_{0_l}\|_2 \simeq \|\mathbf{T}_0^h\|_2$ based on Eq. (5.35). The simulation results in Tables 5.1 to 5.3 show that all pairs of $(\alpha,\beta)$ satisfy $\|\mathbf{F}_0\|_p < 1$. We highlighted the pairs that satisfy the RMC criteria in theorems 3 and 4, for both $l_2$ and $l_\infty$ norms. The results show that the $l_\infty$ norm is more conservative than the $l_2$ norm; therefore, we will focus on the $l_2$ norm.

In 3D structures that are fabricated using AM technologies, the error in previous layers adds up in the upper layers and affects the total heightmap and corresponding standard deviations. HO-SILC can improve the total error by incorporating previous layer errors in the cost function in Eq. (5.3). Figure 5.4 shows the HO-SILC performance for different values of $(\alpha,\beta)$. The results show that HO-SILC can improve the overall performance (smaller total heightmap error) when compared to FO-SILC. Based on the provided information in Tables 5.1 to 5.3, a lower value of $\alpha$ (while $\beta$ is fixed), leads to larger $r_{AIU}$. However, it also degrades the overall performance. Larger values of $\alpha$ impose more weighting on previous layer errors in Eq. (5.2) that results in smaller total errors, $\mathbf{e}_{l,j}$. On the other hand, larger values of $\beta$ for a constant $\alpha$ result in an increase in the achievable $r_{AIU}$ and decrease the total error. Therefore, by proper tuning of higher order parameters, the stability robust-

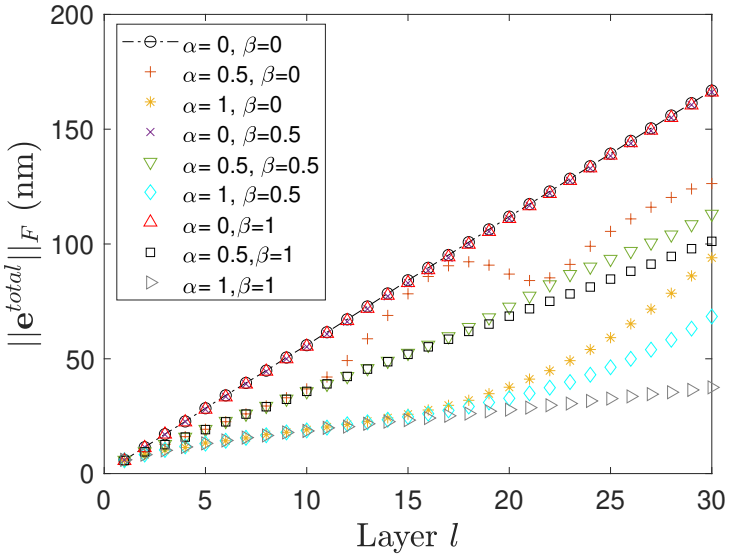


Figure 5.4: **Total error comparison**: HO-SILC results in a lower total error compared to FO-SILC. $\alpha = 0$ and $\beta = 0$ refers to a FO-SILC design that only applies horizontal learning (iteration to iteration). ($L = 30$, $q = 1$, $r = 0.01$, $s = 0.09$).

ness and the performance of the HO-SILC with respect to the total error can be improved. Hereafter, we will set the HO-SILC parameters, $\alpha = 0.9$,$\beta = 0.5$.

Figures 5.5a and 5.5b present the Frobenius norm of the incremental errors, $\Delta\mathbf{e}_{l,j}$, for FO-SILC and HO-SILC controllers based on the LPV model in Section 3.5.2. Figure 5.5a shows that the final incremental errors of the FO-SILC update law are in the same range over the layers. Figure 5.5b shows that by using HO-SILC a significant improvement (around 60% for 6 layers) in the incremental errors over the layers is achieved. The first layer shows the highest error, with the error signals decreasing due to vertical learning through the iterations. In Figure 5.5, the simulation time associated with the controller update in Eq. (5.8) is around 1.34s which is 50% faster compared to the control update time (2.85s) associated with Eq. (5.1) and Figure 5.6 for the linearized CRRN model in Eq. (3.13). The reason is that the LPV plant model is BCCB, and Eq. (5.8) can be used to update the feedforward signal in Figure 5.5.

Figure 5.6 shows the performance of the HO-SILC controller designed using a linearized CRNN model (Eq. (3.13)). Recall that the linearized CRNN model in Eq. (3.13) is from the nonlinear CRNN model used as the *true* model in the simulation. Note that the Jacobian matrix is not BCCB, thus DFT calculations are not possible and the controller derivation requires more time as compared to the HO-SILC algorithm designed with the LPV model in Figure 5.5. In addition, the computation time required to calculate the Jaco-

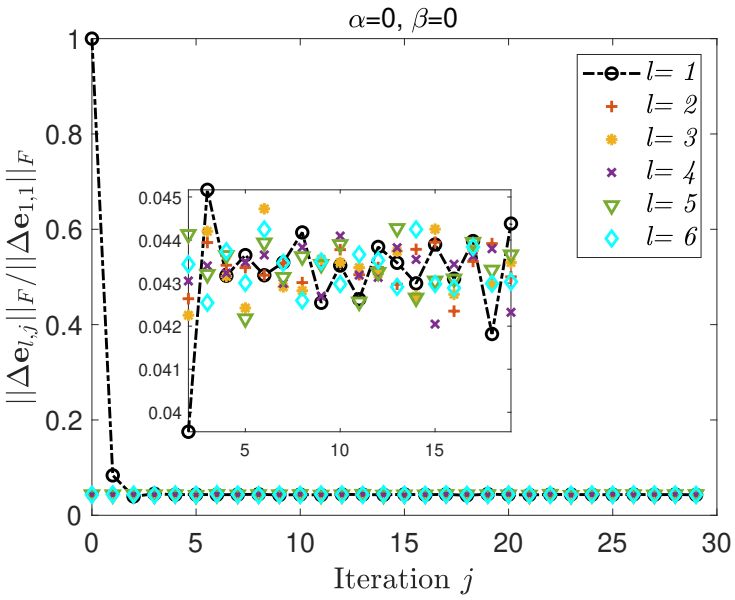


(a)

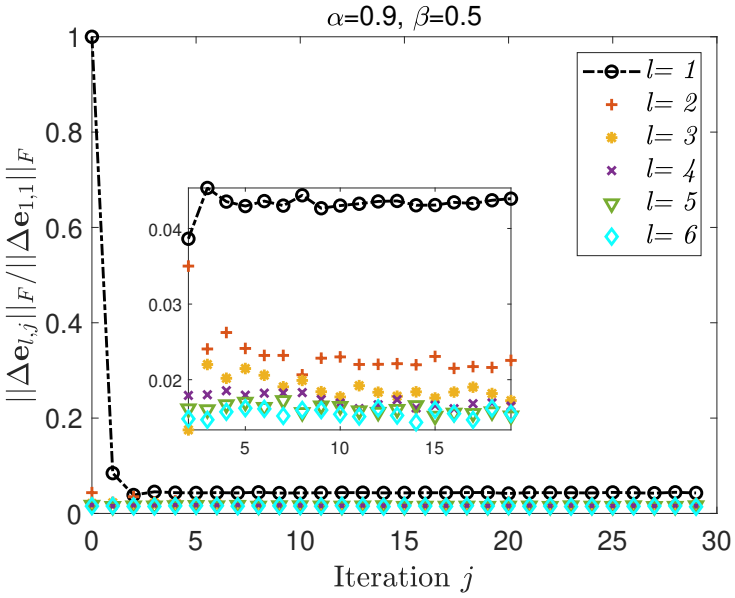


(b)

Figure 5.5: **Convergence of the Frobenius norm of the incremental error**: The LPV model in Section 3.5.2 is used to design the learning filters in Eq. (5.8). The control update time associated with Eq. (5.8) for updating the feedforward signal per iteration in simulation is 1.34 s. Iteration $j = 0$ refers to the first device. ($L = 6$, $q = 1$, $r = 0.01$, $s = 0.09$). a) FO-SILC design with $\alpha = 0$ and $\beta = 0$, which only has horizontal learning (iteration to iteration). No learning happens over layers. b) HO-SILC design with $\alpha = 0.9$ and $\beta = 0.5$. HO-SILC design, which integrates horizontal learning from device to device with vertical learning from previous layers. HO-ILC offers better performance over the layers compared to the FO-SILC.

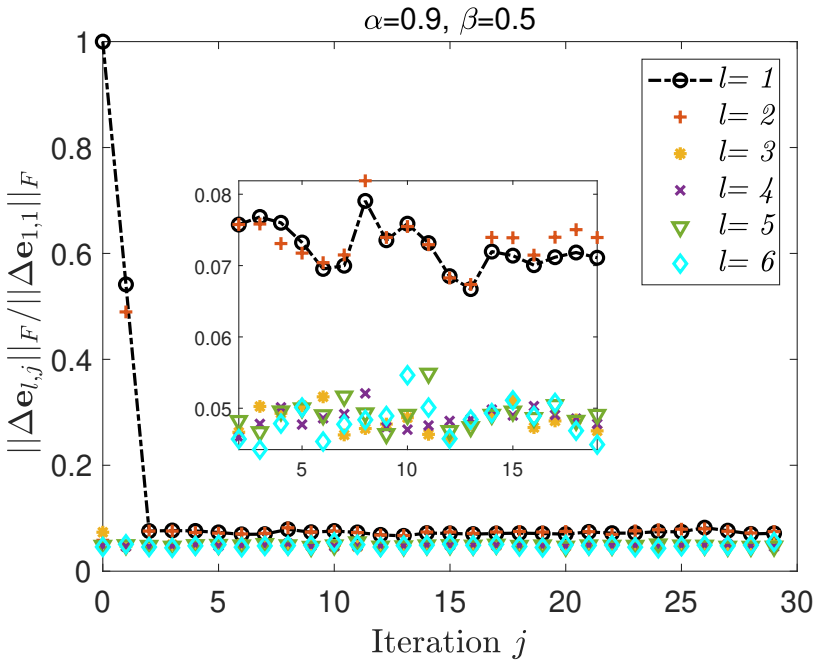


Figure 5.6: **Performance of the HO-SILC with the linearized CRNN model in Eq. (3.13):** Convergence of the Frobenius norm of the incremental error with HO-SILC design in Eq. (5.1) and Eq. (5.4), based on the linearized CRNN model in Eq. (3.13). The average control update time in simulation for updating the feedforward signal per iteration is 2.8 s.

bian matrix in Eq. (3.13) is approximately 3.5 hours, which is a one-time calculation that can be done before running the experiment. The results in Figure 5.6 show that, although the HO-SILC based on the linearized CRNN model considers surface tension effects, the controller performance is similar to the HO-SILC based on the LPV model. The reason is that unlike the inkjet printing process used in [3], the e-jet printing process modeled in this work uses high viscosity inks for which the droplets tend to stay at their deposited locations. The reduction in movement on the surface post printing reduces the surface tension and droplet coalescence-related effects and shows minimal effects on film-formation. Further, model uncertainties due to surface tension of the liquid droplets are often repetitive and thus would be learned through the implementation of the HO-SILC.

Therefore, it is recommended to use a more simple model such as LPV in Section 3.5.2 or the CLR model in Section 3.5.1, to design a robust HO-SILC controller based on the criteria in theorems 1 to 4 and Tables 5.1 to 5.3 that enable the fast DFT calculations in Eq. (5.8).

## 5.7 CONCLUSION

In this chapter, we present a higher-order spatial ILC (HO-SILC) framework for iteration varying uncertain AM systems. We consider iteration varying model uncertainties as interval uncertainties subjected to spatial invariant bounds. In order to leverage DFT based tools for computational efficiency, the iteration varying plant model is considered to be BCCB. An RMC criterion is formalized as a useful tool to predict the stability of the HO-SILC algorithm in the presence of iteration varying model uncertainties. Our analysis considers the RMC criterion as a measure of maximum allowable uncertainty around the nominal plant such that the iterative system remains stable. Simulation results using a model of an e-jet printing system demonstrate that HO-SILC can be successfully employed in AM processes to regulate the input of an iterative model and improve the heightmap reference tracking. We demonstrate that through proper tuning of the higher-order terms of the HO-SILC algorithm, an improved performance in terms of layer-to-layer and overall height errors can be achieved. The improvements performance are especially prevalent at higher layers, where the uncertainties from previous layer variations are more pronounced. Higher order, spatial learning control has applications outside of additive manufacturing systems. For example, any system that exhibits spatially dependent dynamics through a repetitive action (e.g. exoskeletons, robotic pick and place) could benefit from a control framework that compensates for errors across both a spatial and temporal domain. Importantly, spatial interactions are often disjointed temporally and are commonly ignored. The proposed framework addresses this issue by incorporating spatial information into the control law.

## Publications:

1. Afkhami, Zahra, David Hoelzle, and Kira Barton. "Higher-Order Spatial Iterative Learning Control for Additive Manufacturing." In 2021 60th IEEE Conference on Decision and Control (CDC), pp. 6547-6553. IEEE, 2021.

2. Afkhami, Zahra, David Hoelzle, and Kira Barton. "Robust Higher-Order Spatial Iterative Learning Control for Additive Manufacturing systems." IEEE Transactions on Control Systems Technology, 2022 (accepted).

# CHAPTER 6

# Synthesis of Model Predictive Control and Iterative Learning Control for Topography Regulation in Additive Manufacturing

In the previous chapter, we applied higher-order SILC (HO-SILC) to a model of an AM process. This higher-order controller leveraged data from previous devices and previous layers within the same device to construct an optimized input for the next layer of a 3D structure. We term this type of learning controller as backward learning. A drawback of this previously presented HO-SILC framework was that it was overly conservative for systems with minimal model uncertainty since the controller was designed to ensure robustness for the maximum amount of uncertainty, thus causing the system to lose performance advancements.

In addition to the layer to layer dynamics, it is important to consider process constraints within the AM system, such as the requirement of strictly positive control inputs, $f(x,y)$. Model predictive control (MPC) is a control framework that works especially well for constrained systems and incorporates a forward projection process that is useful for AM systems in which the current layers directly impact future layers. MPC has been already applied to AM process in [56] to control 1D height increment with varying reference. MPC exploits the system model to predict performance error signals for multiple steps (here, layers) in the future and consequently make informed control decisions that work to achieve performance gains across all of the layers. This approach is known as a receding horizon strategy in which a sequence of input signals for multiple steps (layers) in the future is planned, and yet only the next control action is applied. The sequence of control inputs will be recomputed once new information is available. In addition, to achieve a less restrictive bound on the prediction horizon, researchers have introduced the implementation of a finite-tail MPC formulation that solves a constrained optimal control problem based on prediction and optimization. Although closed-loop stability is not generally guaranteed

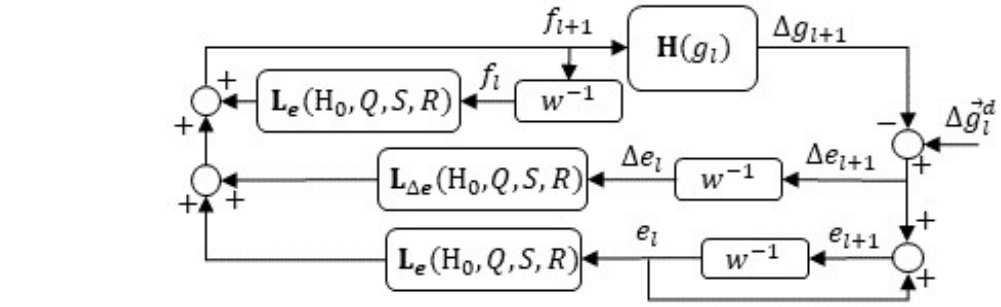


(a)

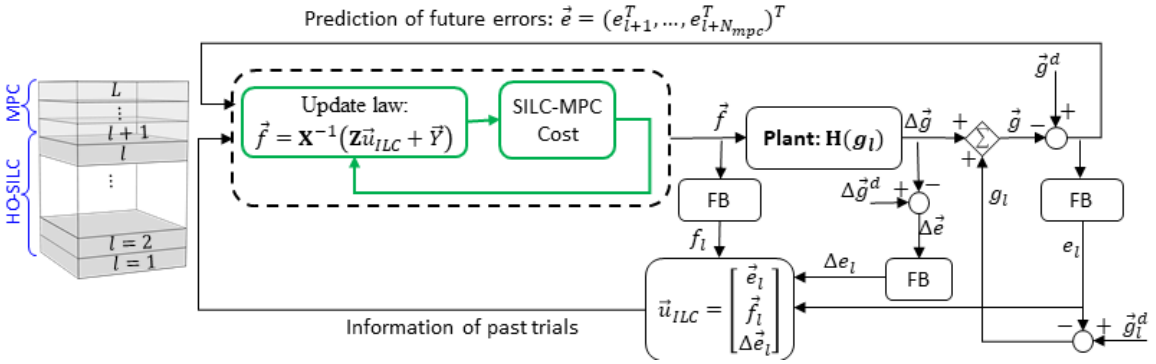


(b)

Figure 6.1: **SILC and SILC-MPC Block diagram comparison**. Learning occurs in the vertical direction. a) SILC framework: SILC utilizes the knowledge from previous layers to predict the optimized input of the next layer. The knowledge here refers to the input signal, $f_l$, layer (or incremental) error, $\Delta e_l$, and total error, $e_l$ at layer $l$, which is the sum of the incremental errors over all layers, $e_l = \sum_{i=1}^{l} \Delta e_i$. b) SILC-MPC framework: Learning occurs from previous layers using SILC design, as well as a prediction of future layer depositions using MPC design, by incorporating a prediction of future layer errors, $e_{l+n}$, to predict the input signal of multiple layers ahead, $\vec{f} = (f_{l+1}, \ldots, f_{l+N_{mpc}})$. At each printing pass, only the input signal of the first layer, $f_{l+1}$, is considered. Here, each layer is one iteration and $w^{-1}$ is the trial-delay operator. $\vec{e} = (\vec{e}_{l+1}^T, \ldots, \vec{e}_{l+N_{mpc}}^T)$, $\vec{g} = (\vec{g}_{l+1}^T, \ldots, \vec{g}_{l+N_{mpc}}^T)$, $\Delta\vec{e} = (\Delta\vec{e}_{l+1}^T, \ldots, \Delta\vec{e}_{l+N_{mpc}}^T)$, and $\Delta\vec{g} = (\Delta\vec{g}_{l+1}^T, \ldots, \Delta\vec{g}_{l+N_{mpc}}^T)$. The FB operator takes a stacked vector, (for example $\vec{e}$), extracts its first block, $\vec{e}_{l+1}$, and applies the shift-delay operator to extract $\vec{e}_l$.

with an MPC framework, adding a final/terminal cost can improve the stability properties through improvements in convergence speed and tracking error. Stochastic and adaptive MPC provide alternative techniques that have been used to achieve these desirable properties ( [87, 88]).

Based on the forward looking framework, the work presented in this chapter investigates whether the integration of SILC with MPC into a combined learning control framework will result in a layer-to-layer process that is more robust to model uncertainty compared to traditional SILC, and yet maintains the high performance advancements expected from these control architectures. We implement an SILC-MPC method that leverages the information from previous layers using spatial iterative learning control (SILC) and projects forward the data from future layers using model predictive control (MPC) to improve the tracking performance of iteration varying AM processes. Note that in the multi-layer structures considered in this work, the layers are built on top of each other, such that the printing behavior for a current layer depends directly on the topography of the previous layers. The goal of this work is to derive an integrated control framework that leverages the information from previous layers using HO-SILC, plus a prediction from future layers using MPC (see Figure 6.1b), to minimize the total error and individual layer errors within an AM process simultaneously, while achieving uniform thin-film fabrication with minimal surface roughness. The novel contributions of this work include:

- Derivation of a higher-order SILC framework for minimizing layer and total errors simultaneously (Figure 6.1a) to more effectively fabricate 3D structures in a layer-by-layer fashion.
- Development of a combined spatial ILC and terminal cost MPC framework that incorporates backward learning through SILC with forward learning using MPC to improve the performance of AM processes.
- Demonstration and analysis of the performance advancements achieved through the implementation of the combined learning control framework on a simulated model of a high-resolution printing process for the fabrication of 3D constructs.

## 6.1 Controller Formulation

In chapters 4 and 5, we used a backward learning method through an SILC design similar to Figure 6.1a that leveraged the data from previous iterations to construct the optimized input. From a manufacturing perspective, our goal was to develop a control framework that

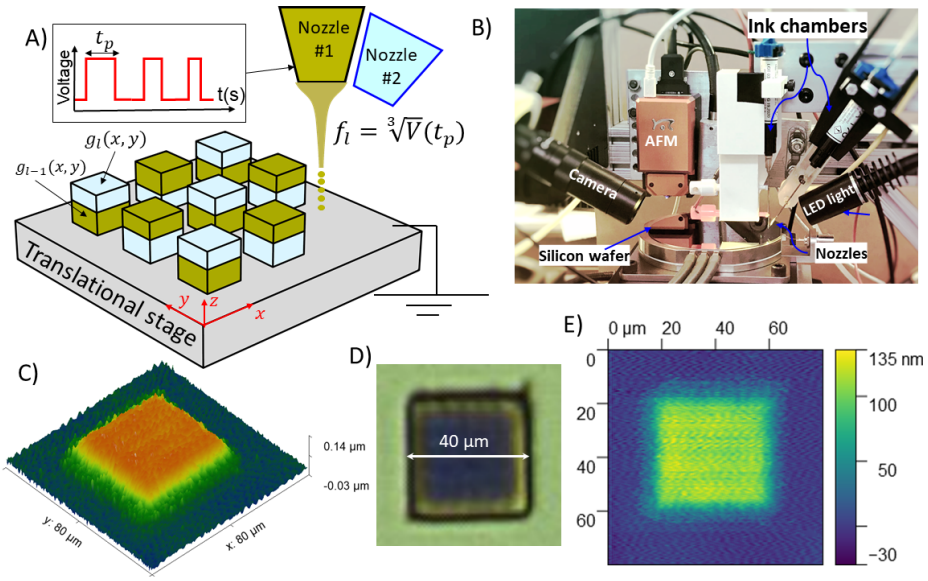


Figure 6.2: **High-resolution fabrication using e-jet printing technology**. A) schematic of an e-jet printer with dual nozzles. B) e-jet Printer testbed located at the University of Michigan. C), D) and E) AFM scans and optical microscopy of a $40 \times 40$ $\mu m^2$ thin-film pattern deposited by the e-jet system in Figure 6.2B.

regulates the deposition process to realize a vertically stacked multi-layer/multi-material structure with consistent layer thickness, which is a highly desirable characteristic in many sensory applications, such as optical sensors where uniformity and periodicity of the layers are of great importance [79, 89]. In these examples, the norm optimal SILC (NO-SILC) cost function was defined based on the layer errors, $\Delta\vec{e}_l$. The proposed SILC resulted in consistent layer deposition with $\Delta\vec{e}_l$ converging from layer-to-layer, resulting in uniform layers. However, SILC did not weight the total build error $\vec{e}_l$, resulting in the total error increasing over the layers. In AM structures, the layer errors add up during the build and may result in a large deviation from the desired height, especially when the layer number is large. Therefore, if the printing objective requires total device dimension convergence as well as layer-by-layer convergence, minimizing the layer errors alone may not be sufficient. To address this need, the work in this chapter investigates a modified backward learning controller that incorporates individual layer as well as total device errors combined with a forward learning approach that uses MPC to achieve a projection in the printing process to enhance the control decisions. The combined control architecture can be found in Figure 6.1.

### 6.1.1 SILC Framework

Similar to previous chapters, we use a norm-optimal SILC (NO-SILC) framework to design robust learning filters. Assuming a constant desired height for all layers, we modify our previous cost function in chapter 5 to minimize the total error and layer error simultaneously. In addition to the incremental values in Eqs. (3.3) and (4.4), the total height and total error are as follows,

$$\vec{g}_l = \sum_{i=1}^{l} \Delta\vec{g}_i = \sum_{i=1}^{l} \mathbf{H}(g_{i-1})\vec{f}_i \tag{6.1a}$$

$$\vec{e}_l \triangleq \vec{g}_l^d - \vec{g}_l = \sum_{i=1}^{l} \Delta\vec{e}_i \tag{6.1b}$$

$$\vec{g}_l^d = \sum_{i=1}^{l} \Delta\vec{g}_i^d, \tag{6.1c}$$

where $\Delta\vec{g}_l^d$ and $\vec{g}_l^d$ are the desired incremental and total build height maps at layer $l$. The following cost function is proposed

$$\mathcal{J}^{ILC} = \Delta\vec{e}_{l+1}^T\mathbf{Q}_{\Delta e}\Delta\vec{e}_{l+1} + \vec{e}_{l+1}^T\mathbf{Q}_1\vec{e}_{l+1} + \vec{f}_{l+1}^T\mathbf{S}_1\vec{f}_{l+1} + (\vec{f}_{l+1} - \vec{f}_l)^{\mathrm{T}}\mathbf{R}_1(\vec{f}_{l+1} - \vec{f}_l), \tag{6.2}$$

where $\mathbf{Q}_{\Delta e}, \mathbf{Q}_1, \mathbf{S}_1, \mathbf{R}_1$ are weighting matrices used to weight the layer errors, total errors, control inputs and change in control inputs. These matrices are generally defined as identity matrices scaled by non-negative scalars such that $\mathbf{Q}_{\Delta e} = q_{\Delta e}\mathbf{I}$, $\mathbf{Q}_1 = q_1\mathbf{I}$, $\mathbf{S}_1 = s_1\mathbf{I}$, $\mathbf{R}_1 = r_1\mathbf{I}$. The optimal feedforward signal is achieved by solving the following optimization problem,

$$\begin{aligned}\frac{\partial\mathcal{J}^{ILC}}{\partial\vec{f}_{l+1}} &= -\mathbf{H}_l^{\mathrm{T}}\mathbf{Q}_1(\vec{e}_l + \Delta\vec{e}_l + \mathbf{H}_{l-1}\vec{f}_l - \mathbf{H}_l\vec{f}_{l+1}) + \mathbf{S}_1\vec{f}_{l+1} \\ &\quad + \mathbf{R}_1(\vec{f}_{l+1} - \vec{f}_l) - \mathbf{H}_l^{\mathrm{T}}\mathbf{Q}_{\Delta e}(\Delta\vec{e}_l + \mathbf{H}_{l-1}\vec{f}_l - \mathbf{H}_l\vec{f}_{l+1}) = 0.\end{aligned} \tag{6.3}$$

Solving for the updated control signal, the SILC update law and learning filters can be shown to simplify to:

$$\vec{f}_{l+1} = \mathbf{L}_f\vec{f}_l + \mathbf{L}_e\vec{e}_l + \mathbf{L}_{\Delta e}\Delta\vec{e}_l \tag{6.4a}$$

$$\boldsymbol{f}_{l+1}(u,v) = (\mathbf{L}_f \circ \boldsymbol{f}_l + \mathbf{L}_e \circ \boldsymbol{e}_l + \mathbf{L}_{\Delta e} \circ \Delta\boldsymbol{e}_l)(u,v) \tag{6.4b}$$

Assuming $\mathbf{H}$ can be written as block circulant with circulant blocks (BCCB) ( [40]), (Eq. (6.4b)) is the equivalent frequency-domain representation of (Eq. (6.4a)). BCCB ma-

trices are defined in more detail in [40].

Similar to previous chapter, the control update, $f_{l+1}(u,v)$, is the 2D discrete Fourier transform (DFT) representation of $f_{l+1}(x,y)$. Note that the update law in Eq. (6.4) is higher order because the total error in a multi-layer structure is a function of the incremental errors from all previous layers, $\vec{e}_l = \sum_{i=1}^{l} \Delta\vec{e}_i$. Importantly, if one wanted to design an iteration invariant controller, the learning filters must be based on the nominal plant $\mathbf{H}_0$ from (Eq. (6.3)) as demonstrated below:

$$\boldsymbol{L}_f(u,v) = \frac{(q_1 + q_{\Delta e})\boldsymbol{H}_0^* \circ \boldsymbol{H}_0 + r_1}{(q_1 + q_{\Delta e})\boldsymbol{H}_0^* \circ \boldsymbol{H}_0 + (s_1 + r_1)}(u,v) \tag{6.5a}$$

$$\boldsymbol{L}_e(u,v) = \frac{q_1 H_0^*}{(q_1 + q_{\Delta e})\boldsymbol{H}_0^* \circ \boldsymbol{H}_0 + (s_1 + r_1)}(u,v) \tag{6.5b}$$

$$\boldsymbol{L}_{\Delta e}(u,v) = \frac{(q_1 + q_{\Delta e})\boldsymbol{H}_0^*}{(q_1 + q_{\Delta e})\boldsymbol{H}_0^* \circ H_0 + (s_1 + r_1)}(u,v) \tag{6.5c}$$

### 6.1.2 Modified SILC-MPC Framework

In this section, we extend the higher-order SILC framework in Section 6.1.1 to an SILC-MPC framework that leverages the information from previous layers, as well as a prediction of future layers to determine an optimized feedforward input signal.The quadratic cost function for the combined controller is defined as,

$$\mathcal{J} = \mathcal{J}^{ILC} + \mathcal{J}^{MPC} = \vec{e}^{\mathrm{T}}\mathbf{Q}\vec{e} + \vec{f}^{\mathrm{T}}\mathbf{S}\vec{f} + \Delta\vec{f}^{\mathrm{T}}\mathbf{R}\Delta\vec{f} \tag{6.6a}$$

$$\mathcal{J}^{MPC} = \mathcal{J}_t + \sum_{j=2}^{\mathrm{N}_{mpc}} \mathcal{J}_{l+j} \tag{6.6b}$$

$$\mathcal{J}_{l+j} = \vec{e}_{l+j}^{T}\mathbf{Q}_j\vec{e}_{l+j} + (\vec{f}_{l+j} - \vec{f}_{l+j-1})^{\mathrm{T}}\mathbf{R}_j(\vec{f}_{l+j} - \vec{f}_{l+j-1}) + \vec{f}_{l+j}^{\mathrm{T}}\mathbf{S}_j\vec{f}_{l+j}, \tag{6.6c}$$

where $\mathbf{Q}_j, \mathbf{S}_j, \mathbf{R}_j$ are weighting matrices that are defined as $\mathbf{Q}_j = q_j\mathbf{I}$, $\mathbf{S}_j = s_j\mathbf{I}$, and $\mathbf{R}_i = r_j\mathbf{I}$, and $q_j, s_j,$ and $r_i$ are positive scalars. $\mathrm{N}_{mpc}$ denotes the MPC horizon. The other components in Eq. (6.6) are defined as:

$$\mathbf{Q} = \begin{bmatrix} \mathbf{Q}_{\Delta e} & \dots & 0 \\ 0 & \mathbf{Q}_1 & \vdots \\ \vdots & \ddots & 0 \\ 0 & \dots & \mathbf{Q}_{\mathrm{N}_{mpc}} + \mathrm{P}_N\mathbf{I} \end{bmatrix}, \quad \mathbf{S} = \begin{bmatrix} \mathbf{S}_1 & \dots & 0 \\ \vdots & \ddots & \vdots \\ 0 & \dots & \mathbf{S}_{\mathrm{N}_{mpc}} \end{bmatrix}, \quad \mathbf{R} = \begin{bmatrix} \mathbf{R}_1 & \dots & 0 \\ \vdots & \ddots & \vdots \\ 0 & \dots & \mathbf{R}_{\mathrm{N}_{mpc}} \end{bmatrix}, \tag{6.7a}$$

$$\vec{f} = \begin{bmatrix} \vec{f}_{l+1} \\ \vec{f}_{l+2} \\ \vdots \\ \vec{f}_{l+\mathrm{N}_{mpc}} \end{bmatrix}, \quad \Delta\vec{f} = \begin{bmatrix} \vec{f}_{l+1} - \vec{f}_{l} \\ \vec{f}_{l+2} - \vec{f}_{l+1} \\ \vdots \\ \vec{f}_{l+\mathrm{N}_{mpc}} - \vec{f}_{l+\mathrm{N}_{mpc}-1} \end{bmatrix}, \quad \vec{e} = \begin{bmatrix} \Delta\vec{e}_{l+1} \\ \vec{e}_{l+1} \\ \vec{e}_{l+2} \\ \vdots \\ \vec{e}_{l+\mathrm{N}_{mpc}} \end{bmatrix}. \tag{6.7b}$$

The MPC cost function in Eq. (6.6b) contains two elements. The first element is the terminal cost, denoted by $\mathcal{J}_t$, that improves closed-loop stability of the MPC algorithm ( [51, 52]). The second term is a projection forward in the layer direction that aims to minimize the total error in future layers by predicting the system behavior in future layers and using it to determine the control input for the next layer. We define the terminal cost as $\mathcal{J}_t \triangleq \vec{e}^{T}_{l+\mathrm{N}_{mpc}}(\mathrm{P_N}\mathbf{I})\vec{e}_{l+\mathrm{N}_{mpc}}$, where $\mathrm{P_N}$ is a positive scalar. The MPC cost function starts from $j = 2$, since $j = 1$ is already taken into account in the HO-SILC algorithm provided in Eq. (6.2). We aim to use the available data from previous printed layers, to minimize both the total and layer errors in order to achieve consistent layer deposition at all layers. Let $\vec{u}_{ILC}$ denote a vector that contains the information from previous layers, such that $\vec{u}_{ILC} = [\vec{e}_l^{\mathrm{T}}, \vec{f}_l^{\mathrm{T}}, \Delta\vec{e}_l^{\mathrm{T}}]^{\mathrm{T}}$. To find the optimal control sequence $\vec{f}^{*}$, the cost function in Eq. (6.6) is differentiated with respect to $\vec{f}$ and equated to zero.

$$\nabla_{\vec{f}}\mathcal{J} = [\frac{\partial\mathcal{J}^{\mathrm{T}}}{\partial\vec{f}_{l+1}}, ..., \frac{\partial\mathcal{J}^{\mathrm{T}}}{\partial\vec{f}_{l+\mathrm{N}_{mpc}}}]^{\mathrm{T}} = \mathbf{X}\,\vec{f} + \mathbf{Z}\,\vec{u}_{ILC} + \vec{y}, \tag{6.8}$$

with $\mathbf{X} \in \mathbb{R}^{n\mathrm{N}_{mpc} \times n\mathrm{N}_{mpc}}$, $\mathbf{Z} \in \mathbb{R}^{n\mathrm{N}_{mpc} \times 3n}$, and $\vec{y} \in \mathbb{R}^{n\mathrm{N}_{mpc} \times 1}$. An analytical expression for $\mathbf{X}$, $\mathbf{Z}$ and $\vec{y}$ can be achieved by deriving the partial derivatives given in Eq. (6.8) using the cost function given in Eq. (6.6). From these derivations, we can determine that the structure of $\mathbf{X}$, $\mathbf{Z}$ and $\vec{y}$ have the following relationships:

$$\begin{aligned} X_{[i,i]} &= \mathbf{H}_0^{\mathrm{T}}\left(\mathrm{P_N}\,\mathbf{I} + \mathbf{Q}_{\Delta e}\Delta(i,1) + \sum_{n=i}^{\mathrm{N}_{mpc}} \mathbf{Q}_n\right)\mathbf{H}_0 + (\mathbf{R}_i + \mathbf{S}_i + \mathbf{R}_{i+1}), \\ X_{[i,j]} &= -\mathbf{H}_0^{\mathrm{T}}(\mathrm{P_N}\,\mathbf{I} + \sum_{n=k}^{\mathrm{N}_{mpc}} \mathbf{Q}_n)\mathbf{H}_0 - \mathbf{R}_k, \qquad j = i+1 \; or \; j = i-1 \\ X_{[i,j]} &= -\mathbf{H}_0^{\mathrm{T}}(\mathrm{P_N}\mathbf{I} + \sum_{n=k}^{\mathrm{N}_{mpc}} \mathbf{Q}_n)\mathbf{H}_0, \qquad\qquad j < i-1 \; or \; j > i+1 \end{aligned} \tag{6.9}$$

where $k = \max(i, j)$ and $\Delta(i, 1) = 1$ if $i = 1$ and is zero otherwise. Similarly $\mathbf{Z}$ has the following format

$$
\begin{aligned}
Z_{[i,1]} &= -\mathbf{H}_0^{\mathrm{T}}(\mathrm{P_N}\,\mathbf{I} + \sum_{n=i}^{\mathrm{N}_{mpc}} \mathbf{Q}_j) \\
Z_{[1,2]} &= -\mathbf{H}_0^{\mathrm{T}}(\mathbf{Q}_1 + \mathbf{Q}_{\Delta e})\mathbf{H}_0 - \mathbf{R}_1 \\
Z_{[1,3]} &= -\mathbf{H}_0^{\mathrm{T}}(\mathbf{Q}_1 + \mathbf{Q}_{\Delta e}) \\
Z_{[i,2]} &= Z_{i,3} = \mathbf{0} \quad i > 1
\end{aligned}
\tag{6.10}
$$

Likewise $\vec{y}$ has the following format:

$$
\begin{aligned}
\vec{y}(1) &= -\mathbf{H}_0^{\mathrm{T}}\left(\mathrm{N}_{mpc}\mathrm{P_N}\,\mathbf{I} + \mathbf{Q}_{\Delta e} + \sum_{n=2}^{\mathrm{N}_{mpc}} (n\mathbf{Q}_n)\right)\vec{r} \\
\vec{y}(i) &= -\mathbf{H}_0^{\mathrm{T}}(\mathrm{N}_{mpc}\mathrm{P_N}\,\mathbf{I} + \sum_{n=i}^{\mathrm{N}_{mpc}} (n\mathbf{Q}_n))\vec{r}, \quad i > 1
\end{aligned}
\tag{6.11}
$$

Assuming $\mathbf{X}$ is invertible, the optimal control input $\vec{f}^*$ is then obtained by solving $\mathbf{X}\,\vec{f}^* + \mathbf{Z}\,\vec{u}_{ILC} + \vec{y} = \vec{0}$ as:

$$
\vec{f}^* = -\mathbf{X}^{-1}(\mathbf{Z}\,\vec{u}_{ILC} + \vec{y}). \tag{6.12}
$$

We only implement the first block of $\vec{f}^*$, which is related to the control input $\vec{f}^*_{l+1}$ of the next layer. The derivation of Eq. (6.9)-Eq. (6.11) is shown in the appendix. Note that although $\mathbf{X}$ is symmetric, and each block matrix of $\mathbf{X}$ and $\mathbf{Z}$ is BCCB, the overall $\mathbf{X}$ and $\mathbf{Z}$ matrices are not BCCB; thus, we have to invert a high dimensional matrix, $\mathbf{X}$, to calculate the optimal solution $\vec{f}^*$. It is important to note that this calculation for the SILC-MCP controller will be computationally more expensive than the update law required for SILC in Eq. (6.4) and Eq. (6.5). Care must be taken to determine when this approach is necessary and the computation burden is acceptable for the given system requirements. Future work will investigate methods to reformulate the SILC-MPC update law in a way that the DFT computations are possible and will result in a reduced computational burden. In addition, future work will focus on the relationship between the invertibility condition of the X matrix and stability and convergence of the SILC-MPC algorithm.

## 6.2 Simulation Validation

In this section, simulation results for the system described in Section 3.4 controlled by the SILC-MPC and modified-SILC frameworks are presented. As described in Figure 6.1b, the SILC-MPC controller uses the information from previous layer depositions ($\vec{f}_l$, $\vec{e}_l$, and $\Delta\vec{e}_l$)

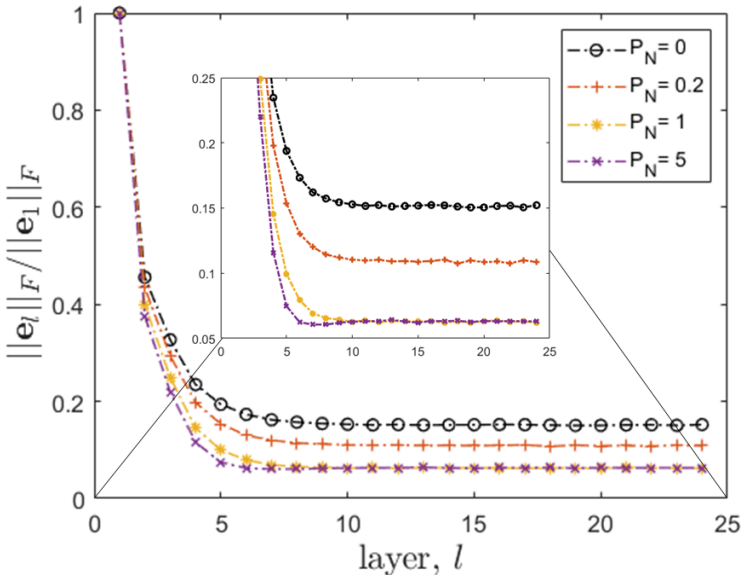


(a)

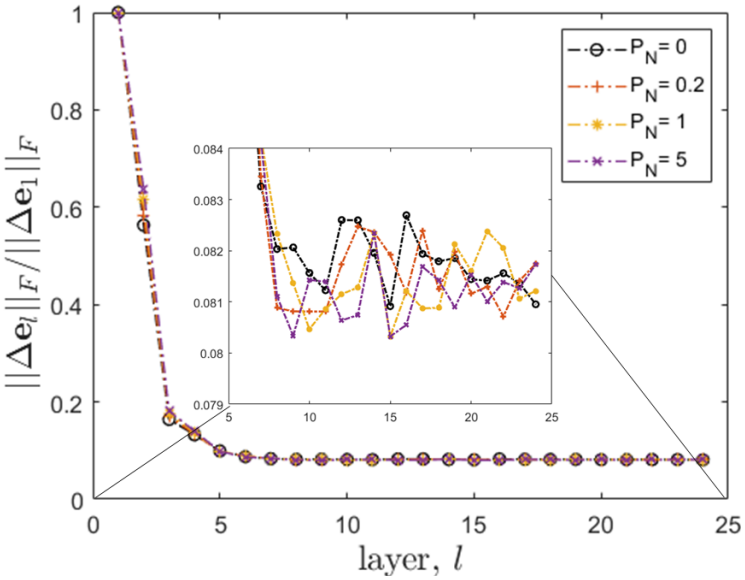


(b)

Figure 6.3: **Effect of terminal cost on convergence properties of SILC-MPC with $\mathbf{N}_{mpc} = 2$.** Adding a terminal cost in Eq. (6.6b) improves the SILC-MPC performance for total error with minimal impact on layer error. a) Normalized total error: higher vales of $P_\mathrm{N}$ lead to decreases in total error. b) Normalized layer error: varying values of $P_\mathrm{N}$ appear to have no effect on the incremental error. Note that terminal cost is only imposed on the total error in Eq. (6.6b)

Table 1: SILC and SILC-MPC parameters and simulation time

| | | $\vec{q}$ | $\vec{s}$ | $\vec{r}$ | $P_N$ | $N_{mpc}$ | time per layer (s) |
|---|---|---|---|---|---|---|---|
| SILC | test 1 | $\frac{1}{\sqrt{26}}\begin{bmatrix}1\\5\end{bmatrix}$ | 0.03 | 0.01 | – | – | 1.22 |
| | test 2 | $\frac{1}{\sqrt{2}}\begin{bmatrix}1\\1\end{bmatrix}$ | 0.03 | 0.01 | – | – | 1.22 |
| | test 3 | $\frac{1}{\sqrt{26}}\begin{bmatrix}5\\1\end{bmatrix}$ | 0.03 | 0.01 | – | – | 1.22 |
| SILC-MPC | test 4 | $\frac{1}{\sqrt{3}}\begin{bmatrix}1\\1\\1\end{bmatrix}$ | $\frac{0.03}{\sqrt{2}}\begin{bmatrix}1\\1\end{bmatrix}$ | $\frac{0.01}{\sqrt{2}}\begin{bmatrix}1\\1\end{bmatrix}$ | 1 | 2 | 2.59 |
| | test 5 | $\frac{1}{\sqrt{3}}\begin{bmatrix}1\\1\\1\end{bmatrix}$ | $\frac{0.03}{\sqrt{2}}\begin{bmatrix}1\\1\end{bmatrix}$ | $\frac{0.01}{\sqrt{2}}\begin{bmatrix}1\\1\end{bmatrix}$ | 0 | 2 | 2.59 |
| | test 6 | $\frac{1}{\sqrt{6}}\begin{bmatrix}1\\1\\1\\1\\1\\1\end{bmatrix}$ | $\frac{0.03}{\sqrt{5}}\begin{bmatrix}1\\1\\1\\1\\1\end{bmatrix}$ | $\frac{0.01}{\sqrt{5}}\begin{bmatrix}1\\1\\1\\1\\1\end{bmatrix}$ | 0 | 5 | 20.9 |

through an SILC design, and leverages a prediction of what will happen in future depositions ($\vec{e}_{l+2}$, ..., $\vec{e}_{N_{\text{mpc}}}$) through an MPC design, to estimate an optimized feedforward signal for future layer depositions, $\vec{f}_{l+1}$, ..., $\vec{f}_{l+N_{mpc}}$. However, at each printing pass, we only implement the current layer input signal $\vec{f}_{l+1}$, recalculating the feedforward signals each layer. A multi-layer structure similar to Figure 6.2 with 100$\mu$m ×100$\mu$m spatial resolution, 150 nm layer thickness resolution, and 25 layers is considered. For the first iteration, $l = 1$, we use a nonzero input signal such that the first layer thickness was around $130 \pm 22$ nm, which is computed based on knowledge of conventional pre-prints.

Method M3 in Section 3.5.2 is used to estimate the impulse response for the learning filters in Eqs. (6.5) and (6.9) to (6.11), that results in a BCCB plant matrix. The simulation environment approximates the true model using the M2 method in Section 3.5.2 for a given layer. To better represent the printing environment, a normally distributed iteration-varying white noise signal, $\Delta h_l$, is added to the plant model, with a mean and variance of 0.00 and 0.2, respectively. Repetitive model uncertainty is also added to represent unmodeled surface variations or initial tilts within the system and is represented by $\Delta h_{rep} = 0.1 * h_0$. Combining these features together, the iteration varying spatial impulse response used for

Eq. (3.2) will be $h_l = h(g_l) + \Delta h_l + \Delta h_{rep}$.

To design the weighting parameters for the SILC-MPC cost function in Eq. (6.6), we define the following vectors, $\vec{q} = [q_{\Delta e}, q_1, ..., q_{\mathrm{N}_{mpc}}]^T, \vec{s} = [s_1, ..., s_{\mathrm{N}_{mpc}}]^T, \vec{r} = [r_1, ..., r_{\mathrm{N}_{mpc}}]^T$. The weighting coefficients for the two frameworks are presented in test1-test3 and test4-test6 of Table 1, respectively. The weighting parameters are designed to be equally weighted such that $\|\vec{q}\| = 1, \|\vec{s}\| = 0.03, \|\vec{r}\| = 0.01$, which are the same weighting parameters that we used in our prior work [4].

Figure 6.3 shows the effect of terminal cost in Eq. (6.6) , $\mathcal{J}_t \triangleq \vec{e}^T_{l+\mathrm{N}_{mpc}}(\mathrm{P_N}\mathbf{I})\vec{e}_{l+\mathrm{N}_{mpc}}$, on the SILC-MPC performance. As demonstrated in MPC literature ( [53, 54, 90]), adding a terminal cost improves the convergence and stability properties of the SILC-MPC algorithm with respect to total error and can regulate both layer and total errors at the same time. Next, we set $\mathrm{P_N} = 1$ and investigate the effect of mpc horizon on the controller performance.

The performance of the SILC and SILC-MPC controllers is compared in Figure 6.4 and Table 1. Tests 1-3 are related to the SILC framework with $\vec{q} = [q_{\Delta e}, q_1 = q_e]^T, \vec{s} = [0.03], \vec{r} = [0.01]$, while tests 4-6 are related to the SILC-MPC framework. The simulation results imply that there is a trade-off between performance and computation time of the SILC-MPC controller. The SILC-MPC framework generally has lower total error and surface roughness compared to the SILC controller and can regulate both layer and total error at the same time. However, the SILC-MPC framework is computationally more expensive than the SILC controller. Based on the information in the last column of Table 1, the simulation time for updating the feedforward signal per layer for the SILC controller is 50% lower as compared to the SILC-MPC controller with a terminal cost. Comparing tests 5 and 6, it is observed that although higher values of the receding horizon, $N_{mpc}$, enhance the SILC-MPC performance, the update-law takes more time to update the input signal. The reasons for these differences are that 1) matrices $\mathbf{X}$, $\mathbf{Z}$ and $\vec{y}$ are high dimensional compared to the SILC learning filters $\mathbf{L}_f$, and $\mathbf{L}_e$, 2) the structure of $\mathbf{H}_0$ allows for the use of fast DFT computations in Eq. (6.5) that do not require inverse matrix calculations, while in the SILC-MPC update law, $\vec{f}^* = -\mathbf{X}^{-1}(\mathbf{Z}\,\vec{u}_{ILC} + \vec{y})$, $\mathbf{X}$ is not BCCB and cannot use DFT calculations.

Similar to traditional MPC in [51,55,90,91], simulation results in Figure 6.4b show that as the MPC horizon increases, the performance of an SILC-MPC control law without the terminal cost (tests 5 and 6, $P_\mathrm{N} = 0$) approaches an SILC-MPC with terminal cost (test 4, $P_\mathrm{N} = 1$). This will be important especially in AM processes in which, high-dimensionality is problematic. Therefore; instead of high mpc horizons (test 6) that result in high dimensional matrices and consequently slower simulation time, it is beneficial to use a short horizon, $\mathrm{N}_{mpc} = 2$, with terminal cost (test 4). Comparing the simulation results in Fig-

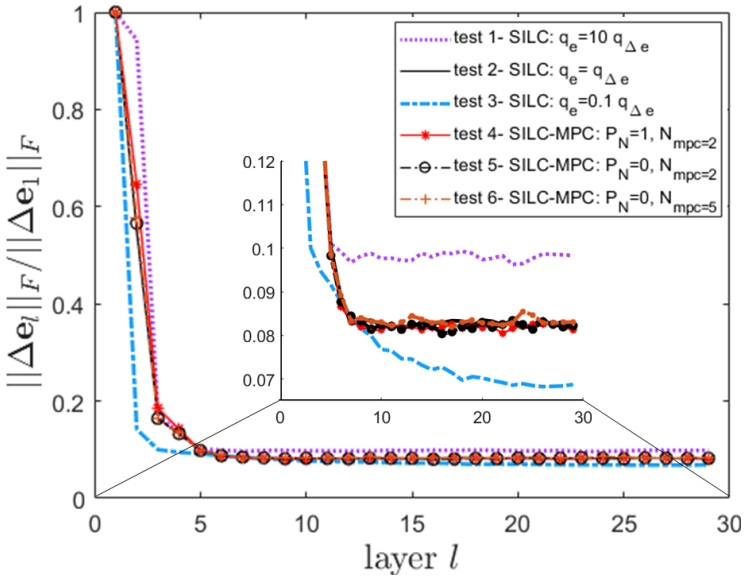


(a)

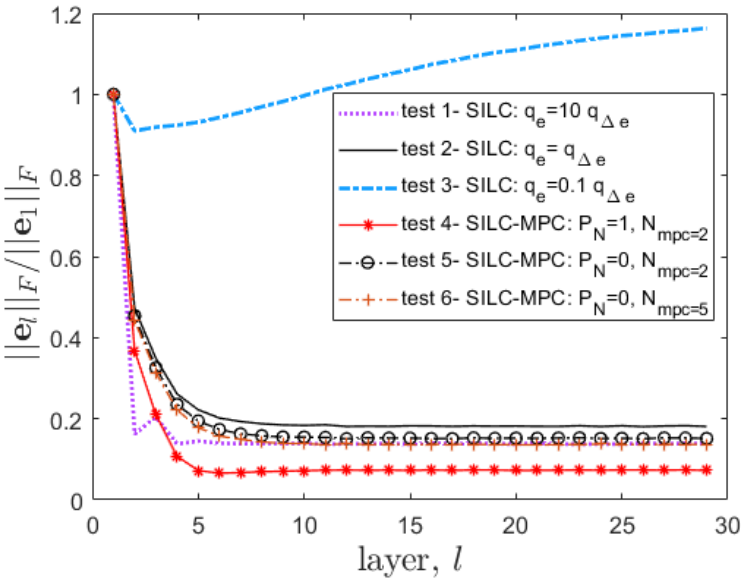


(b)

Figure 6.4: **SILC (tests 1-3) and SILC-MPC (tests 4-6) convergence comparison with** $\|\vec{q}\| = 1$**,** $\|\vec{r}\| = 0.01$**,** $\|\vec{s}\| = 0.03$. SILC-MPC with a terminal cost (test4) results in the lowest combined layer and total errors.a) Normalized layer error versus layer number: Test 3 with the largest $q_{\Delta e}$ gain (smallest $q_e$) (see Table 1) converges faster to a lower final value for layer error. If repeatable layer deposition is desirable, the SILC controller in test 3 is a good choice. b) Normalized total error versus layer index: similar to the results in [4], total error increases over the build if layer error is emphasized.

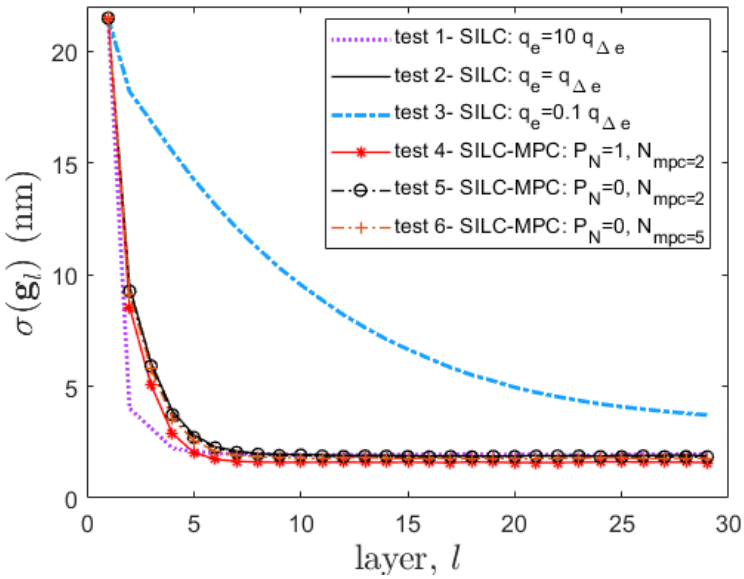


(a)

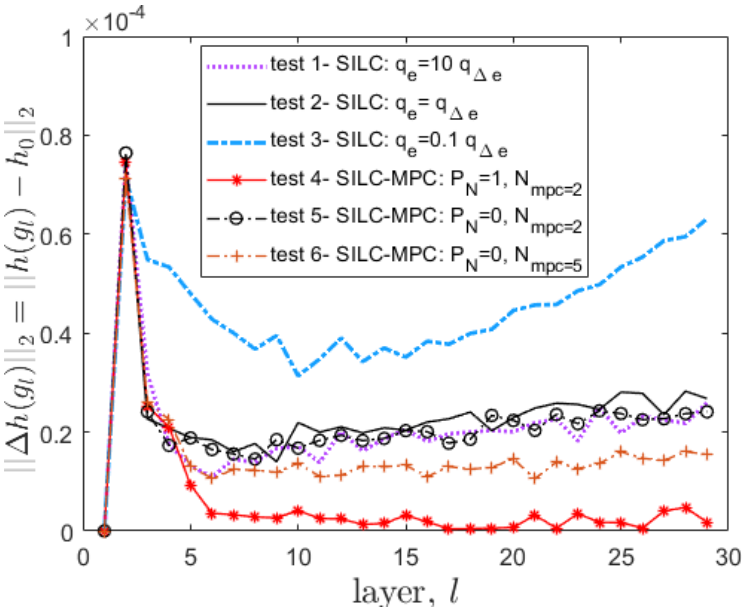


(b)

Figure 6.5: **SILC (tests 1-3) and SILC-MPC (tests 4-6) convergence comparison with $\|\vec{q}\| = 1$, $\|\vec{r}\| = 0.01$, $\|\vec{s}\| = 0.03$.** a) Surface roughness of total height versus layer index: roughness in Eq. (2.1b), which is an indication of layer flatness, decreases over the layers for all tests. Importantly, lower roughness values result in smaller deviations from the nominal plant $h_l(x,y) \rightarrow h_0$, which is confirmed in Figure 6.5b. b) Model uncertainty calculated by the difference between $h(g_l)$ and $h0$ (see Section 5.4.2) derived using the M3 method from [2] for NOA170 in [4].

ure 6.4a-Figure 6.5b, the SILC-MPC controller with a terminal cost formulation in test 4 provides a more robust and stable controller that results in decreases to the layer and total errors simultaneously, leading to highly uniform stacked thin-films with low surface roughness.

## 6.3 CONCLUSION

In this work, we present a novel spatial topography controller to enable enhanced deposition at the micro-scale. The framework combines spatial iterative learning control with model predictive control to achieve enhanced performance and robustness. The proposed controller is robust to stochastic and repetitive model uncertainty. Simulation results of an e-jet printed structure controlled by the SILC-MPC framework indicate that high-quality thin-films with uniform and repeatable thickness resolutions are achievable by tuning the MPC terminal cost and ILC parameters. The results imply that an SILC-MPC framework generally has better performance compared to a traditional SILC controller. However, the SILC update law is much faster (50%) compared to the SILC-MPC algorithm. Future work should consider non-negativity constraints in the input along with experimental validations. In addition, reformulation of the SILC-MPC update law in a way that DFT computations are possible to reduce the computation times is an interesting extension to explore.

# Appendix

In this section, we describe step by step derivation of the analytical solution of the SILC-MPC framework presented in equations (Eq. (6.9)-Eq. (6.11)). Solving Eq. (6.6) and Eq. (6.8) requires knowledge of future error signals, $\vec{e}_{l+j}$. Although we do not know these values, we can estimate them based on the values that are known from previous layer depositions,

$$\vec{e}_{l+j} = \vec{e}_l + \sum_{n=1}^{j} (\vec{\Delta e}_{l+n}) = \vec{e}_l + j\vec{r} - \sum_{n=1}^{j} \mathbf{H}_{l+n-1} \vec{f}_{l+n}. \tag{6.13}$$

For a single material deposition, we assume the desired height is constant for all layers such that $\Delta\vec{g}_l^d = \Delta\vec{g}_{l+n}^d = \vec{r}$. In addition, the plant spatial dynamics are noncausal in the spatial domain, meaning that the applied input at a given location will affect the output in the advanced layers and surrounding coordinates ( [33, 40]). This means that the error signals of future layers are functions of the input signal from prior layers, $\frac{\vec{e}_{l+j}}{\vec{f}_{l+i}} \neq 0, \forall i \leq j$. Note, the

error signals of previous layers are not function of future layer inputs, $\frac{\vec{e}_{l+j}}{\vec{f}_{l+i}} = 0, \forall i > j$. From Eq. (6.13) we have

$$\frac{\partial \vec{e}_{l+j}}{\partial \vec{f}_{l+i}} = \mathbf{0}, \quad j < i \tag{6.14a}$$

$$\frac{\partial \vec{e}_{l+j}}{\partial \vec{f}_{l+i}} = -\mathbf{H}_{l+i-1}, \quad j \geq i \tag{6.14b}$$

To determine $\mathbf{X}$, $\mathbf{Z}$ and $\vec{y}$ from Eq. (6.8), we need to calculate the partial derivative of the cost function in Eq. (6.6) with respect to the future layer input signals, $\frac{\partial \mathcal{J}}{\partial \vec{f}_{l+i}}$. For $i = 1$, the situation is different, $\frac{\partial \mathcal{J}}{\partial \vec{f}_{l+1}} = \frac{\partial \mathcal{J}^{mpc}}{\partial \vec{f}_{l+1}} + \frac{\partial \mathcal{J}^{ILC}}{\partial \vec{f}_{l+1}}$. We already calculated $\frac{\partial \mathcal{J}^{ILC}}{\partial \vec{f}_{l+1}}$ in (Eq. (6.3)), now we need to calculate $\frac{\partial \mathcal{J}^{mpc}}{\partial \vec{f}_{l+1}}$ as follows

$$\begin{aligned}\frac{\partial \mathcal{J}^{mpc}}{\partial \vec{f}_{l+1}} = &-\mathbf{H}_l^{\mathrm{T}} \sum_{n=2}^{\mathrm{N}_{mpc}} \mathrm{Q}_{\mathrm{n}}(\vec{e}_l + n\vec{r} - \sum_{k=1}^{\mathrm{N}_{mpc}} \mathbf{H}_{l+k-1}\vec{f}_{l+k}) - \\ &r_2(\vec{f}_{l+2} - \vec{f}_{l+1}) - \mathbf{H}_l^{\mathrm{T}} \mathrm{P}_{\mathrm{N}} (\vec{e}_l + \mathrm{N}_{mpc}\vec{r} - \sum_{k=1}^{\mathrm{N}_{mpc}} \mathbf{H}_{l+k-1}\vec{f}_{l+k}).\end{aligned} \tag{6.15}$$

For $i > 1$, $\frac{\partial \mathcal{J}}{\partial \vec{f}_{l+i}} = \frac{\partial \mathcal{J}^{mpc}}{\partial \vec{f}_{l+i}} = -\mathbf{H}_{l+i-1}^{\mathrm{T}} \mathrm{P}_{\mathrm{N}}(\vec{e}_l + \mathrm{N}_{mpc}\vec{r} - \sum_{n=1}^{\mathrm{N}_{mpc}} \mathbf{H}_{l+n-1}\vec{f}_{l+n}) + \sum_{j=2}^{\mathrm{N}_{mpc}} \frac{\partial \mathcal{J}_{l+j}}{\partial \vec{f}_{l+i}}$. Depending on the values of $i$ and $j$, $\frac{\partial \mathcal{J}_{l+j}}{\partial \vec{f}_{l+i}}$ is as follows

$$\begin{aligned}i = j: \; = &-q_j \mathbf{H}_{l+i-1}^{\mathrm{T}}(\vec{e}_l + j\vec{r} - \sum_{n=1}^{\mathrm{N}_{mpc}} \mathbf{H}_{l+n-1}\vec{f}_{l+n}) + s_j\vec{f}_{l+j} \\ &+ r_j(\vec{f}_{l+j} - \vec{f}_{l+j-1})\end{aligned} \tag{6.16a}$$

$$\begin{aligned}j = i+1: \; = &-q_j \mathbf{H}_{l+i-1}^{\mathrm{T}}(\vec{e}_l + j\vec{r} - \sum_{n=1}^{\mathrm{N}_{mpc}} \mathbf{H}_{l+n-1}\vec{f}_{l+n}) \\ &- r_j(\vec{f}_{l+j} - \vec{f}_{l+i})\end{aligned} \tag{6.16b}$$

$$j > i+1: \; = -q_j \mathbf{H}_{l+i-1}^{\mathrm{T}}(\vec{e}_l + j\vec{r} - \sum_{n=1}^{\mathrm{N}_{mpc}} \mathbf{H}_{l+n-1}\vec{f}_{l+n}). \tag{6.16c}$$

and zero for $i > j$. Summing up Eq. (6.16) over $j = 2, ..., \mathrm{N}_{mpc}$ and adding up the terminal cost components, and considering (Eq. (6.3)) and Eq. (6.15), $\mathbf{X}$, $\mathbf{Z}$ and $\vec{y}$ are calculated based on the nominal plant as presented in (Eq. (6.9)-Eq. (6.11)).

# CHAPTER 7

# Experimental Validations

In this chapter, we present the first experimental application of the SILC framework applied to systems with interval uncertainty described in chapters 3 to 5. The SILC model is based on a 2D-spatial impulse response presented in chapter 3, and is used with the proposed control framework to fabricate multi-layer structures using a custom electrohydrodynamic jet (e-jet) printing system, in which complex structures are deposited by direct addition of a build material on the surface in liquid form. Jet-based 3D printing processes are environmentally friendly, and facilitate multi-material fabrication on non-planar surfaces (compared to Lithography) due to the liquid form of the build material. The e-jet printer is a microscale AM-system, integrated with an in-situ microscale metrology system in the form of an atomic force microscope (AFM) for *in situ* quality monitoring. Throughout this chapter, we demonstrate that a spatial iterative learning controller is capable of automating the deposition process of an e-jet printer by learning through successive iterations, without requiring a human operator to heuristically tune the process parameters. A central computer and custom-written Python script is used to coordinate the e-jet printer with the integrated AFM. Although real-time measurements at the micro scale are not available, using our integrated metrology system, we are able to register spatial coordinates on the substrate and measure the topography in a run-to-run fashion. Additionally, through a series of automated processing techniques in the python code, we are able to automate a multi-layer deposition process with post-processing AFM scan analysis to be integrated with our SILC control framework for precision patterning at the microscale.

## 7.1 Experimental Setup

To experimentally validate the model-based controllers previously developed in chapters 4 and 5, the reference device structure is selected to be a flat layer height map, $\Delta g_l^d(x,y) = 150$ nm, and the number of the layers is considered L = 4. We use drop-on-demand printing to

deposit individual droplets of Loctite3526 on predefined locations on the substrate. Successive droplets are placed at a certain distance (center to center) from each other, defined as pitch, to form a film as presented previously in Figures 1.3 and 2.6b. The pitch size is set to 5 $\mu m$ for a domain of $11 \times 11$ pixels (121 droplets), which results in a spatial resolution of 55 $\mu$m $\times$ 55 $\mu$m as presented in Figure 7.3. The process parameters are chosen to be: nozzle size = 2 $\mu$m, standoff height = 40 $\mu$m, high voltage $V_h$ = 600 V, low voltage $V_l$ = 200 V. Each layer is printed in a single printing pass and cured successively. The input will be constrained (saturated $f(x,y) \geq 0$) to non-negative values to ensure an additive process. It is important to note that the input of the first iteration at the first layer is set to zero, $f_{1,1}(x,y) = \mathbf{0}$, implying that there is no prior knowledge of the appropriate input signal (here pulsewidth). This results in no material being deposited during the first iteration (see Figures 7.5 to 7.8).

***Process Variability***: As mentioned before, AM processes are innately iteration varying due to layer dynamics, as well as changes in system dynamics that can occur from time-to-time. Here we use the CLR model presented in Section 3.5.1 as the baseline model from which we estimate a nominal model that is used within the controllers in chapters 4 and 5. The input signal is pulsewidth, and the output is heightmap at each discrete spatial coordinate in the XY frame as presented in Figures 7.2 and 7.3. Process variability was attributed to slight variations in the process parameters such as nozzle size variations (inner diameter variation of 15%), standoff height offsets (substrate leveled across a 10 mm $\times$ 10 mm region), and room temperature fluctuations. Further, process instabilities were observed to introduce additional variability in the process dynamics. For example, during the deposition of Loctite3526, we noticed that clogging of a 2$\mu$m nozzle resulted in a 25 ms shift in the range of feasible pulsewidths for the input signal. More specifically, after printing for four hours, in order to achieve consistent behavior, we had to apply pulsewidths in the range of $40ms < t_p < 80ms$ instead of the $15ms < t_p < 55ms$ range used at the beginning of the experiment, which introduces a repetitive model uncertainty to the system.

***Model Uncertainty***: To quantify the maximum amount of model uncertainty observed during the deposition of Loctite3526, we conducted 45 system identification experiments (described in Section 3.5.1) over 15 days. To reduce the effects of clogging, we used a new 2$\mu$m nozzle each day. During each experiment, 10 devices are printed on a $7 \times 9$ spatial domain as explained in Section 3.5.1. We determine the impulse response ($h_f$) for each experiment, and calculate the maximum and minimum value of each element in $h_f$ across all 45 experiments. These values are used to estimate the upper and lower bounds on the impulse response such that $\underline{h} \preceq h_f \preceq \overline{h}$, where $\preceq$ is element wise inequality. The maximum uncertainty radius is then calculated using $\Delta h_r \triangleq \frac{\overline{h} - \underline{h}}{2}$, as described in [39] and chapter 5.

The plant matrix bounds and maximum uncertainty radius $\underline{\mathbf{H}}$, $\overline{\mathbf{H}}$, $\Delta\mathbf{H}_r$ are calculated from $\underline{h}$, $\overline{h}$, and $h_r$, respectively, using the BCCB construction method described in Section 3.2. We then apply the center matrix definition from [39] such that $h_c = \frac{\bar{h}+\underline{h}}{2}$ is used to calculate the nominal impulse response as follows:

$$h_c = \begin{bmatrix} 0.088 & 0.089 & 0.196 & 0.089 & 0.088 \\ 0.089 & 0.196 & 0.422 & 0.196 & 0.089 \\ 0.196 & 0.422 & 0.735 & 0.422 & 0.196 \\ 0.089 & 0.196 & 0.422 & 0.196 & 0.089 \\ 0.088 & 0.089 & 0.196 & 0.089 & 0.088 \end{bmatrix} (\frac{nm}{ms}) \tag{7.1}$$

Note that the center matrix in Eq. (7.1) is very close to the impulse response in Section 3.5.1. This further confirms our assumption that the existing model uncertainty due to nozzle size variations or clogging is repetitive, and that the proposed SILC will be able to learn this repetitive model uncertainty and account for it in the update law. The norm of the maximum uncertainty of the plant matrix for Loctite 3526 across all 45 experiments is $\|\Delta\mathbf{H}_r\|_2 = 0.356\frac{nm}{ms}$, which is approximately half of the magnitude of the maximum element of the $h_f$ in Section 3.5.1.

***E-jet printer***: We use the integrated e-jet printer/AFM system in Figure 7.1, house in the Barton Research Lab at the University of Michigan. The system resides within a semi-cleanroom space mounted on a passive-vibration-isolation optical table. The substrate is mounted atop a stacked kinematic motorized X,Y, and Z stages with 0.1 $\mu$m accuracy and 0.01 $\mu$m resolution. Each stage has auxiliary analog and digital inputs and outputs that are used to control ancillary equipment in Figure 7.1. The nozzle is controlled with a separate motorized micrometer Z stage, which allows the user to move the nozzle independently from the substrate. All axes are controlled with motion composer software, an Aerotech A3200 software based controller, on a PC running Windows 10. An AFM tool is mounted to a truss constructed from T-slotted aluminum framing, while the nozzle is installed on a separate vertical aluminum frame as presented in Figure 7.1a. In these experiments, we focus on the deposition of a a single material (Loctite3526), An Infinity microscope camera with a 2.5×–20× zoom lens (Edmond Optics VZM1000i) is used for printing visualizations or setting the standoff height at the beginning of the experiment. We apply pressurized air to the nozzle liquid reservoir along with high voltage to the nozzle tip to push liquid ink through the nozzle inner capillary. Once the ink reaches the nozzle tip, the back pressure is set to atmospheric pressure. A pulsed signal at predefined low and high voltages (Figure 7.1a) is generated from the DAQ (Figure 7.1c) and amplified with a 200 × gain amplifier (Figure 7.1d).

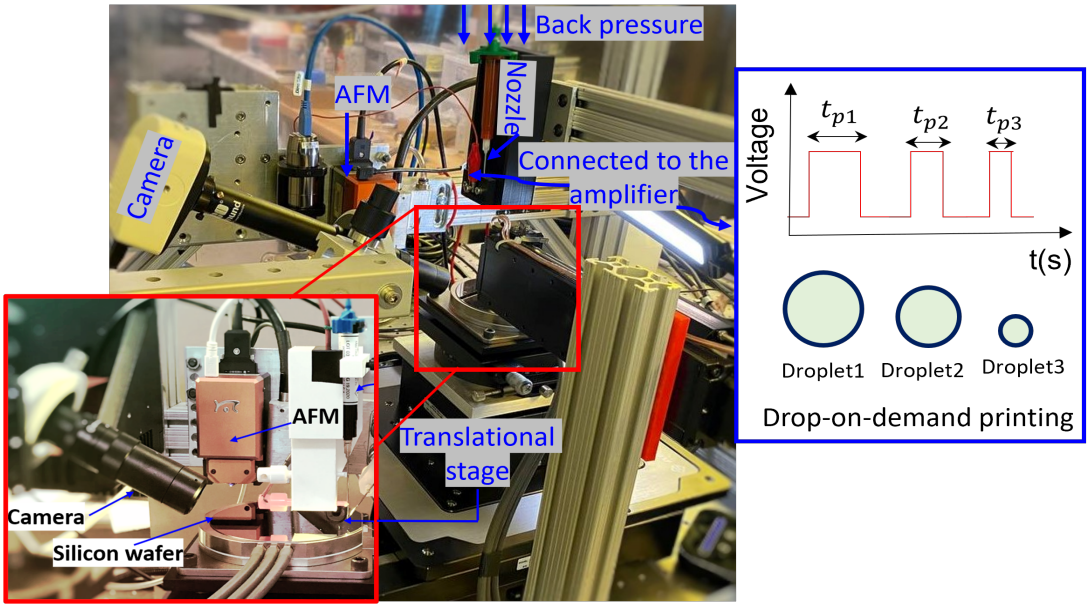


(a)


(b)

(c)

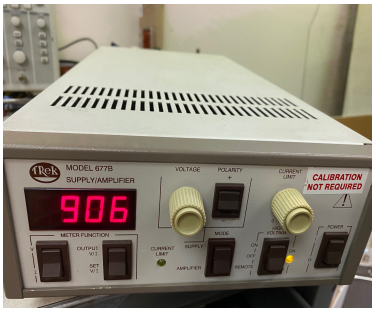


(d)

(e)

(f)

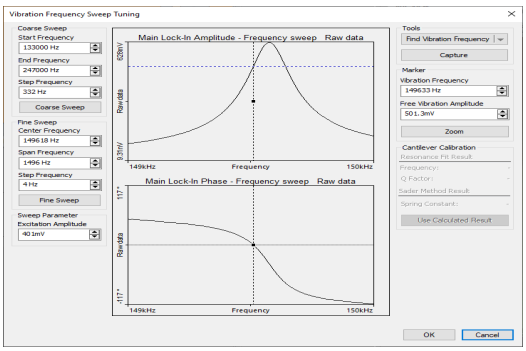


(g)

Figure 7.1: E-jet Manufacturing system. b) UV curing system: Dymax Bluewave 200. c) Data Acquisition System (DAQ): National Instruments NI USB-6251. d) High Voltage Power Supply and Amplifier: Trek 677B. e) Lumenera INFINITY 2-1R Microscopy Monochrome Camera. f) Nanosurf Nanite AFM on left and the 3D printed UV cure outlet box on the right. g) Vibration frequency sweep tuning of phase contrast mode of AFM.

***UV curing system:*** The UV light generated from a Dymax Bluewave 200 (Figure 7.1b) is used to cure the deposited patterns.The Dymax Bluewave 200 has a mechanical shutter that will be open by a motor drive auxiliary digital output and the generated UV light will be guided through a custom printed 3D focusing box shown in Figure 7.1f (next to the AFM) The UV box is mounted on the T-slotted aluminum framing, next to the AFM.The substrate is shuttled to this location once a new pattern has been deposited.

***AFM subsystem***: We use an Atomic Force Microscope (AFM), Nanosurf Nanite AFM driven by C3000 control electronics for inline quality control, to measure the output signal, $g(x,y)$, at each iteration. The AFM location is recorded and maintained for wafer registration purposes. The substrate will be shuttled to the AFM location in less than 3 s.The Phase contrast imaging mode of the AFM is used to collect the spatial XY, and lateral height data of features on the substrate. The phase contrast is a type of dynamic mode, also known as tapping mode, that refers to the phase channel information (the bottom figure in Figure 7.1g) that is collected during the scanning of the features based on the contrast of the deposited inks. The AFM cantilever tip oscillates vertically at a high frequency, close to its resonance frequency, while it has a gentle contact with the sample as shown in the upper figure of Figure 7.1g. Depending on the deposited topography, the amplitude and phase of the cantilever tip varies across the XY domain and will be used to estimate the height of the features at each spatial location. The maximum allowable scan size is 110 $\mu$m $\times$ 110 $\mu$m and 22 $\mu$m vertical range. Although the AFM range is 22 $\mu$m, the scanning time per line should be high (slow scan) for thick samples in order to avoid AFM tip jumps in locations such as the corner of a rectangle pattern where height deference exists.

## 7.2 Experimental Methods:

In this section, we present individual steps used to implement the SILC methods developed in chapters 4 and 5. Our aim is to achieve automated transfers between the printer, UV station (Figures 7.1b and 7.1f), and AFM to automatically deposit multi-layer structures and enable in-situ metrology and quality monitoring.

**step$_0$− Wafer Registration:**

$a_1$ : A plus mark is deposited on the substrate and the center location $(x_0, y_0)$ is recorded in the python code as datum.

$a_2$ : The offset between the nozzle tip centroid and center of the AFM scan in Figure 7.2a is calculated as $(\delta x, \delta y)$ and deducted from all nozzle to AFM distances

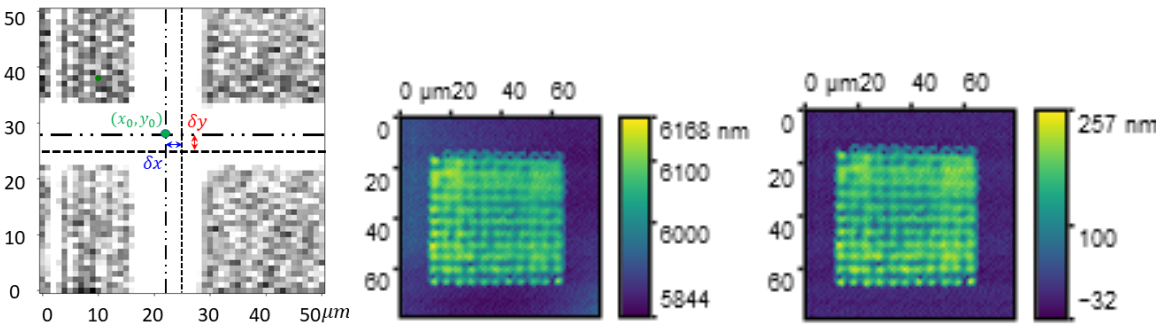


(a) (b) (c)

Figure 7.2: **Post-processing.** a) Wafer registration **step**$_0$: A plus mark is printed on the substrate and the its center location will be used to register the spatial coordinates on the wafer. b) AFM raw scan. Due to the AFM tip thermal drift, the bare area around the pattern does not have consistent height value. The height value need to be leveled such that all silicon area locatiopns have zero height value. c) Processed data **step**$_2$: The *flatten based leveling* function in Gwydion software is used to process the scan data relative to the bare silicon area around the sample .

in the python code. This step ensures that the nozzle's centroid is aligned with the center of the AFM scans.

$a_3$ : The spatial coordinate of every point on the wafer is calculated relative to the datum $(x-(x_0+\delta x), y-(y_0+\delta y))$. For example, the coordinate of the datum after registration is $(x_{datum}, y_{datum}) = (0,0)$.

**step**$_1$ – **E-jet Fabrication:** Time = 2 minutes 50 seconds

$b_1$ : The substrate is transferred to a predefined blank location form the datum and a $3 \times 3$ dot pattern is deposited with pitch equal to 10 $\mu$m (Figure 7.3). The location of the first droplet of each pattern is recorded in the python code $(x_{reg_j}, y_{reg_j})$.

$b_2$ : To prevent or resolve clogging issues in the nozzle, the substrate is shuttled to another predefined location $(x_{d_j}, y_{d_j})$ and a single droplet is printed at a high DC voltage (e.g. 650 V) for 2 (s).

$b_3$ : To mitigate first-droplet effects, the substrate moves to a predefined location, $(x_{pre_j}, y_{pre_j})$, and an $11 \times 11$ pre-pattern is printed with the NO-SILC input signal calculated in **step**$_3$. Note that steps ($b_2$ and $b_3$) will not be used in any ILC calculations.

$b_4$ : The substrate now moves to $(x_{reg}+a, y_{reg})$ as presented in Figure 7.3a and the

true $11 \times 11$ pattern is deposited with pitch = $5\mu$m using the calculated NO-SILC pulsewidth (input) from Eq. (5.8) and **step**$_3$.

$b_5$ : The substrate is shuttled to the UV-curing station, and the UV light is applied for 10 s.

$b_6$ : The substrate is shuttled back to the nozzle location.

**step**$_2$ – **Topography Measurement and Post-processing:** Time = 2 minutes 15 seconds

$c_1$ : The substrate moves to the AFM scanner station, where the center of the $3 \times 3$ registration pattern is placed directly under the AFM tip $(x_{reg_j} - (x_0 + \delta x), x_{reg_j} - (y_0 + \delta y))$, and the topography and coordinates of the registration dots are measured for post-processing purposes.

$c_2$ : The substrate moves such that the center of the pattern is located under the AFM tip and its topography is measured, $\bar{g}_{l,j}$, using the scan parameters: 79 $\mu$m $\times$ 79 $\mu$m scan size, with 79 points per line, and 0.5 s per line scan time.

$c_3$ : The *flatten base* leveling function in Gwyddion software is used to process the raw AFM data relative to the bare area around the pattern (Figure 7.2c).

$c_4$ : The AFM scans are cropped in the python code such that the information in the area of interest ($55 \times 55$ $\mu$m$^2$) is extracted as described in Figure 7.6. The $block - reduce()$ function in python is used to downsample the $55 \times 55$ $\mu$m$^2$ cropped AFM scans to $11 \times 11$ pixelized scans and evaluate the discretized output function, $g_{l,j}$, in Eq. (3.4).

$c_5$ : The layer height is calculated by subtracting two successive total height maps of the same device, $j$, as $\Delta g_{l,j} = g_{l,j} - g_{l-1,j}$. Note that at the first layer, $l = 1$, $g_{l,j} = \Delta g_{l,j}$.

$c_6$ : The layer and total errors are calculated as: $\Delta e_{l,j} = \Delta g^d - \Delta g_{l,j}$ and $e_{l,j} = g^d - g_{l,j}$, respectively. Note that for this particular example, $\Delta g^d$ is set as the desired output, and in our case is a flat layer with 150 nm layer height, $\Delta g^d = 150 * \mathbf{1}_{11\times11}$(nm), while $\mathbf{1}$ is a matrix of ones.

**step**$_3$ – **HO-SILC update law:** Time = 10 seconds

$d_1$ : The feedforward signal is calculated according to Eq. (5.8).

$d_2$ : Steps 1-3 are repeated, while the HO-SILC in Eq. (5.8) uses the input and error signals of previous depositions.

In summery, in order to fully automate the deposition process using e-jet process the overall time to print a process a single layer is approximately 5 minutes and 15 s. Note that, in $b_3$, the first-droplet effects in drop-on-demand printing refer to the fact that the initial printed droplets at a fixed setting usually have a different volume compared to the other droplets within the set. In $c_2$, we selected a 79 $\mu$m $\times$ 79 $\mu$m scan size, because we needed a bare area around the sample for post processing purposes. The scan duration varies depending on the scan parameters, such as scan size, time per line and point per lines. The overall scan time was approximately 1 minutes and 20 seconds to scan each layer in Figure 7.3.

## 7.3 Experimental Results

To compare the effects of the Norm optimal SILC tuning parameters, the performance of the SILC algorithm using the Frobenius norm is demonstrated in Figure 7.4 for different values of the penalty terms $r$ and $s$ in layer one with higher-order parameters, $(\alpha,\beta) = (0.9, 0.5)$. We selected the NO-SILC tuning parameters in Figure 7.4 based on our analysis in chapter 5, such that they satisfy the nominal stability criteria ($\|\mathbf{F}_0\|_2 < 1$, $\rho(\mathbf{T}_0^h < 1)$) and theorems 2 to 4 are satisfied. Another criteria that we used was to ensure that each element of the cost function in Eq. (5.3) had comparable impact. For example, we found that if $(\vec{f}_{l,j+1} - \vec{f}_{l,j})^T \mathbf{R}(\vec{f}_{l,j+1} - \vec{f}_{l,j})$ was too small compared to the other terms in Eq. (5.3), the controller would not attenuate noise in the system and easily became unstable. We resolved this issue by selecting a larger $r$ value. It should be noted that other systems may not require similarly weighted elements within the cost function. However, it is useful for sensitivity analysis. An example of this analysis can be seen by comparing the outputs from the tests with weighting gains $(q, s, r) = (1, 1, 0.5)$ and $(q, s, r) = (1, 1, 5)$ in Figure 7.4.

The weighting coefficients enable NO-SILC to control the rate of convergence, the final converged error, and the converged output (Figure 7.4). ILC is known to be robust to repetitive model uncertainty and disturbances. In chapter 5, we demonstrated that the higher order parameters and the SILC tuning parameters should be designed such that the maximum amount of uncertainty in the system, $\|\Delta\mathbf{H}_r\|_2$, is smaller than the robustness radius, $r_{AIU}$. Note that the $r_{AIU}$ is a design parameter that can be tuned by NO-SILC or higher-order SILC parameters $(q, s, r, \alpha, \beta)$. However, we should note that this is an approximation based on our understanding of the model dynamics, meaning that there might be situations where $\|\Delta\mathbf{H}_r\|_2 > r_{AIU}$, and the system with an integrated ILC framework remains stable. The conservativeness of this condition stems from two factors, 1) the way that $\Delta\mathbf{H}_r$ is experimentally calculated, 2) the norm assumptions in proof of theorems 3 and 4 and corol-

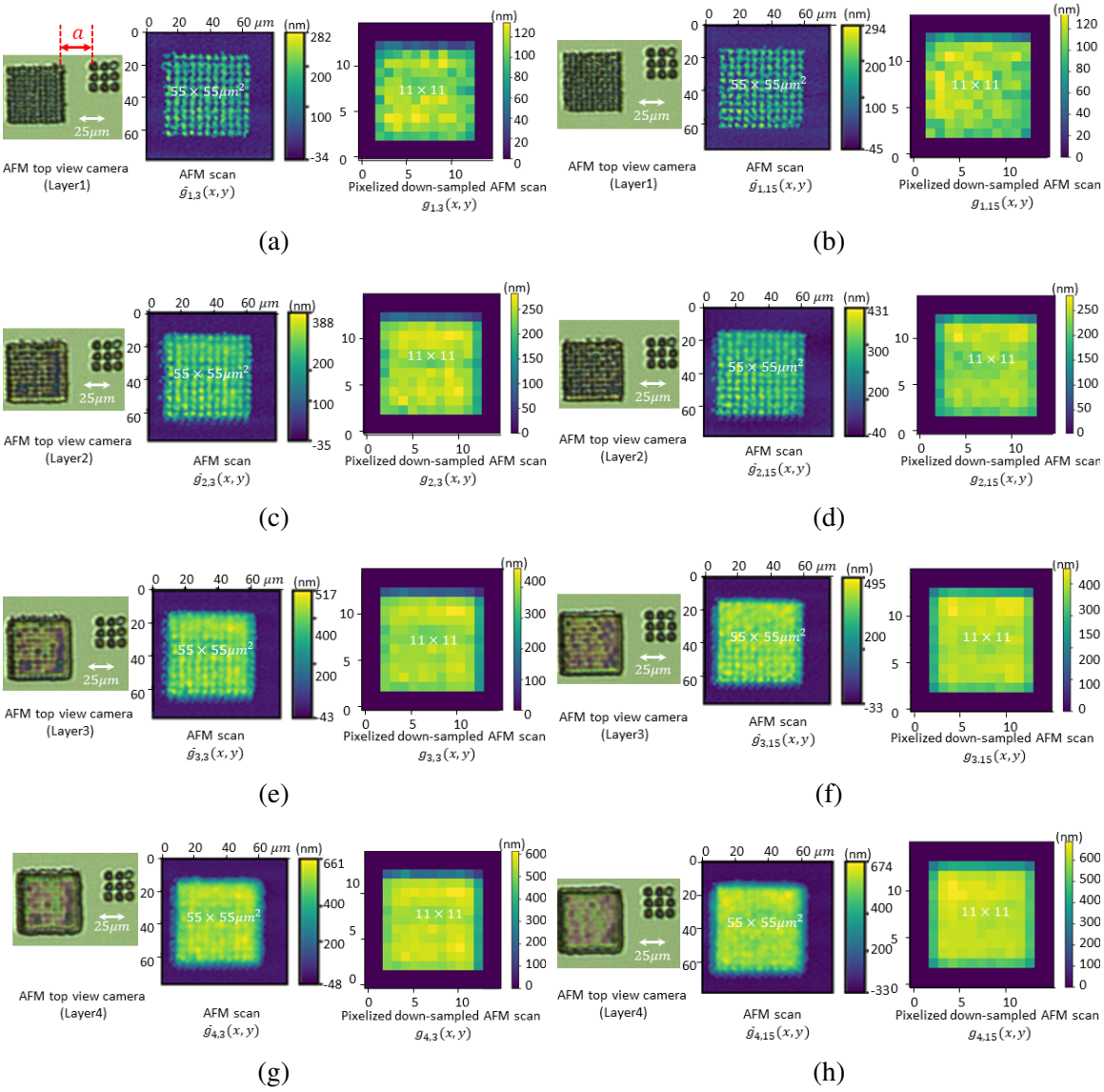


Figure 7.3: **Registration and data processing of iterations 3 and 15 output functions:** The die dimension is 55 $\mu$m × 55 $\mu$m, which is downsampled to 11 × 11 discretized XY grid with pitch of 5 $\mu$m. $\bar{g}_{l,j}(x,y)$ refers to oversampled AFM scans, while $g_{l,j}(x,y)$ refers to down-sampled output data (height) that is used in Eq. (3.4). The desired layer height is 150 nm and the ink is Loctite3526. The three by three dots are printed to register spatial coordinates on the substrate. All patterns are printed at a known distance, $a$, from the first registration droplet as described in Figure 7.3a. The ILC tuning parameters are (q,s,r)=(1,10,5), and the HO-SILC parameters are ($\alpha$,$\beta$)=(0.9,0.9). a,c,e,g) Data regarding the third device. b,d,f,h) Data regarding the last device.

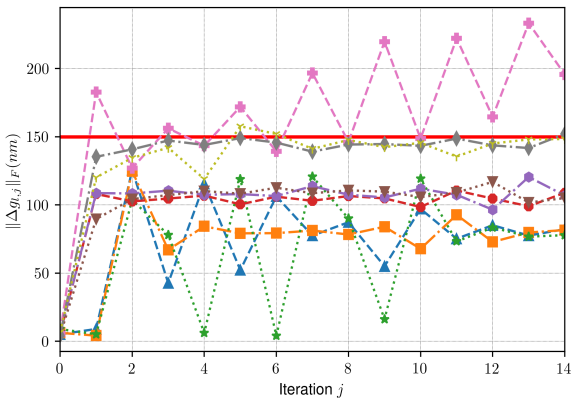


(a)

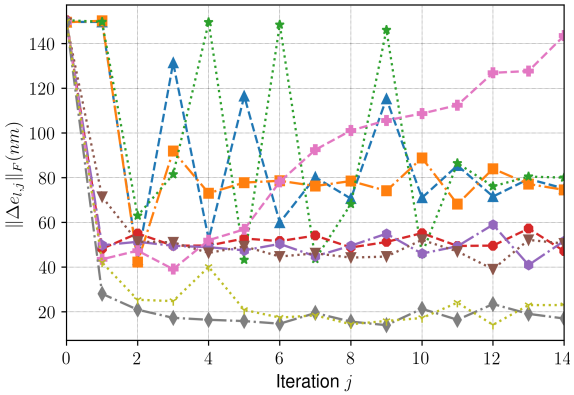


(b)

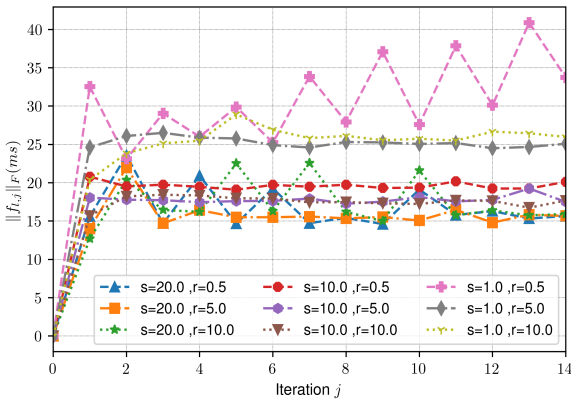


(c)

| q | s | r | $r_{AIU}$ | $\|\mathbf{F}_0\|_2$ | $\|\mathbf{T}_{h_0}\|_2$ | $\rho(\mathbf{T}_0^h)$ |
|---|---|---|---|---|---|---|
| 1.0 | 20.0 | 0.5 | 8.713 | 0.024 | 0.024 | 0.024 |
| 1.0 | 20.0 | 5.0 | 6.522 | 0.178 | 0.153 | 0.153 |
| 1.0 | 20.0 | 10.0 | 5.742 | 0.275 | 0.220 | 0.220 |
| 1.0 | 10.0 | 0.5 | 5.020 | 0.046 | 0.044 | 0.044 |
| 1.0 | 10.0 | 5.0 | 3.563 | 0.275 | 0.220 | 0.220 |
| 1.0 | 10.0 | 10.0 | 3.373 | 0.378 | 0.283 | 0.283 |
| 1.0 | 1.0 | 0.5 | 0.730 | 0.276 | 0.221 | 0.221 |
| 1.0 | 1.0 | 5.0 | 1.137 | 0.537 | 0.366 | 0.366 |
| 1.0 | 1.0 | 10.0 | 1.490 | 0.566 | 0.380 | 0.380 |

(d)

Figure 7.4: **Effects of the NO-SILC tuning parameters:** SILC convergence plots for different values of the NO tuning parameters with Loctite material. a) Average height versus device number. b) Incremental layer error versus layer number. c) Input signal versus device number. Iteration j = 0 refers to the first device, and the data is related to the first layer with $(\alpha,\beta) = (0.9, 0.5)$.

lary 1.1. So in design of the nine experiments in Figure 7.4, we selected the NO-SILC or higher-order SILC parameters $(q, s, r, \alpha, \beta)$ in Figure 7.4d such that the nominal system is stable ( $\|\mathbf{F}_0\|_2 < 1$) and the maximum uncertainty of the system remains less than the robustness radius, $\Delta\mathbf{H}_r < r_{AIU}$, while $\Delta\mathbf{H}_r$ is experimentally measured to be $\|\Delta\mathbf{H}_r\|_2 = 0.356\frac{nm}{ms}$. Note that higher values of $r_{AIU}$ result in better robustness to model uncertainty, but at the expense of performance, as will be shown through the following experimental results.

Based on the formulation of the norm optimal controller, we know that increasing the value of the input penalty, $s$, will decrease performance (e.g. increase the converged error) while improving robustness (e.g. larger $r_{AIU}$ value, see the table in Figure 7.4d). This is confirmed in Figure 7.4b in which, for a constant $r = 5$, increasing $s = 1$ to $s = 20$ re-

sults in a converged error norm that increases from 15 nm to 80 nm. This observation follows the well known performance/robustness trade off in control literature [92]. In addition, the value of $r$ is shown to produce a tradeoff between reducing the convergence rate (small $r$), and improving noise attenuation (large $r$). This is confirmed in Figure 7.4b in which, for a constant $s = 10$, the test with $r = 10$ converges to its final error after three iterations, compared to the tests, with $r = 0.5$ and $r = 5$, that converge to their final values after two iterations. We should note that although the effect of $r$ on convergence speed is not appreciable, we still need high values of $r$ for noise attenuation. For example, in test with $(s, r) = (1, 0.5)$, the system easily became unstable after 6 iterations. We believe that although the robustness radius in Figure 7.4d satisfies theorems 3 and 4 for all cases and could reject the repetitive model uncertainties in the system due to nozzle clogging or other environmental conditions, the HO-SILC design with $(q, s, r) = (1, 1, 0.5)$ could not reject the high frequency noises in the system and eventually resulted in non-monotonic response. In this case, the combined effect of low robustness ($r_{AIU} = 0.730$) due to small $s$, and the controller inability to attenuate the system noise due to small $r$, eventually led to the instability. More research still needs to be done to provide safety factors that consider the neglected fast dynamics and high frequency noise in the sensor measurements (AFM), the actuator (DAQ and amplifier) or our XYZ Aerotech stages in order to achieve design and control fidelity.

It should be mentioned that in cases with $(s, r) = (20, 0.5)$ and $(20, 10)$, norm of the predicted input signal (pulse-width) in Figure 7.4c is none zero, however, it is not enough to pull material out of the nozzle and in most of the discretized spatial locations, no material was printed (the average incremental height is zero, $\Delta\bar{g}(x, y) = 0$ nm or close to zero) at some of the iterations. This can be resolved using an MPC design, by imposing a lower limit on the input signal, as suggested in the chapter 8.

The spatial domain demonstration of the e-jet/AFM system regulated by a higher-order SILC to fabricate multi-layer structures is shown in Figure 7.3. The actual flat patterns are printed on a predefined distance form the first droplet of the three-by-three dots pattern that were printed for spatial domain registration on the Silicon wafer. The figures on the left are related to the samples that were printed at the third iteration, while the figures on the right are related to the samples that were printed at the last iteration. The first images are related to the AFM top view camera, the second images are the post-processed AFM data, and the last images are the pixelized downsampled AFM data that are used for output data in mathematical formulations. To deal with the oversampling of the AFM and convert the $(79 \times 79 \mu m^2)$ scan images to discretized output with $(11 \times 11)$ dimension, the AFM scans are cropped in the python code such the information in the area of interest $(55 \times 55 \mu m^2)$

| q | s | r | $\alpha$ | $\beta$ | $r_{AIU}$ | $\|\|\mathbf{F}_0\|\|_2$ | $\|\|\mathbf{T}_{h_0}\|\|_2$ | $\rho(\mathbf{T}_0^h)$ |
|---|---|---|---|---|---|---|---|---|
| 1.0 | 10.0 | 5.0 | 0.0 | 0.0 | 5.169 | 0.333 | 0.333 | 0.333 |
| 1.0 | 10.0 | 5.0 | 0.9 | 0.5 | 3.563 | 0.275 | 0.220 | 0.220 |
| 1.0 | 10.0 | 5.0 | 0.9 | 0.9 | 3.946 | 0.257 | 0.211 | 0.211 |
| 1.0 | 1.0 | 5.0 | 0.0 | 0.0 | 0.824 | 0.833 | 0.833 | 0.833 |
| 1.0 | 1.0 | 5.0 | 0.9 | 0.5 | 1.137 | 0.537 | 0.366 | 0.366 |
| 1.0 | 20.0 | 0.5 | 0.0 | 0.0 | 8.834 | 0.024 | 0.024 | 0.024 |
| 1.0 | 20.0 | 0.5 | 0.0 | 0.9 | 8.839 | 0.024 | 0.023 | 0.023 |
| 1.0 | 20.0 | 0.5 | 0.9 | 0.0 | 8.379 | 0.024 | 0.024 | 0.024 |
| 1.0 | 20.0 | 0.5 | 0.9 | 0.9 | 8.722 | 0.023 | 0.023 | 0.023 |

Table 7.1: Effect of higher-order parameters and NO-SILC on HO-SILC robustness and nominal stability. For better visualization, the FO-SILC data are shown with a light blue background.

are extracted. We use $block-reduce()$ function in python to downsample the $55\times55\mu m^2$ cropped AFM scans to $11\times11$ pixelized output data as presented in Figure 7.3.

Figure 7.5 compares the performance of the HO-SILC in experiment versus simulation, and demonstrates that the simulation is able to predict the behavior of actual additive process. For better visualization, the simulation results are shown with a light gray background. It can be observed that the HO-SILC framework enables learning not only on the horizontal direction from device-to-device, but also from layer-to-layer and eventually leads to layer errors convergence over layers and devices in both simulation and experiment. As expected, there are more iteration varying parameters, disturbances, and noise in the physical system that resulted in less smooth convergence behavior compared to the simulations. We believe that these parameters are non-repetitive, however due to time- and length-scale of the $\mu-$AM process, we cannot measure them. Note that the experiment and simulation data in Figures 7.5g and 7.5h both predict approximately 20 ms for the first layer, however, the experimental layer error at the first layer in Figure 7.5a is higher compared to the simulation layer error in Figure 7.5b (58 nm compared to 40 nm). Note that the AFM has around 10 nm noise and can introduce noise to the output measurements that were not considered in the simulation. Due to layer-to-layer learning resulted from nonzero higher-order parameters ($\alpha$,$\beta$), the pulse-width was predicted to be higher at the higher layers which resulted in a better performance with respect to the layer error. Figures 7.5g and 7.5h, shows that higher values of the input signal (pulse-width) is needed during the experiment compared to the simulation. For example, the simulation expected 25 ms at printing of layer four, while during the experiment the algorithm calculated approximately 40 ms. We believe that there are two justification for this observation, 1) the

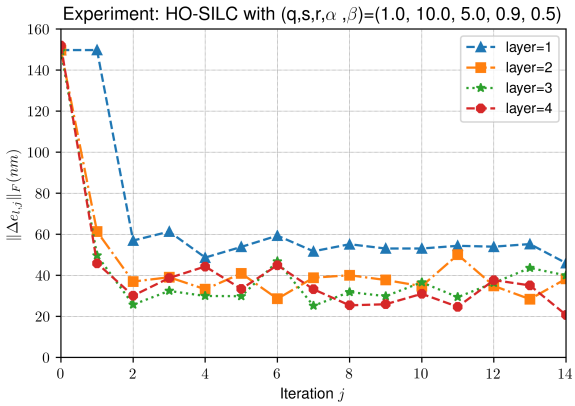
Experiment: HO-SILC with (q,s,r,α ,β)=(1.0, 10.0, 5.0, 0.9, 0.5)
layer=1
layer=2
layer=3
layer=4
Iteration j

(a)

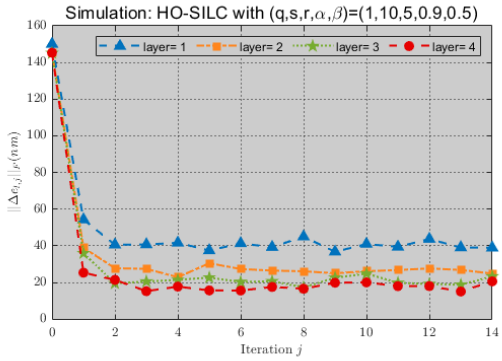
Simulation: HO-SILC with (q,s,r,α,β)=(1,10,5,0.9,0.5)
layer= 1
layer= 2
layer= 3
layer= 4
Iteration j

(b)

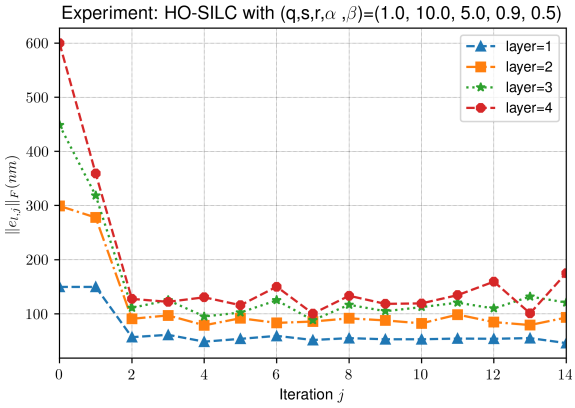
Experiment: HO-SILC with (q,s,r,α ,β)=(1.0, 10.0, 5.0, 0.9, 0.5)
layer=1
layer=2
layer=3
layer=4
Iteration j

(c)

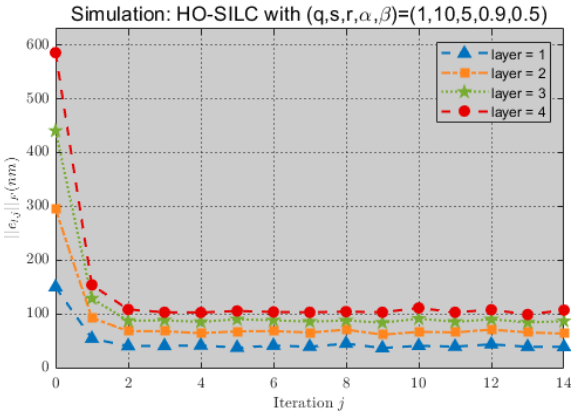
Simulation: HO-SILC with (q,s,r,α,β)=(1,10,5,0.9,0.5)
layer = 1
layer = 2
layer = 3
layer = 4
Iteration j

(d)

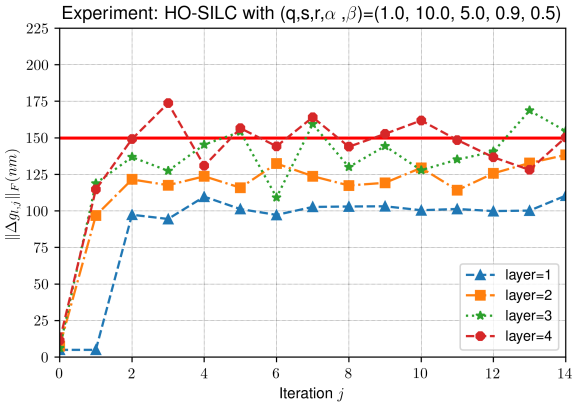
Experiment: HO-SILC with (q,s,r,α ,β)=(1.0, 10.0, 5.0, 0.9, 0.5)
layer=1
layer=2
layer=3
layer=4
Iteration j

(e)

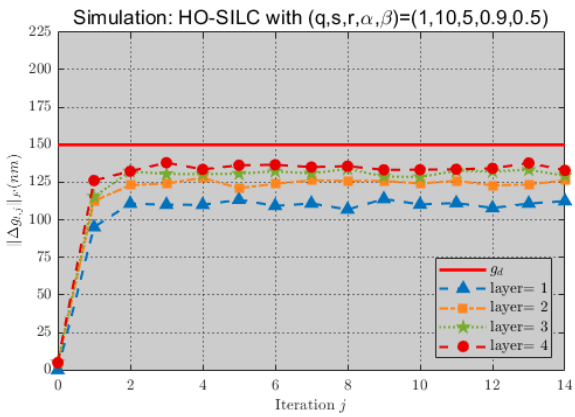
Simulation: HO-SILC with (q,s,r,α,β)=(1,10,5,0.9,0.5)
layer= 1
layer= 2
layer= 3
layer= 4
Iteration j

(f)

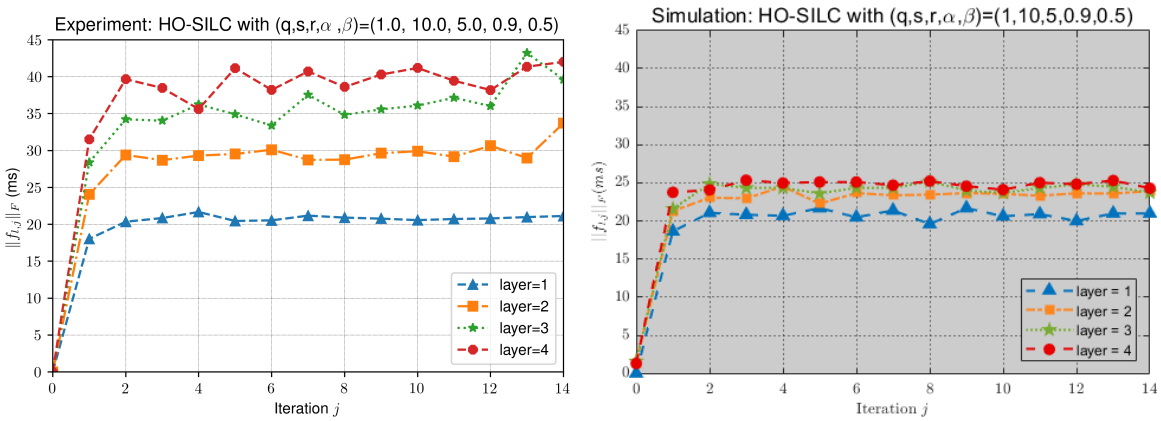


(g) (h)

Figure 7.5: **Experimental validation of the HO-SILC**: The figures on the right are the simulation results based on the HO-SILC developed in in chapter 5 and [5]. The figures on the left are experiment results from implementation of the HO-SILC in in chapter 5 to e-jet printing process.

effect of the nozzle clogging is more pronounced at the higher layers, 2) the electric field is weaker at higher layers and the electric charges could not be released to the substrate due to isolation properties of the polymer ink.

Figure 7.6 compares two HO-SILC designs with nonzero higher-order parameters to a FO-SILC design with no learning in the vertical direction due to zero higher-order parameters, $(\alpha,\beta) = (0,0)$. For better visualization, the FO-SILC results are shown with a light blue background. The Experimental results demonstrate that both HO-SILC designs outperform the FO-SILC design with respect to the layer and total error. The effect of layer-to-layer learning can be seen at the second iteration, $j = 2$. While the FO-SILC predicts 18 ms pulsewidth at iteration $j = 2$, at all layers which results in no material deposition, the HO-SILC learns from past layers at the same iterations and predict a higher input signal at $j = 2$ at higher layers that eventually resulted in a material deposition at those layers ($l \geq 2$). The layer error with the HO-SILC designs at the fourth layer is measured approximately 20 nm compared the 65 nm resulted from a FO-SILC. Given that the desired height increments at all layers is 150 nm, the FO-SILC design resulted in less material deposition at all layers. On the other hand, the HO-SILC designs could successfully learn form their past mistakes at the first layer and put down more material at the higher layers and increase the incremental height to approximately 150 nm. In addition, the total error at the fourth layer of both HO-SILC is measured to be approximately 110 nm compared to approximately 250 nm resulted from the FO-SILC design. This is a important advancement in fabrication of multi-layered micron sized structures, where the dimensionality plays an important role.

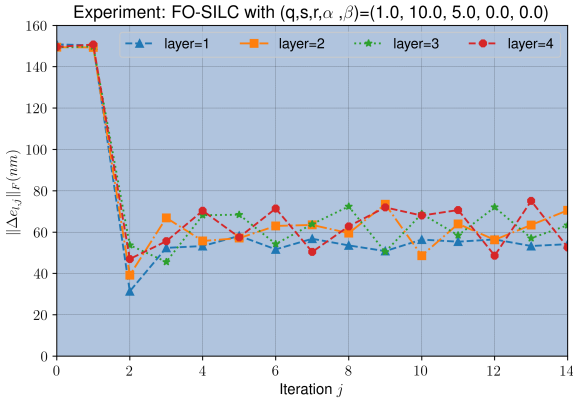
Experiment: FO-SILC with (q,s,r,α ,β)=(1.0, 10.0, 5.0, 0.0, 0.0)
layer=1
layer=2
layer=3
layer=4
$\|\Delta e_{l,j}\|_F(nm)$
Iteration $j$

(a)

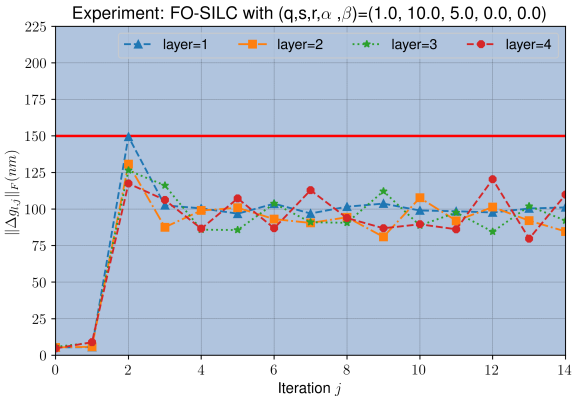
Experiment: FO-SILC with (q,s,r,α ,β)=(1.0, 10.0, 5.0, 0.0, 0.0)
layer=1
layer=2
layer=3
layer=4
$\|\Delta g_{l,j}\|_F(nm)$
Iteration $j$

(b)

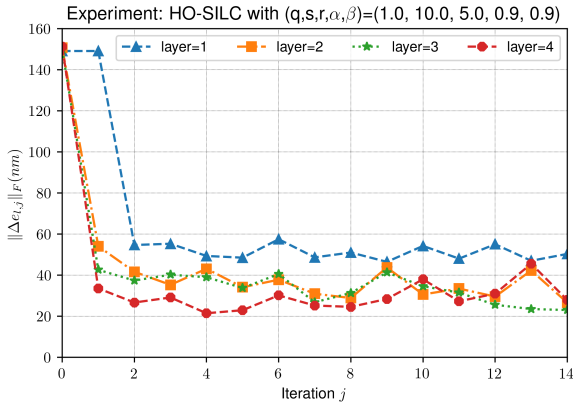
Experiment: HO-SILC with (q,s,r,α,β)=(1.0, 10.0, 5.0, 0.9, 0.9)
layer=1
layer=2
layer=3
layer=4
$\|\Delta e_{l,j}\|_F(nm)$
Iteration $j$

(c)

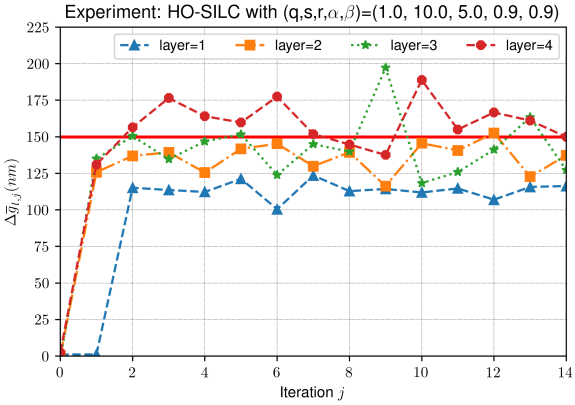
Experiment: HO-SILC with (q,s,r,α,β)=(1.0, 10.0, 5.0, 0.9, 0.9)
layer=1
layer=2
layer=3
layer=4
$\Delta\bar{g}_{l,j}(nm)$
Iteration $j$

(d)

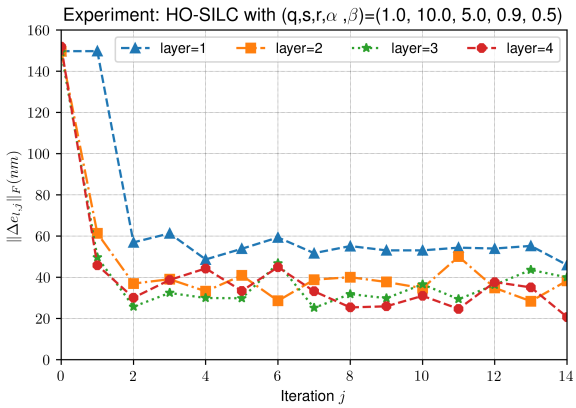
Experiment: HO-SILC with (q,s,r,α ,β)=(1.0, 10.0, 5.0, 0.9, 0.5)
layer=1
layer=2
layer=3
layer=4
$\|\Delta e_{l,j}\|_F(nm)$
Iteration $j$

(e)

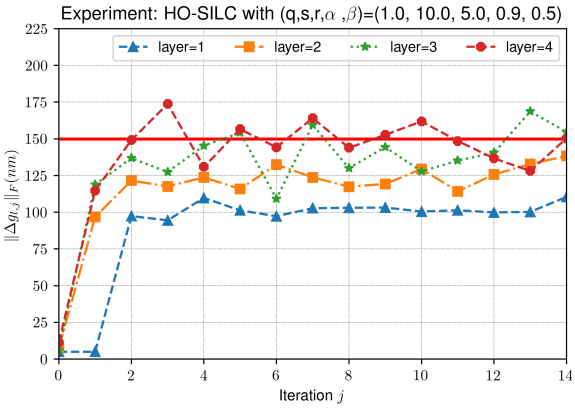
Experiment: HO-SILC with (q,s,r,α ,β)=(1.0, 10.0, 5.0, 0.9, 0.5)
layer=1
layer=2
layer=3
layer=4
$\|\Delta g_{l,j}\|_F(nm)$
Iteration $j$

(f)

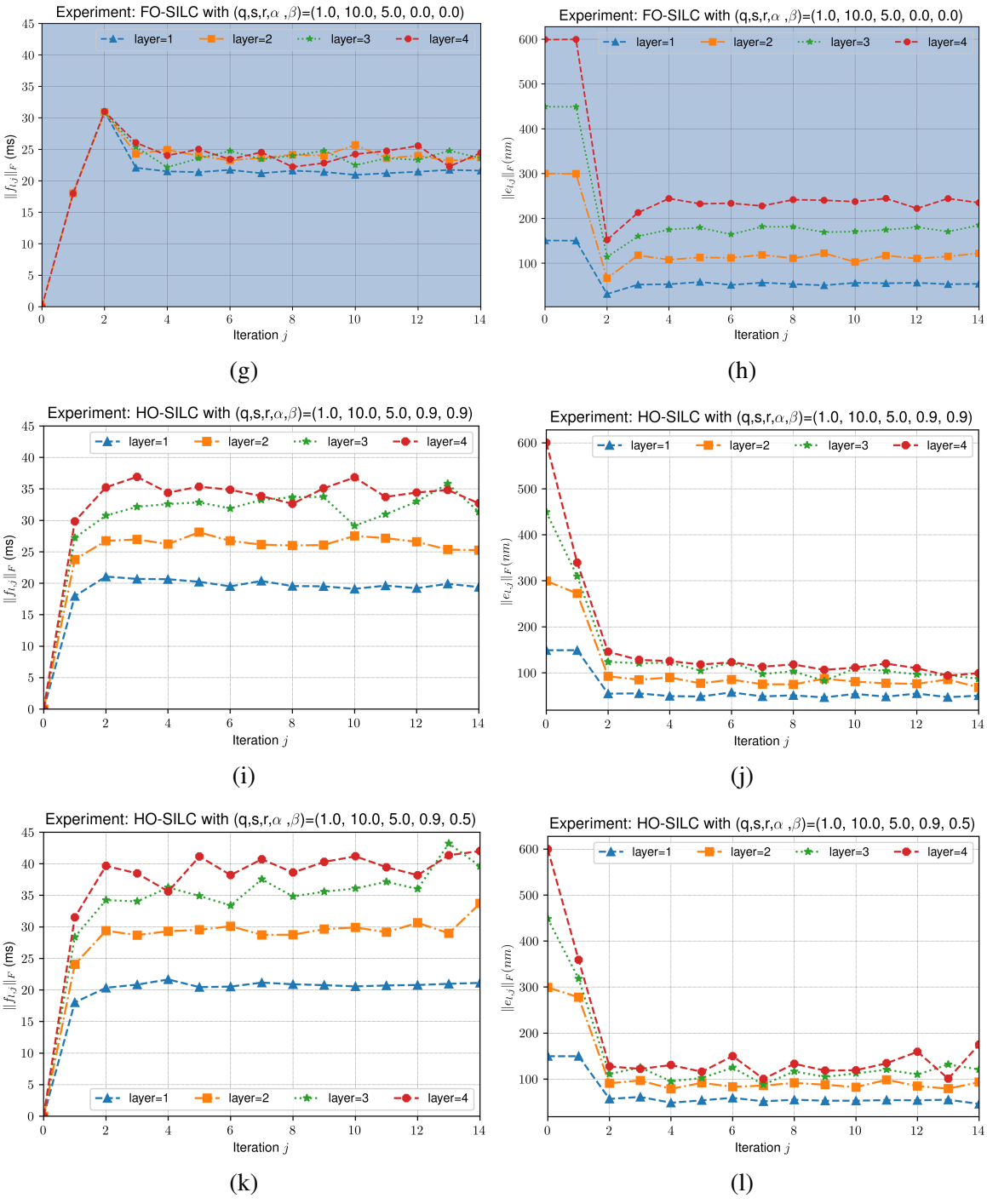


Figure 7.6: **FO-SILC and HO-SILC convergence comparison:** HO-SILC outperforms the FO-SILC with respect to the layer and total errors. Higher layers have lower layer errors because of the integration of the vertical learning due to none zero higher order parameters.

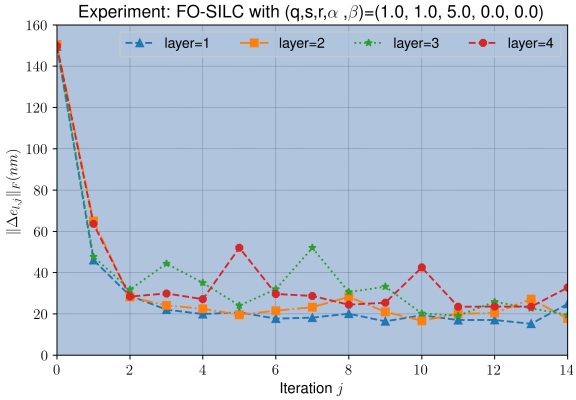
Experiment: FO-SILC with (q,s,r,$\alpha$ ,$\beta$)=(1.0, 1.0, 5.0, 0.0, 0.0)
layer=1
layer=2
layer=3
layer=4
$\|\Delta e_{i,j}\|_F(nm)$
Iteration $j$

(a)

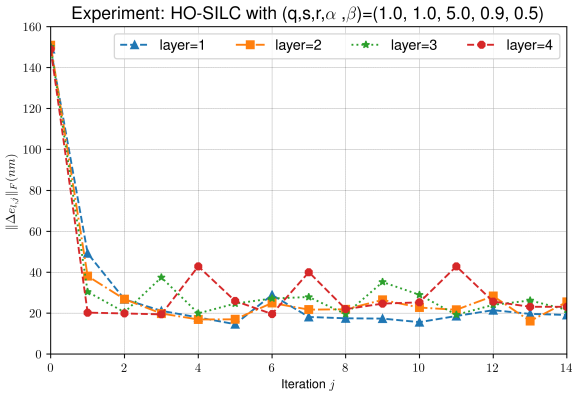
Experiment: HO-SILC with (q,s,r,$\alpha$ ,$\beta$)=(1.0, 1.0, 5.0, 0.9, 0.5)
layer=1
layer=2
layer=3
layer=4
$\|\Delta e_{i,j}\|_F(nm)$
Iteration $j$

(b)

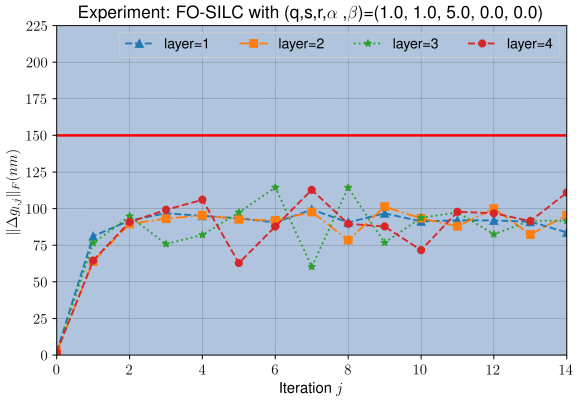
Experiment: FO-SILC with (q,s,r,$\alpha$ ,$\beta$)=(1.0, 1.0, 5.0, 0.0, 0.0)
layer=1
layer=2
layer=3
layer=4
$\|\Delta g_{i,j}\|_F(nm)$
Iteration $j$

(c)

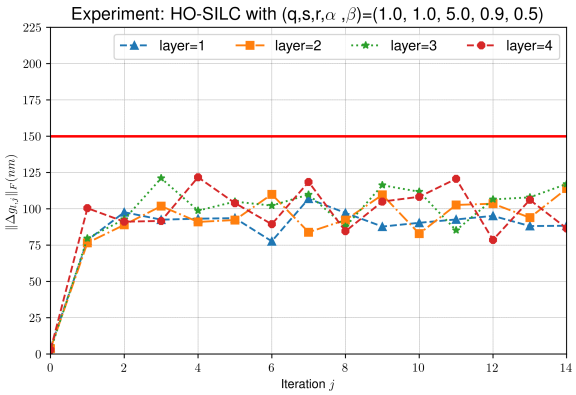
Experiment: HO-SILC with (q,s,r,$\alpha$ ,$\beta$)=(1.0, 1.0, 5.0, 0.9, 0.5)
layer=1
layer=2
layer=3
layer=4
$\|\Delta g_{i,j}\|_F(nm)$
Iteration $j$

(d)

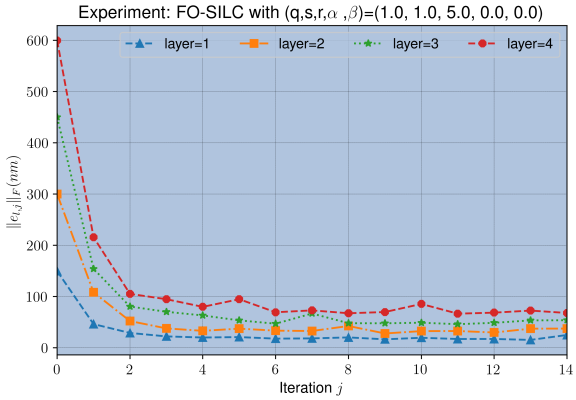
Experiment: FO-SILC with (q,s,r,$\alpha$ ,$\beta$)=(1.0, 1.0, 5.0, 0.0, 0.0)
layer=1
layer=2
layer=3
layer=4
$\|e_{i,j}\|_F(nm)$
Iteration $j$

(e)

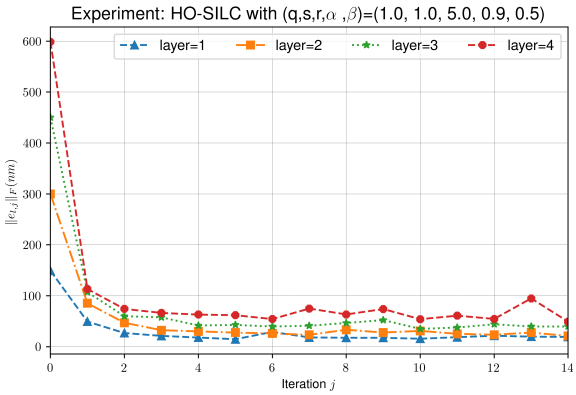
Experiment: HO-SILC with (q,s,r,$\alpha$ ,$\beta$)=(1.0, 1.0, 5.0, 0.9, 0.5)
layer=1
layer=2
layer=3
layer=4
$\|e_{i,j}\|_F(nm)$
Iteration $j$

(f)

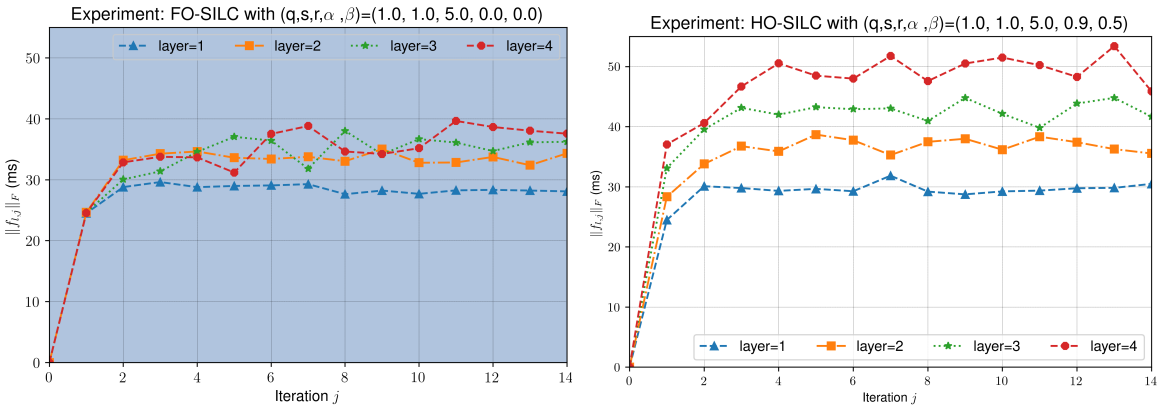


(g) (h)

Figure 7.7: **Effect of Higher-order SILC parameters**: The convergence behavior of the HO-SILC does not have a huge improvement over the FO-SILC due to low value of $s$ as compared with Figure 7.6.

To test the repeatability of the HO-SILC algorithm in Figure 7.6, we compared the performance of the HO-SILC with a FO-SILC design in Figure 7.7 with another sets of the design parameters $(q, s, r, \alpha, \beta)$. Unlike Figure 7.6, the convergence behavior of the HO-SILC does not have a huge improvement over the FO-SILC in Figure 7.7. The total error at the last layer for the FO-SILC is approximately 90 nm in Figure 7.7e compared to 75 nm in the Figure 7.7f for the total error of the HO-SILC design. Comparing the norm of the input signal in Figures 7.7g and 7.7h, it can be seen that the HO-SILC generates higher values of the input signal at the higher layers, which resulted in slightly higher material addition in Figure 7.7d compared to Figure 7.7c. Assuming that the nozzle is not clogged, we can conclude that a well-designed FO-SILC can be sufficient to close the topography loop iteratively and adding the higher order parameters might not always improve the convergence properties significantly.

It should be mentioned that the convergence behavior of the FO-SILC is more smooth compared to the convergence figures of the HO-SILC designs in Figure 7.6. We believe this can be due to higher value of robustness radius, $r_{AIU}$, for the first row of Table 7.1, compared to the second and third rows which are related to HO-SILC designs in Figure 7.6. On the other hand, the robustness radius, $r_{AIU}$, for the HO-SILC in the fifth row of Table 7.1 is higher than the $r_{AIU}$ in the fourth row related to the FO-SILC design in Figure 7.7. Therefore, the robustness properties ($r_{AIU}$) and the nominal parameters ($\|\mathbf{F}_0\|_2\|$ and $\|\mathbf{T}_{h_0}\|_2$) can be deteriorated or improved by adding the higher-order parameters ($\alpha$,$\beta$), based on the data in Table 7.1 Figure 7.4d. This is consistent with our claims in chapter 5, that the robustness radius is a function of higher-order parameters as well as tuning parameters.

In [50], it was claimed that a well-designed higher-order ILC can have a better performance than a poorly-designed first-order ILC; however, opposite might happen if the design parameters are not selected correctly. The authors presented anecdotal evidence of merit to justify either HO- or FO-ILC depending on the situation. During various experiments in this chapter, we have not observed that the FO-SILC outperforms the HO-SILC when the NO tuning parameters $(q, s, r)$ are fixed. However, comparing the FO-SILC performance in Figure 7.7 with the HO-SILC behavior in Figure 7.6, where different values of NO tuning parameters are used, we can see that the the FO-SILC design in Figure 7.7 outperforms the HO-SILC in Figure 7.6 with respect to the layer and total errors, at the cost of loosing robustness in Table 7.1.

To investigate the effect of the higher-order SILC parameters, we run the e-jet process for four different sets of $\alpha$ and $\beta$ in Figure 7.8. For better visualization, the FO-SILC results are shown with a light blue background. The results show that at all cases, the HO-SILC design outperforms the FO-SILC design with respect to the layer and total errors. Interestingly, for nonzero higher-order SILC, the performance of the HO-SILC is similar for all three cases. One reason could be the stability parameters such as robustness radius, $r_{AIU}$, and nominal matrices, $\|\mathbf{F}_0\|_2$ and $\|\mathbf{T}_{h_0}\|_2$, in all three HO-SILC designs are approximately equal, due to high value of the $s$ parameter.

## 7.4 Conclusion

In this chapter, we implemented the proposed FO-SILC and HO-SILC frameworks in chapters 4 and 5, to iteratively close the topography loop in a microscale additive manufacturing process, termed e-jet printing. We were able to achieve high fidelity $\mu$-AM through autonomous control of material addition in a layer-by-layer manner in e-jet printing process by design and integration of FO-SILC and HO-SILC frameworks. The proposed HO-SILC framework combines device-to-device learning with layer-to-layer learning to generate a feedforward signal that addresses error propagation over layers. In order to achieve computational efficiency through DFT calculations, we used BCCB plant matrix in Section 3.5.1. In addition, we used the RMC criterion in chapter 5 as a useful technique to select the design parameters. Comparing the experimental results with the simulation data in chapter 5, we found out that our e-jet printing process is more iteration varying than we expected. We believe that these iteration varying behaviors come from non-repetitive model uncertainties and disturbances resulted from sudden changes in the jetting behavior of the ink or existing noises in our measurements, that are not measurable during the fabrication process. The experimental results demonstrate

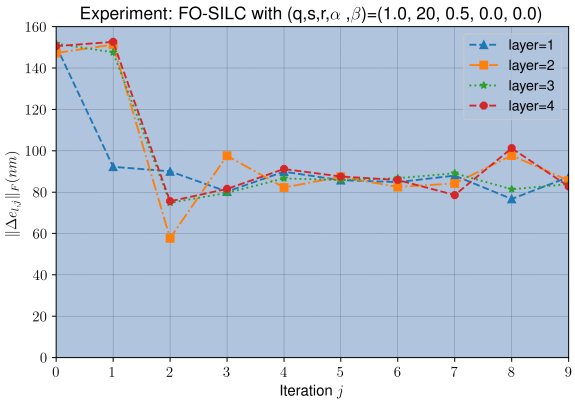
Experiment: FO-SILC with (q,s,r,$\alpha$ ,$\beta$)=(1.0, 20, 0.5, 0.0, 0.0)
layer=1
layer=2
layer=3
layer=4
$\|\Delta a_{i,j}\|_F(nm)$
Iteration $j$

(a)

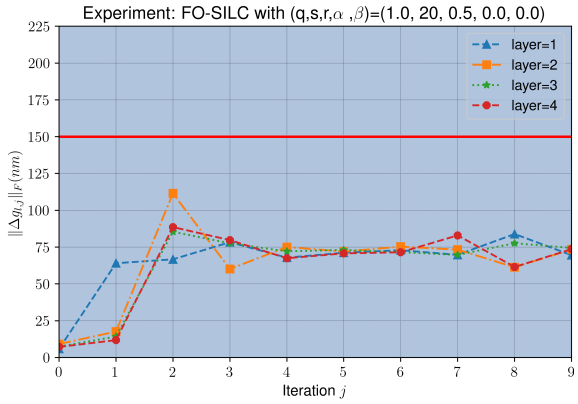
Experiment: FO-SILC with (q,s,r,$\alpha$ ,$\beta$)=(1.0, 20, 0.5, 0.0, 0.0)
layer=1
layer=2
layer=3
layer=4
$\|\Delta g_{i,j}\|_F(nm)$
Iteration $j$

(b)

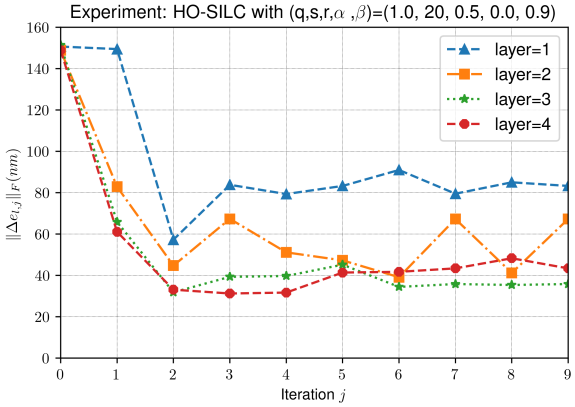
Experiment: HO-SILC with (q,s,r,$\alpha$ ,$\beta$)=(1.0, 20, 0.5, 0.0, 0.9)
layer=1
layer=2
layer=3
layer=4
$\|\Delta e_{i,j}\|_F(nm)$
Iteration $j$

(c)

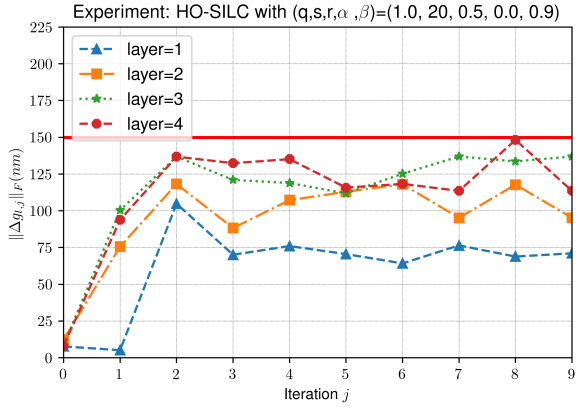
Experiment: HO-SILC with (q,s,r,$\alpha$ ,$\beta$)=(1.0, 20, 0.5, 0.0, 0.9)
layer=1
layer=2
layer=3
layer=4
$\|\Delta g_{i,j}\|_F(nm)$
Iteration $j$

(d)

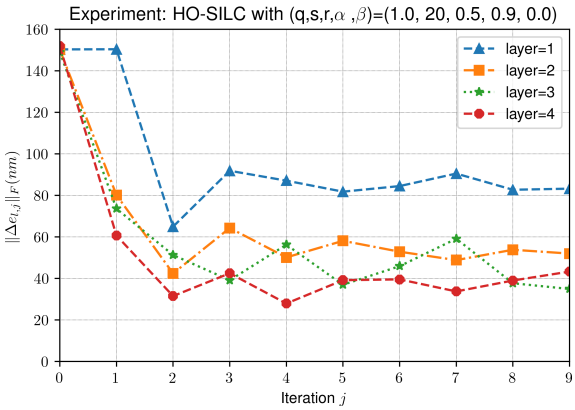
Experiment: HO-SILC with (q,s,r,$\alpha$ ,$\beta$)=(1.0, 20, 0.5, 0.9, 0.0)
layer=1
layer=2
layer=3
layer=4
$\|\Delta e_{i,j}\|_F(nm)$
Iteration $j$

(e)

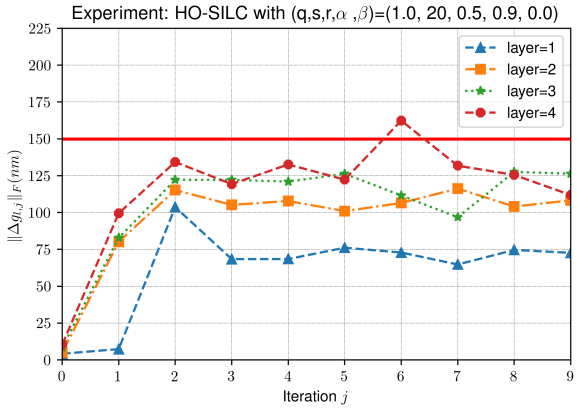
Experiment: HO-SILC with (q,s,r,$\alpha$ ,$\beta$)=(1.0, 20, 0.5, 0.9, 0.0)
layer=1
layer=2
layer=3
layer=4
$\|\Delta g_{i,j}\|_F(nm)$
Iteration $j$

(f)

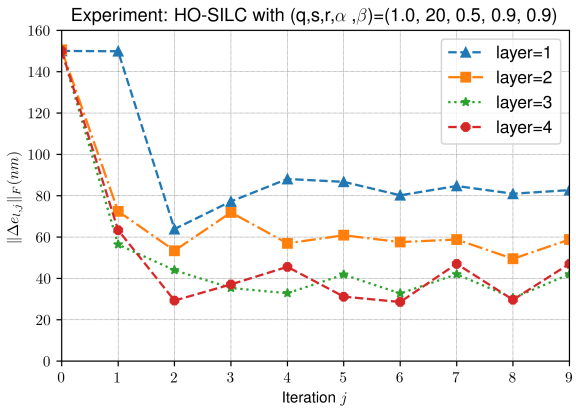
Experiment: HO-SILC with (q,s,r,$\alpha$ ,$\beta$)=(1.0, 20, 0.5, 0.9, 0.9)
$\|\Delta e_{i,j}\|_F(nm)$
Iteration $j$
layer=1
layer=2
layer=3
layer=4

(g)

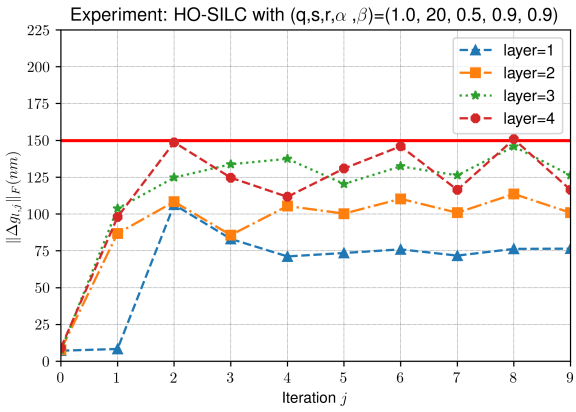
Experiment: HO-SILC with (q,s,r,$\alpha$ ,$\beta$)=(1.0, 20, 0.5, 0.9, 0.9)
$\|\Delta g_{i,j}\|_F(nm)$
Iteration $j$
layer=1
layer=2
layer=3
layer=4

(h)

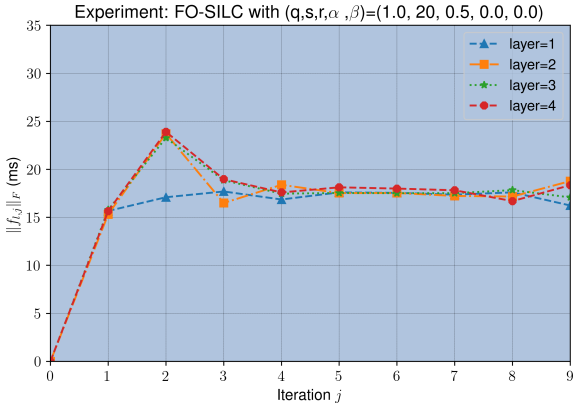
Experiment: FO-SILC with (q,s,r,$\alpha$ ,$\beta$)=(1.0, 20, 0.5, 0.0, 0.0)
$\|f_{i,j}\|_F$ (ms)
Iteration $j$
layer=1
layer=2
layer=3
layer=4

(i)

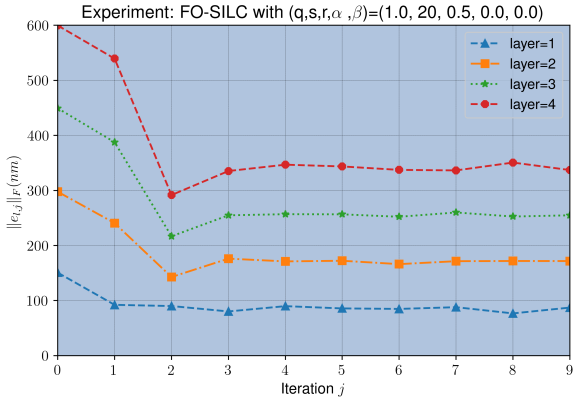
Experiment: FO-SILC with (q,s,r,$\alpha$ ,$\beta$)=(1.0, 20, 0.5, 0.0, 0.0)
$\|e_{i,j}\|_F(nm)$
Iteration $j$
layer=1
layer=2
layer=3
layer=4

(j)

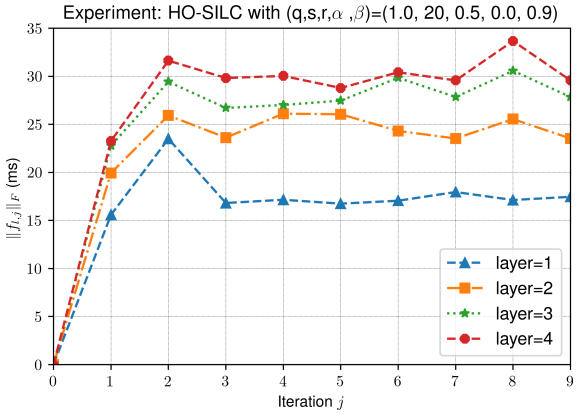
Experiment: HO-SILC with (q,s,r,$\alpha$ ,$\beta$)=(1.0, 20, 0.5, 0.0, 0.9)
$\|f_{i,j}\|_F$ (ms)
Iteration $j$
layer=1
layer=2
layer=3
layer=4

(k)

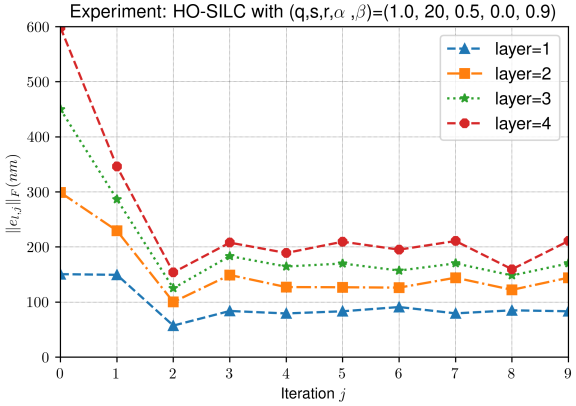
Experiment: HO-SILC with (q,s,r,$\alpha$ ,$\beta$)=(1.0, 20, 0.5, 0.0, 0.9)
$\|e_{i,j}\|_F(nm)$
Iteration $j$
layer=1
layer=2
layer=3
layer=4

(l)

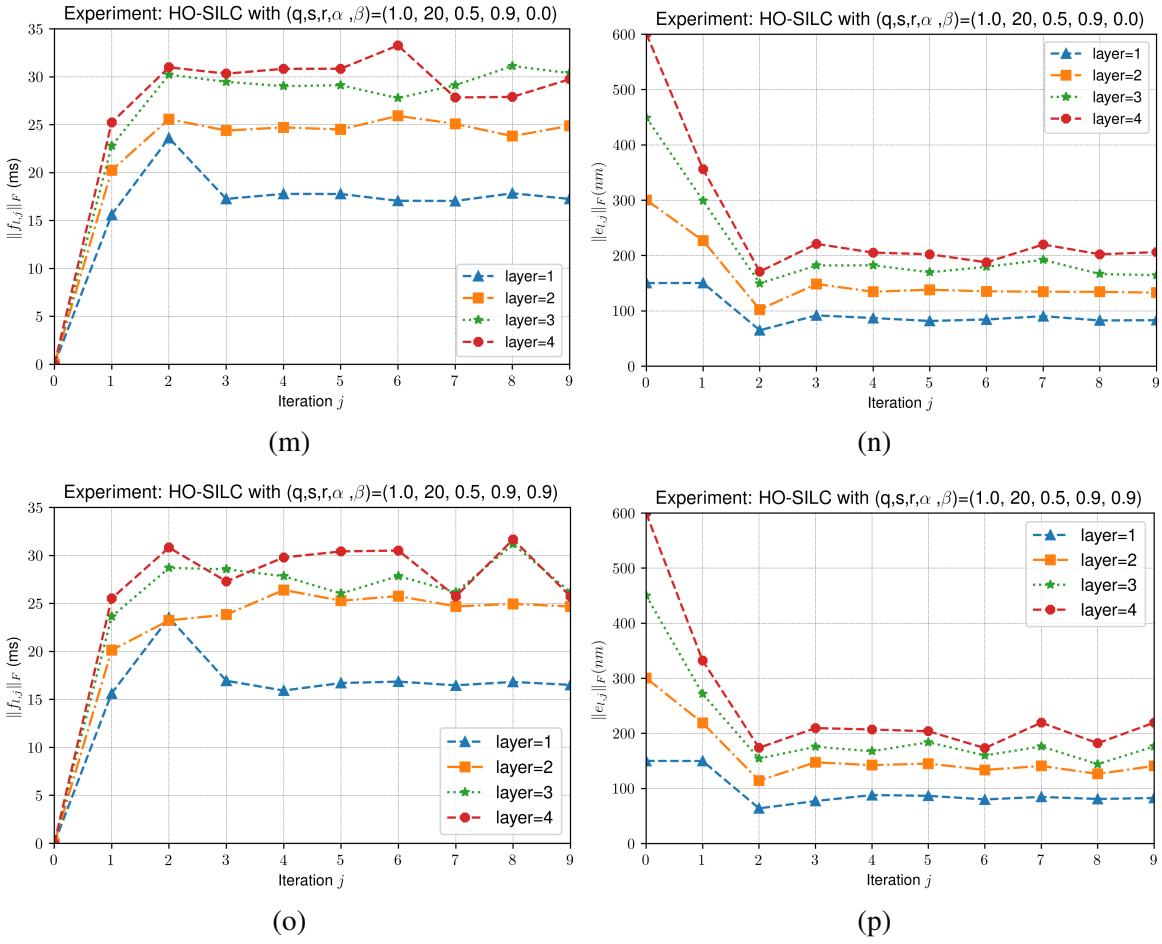


Figure 7.8: SILC convergence for different values of the higher order parameters.

that the proposed controllers are able to reject the repetitive model uncertainties that are resulted from nozzle clogging or environmental changes. Through multiple experiments and using various design parameters, we demonstrated that adding layer-to-layer learning to a FO-SILC can significantly improve the process performance. However, we observed that the convergence behavior of a SILC design, whether FO-SILC or HO-SILC, is limited by robustness/performance trade off.

# CHAPTER 8

# Conclusions and Future work

This dissertation provides important research advancements towards the fabrication of repeatable, thin-film functional devices through modeling and spatially derived control solution for improving the performance of a micro scale additive manufacturing (AM) process. Thought this dissertation, we investigate Electrohydrodynamic jet (e-jet) printing as a $\mu$-AM technique for its capability in depositing thin-film devices with microscale spatial resolution and nanoscale thickness resolution. Our aim is to understand material interactions at the microscale and use that knowledge to make a better control decision during the fabrication process in order to automate and auto-regulate material addition at the microscale. The research is validated through both simulation models and experimental testing with a custom-built e-jet system within the lab. An empirical model for the deposition process is developed in chapter 2 that relates the process and material parameters to the thickness and uniformity of the thin-film devices and subsequently helps us identify a set of compatible materials that enable multi-material deposition. To tackle the unique challenges on the $\mu$-AM processes and achieve autonomous control of material addition in a layer-by-layer manner, we apply different types of offline run-to-run learning-based controllers that incorporate model uncertainties and spatially varying dynamics, to close the topography loop iteratively. To address the combined challenges of multiple plant dynamics due to multiple build materials and varying initial conditions due to roughness of the previous layer surface, we developed a first-order SILC (FO-SILC) in chapter 4, that leverages the information from the most recent deposition to update its control signal. We were able to improve robustness of the FO-SILC controller and enable high fidelity $\mu$-AM, by integration of the layer-to-layer learning into the update law that resulted in a novel HO-SILC method in chapter 5. In chapter 7, we demonstrate both FO-SILC and HO-SILC are able to auto regulate the e-jet process without human intervention, despite the iteration varying parameters and process variability. The experimental results in chapter 7 demonstrate the fabrication accuracy of e-jet printing with both types of proposed controllers. It was observed that although there is a trade off between performance and robustness, which is

well-known in control literature [92], by proper tuning of the higher-order parameters, performance of the process can be improved, while the robustness is maintained. We further improved the HO-SILC controller in chapter 5 by projecting forward the data from future layers using model predictive control (MPC) and combining it with the information from previous layers using spatial iterative learning control (SILC) to form a novel SILC-MPC framework. Simulation results of an e-jet printed structure controlled by the SILC-MPC framework indicate that high-quality thin-films with uniform and repeatable thickness resolutions are achievable by tuning the MPC terminal cost and ILC parameters. It was shown that the proposed SILC-MPC controller is robust to stochastic and repetitive model uncertainty. The results imply that SILC-MPC framework generally has better performance compared to a traditional SILC controller. However, the SILC update law is much faster (50%) compared to the SILC-MPC algorithm. Future work should focus on implementation of the SILC-MPC on the experimental e-jet printing platform. In the next sections, I discuss the remaining research directions that should be investigated in the future work.

## 8.1 Unconstrained SILC-MPC framework

In chapter 6, we demonstrated a forward learning approach using a projection in the printing process that enhanced the control decisions in simulation. Future work should focus on experimental validation of the proposed SILC-MPC framework. Additionally, through the formulation of the SILC-MPC framework in chapter 6, I have identified the following important research questions that should be addressed:

1. What are the feasibility conditions for Eq. (6.12) to be computationally tractable?
2. Can the high dimensionality of the problem (e.g. $\mathbf{X}$ matrix in Eq. (6.12)) be reduced with minimal effect on the performance or robustness of the controller?
3. Can the problem be formulated to enable stability and convergence analysis? For example, is $\mathbf{X}$ in Eq. (6.12) always invertible, or are there assumptions that lead to matrix structures that allow for frequency domain transformation?

## 8.2 Constrained SILC-MPC

An important consideration in additive manufacturing processes is the constraint on the direction of material addition. In chapters 4 to 6, the proposed controllers did not consider a non-negativity constraint of the input signal. Instead, a saturation function was used to

force the negative inputs to zero. To tackle the input-constraint of the AM process, future work should consider a input constraint SILC-MPC method. To ensure that this practical requirement is followed, $\vec{f}$ must be constrained to be larger than $\vec{0}$. Furthermore, practical applications of the printing process require an upper limit to the quantity of material deposited to ensure stable printing based on physical constraints of the printhead. Therefore, $\vec{f}$ is further constrained to be less than $\vec{F}_{max} > \vec{0}$. This gives the resulting quadratic program.

$$\begin{aligned} \underset{\vec{f}}{\text{minimize}} \quad & \mathcal{J} \\ \text{subject to} \quad & \vec{0} \leq \vec{f} \leq \vec{F}_{max}, \end{aligned} \tag{8.1}$$

where $\mathcal{J}$ is the cost function in Eq. (6.6a). The solution to this problem provides a spatially distributed, SILC-MPC constrained input sequence that can be deposited at subsequent layers and iterations. Note that the cost function in Eq. (8.1) is convex with respect to $\vec{f}$. The AM-constraint in Eq. (8.1) can be rewritten as the following convex and affine function with respect to $\vec{f}$,

$$C(\vec{f}) = \begin{bmatrix} \mathbf{I} \\ \mathbf{-I} \end{bmatrix} \vec{f} - \begin{bmatrix} \vec{F}_{max} \\ \vec{0} \end{bmatrix} \leq \vec{0}. \tag{8.2}$$

To solve the constraint problem in Eq. (8.1), the following Lagrangian is proposed:

$$L(\vec{f}, \lambda) = \mathcal{J} + \lambda C(\vec{f}), \tag{8.3}$$

where $\lambda$ is a positive scalar called the Lagrange multiplier. Suppose that $\vec{f}^*$ is a minimizer, the following necessary condition holds from Karush-Kuhn-Tucker (KKT) conditions [93].

$$\begin{aligned} \nabla_{\vec{f}} L(\vec{f}^*, \lambda) &= \vec{0} \\ C(\vec{f}) &\leq \vec{0} \\ \lambda &\geq 0 \end{aligned} \tag{8.4}$$

Future work should focus on deriving solutions to the SILC-MPC optimization problem given in Eq. (8.4). Research questions related to the constrained SILC-MPC problem include:

1. How does the reframing of the problem into the constrained formulation of (8.4) impact the complexity of the robustness and convergence proofs?

2. Are there assumptions that lead to matrix structures that allow for transformation into the frequency domain?

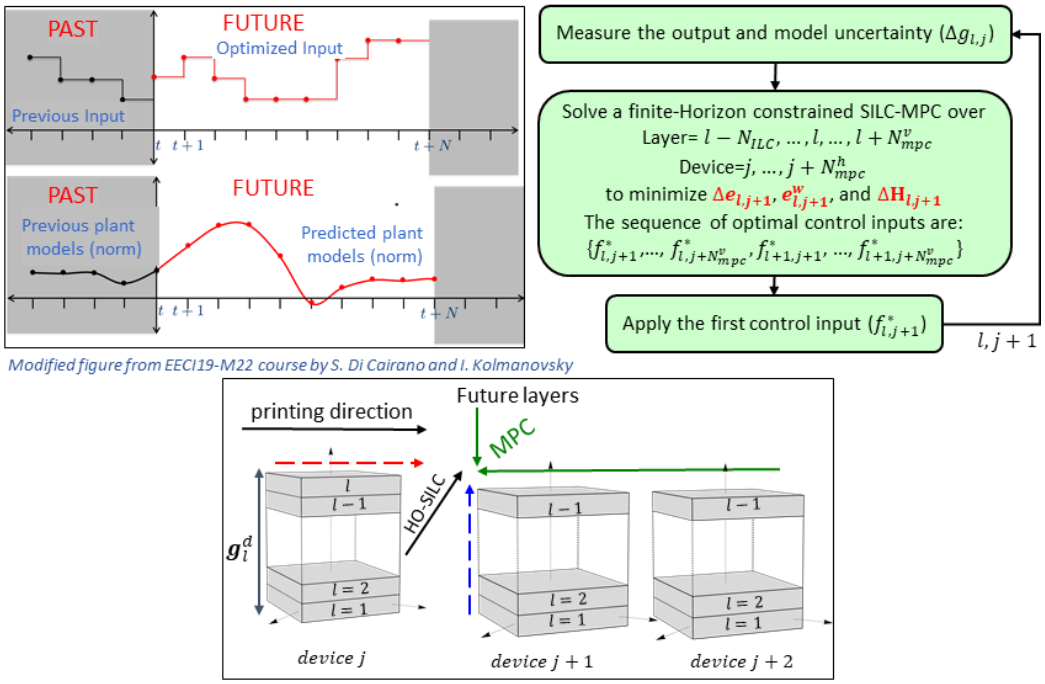


Figure 8.1: **data-driven MPC**: a data-driven MPC is proposed that predict the plant model in future trials ($\mathbf{H}_{l+,j+}$). SILC-MPC cost function will minimize the tracking error, as well as model uncertainty ($\Delta\mathbf{H}_{l+,j+}$). ($l+$, $j+$) refers future layers and iterations.

## 8.3 Development of a data-driven MPC to minimize variations in the plant models

Thus far, we have been dealing with an iteration varying system, in which our ability to achieve robustness is highly dependent on the magnitude of the plant model variations ($\Delta\mathbf{H}_{l,j}$). From the additive manufacturing standpoint, model uncertainties play a big role in terms of prediction of material spreading and can influence our ability to implement either SILC or SILC-MPC especially in multi-layered structures in which, layers at later iterations suffer from larger surface variations. In this work, we assume that the plant models are known from either methods in chapter 3. In order to achieve robustness, we designed the SILC learning filters for the maximum amount of model uncertainty (worst case uncertainty); as such, the SILC algorithm was overly robust.

Future work should investigate whether a data-driven MPC can reduce model uncertainty and improve the robustness of the SILC control framework. Therefore, I suggest the implementation of a fully data-driven MPC in combination with the developed SILC framework to achieve improved performance and robustness. The data-driven MPC should assume that there is no prior knowledge of the plant models. The proposed method can

use the concept of model predictive control to estimate the plant models using the information collected from previous iterations as presented in Figure 8.1, and account for model mismatches in the controller such that the iterative model converges to the nominal model, $\mathbf{H}_{l,j} \rightarrow \mathbf{H}_0$ (or $\Delta\mathbf{H}_{l,j} \rightarrow \mathbf{0}$). Compared to optimizations in Eqs. (5.3), (6.6a) and (8.1), the proposed MPC should be used to design the input signal to minimize not only the tracking error, but also the variations in the plant model in order to maintain consistency so that the plant model remains near the nominal model. I hypothesize that this forward projection will make the iterative model in Eq. (3.2) inherently more robust to model uncertainty. In this case, we can relax weighting on the robustness and enhance the weighting on the performance to design more aggressive controllers that achieve higher performance. Research questions related to this proposed work include:

1. What machine learning algorithm should be used to maximize performance?
2. What amount of data will be necessary to achieve reasonable model matching to ensure a robust control design?
3. Will the design of the SILC cost function impact the model identification of that data-driven MPC?

## 8.4 Practical Considerations:

Although this research is originally motivated by thin-film micro-devices that are fabricated using e-jet printing, the contributions of this research can be applied to improve the performance of any AM process that aims to fabricate multi-material 3D structures with flexible designs and non-uniform thickness resolutions. The potential AM processes include Inkjet printing, FDM 3D printing, or even metal AM processes such as Direct Energy Deposition (DED) in [56]. Note that although we were able to fully automate the deposition process in e-jet printing, the experimental steps in Section 7.2 are still too slow and should be improved for rapid production. The printing process, substrate transfers and data processing steps in Section 7.2 take about 5 minutes for each layer and part of the reason is the oversampling of our metrology system which makes the scanning process and output measurements slow. To deal with the unnecessary oversampling and extract the value of the output at discredited locations, we downsampled the AFM scans to lower resolutions. To achieve rapid production, faster metrology tools such as Keyence 3D laser scanning confocal microscopes (VK-X Series) are proposed. In addition, lower resolution metrology tools such as profilometer in [94], 2-D height profile laser sensor in [3], and optical sensor in [95]

can be used in lower resolution AM processes such as Injket printing for faster output measurement. It should be mentioned that because of the fact that all controllers designed in this work are model-based, the system identification experiment (Section 3.5), should be run before implementing the controller to the system. Interestingly, the SILC paradigm does not need a very accurate model to predict the behavior of the system and can learn the repetitive model uncertainty and disturbances of the system. The model uncertainty during the deposition process is mainly repetitive, resulted from a shift in the pulsewidth range due to clogging or nozzle size variations. Therefore, the repetitive model uncertainty can be learned by the SILC part of the controller, and one system identification experiment should be sufficient to predict the behavior of the system. Therefore, to predict the behavior of the system in chapter 7, we run the system identification in Section 3.5.1 once before the controller implementation that took about 2 hours. The 45 system identifications explained in Section 7.1 has been used to find the maximum amount of the uncertainty in the system which can be ignored by approximately assuming the maximum magnitude of the uncertainty in the system by half of the maximum element of the impulse response.

In addition, the proposed control frameworks developed in this work have applications outside of additive manufacturing systems. For example, any system that exhibits spatially dependent dynamics through a repetitive action (e.g. exoskeletons, robotic pick and place) could benefit from a control framework that compensates for errors across both a spatial and temporal domain. Importantly, spatial interactions are often disjointed temporally and are commonly ignored. The proposed framework here addresses this issue by incorporating spatial information into the control law.

# BIBLIOGRAPHY


[1] Iezzi, B., Afkhami, Z., Sanvordenker, S., Hoelzle, D., Barton, K., and Shtein, M., "Electrohydrodynamic Jet Printing of 1D Photonic Crystals: Part II—Optical Design and Reflectance Characteristics," *Advanced Materials Technologies*, Vol. 5, No. 10, 2020, pp. 2000431.

[2] Pannier, C., Wu, M., Hoelzle, D., and Barton, K., "LPV models for jet-printed heightmap control," *2019 American Control Conference (ACC)*, IEEE, 2019, pp. 5402–5407.

[3] Inyang-Udoh, U. and Mishra, S., "A Physics-Guided Neural Network Dynamical Model for Droplet-Based Additive Manufacturing," *IEEE Transactions on Control Systems Technology*, 2021.

[4] Afkhami, Z., Hoelzle, D. J., and Barton, K. L., "Robust higher-order spatial iterative learning control for additive manufacturing systems," *IEEE Trans. Control Syst. Technol., under review*, 2022.

[5] Afkhami, Z., Hoelzle, D., and Barton, K., "Robust Higher-Order Spatial Iterative Learning Control for Additive Manufacturing systems," *accepted to IEEE Transactions on Control Systems Technology*, IEEE, 2022.

[6] Gibson, I., Rosen, D., and Stucker, B., *Additive manufacturing technologies: 3D printing, rapid prototyping, and direct digital manufacturing, second edition*, Springer, 2015.

[7] Theiler, P. M., Lütolf, F., and Ferrini, R., "Non-contact printing of optical waveguides using capillary bridges," *Optics express*, Vol. 26, No. 9, 2018, pp. 11934–11939.

[8] Calvo, M. E. and Míguez, H., "Flexible, adhesive, and biocompatible Bragg mirrors based on polydimethylsiloxane infiltrated nanoparticle multilayers," *Chemistry of Materials*, Vol. 22, No. 13, 2010, pp. 3909–3915.

[9] Zhu, X., Xu, Q., Li, H., Liu, M., Li, Z., Yang, K., Zhao, J., Qian, L., Peng, Z., Zhang, G., et al., "Fabrication of high-performance silver mesh for transparent glass heaters via electric-field-driven microscale 3D printing and UV-assisted microtransfer," *Advanced Materials*, Vol. 31, No. 32, 2019, pp. 1902479.

[10] Zhu, X., Li, Z., Hu, Y., Li, H., Yang, J., and Lan, H., "Facile fabrication of defogging microlens arrays using electric field-driven jet printing," *Optics & Laser Technology*, Vol. 123, 2020, pp. 105943.

[11] Szczech, J. B., Megaridis, C. M., Gamota, D. R., and Zhang, J., "Fine-line conductor manufacturing using drop-on demand PZT printing technology," *IEEE transactions on electronics packaging manufacturing*, Vol. 25, No. 1, 2002, pp. 26–33.

[12] Duraisamy, N., Muhammad, N. M., Kim, H.-C., Jo, J.-D., and Choi, K.-H., "Fabrication of TiO2 thin film memristor device using electrohydrodynamic inkjet printing," *Thin Solid Films*, Vol. 520, No. 15, 2012, pp. 5070–5074.

[13] Wu, Y., Shen, H., Ye, S., Yao, D., Liu, W., Zhang, J., Zhang, K., and Yang, B., "Multifunctional reversible fluorescent controller based on a one-dimensional photonic crystal," *ACS applied materials & interfaces*, Vol. 8, No. 42, 2016, pp. 28844–28852.

[14] Karl, M., Glackin, J. M., Schubert, M., Kronenberg, N. M., Turnbull, G. A., Samuel, I. D., and Gather, M. C., "Flexible and ultra-lightweight polymer membrane lasers," *Nature communications*, Vol. 9, No. 1, 2018, pp. 1–7.

[15] Sirringhaus, H., Kawase, T., Friend, R., Shimoda, T., Inbasekaran, M., Wu, W., and Woo, E., "High-resolution inkjet printing of all-polymer transistor circuits," *Science*, Vol. 290, No. 5499, 2000, pp. 2123–2126.

[16] Chang, P. C., Lee, J., Huang, D., Subramanian, V., Murphy, A. R., and Fréchet, J. M., "Film morphology and thin film transistor performance of solution-processed oligothiophenes," *Chemistry of materials*, Vol. 16, No. 23, 2004, pp. 4783–4789.

[17] Manfredi, G., Lova, P., Di Stasio, F., Rastogi, P., Krahne, R., and Comoretto, D., "Lasing from dot-in-rod nanocrystals in planar polymer microcavities," *RSC advances*, Vol. 8, No. 23, 2018, pp. 13026–13033.

[18] Ferrarese Lupi, F., Giammaria, T., Volpe, F., Lotto, F., Seguini, G., Pivac, B., Laus, M., and Perego, M., "High aspect ratio PS-b-PMMA block copolymer masks for lithographic applications," *ACS applied materials & interfaces*, Vol. 6, No. 23, 2014, pp. 21389–21396.

[19] Ramírez Quiroz, C. O., Bronnbauer, C., Levchuk, I., Hou, Y., Brabec, C. J., and Forberich, K., "Coloring semitransparent perovskite solar cells via dielectric mirrors," *ACS nano*, Vol. 10, No. 5, 2016, pp. 5104–5112.

[20] Anderson, N., Prabhat, P., and Erdogan, T., "Ion-beam sputtered (IBS) thin-film interference filters for nonlinear optical imaging," *Multiphoton Microscopy in the Biomedical Sciences XII*, Vol. 8226, International Society for Optics and Photonics, 2012, p. 82260O.

[21] Wang, J., Wang, L., Song, Y., and Jiang, L., "Patterned photonic crystals fabricated by inkjet printing," *Journal of Materials Chemistry C*, Vol. 1, No. 38, 2013, pp. 6048–6058.

[22] Pannier, C. P., Barton, K., Hoelzle, D., and Wang, Z., "A model of liquid-drop spreading for electrohydrodynamic jet printing," *Dynamic Systems and Control Conference*, Vol. 57250, American Society of Mechanical Engineers, 2015, p. V002T34A012.

[23] Minemawari, H., Yamada, T., Matsui, H., Tsutsumi, J., Haas, S., Chiba, R., Kumai, R., and Hasegawa, T., "Inkjet printing of single-crystal films," *Nature*, Vol. 475, No. 7356, 2011, pp. 364–367.

[24] Huang, Y., Leu, M. C., Mazumder, J., and Donmez, A., "Additive manufacturing: current state, future potential, gaps and needs, and recommendations," *Journal of Manufacturing Science and Engineering*, Vol. 137, No. 1, 2015.

[25] Jang, J., Kang, H., Chakravarthula, H. C. N., and Subramanian, V., "Fully Inkjet-Printed Transparent Oxide Thin Film Transistors Using a Fugitive Wettability Switch," *Advanced Electronic Materials*, Vol. 1, No. 7, 2015, pp. 1500086.

[26] Kelly, A. G., Hallam, T., Backes, C., Harvey, A., Esmaeily, A. S., Godwin, I., Coelho, J., Nicolosi, V., Lauth, J., Kulkarni, A., et al., "All-printed thin-film transistors from networks of liquid-exfoliated nanosheets," *Science*, Vol. 356, No. 6333, 2017, pp. 69–73.

[27] Camposeo, A., Persano, L., Farsari, M., and Pisignano, D., "Additive manufacturing: applications and directions in photonics and optoelectronics," *Advanced optical materials*, Vol. 7, No. 1, 2019, pp. 1800419.

[28] Hoath, S. D., *Fundamentals of inkjet printing: the science of inkjet and droplets*, John Wiley & Sons, 2016.

[29] Park, J.-U., Hardy, M., Kang, S. J., Barton, K., Adair, K., Mukhopadhyay, D. K., Lee, C. Y., Strano, M. S., Alleyne, A. G., Georgiadis, J. G., Ferreira, P. M., and Rogers, J. A., "High-resolution electrohydrodynamic jet printing," *Nat. Mater.*, Vol. 6, No. 10, aug 2007, pp. 782–789.

[30] Onses, M. S., Sutanto, E., Ferreira, P. M., Alleyne, A. G., and Rogers, J. A., "Mechanisms, capabilities, and applications of high-resolution electrohydrodynamic jet printing," *Small*, Vol. 11, No. 34, 2015, pp. 4237–4266.

[31] Han, Y. and Dong, J., "Electrohydrodynamic printing for advanced micro/nanomanufacturing: Current progresses, opportunities, and challenges," *Journal of Micro and Nano-Manufacturing*, Vol. 6, No. 4, 2018.

[32] Sutanto, E., Shigeta, K., Kim, Y., Graf, P., Hoelzle, D., Barton, K., Alleyne, A., Ferreira, P., and Rogers, J., "A multimaterial electrohydrodynamic jet (E-jet) printing system," *Journal of Micromechanics and Microengineering*, Vol. 22, No. 4, 2012, pp. 045008.

[33] Pannier, C. P., Ojeda, L., Wang, Z., Hoelzle, D., and Barton, K., "An electrohydrodynamic jet printer with integrated metrology," *Mechatronics*, Vol. 56, dec 2018, pp. 268–276.

[34] Schlisske, S., Held, M., Rödlmeier, T., Menghi, S., Fuchs, K., Ruscello, M., Morfa, A. J., Lemmer, U., and Hernandez-Sosa, G., "Substrate-independent surface energy tuning via siloxane treatment for printed electronics," *Langmuir*, Vol. 34, No. 21, 2018, pp. 5964–5970.

[35] Wang, Y., Gao, F., and Doyle, F. J., "Survey on iterative learning control, repetitive control, and run-to-run control," 2009.

[36] Norrlöf, M. and Gunnarsson, S., "Time and frequency domain convergence properties in iterative learning control," *International Journal of Control*, Vol. 75, No. 14, 2002, pp. 1114–1126.

[37] Meng, D. and Moore, K. L., "Robust iterative learning control for nonrepetitive uncertain systems," *IEEE Trans. Automat. Contr.*, 2017.

[38] Ahn, H.-S., Moore, K. L., and Chen, Y., *Iterative learning control: robustness and monotonic convergence for interval systems*, Springer Science & Business Media, 2007.

[39] Altin, B., Wang, Z., Hoelzle, D. J., and Barton, K., "Robust monotonically convergent spatial iterative learning control: interval systems analysis via discrete Fourier transform," 2018.

[40] Hoelzle, D. J. and Barton, K. L., "On Spatial Iterative Learning Control via 2-D Convolution: Stability Analysis and Computational Efficiency," *IEEE Trans. Control Syst. Technol.*, 2016.

[41] Hoelzle, D. J. and Barton, K. L., "A new spatial iterative learning control approach for improved micro-additive manufacturing," *2014 American Control Conference*, IEEE, 2014, pp. 1805–1810.

[42] Afkhami, Z., Pannier, C., Aarnoudse, L., Hoelzle, D., and Barton, K., "Spatial Iterative Learning Control for Multi-material Three-Dimensional Structures," *ASME Letters in Dynamic Systems and Control*, Vol. 1, No. 1, 2020.

[43] Aarnoudse, L., Pannier, C., Afkhami, Z., Oomen, T., and Barton, K., "Multi-layer spatial iterative learning control for micro-additive manufacturing," *IFAC-PapersOnLine*, Vol. 52, No. 15, 2019, pp. 97–102.

[44] Wang, Z., Pannier, C., Ojeda, L., Barton, K., and Hoelzle, D. J., "An application of spatial iterative learning control to micro-additive manufacturing," *2016 American Control Conference (ACC)*, IEEE, 2016, pp. 354–359.

[45] Bristow, D. A., Tharayil, M., and Alleyne, A. G., "A survey of iterative learning control," *IEEE control systems magazine*, Vol. 26, No. 3, 2006, pp. 96–114.

[46] Bu, X., Yu, F., Fu, Z., and Wang, F., "Stability analysis of high-order iterative learning control for a class of nonlinear switched systems," *Abstract and Applied Analysis*, Vol. 2013, Hindawi, 2013.

[47] Wei, Y.-S. and Li, X.-D., "Robust higher-order ILC for non-linear discrete-time systems with varying trail lengths and random initial state shifts," *IET Control Theory & Applications*, Vol. 11, No. 15, 2017, pp. 2440–2447.

[48] Bien, Z. and Huh, K. M., "Higher-order iterative learning control algorithm," *IEE Proceedings D (Control Theory and Applications)*, Vol. 136, IET, 1989, pp. 105–112.

[49] Chen, Y., Gong, Z., and Wen, C., "Analysis of a high-order iterative learning control algorithm for uncertain nonlinear systems with state delays," *Automatica*, Vol. 34, No. 3, 1998, pp. 345–353.

[50] Phan, M. Q. and Longman, R. W., "Higher-order iterative learning control by pole placement and noise filtering," *IFAC Proceedings Volumes*, Vol. 35, No. 1, 2002, pp. 25–30.

[51] Rawlings, J. B., Mayne, D. Q., and Diehl, M., *Model predictive control: theory, computation, and design*, Vol. 2, Nob Hill Publishing Madison, WI, 2017.

[52] Li, D., He, S., Xi, Y., Liu, T., Gao, F., Wang, Y., and Lu, J., "Synthesis of ILC–MPC controller with data-driven approach for constrained batch processes," *IEEE Transactions on Industrial Electronics*, Vol. 67, No. 4, 2019, pp. 3116–3125.

[53] Lee, K. S., Chin, I.-S., Lee, H. J., and Lee, J. H., "Model predictive control technique combined with iterative learning for batch processes," *AIChE Journal*, Vol. 45, No. 10, 1999, pp. 2175–2187.

[54] Xie, S. and Ren, J., "Iterative learning-based model predictive control for precise trajectory tracking of piezo nanopositioning stage," *2018 Annual American Control Conference (ACC)*, IEEE, 2018, pp. 2922–2927.

[55] Rosolia, U. and Borrelli, F., "Learning model predictive control for iterative tasks. a data-driven control framework," *IEEE Transactions on Automatic Control*, Vol. 63, No. 7, 2017, pp. 1883–1896.

[56] Gegel, M. L., Bristow, D. A., and Landers, R. G., "Model predictive height control for direct energy deposition," *Dynamic Systems and Control Conference*, Vol. 59148, American Society of Mechanical Engineers, 2019, p. V001T10A006.

[57] Yu, Q. and Hou, Z., "Data-driven predictive iterative learning control for a class of multiple-input and multiple-output nonlinear systems," *Transactions of the Institute of Measurement and Control*, Vol. 38, No. 3, 2016, pp. 266–281.

[58] Wang, L., Freeman, C. T., and Rogers, E., "Predictive iterative learning control with experimental validation," *Control Engineering Practice*, Vol. 53, 2016, pp. 24–34.

[59] Jewell, J., Scherer, A., McCall, S., Lee, Y.-H., Walker, S., Harbison, J., and Florez, L., "Low threshold electrically-pumped vertical-cavity surface-emitting microlasers," *Optics News*, Vol. 15, No. 12, 1989, pp. 10–11.

[60] Lissberger, P. and Wilcock, W., "Properties of all-dielectric interference filters. II. Filters in parallel beams of light incident obliquely and in convergent beams," *JOSA*, Vol. 49, No. 2, 1959, pp. 126–130.

[61] Howell, I. R., Li, C., Colella, N. S., Ito, K., and Watkins, J. J., "Strain-tunable one dimensional photonic crystals based on zirconium dioxide/slide-ring elastomer nanocomposites for mechanochromic sensing," *ACS applied materials & interfaces*, Vol. 7, No. 6, 2015, pp. 3641–3646.

[62] Lova, P., Manfredi, G., and Comoretto, D., "Advances in functional solution processed planar 1D photonic crystals," *Advanced Optical Materials*, Vol. 6, No. 24, 2018, pp. 1800730.

[63] Park, J.-U., Hardy, M., Kang, S. J., Barton, K., Adair, K., kishore Mukhopadhyay, D., Lee, C. Y., Strano, M. S., Alleyne, A. G., Georgiadis, J. G., et al., "High-resolution electrohydrodynamic jet printing," *Nature materials*, Vol. 6, No. 10, 2007, pp. 782–789.

[64] Cloupeau, M. and Prunet-Foch, B., "Electrohydrodynamic spraying functioning modes: a critical review," *Journal of Aerosol Science*, Vol. 25, No. 6, 1994, pp. 1021–1036.

[65] Lee, S.-H. and Cho, Y.-J., "Characterization of silver inkjet overlap-printing through cohesion and adhesion," *Journal of Electrical Engineering and Technology*, Vol. 7, No. 1, 2012, pp. 91–96.

[66] Park, J., Kim, B., Kim, S.-Y., and Hwang, J., "Prediction of drop-on-demand (DOD) pattern size in pulse voltage-applied electrohydrodynamic (EHD) jet printing of Ag colloid ink," *Applied Physics A*, Vol. 117, No. 4, 2014, pp. 2225–2234.

[67] Owens, D. K. and Wendt, R., "Estimation of the surface free energy of polymers," *Journal of applied polymer science*, Vol. 13, No. 8, 1969, pp. 1741–1747.

[68] Wu, S., "Calculation of interfacial tension in polymer systems," *Journal of Polymer Science Part C: Polymer Symposia*, Vol. 34, Wiley Online Library, 1971, pp. 19–30.

[69] Saad, S. M., Policova, Z., and Neumann, A. W., "Design and accuracy of pendant drop methods for surface tension measurement," *Colloids and Surfaces A: Physicochemical and Engineering Aspects*, Vol. 384, No. 1-3, 2011, pp. 442–452.

[70] Ionita, E., Ionita, M., Stancu, E., Teodorescu, M., and Dinescu, G., "Small size plasma tools for material processing at atmospheric pressure," *Applied Surface Science*, Vol. 255, No. 10, 2009, pp. 5448–5452.

[71] Israelachvili, J. N. and Gee, M. L., "Contact angles on chemically heterogeneous surfaces," *Langmuir*, Vol. 5, No. 1, 1989, pp. 288–289.

[72] Pannier, C. P., Diagne, M., Spiegel, I. A., Hoelzle, D. J., and Barton, K., "A dynamical model of drop spreading in electrohydrodynamic jet printing," *Journal of Manufacturing Science and Engineering*, Vol. 139, No. 11, 2017.

[73] Taylor, M., Urquhart, A. J., Zelzer, M., Davies, M. C., and Alexander, M. R., "Picoliter water contact angle measurement on polymers," *Langmuir*, Vol. 23, No. 13, 2007, pp. 6875–6878.

[74] Doumanidis, C. and Skordeli, E., "Distributed-parameter modeling for geometry control of manufacturing processes with material deposition," *J. Dyn. Sys., Meas., Control*, Vol. 122, No. 1, 2000, pp. 71–77.

[75] Guo, Y., Peters, J., Oomen, T., and Mishra, S., "Control-oriented models for ink-jet 3D printing," *Mechatronics*, Vol. 56, 2018, pp. 211–219.

[76] Wang, Z., Sammons, P. M., Pannier, C. P., Barton, K., and Hoelzle, D. J., "System Identification of a Discrete Repetitive Process Model for Electrohydrodynamic Jet Printing," *2018 Annual American Control Conference (ACC)*, IEEE, 2018, pp. 4464–4471.

[77] Moore, K. L., "An iterative learning control algorithm for systems with measurement noise," *Proceedings of the 38th IEEE Conference on Decision and Control (Cat. No. 99CH36304)*, Vol. 1, IEEE, 1999, pp. 270–275.

[78] Norrlof, M. and Gunnarsson, S., "A frequency domain analysis of a second order iterative learning control algorithm," *Proceedings of the 38th IEEE Conference on Decision and Control (Cat. No. 99CH36304)*, Vol. 2, IEEE, 1999, pp. 1587–1592.

[79] Afkhami, Z., Iezzi, B., Hoelzle, D., Shtein, M., and Barton, K., "Electrohydrodynamic Jet Printing of One-Dimensional Photonic Crystals: Part I—An Empirical Model for Multi-Material Multi-Layer Fabrication," *Advanced Materials Technologies*, Vol. 5, No. 10, 2020, pp. 2000386.

[80] Amann, N., Owens, D. H., and Rogers, E., "2D systems theory applied to learning control systems," *Proceedings of 1994 33rd IEEE Conference on Decision and Control*, Vol. 2, IEEE, 1994, pp. 985–986.

[81] Rogers, E. and Owens, D. H., *Stability analysis for linear repetitive processes*, Vol. 175, Springer, 1992.

[82] Chu, B. and Owens, D. H., "Iterative learning control for constrained linear systems," *International Journal of Control*, Vol. 83, No. 7, 2010, pp. 1397–1413.

[83] Cayley, A., "A Memoir on the Theory of Matrices." *Proceedings of the Royal Society of London Series I*, Vol. 9, 1857, pp. 100–101.

[84] Crilly, T., "Cayley's anticipation of a generalised Cayley-Hamilton theorem," *Historia Mathematica*, Vol. 5, No. 2, 1978, pp. 211–219.

[85] Szabo, F., *The linear algebra survival guide: illustrated with Mathematica*, Academic Press, 2015.

[86] Blondel, V. D., Theys, J., and Tsitsiklis, J. N., "When is a pair of matrices stable?" *Unsolved problems in mathematical systems and control theory*, 2004, pp. 304.

[87] Sun, J., Park, H., Kolmanovsky, I., and Choroszucha, R., "Adaptive model predictive control in the IPA-SQP framework," *52nd IEEE Conference on Decision and Control*, IEEE, 2013, pp. 5565–5570.

[88] Bichi, M., Ripaccioli, G., Di Cairano, S., Bernardini, D., Bemporad, A., and Kolmanovsky, I. V., "Stochastic model predictive control with driver behavior learning for improved powertrain control," *49th IEEE conference on decision and control (CDC)*, IEEE, 2010, pp. 6077–6082.

[89] Lequime, M., Abel-Tiberini, L., Mathieu, K., Berthon, J., and Lumeau, J., "2× 2-array pixelated optical interference filters," *Optical Systems Design 2015: Advances in Optical Thin Films V*, Vol. 9627, International Society for Optics and Photonics, 2015, p. 96270V.

[90] Pannek, L. G. J. and Grüne, L., "Nonlinear Model Predictive Control: Theory and Algorithms," *Nonlinear Model Predictive Control*, Springer, 2011, pp. 2267–2274.

[91] Vallon, C. and Borrelli, F., "Task decomposition for iterative learning model predictive control," *2020 American Control Conference (ACC)*, IEEE, 2020, pp. 2024–2029.

[92] Boulet, B. and Duan, Y., "The fundamental tradeoff between performance and robustness-a new perspective on loop shaping-classic control revisited part ii," *Ieee Control Systems Magazine*, Vol. 27, No. 3, 2007, pp. 30–44.

[93] Hanson, M. A., "Invexity and the Kuhn–Tucker theorem," *Journal of mathematical analysis and applications*, Vol. 236, No. 2, 1999, pp. 594–604.

[94] Sitthi-Amorn, P., Ramos, J. E., Wangy, Y., Kwan, J., Lan, J., Wang, W., and Matusik, W., "MultiFab: a machine vision assisted platform for multi-material 3D printing," *Acm Transactions on Graphics (Tog)*, Vol. 34, No. 4, 2015, pp. 1–11.

[95] Lu, L., Zheng, J., and Mishra, S., "A layer-to-layer model and feedback control of inkjet 3-d printing," *IEEE/ASME Transactions on Mechatronics*, Vol. 20, No. 3, 2014, pp. 1056–1068.